Transition Metal Oxide Nanoparticles Decorated Carbon Nanomaterials as Earth-Abundant Electrocatalysts for Zinc-Air Batteries

by

Yingjie He

A thesis submitted in partial fulfillment of the requirements for the degree of

Doctor of Philosophy

Department of Chemistry
University of Alberta

Abstract

As awareness of global warming increases and the geopolitically influenced energy supply fluctuates, the global economy is in dire need of a transition from fossil fuels to renewable energy sources. Although renewable energies are sustainable and have favorable environmental impacts, they suffer from their intrinsic intermittency. This creates an imbalance between energy supply and demand on the electric grid. An efficient and cost-effective stationary energy storage technology has the potential of mitigating the energy imbalance while helping to realize the full potential of renewables. Recently zinc-air batteries have become a popular candidate for stationary energy storage owing, in part, to their low cost, high energy density, and safe design. The biggest challenge in commercializing zinc-air batteries, however, is the development of affordable electrocatalysts for the oxygen reduction and oxygen evolution reactions (ORR and OER, respectively) at the air electrode. Traditionally, precious metals such as platinum and ruthenium oxide are used. These materials have obvious drawbacks such as high cost and low earth-abundance. In recent years, transition metal oxide nanomaterials have been explored as alternatives to precious-metal-based catalysts due to their abundance and affordability. Carbon nanomaterials have also garnered attention because of their high surface area, electronic conductivity, and affordability. This dissertation describes the synthesis and characterization of hybrid electrocatalysts that combine

transition metal oxide nanoparticles and carbon nanomaterials. These hybrid catalysts outperform common precious metal benchmarks by large margins.

Chapter 1 introduces the current global energy outlook and its associated environmental impact. Subsequent discussion outlines the components and working principles of zinc-air batteries while providing context of the described work in the form of a high-level literature review. Finally, this chapter concludes with detailed descriptions of key characterization techniques used throughout the summarized experiments in Chapters 2 - 4.

Chapter 2 presents an investigation of a hybrid material, namely manganese oxide decorated hollow mesoporous carbon nanospheres (Mn_3O_4@HMC), as an efficient ORR catalyst for zinc-air batteries. This material was characterized thoroughly using a wide range of techniques and exhibits comparable catalytic performance in both half-cell and full-cell electrochemical testing to commercial benchmark Pt-Ru (30% platinum and 15% ruthenium dioxide on carbon black).

Chapter 3 expands on the foundation of Chapter 2, investigating the decoration of hollow mesoporous carbon (HMC) with other transition metal oxide nanoparticles. This study provided hybrids that excel in catalyzing ORR or OER. More importantly, cobalt oxide nanoparticle decorated HMC (Co_3O_4@HMC)

exhibited excellent bifunctional catalytic activity toward both ORR and OER, outperforming Pt-Ru in both reactions.

Chapter 4 describes a novel annealing method that generates hollow carbon cubes and simultaneously introduces catalytically active metal oxides and alloy nanoparticles using cobalt-based zeolitic imidazolate frameworks (ZIF-67) as a sacrificial template. This method eliminates the need for the dangerous hydrofluoric acid (HF) etching step in the traditional synthesis of hollow carbon nanomaterials (e.g., HMC). The hybrid exhibits promising bifunctional catalytic activity toward both ORR and OER as well as good durability in zinc-air batteries.

Chapter 5 summarizes and concludes the entire dissertation and provides insight into potential future projects.

Preface

This thesis focuses on the synthesis, characterization, and electrochemical testing of precious metal-free electrocatalysts for rechargeable alkaline zinc-air batteries. The work summarized in Chapters 2, 3, and 4 are my original work. All my research projects were conducted in collaboration with Dr. Douglas Ivey's group in the Department of Chemical and Materials Engineering at the University of Alberta.

In these projects, transmission electron microscopy (TEM) was performed by Dr. Haoyang Yu and Chuyi Ni from our group. Sarah Milliken conducted the X-ray photoelectron spectroscopy (XPS) and part of the powder X-ray diffraction (PXRD) measurements. Drew Aasen, Alexandra McDougall, Matthew Labbe, and Zahra Abedi from Dr. Ivey's group performed the electrochemical testing.

Versions of Chapters 2 and 3 of this thesis have been published as:

Chapter 2: He, Y.; Aasen, D.; Yu, H.; Labbe, M.; Ivey, D. G.; Veinot, J. G. C. Mn_3O_4 Nanoparticle Decorated Hollow Mesoporous Carbon Spheres as an Efficient Catalyst for Oxygen Reduction Reaction in Zn-Air Batteries. *Nanoscale Adv*. **2020**, *2*, 3367–3374.

Chapter 3: He, Y.; Aasen, D.; McDougall, A.; Yu, H.; Labbe, M.; Ni, C.; Milliken, S.; Ivey, D. G.; and Veinot, J. G. C. Hollow Mesoporous Carbon Nanospheres

Decorated with Metal Oxide Nanoparticles as Efficient Earth-Abundant Zinc-Air Battery Catalysts. *ChemElectrochem* **2021**, *8* (8), 1455–1463.

Also, a version of Chapter 4 is currently being prepared as a manuscript for submission.

Dedication

I dedicate this thesis to my parents, who have always loved and supported me unconditionally. Words cannot begin to describe my gratitude for your love and care.

我将这篇毕业论文献给一直无条件的爱我与支持我的父母。春晖寸草，父母的养育之恩永远报答不尽。

Acknowledgements

I am truly grateful to my supervisor, Dr. Jonathan Veinot, for providing me with every opportunity I could ever wish for in both my undergraduate and graduate studies. His support and guidance have been tremendously helpful to my research and my personal growth. His deep knowledge and impeccable character set a great example of what a true scientist and mentor should be. I will always be proud to have been his student.

I would like to thank my supervisory committee members Drs. Rik Tykwinski, Tom Nilges, and Julie Gibbs for their continuous support and guidance in the past five years. I also want to thank Dr. Douglas Ivey for the collaboration and conference opportunities he provided during my entire PhD.

I would like to thank all my group members who have helped me grow as a person. My special thanks go to Sarah Milliken. We have been through so much together, on both a professional and personal level. I am truly grateful to have her as a colleague and as a friend. I would also like to express my appreciation to my collaborators from the Ivey group. The work presented in this thesis would not have been possible without them.

I would like to thank Future Energy System (FES), Natural Sciences and Engineering Research Council (NSERC), Alberta Innovates, and Alberta / Technical

University of Munich International Graduate School for Hybrid Functional Materials (ATUMS) for their support in research funding and conference opportunities.

Table of Contents

List of Tables

List of Figures

List of Symbols, Nomenclature, and Abbreviations

Å	Angstrom
φ	Work function
η	Overpotential
λ	Wavelength
θ	Incident angle
h	Planck's constant
ν	Frequency
ν	Kinematic viscosity
ω	Rotating speed
ω	Radial frequency
Φ	Phase shift
A	Area
c	BET constant
C_{O2}	Bulk O_2 concentration
d	d-spacing
D_0	Diffusion coefficient
E_1	Heat of adsorption for the first layer
E_L	Heat of adsorption for the next layers
f	Applied frequency
i	Current
i_L	Diffusion-limiting current
i_K	Kinetic-limiting current
I_0	Maximum current (amplitude)
I_t	Current at time t
j	Current density
j_K	Kinetic-limiting current density
j_L	Diffusion-limiting current density
j_{max}	Maximum current density
$j_{measured}$	Measured current density
F	Faradaic constant
k	Electron transfer rate constant
m	Mass
n	Electron transfer number
N	Avogadro's number
p	Equilibrium pressure of adsorbates

p_0	Saturation pressure of adsorbates
R	Gas constant
s	Adsorption cross section of adsorbate
S_{total}	Total surface area
S_{BET}	BET specific surface area
t	Time
T	Temperature
v	Volume
V	Molar volume of the adsorbate
v_m	Volume of adsorbed gas when surface is covered by a monolayer
E_0	Maximum potential (amplitude)
$E_{1/2}$	Half-wave potential
E_{charge}	Charging potential
$E_{discharge}$	Discharge potential
$E_{equalibrium}$	Equilibrium potential
$E_{measured}$	Measured potential
E_{OC}	Open-circuit potential
E_{onset}	Onset potential
E_t	Applied potential at time t
$E_{vs\ MMO}$	Equilibrium potential vs. Hg/HgO
$E_{vs\ SHE}$	Equilibrium potential vs. SHE
R_{CT}	Charge-transfer resistance
R_{ohmic}	Ohmic resistance
Z	Impedance
Z_0	Amplitude of impedance
Z_i	Imaginary part of impedance
Z_r	Real part of impedance
2D	Two dimensional
3D	Three dimensional
AC	Alternating current
Ag/AgCl	Silver chloride electrode
ALD	Atomic layer deposition
BE	Binding energy
BET	Brunauer, Emmett and Teller
BF	Bright field
CNT	Carbon nanotube
Co_3O_4@HMC	Co_3O_4 nanoparticle decorated hollow mesoporous carbon nanospheres

CoNi@HCC	CoNi nanoparticle decorated hollow carbon cubes
CV	Cyclic voltammetry
DF	Dark field
EDX/EDS	Energy dispersive X-ray spectroscopy
EIS	Electrochemical impedance spectroscopy
FTIR	Fourier-transform infrared spectroscopy
GC	Glassy carbon
GDL	Gas diffusion layer
HAADF	High angle annular dark field
HER	Hydrogen evolution reaction
HF	Hydrofluoric acid
Hg/HgO	Mercury/mercury oxide electrode
HCC	Hollow carbon cube
HMC	Hollow mesoporous carbon
HRTEM	High resolution transmission electron microscopy
Ir/C	Iridium on carbon black
K-L	Koutecký–Levich
KE	Kinetic energy
LSV	Linear sweep voltammetry
Mn_3O_4@HMC	Mn_3O_4 nanoparticle decorated hollow mesoporous carbon nanospheres
MOF	Metal organic framework
MPL	Microporous layer
NP	Nanoparticle
OER	Oxygen evolution reaction
ORR	Oxygen reduction reaction
PDA	Polydopamine
Pt/C	Platinum on carbon black
Pt-Ru	30% Pt and 15% RuO_2 on carbon black
Pt-RuO_2/C	Platinum and ruthenium oxide on carbon black
PXRD	Powder X-ray diffraction
RDE	Rotating disk electrode
RHE	Reversible hydrogen electrode
RTIL	Room temperature ionic liquids
SAED	Selected area electron diffraction
SE	Secondary electron
SEM	Scanning electron microscopy
SHE	Standard hydrogen electrode
SiO_2@C	SiO_2 nanoparticle encapsulated in carbonized shell

STEM	Scanning transmission electron microscopy
TEM	Transmission electron microscopy
TEOS	Tetraethoxysilane
Tris	Tris(hydroxymethyl)amino-methane
XPS	X-ray photoelectron spectroscopy
ZIF	Zeolitic imidazolate framework
Zn-air	Zinc-air

Chapter 1: Introduction

1.1 Global Energy Outlook

As more countries have experienced more urbanization and industrialization, global energy consumption and the associated carbon dioxide (CO_2) emission have skyrocketed in the past few decades.[1] The main cause for increased CO_2 emissions is society's widespread dependance on fossil fuels.[2] Looking to the past decade, 45% of CO_2 emissions can be attributed to the energy sector (i.e., electricity and heat production).[3] Over 23% of CO_2 originated from industries such as materials production and manufacturing.[3] The transportation sector including land transport, marine, and aviation generated 22.5% of the total CO_2 emission.[3] The remaining 9.5% fossil CO_2 originated from activities such as fishing and agriculture.[3]

As CO_2 is one of the greenhouse gases, elevated CO_2 levels contribute to global warming by absorbing outgoing energy from the Earth and reemitting it back, effectively trapping the heat and increasing earth's temperature.[4] To mitigate the effects of global warming, the energy sector is starting to decarbonize the economy and replacing fossil fuels with renewable energy sources such as wind, solar, and hydroelectric powers.[5]

Renewable energies, in comparison to fossil fuels, benefit from their sustainability and limited environmental impact.[6] Renewable energy sources include but are not limited to solar, wind, hydropower, geothermal, and biofuels.[7] Energy

harvesting from renewable energy sources, especially solar and wind power, has witnessed tremendous growth in the past few years, achieving 4% and 7% in global installed capacity, respectively.[8] However, renewables like solar and wind power still suffer from their intrinsic intermittency.[9] That is, the electricity generation from these energy sources is inconsistent. As energy consumption and the fluctuation of renewable energy production are unlikely to synchronize, the intermittency essentially creates a mismatch between electricity supply and demand. This issue is further complicated by the ever-growing global energy consumption.[10] One common solution to mitigate the intermittency is to implement backup energy storage technologies to moderate fluctuations in energy supply.[11] In doing so, the excess electricity in the grid can be stored during times of energy surplus and later released during electricity deficit. If this is to be realized, efficient and cost-effective stationary energy storage technologies are urgently needed to create a more stable and environmentally responsible electrical grid.

1.2 Zinc-Air Batteries

1.2.1 Zinc-Air battery overview

Batteries are attractive candidates for grid-level stationary energy storage due to their high efficiency, scalability, and ease of installation.[11-13] Zinc-air batteries (Zn-air) have gained considerable attention in light of their advantages over

conventional lithium-ion batteries. Zn-air batteries have the potential for substantially higher theoretical energy density (1353 Wh kg^{-1} excluding oxygen) than Li-ion batteries (≤350 Wh kg^{-1}), as shown in Figure 1-1.[14-16] They are also considerably cheaper than Li-ion batteries ($100 kW^{-1} h^{-1} vs. $150 kW^{-1} h^{-1}) due to the abundance and low cost of their raw materials.[15] This cost advantage is expected to improve with a predicted cost of $10 kW^{-1} h^{-1} for optimized Zn-based systems.[17] The advantages of Zn-air batteries expand to safety because they utilize aqueous electrolyte that eliminates the risk of fire or explosion.[18]

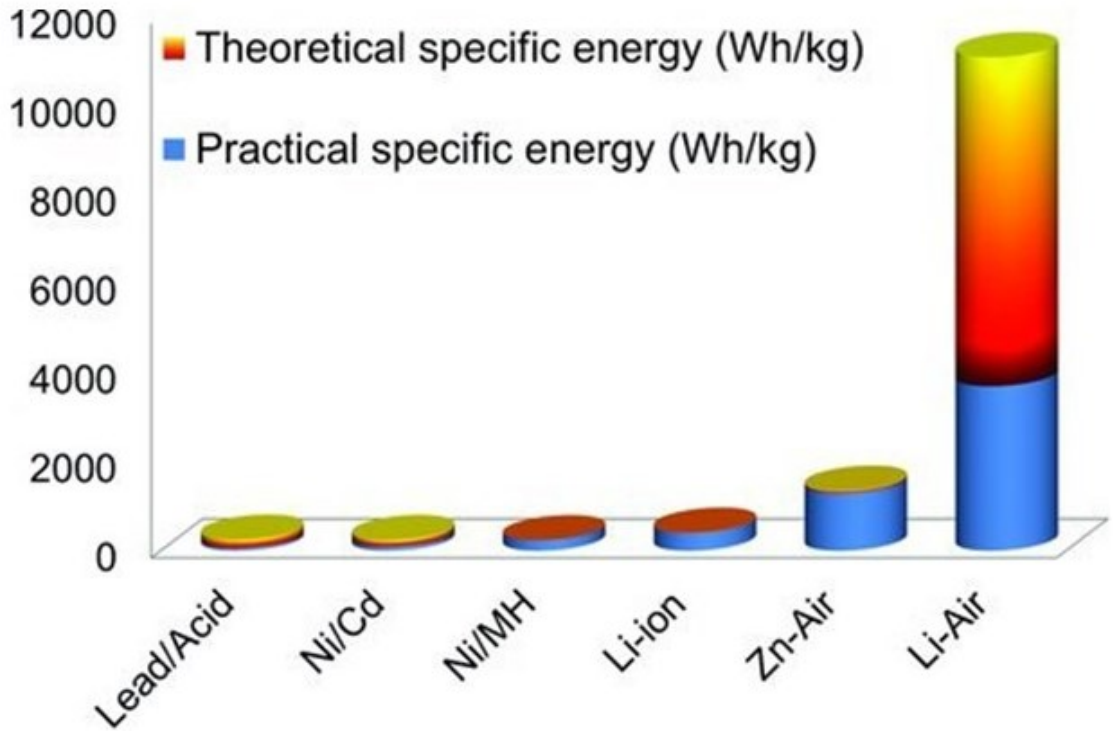

Figure 1-1. Theoretical and practical energy densities of various types of rechargeable batteries. Reproduced with permission.[16] Copyright 2010, John Wiley and Sons.

Figure 1-2 shows the common design of an aqueous alkaline Zn-air battery, including gas diffusion layer (GDL), catalyst layer, separator, electrolyte, and the Zn electrode.[18] In practice, the catalyst layer is usually deposited onto the side of the GDL facing the electrolyte. The catalyst-loaded GDL is commonly referred to as air electrode. The separator is only used in small coin cells.

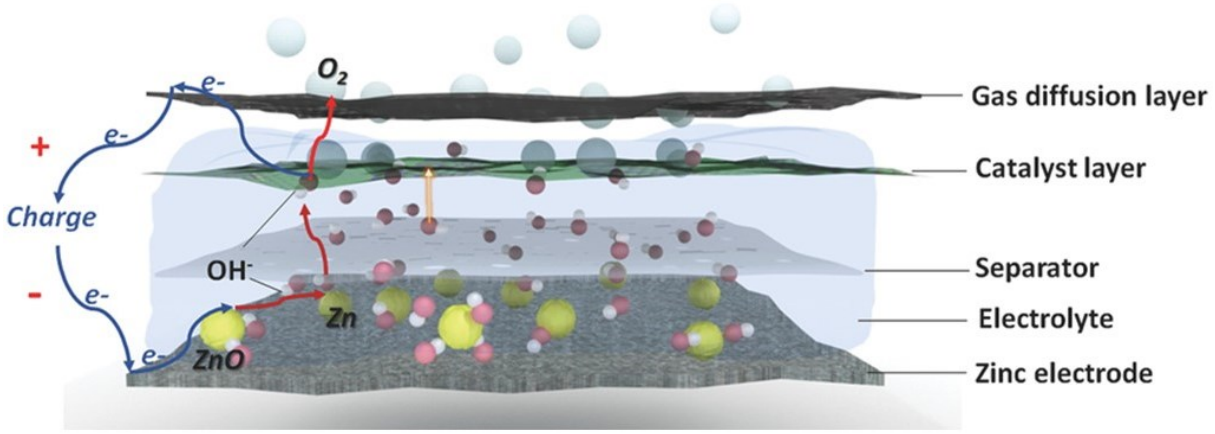

Figure 1-2. Pictorial representation of an aqueous alkaline Zn-air battery during recharging. Reproduced with permission.[18] Copyright 2016, John Wiley and Sons.

1.2.2 Half-reactions active in Zn-air batteries

Zn-air batteries function on the principle of separating the oxidation of metallic Zn into two half-reactions.[16] When the battery discharges, the following forward reactions occur:

Zn electrode:

$$Zn + 4OH^- \rightleftharpoons Zn(OH)_4^{2-} + 2e^- \qquad E^0 = -1.25\ V\ vs.SHE \qquad (1\text{-}1)$$

Upon realization of $Zn(OH)_4^{2-}$ saturation in the electrolyte:

$$Zn(OH)_4^{2-} \rightleftharpoons ZnO + H_2O + 2OH^- \qquad (1\text{-}2)$$

Air electrode:

$$O_2 + 2H_2O + 4e^- \rightleftharpoons 4OH^- \qquad E^0 = 0.401\ V\ vs.SHE \qquad (1\text{-}3)$$

Overall reaction:

$$2Zn + O_2 \rightleftharpoons 2ZnO \qquad E^0 = 1.65\ V \qquad (1\text{-}4)$$

During discharge, the metallic Zn electrode reacts with OH^- ions in the alkaline electrolyte to form zincate anions $[Zn(OH)_4]^{2-}$ and electrons (Eq. 1-1). Once the electrolyte is saturated with $[Zn(OH)_4]^{2-}$, $[Zn(OH)_4]^{2-}$ decomposes into ZnO (Eq. 1-2). Simultaneously, the electrons travel through the external circuit and arrive at the air electrode. At the air electrode, atmospheric O_2 diffuses through the gas diffusion layer (GDL) and arrive at the catalyst layer, where the O_2 is reduced by the electrons to form OH^-, replenishing the electrolyte. This process is commonly referred to as the oxygen reduction reaction (ORR; Eqn. 1-3). Although O_2 participates in the half-reactions, it is not stored inside the batteries. The high energy density of Zn-air batteries partially originates from the fact that Zn-air batteries utilize atmospheric

O_2 molecules as one of the reactants in the half-reactions.[19] When Zn-air batteries are recharged, the reverse reactions of those summarized in Eqs. 1-1, 1-2, and 1-3 occur. At the air electrode, the reverse reaction of ORR regenerates O_2 and is commonly referred to as oxygen evolution reaction (OER).

Both ORR and OER have high activation energy barriers and are thus kinetically sluggish.[20] As a result, polarization can be observed at the air electrode (Figure 1-3).[16] Polarization is a phenomenon in which the observed electrode potential deviates from its equilibrium potential upon passage of faradaic current.[21] Faradaic current is defined as the rate at which electrons are transferred across the electrode-electrolyte interface as a result of reduction or oxidation reactions.[22] Non-faradaic current is generated due to other processes such as double-layer charging in the absence of any redox reactions.[23] The extent of polarization is termed overpotential (η) and is calculated using the following equation:

$$\eta = E_{measured} - E_{equilibrium} - iR_{ohmic} \quad (1\text{-}5)$$

where $E_{measured}$ represents the experimentally measured working electrode potential, $E_{equilibrium}$ is the theoretical equilibrium potential, i represents current, and R_{ohmic} is the ohmic resistance in the circuit.[24] In other words, overpotential is the potential difference between the thermodynamically calculated equilibrium potential ($E_{equililibrium}$) and the measured potential ($E_{measured}$) at which the associated redox

reactions actually take place, excluding potential drop due to ohmic resistance in other parts of the circuit.[25] High overpotentials have negative impact on Zn-air batteries. As shown in Figure 1-3, the overpotential in ORR (discharge reaction) reduces the practical discharge potential and the OER overpotential raises the charging potential of the batteries, resulting in a decrease in battery efficiency. To reduce the overpotentials and improve Zn-air battery performance, ORR and OER electrocatalysts are required.

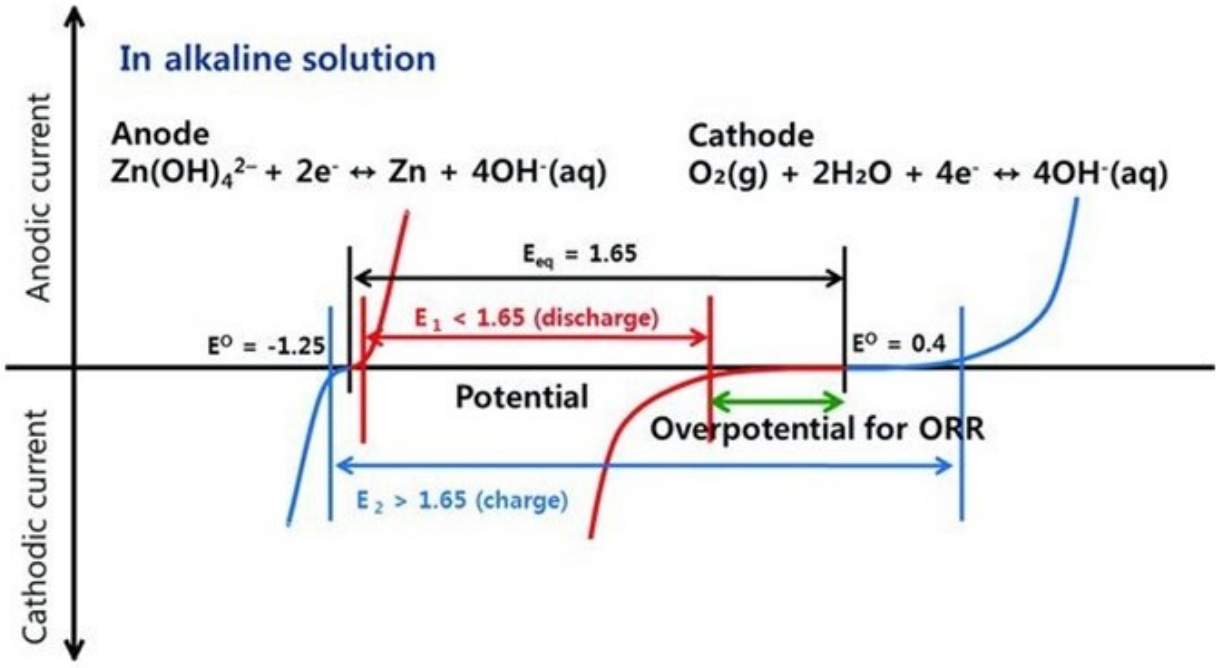

Figure 1-3. Schematic of alkaline Zn-air battery polarization curves. Reproduced with permission.[16] Copyright 2010, John Wiley and Sons.

1.2.3 Accepted ORR and OER mechanisms in Zn-air batteries

It is generally accepted that the ORR can proceed via a two-electron (2e) or four-electron (4e) pathway. The detailed mechanisms of the pathways are shown below:[26-28]

2e $$O_2 + H_2O + 2e^- \rightarrow HO_2^- + OH^- \quad (1\text{-}6)$$

4e $$O_2 + 2H_2O + 4e^- \rightarrow 4OH^- \quad (1\text{-}7)$$

The OH_2^- generated from the 2-electron pathway (Eqn. 1-6) can be further reduced by electrons:

2e' $$HO_2^- + H_2O + 2e^- \rightarrow 3OH^- \quad (1\text{-}8)$$

or go through disproportionation:

2e'' $$2HO_2^- \rightarrow 2OH^- + O_2 \quad (1\text{-}9)$$

The two-electron pathway is generally considered undesirable because it generates HO_2^- that can potentially corrode the electrode assembly.[29] Therefore, the 4-electron pathway (Eqn. 1-7) is usually preferred for ORR in Zn-air battery applications. Precious-metal-based catalysts such as Pt/C (platinum on carbon black) almost exclusively utilize the 4-electron pathway.[30] An electrochemical technique, namely rotating disk electrode (RDE) voltammetry, is often applied to determine which pathway dominates a catalyst behavior. RDE is explained in detail in Section 1.5.3.

The mechanism of OER can be divided into the following elementary steps:[31-33]

$$* + OH^- \rightarrow HO^* + e^- \quad (1\text{-}10)$$

$$HO^* + OH^- \rightarrow O^* + H_2O + e^- \quad (1\text{-}11)$$

$$2O^* \rightarrow 2* + O_2 \quad (1\text{-}12)$$

$$O^* + OH^- \rightarrow HOO^* + e^- \quad (1\text{-}13)$$

$$HOO^* + OH^- \rightarrow * + O_2 + H_2O + e^- \quad (1\text{-}14)$$

where * represents active sites on the catalyst, and O^*, HOO^*, and HO^* denote adsorbed intermediates. There are also two pathways for these steps. A catalyzed OER can either go through Eq. 1-10 to 1-12, regenerating O_2 through the dissociation of O^*, or go through Eq. 1-10, 1-11, 1-13, and 1-14.[33]

1.2.4 Zinc electrode

As Zn-air batteries utilize atmospheric O_2 which provides a virtually unlimited supply; hence, the capacity of these batteries solely depends on the quantity of available metallic Zn.[34] However, phenomena such as dendrite growth, shape change, and passivation on the Zn electrode can cause loss of battery capacity, particularly after long-term cycling.[35-37] Moreover, the hydrogen evolution reaction (HER) can occur on the Zn surface, which corrodes the electrode and reduces the functional

Zn.[38] Solutions to these important issues such as high surface area electrodes, binders, electrode additives, and electrolyte additives have been studied to mitigate these issues.[39-42] A detailed discussion of Zn electrode behavior is beyond the scope of the present thesis and the reader is directed to recent reviews.[43, 44]

1.2.5 Electrolyte

As one might expect, the electrolyte in Zn-air batteries plays a pivotal role by influencing ionic conductivity and interfacial properties that, in turn, impact capacity retention, cycling stability, and charging and discharging potentials.[18, 45] Aqueous and non-aqueous electrolytes have been explored aggressively for Zn-air battery applications. To date, aqueous electrolytes still dominate in Zn-air batteries due to benefits such as high ionic conductivity, low cost and toxicity, as well as non-flammability.[46] Compounding the appeal of water-based electrolytes, non-aqueous systems such as room temperature ionic liquids (RTILs) and solid-state electrolytes suffer from low energy density and low conductivity that result in poor battery performances.[47] Among aqueous systems, alkaline electrolytes are the most popular owing to the associated favorable (fast) kinetics of zinc chemistry, high O_2 solubility, high solubility of zinc salt, and large selection of electrocatalysts.[48] Potassium hydroxide (KOH), sodium hydroxide (NaOH), and lithium hydroxide (LiOH) are among the most widely adopted alkaline electrolytes.[49] KOH solutions are preferred for most Zn-air battery applications because of their high ionic conductivity (0.625

S cm^{-1}), high oxygen diffusion coefficients (1.7×10^{-7} mol cm^{-3}), and low viscosity (1.6×10^{-2} cm^2 s^{-1}; all numbers provided are for 6 M KOH at 25˚C).[50, 51] As the concentration of KOH affects the electrolyte properties and battery performance, specific concentrations of aqueous KOH solutions are used in different electrochemical testing techniques. Details are provided in Section 1.5.

1.2.6 Gas diffusion layers

The gas diffusion layer (GDL) is an essential component in Zn-air batteries and is part of the air electrode. The GDL provides a bilayer structure that allows for drastically different physical properties in each layer (Figure 1-4). The backing layer (facing atmospheric O_2) consisting of carbon fiber is macroporous and hydrophobic.[52] The macroporosity facilitates efficient and uniform distribution of the atmospheric O_2, while the hydrophobicity prevents flooding.[18, 53-55] Flooding is a phenomenon where electrolyte accumulates inside the GDL due to poor water management; this can occur as a result of changes in wettability inside GDL arising from long-term electrochemical testing.[56, 57] Flooding has catastrophic effect on Zn-air battery performance; the electrolyte blocks the pores and reduces O_2 mass transport from the atmosphere to the catalyst layer.[57] Aside from O_2 transport and flooding prevention, the backing layer also provides mechanical support, enhancing GDL properties making them flexible and resistant to compression.[58] The microporous layer (MPL, lower blue layer facing electrolyte), which comprises

carbon black, is less hydrophobic.[18] The catalyst layer is created by depositing electrocatalysts on the lower side of MPL (facing electrolyte). The microporosity and hydrophobicity further prevent flooding, as it demands a higher pressure for the water formed at the catalyst layer to access the macropores in the upper layer.[59, 60] The presence of slight hydrophilicity in the MPL improves lateral water diffusion at the MPL-catalyst layer interface, which also counters flooding in the catalytically active areas.[61] In addition to water management, the MPL also minimizes contact resistance, improves conductivity, and acts as a support for electrocatalysts.[18, 62] It is important to note that the macroporosity and microporosity mentioned here are industry standardized terminologies/jargon.[63] They are not to be confused by the strict definitions in materials science, where micropores are less than 2 nm in diameter while macropores are larger than 50 nm.[64] A catalyst-loaded GDL is commonly referred to as the air electrode.

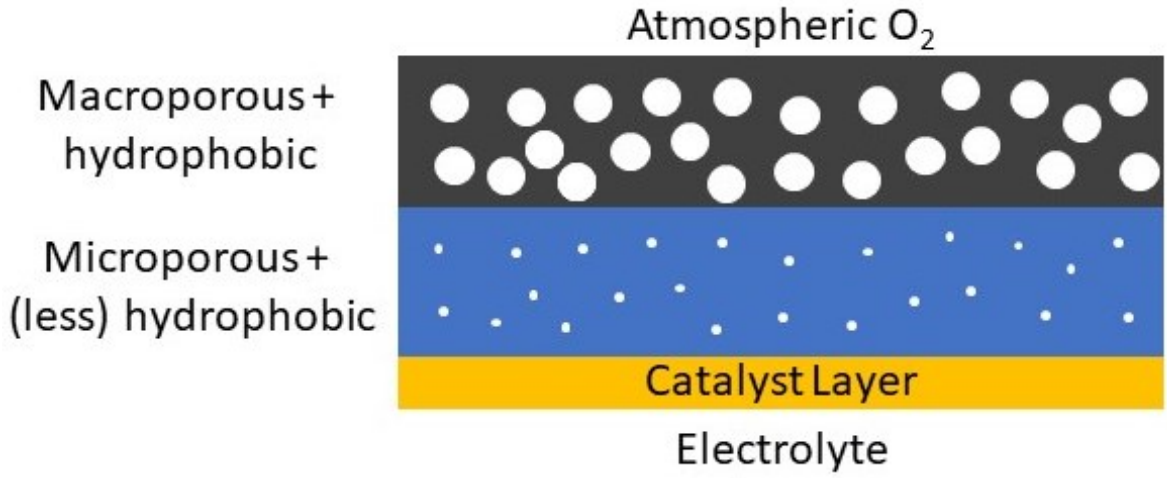

Figure 1-4. Schematic of a gas diffusion layer (GDL) bilayer structure.

1.3 ORR and OER Electrocatalysts

As both ORR and OER experience high activation energy barriers, electrocatalysts are required for Zn-air batteries to function efficiently. Ideally, bifunctional electrocatalysts that facilitate both reactions are desired because separating ORR and OER into different electrodes complicates battery design. In the following section, common metrics used to evaluate Zn-air battery electrocatalysts and a selection of example catalysts from academic literature are discussed.

Many techniques and metrics are used to examine electrocatalysts in Zn-air battery community. The most common way to evaluate catalysts is through linear sweep voltammetry (LSV). In LSV, features such as onset potential (E_{onset}) and half-wave potential ($E_{1/2}$) can be observed.[65, 66] E_{onset} is the potential at which the reaction proceeds with the assistance from electrocatalysts. It is defined as the potential at which the absolute value of measured current density surpasses a certain value (10 mA cm^{-2} in this work). E_{onset} is used to calculated overpotential (η) via Eqn. 1-5 from Section 1.2.2. A small overpotential indicates good catalytic activity and the closer E_{onset} is to equilibrium potential ($E_{equilibrium}$), the better the catalyst. In the context of Zn-air battery, a good bifunctional catalyst should have a relatively positive E_{onset} for ORR and a relatively negative E_{onset} for OER. The difference between E_{onset} values for ORR and OER is sometimes used to represent a catalyst's bifunctional

activity, as a small difference indicates a good bifunctional catalyst. $E_{1/2}$ is defined as the potential at which current density reaches half of its maximum or limiting value. $E_{1/2}$ is used in identical fashion to E_{onset}. In reality, E_{onset} and $E_{1/2}$ are defined differently (e.g., they may be defined at 2, 5, or 10 mA cm^{-2}) across literature and are measured against various reference electrodes, making it difficult to compare catalysts from different works. Therefore, it is common practice for authors to include electrochemical data for commercial benchmarks such as platinum (Pt) and ruthenium oxide (RuO_2) for direct comparison. In literature, electrocatalysts are often incorporated into homemade prototype Zn-air battery cells whose discharge and charging potentials are measured ($E_{discharge}$ and $E_{charging}$, respectively). As mentioned in Section 1.2.2, the overpotential reduces $E_{discharge}$ and increases $E_{charging}$, resulting in poor battery efficiency. Zn-air battery efficiency is defined by the following equation:

$$Efficiency\ \% = \frac{E_{discharge}}{E_{charging}} \times 100\% \qquad (1\text{-}15)$$

In other words, a good bifunctional catalyst should have a high $E_{discharge}$ and low $E_{charging}$ due to its ORR and OER catalytic activities, resulting in high efficiency. Alternative to efficiency, discharge-charge voltage gap is sometimes used to reflect the bifunctional activity of a catalyst. A small voltage gap, similar to high efficiency, represents a good bifunctional catalyst. A good ORR catalyst with high $E_{discharge}$

could also potentially result in high peak power density from the battery. Zn-air batteries loaded with catalysts of interest are often cycled to evaluate the durability of the catalysts. $E_{discharge}$, $E_{charging}$, and efficiency are measured before and after the cycling. The working principles and procedures of these techniques are explained in detail in Section 1.5.

1.3.1 Precious metals

Traditionally, platinum (Pt) is used for ORR owing to its high catalytic activity.[67] However, Pt is a poor OER catalyst due to the formation of an oxide outer layer through which OH^- needs to diffuse to trigger OER.[68] Ruthenium oxide (RuO_2) or iridium oxide (IrO_2) are excellent OER catalysts, but they have poor ORR activity.[69, 70] All these catalysts contain precious metals, whose scarcity and high cost greatly hinder the large-scale commercialization of Zn-air batteries. Moreover, precious-metal-based catalysts are usually dispersed onto carbon support with high surface area (e.g., carbon black). During Zn-air battery operation, the precious metal particles can agglomerate and/or detach from the carbon support, resulting in the loss of electrochemical surface area.[71] This causes precious-metal-based catalysts to have poor durability in rechargeable Zn-air batteries.

There are several methods that can increase the feasibility of precious-metal catalysts. The first is to utilize precious metal nanomaterials. In the context of

electrocatalysis, precious metal nanomaterials provide higher surface area per unit weight, tunable surface chemistry, and stronger synergistic effects between the metal and carbon support.[72] Nanomaterials also possess dense low-coordinated species such as edges and steps that are more likely to promote reactions due to their higher surface free energy.[73] Precious metal catalysts with a variety of morphologies have been explored for Zn-air battery applications. Pt nanowires have shown superior catalytic activity to that of commercial platinum on carbon black (Pt/C), displaying more positive onset potential (E_{onset}) in ORR.[74] RuO_2 nanosheets exhibited an overpotential of 215 mV in OER against reversible hydrogen electrode (RHE), outperforming bulk RuO_2 which had an overpotential of 498 mV.[75] Other morphologies such as nanocages, nano-octahedra, and nanoplates of precious metals have also been explored as ORR and OER catalysts.[76-78]

The second method involves alloying precious metals with affordable transition metals. This approach not only reduces cost, but also enhances the catalytic activity and durability of the catalyst. Porous films of $Pt_{1.1\%}Fe_{8.8\%}Ni$ exhibited excellent ORR performance with an E_{onset} of 1.0 V and a half-wave potential ($E_{1/2}$) of 0.87 V (vs. RHE).[79] Both these values are 20 mV more positive than commercial Pt/C. Zn-air batteries equipped with $Pt_{1.1\%}Fe_{8.8\%}Ni$ porous films delivered a remarkable peak power density of 175.0 mW cm^{-2} at 330 mA cm^{-2}, significantly higher than commercial Pt/C+RuO_2 (69.6 mW cm^{-2} at 100 mA cm^{-2}).

The Zn-air battery maintained an impressive voltage gap of 0.64 V after 400 h of cycling, while the voltage gap of Pt/C+RuO_2 deteriorated to 0.82 V after just 5 h.

Doping precious metals with main group elements has also seen some success with associated improvements in catalytic activity. When the PtCo alloy is doped with interstitial F (denoted as PtCoF), excellent ORR E_{onset} of 0.95 V (vs. RHE), superior to undoped PtCo (0.92 V), is achieved.[80] The $E_{1/2}$ of PtCoF (0.88 V) is also more positive than PtCo (0.86 V). Interestingly, the OER overpotential was also improved by 17 mV after F-doping. Zn-air batteries equipped with PtCoF not only experienced a peak power density of 125 mW cm^{-2}, but also a small voltage gap of 0.9 V after 240 h of cycling. In contrast, commercial Pt/C+RuO_2 only displayed 55 mW cm^{-2} of peak power density and a large voltage gap of 1.03 V after cycling. This suggests that doping also mitigates the poor durability of precious metal catalysts.

1.3.2 Transition metal oxides

Transition metals and their oxides are desirable for electrocatalyst applications owing to their high abundance and low cost. First-row transition metals can also benefit from their low toxicity.[81] In recent years, transition metals such as manganese (Mn), cobalt (Co), iron (Fe), and nickel (Ni), as well as their oxides have been studied extensively as alternatives to more expensive precious metals as Zn-air battery catalysts.

Despite substantial research, the community's understanding of the mechanism of transition metal oxide catalyzed ORR in alkaline solution is still very limited. Recently, a reasonable mechanism has been proposed.[82-86] In the 4-electron pathway, the reaction can be divided into the following elementary steps:

$$M^{(m+1)+}\text{-}O^{2-} + H_2O + e^- \rightarrow M^{m+}\text{-}OH^- + OH^- \quad (1\text{-}16)$$

$$O_2 + e^- \rightarrow O_{2,ads}^- \quad (1\text{-}17)$$

$$M^{m+}\text{-}OH^- + O_{2,ads}^- \rightarrow M^{(m+1)+}\text{-}O\text{-}O^{2-} + OH^- \quad (1\text{-}18)$$

$$M^{(m+1)+}\text{-}O\text{-}O^{2-} + H_2O + e^- \rightarrow M^{m+}\text{-}O\text{-}OH^- + OH^- \quad (1\text{-}19)$$

$$M^{m+}\text{-}O\text{-}OH^- + e^- \rightarrow M^{(m+1)+}\text{-}O^{2-} + OH^- \quad (1\text{-}20)$$

In the two-electron pathway, HO_2^- ions are produced after Eq. 1-18:

$$M^{(m+1)+}\text{-}O\text{-}O^{2-} + H_2O + e^- \rightarrow M^{m+}\text{-}OH^- + HO_2^- \quad (1\text{-}21)$$

On the surface of transition metal oxides, OER proceeds via the elementary steps summarized in Section 1.2.3, Eqs. 1-10 to 1-14.

Cobalt oxides (CoO_x) are excellent candidates for Zn-air batteries. This is particular true for spinel Co_3O_4 which is an efficient bifunctional electrocatalyst due to the presence of Co^{2+} and Co^{3+}. Co^{2+} is suggested to effectively promote ORR, whereas Co^{3+} can facilitate OER.[87-89] Hollow Co_3O_4 nanospheres have exhibited promising OER activity, with overpotential of 352 mV (vs. RHE), lower than 384

mV of iridium on carbon black (Ir/C).[90] These hollow Co_3O_4 also displayed an E_{onset} of 0.87 V for ORR, comparable to the 0.91 V of Pt/C. After cycling for 200 h, hollow Co_3O_4 nanospheres maintained a higher discharge potential and lower charging potential than Pt/C. In another study, Co_3O_4 nanoparticles (NPs) supported by carbon nanofiber (C-CoPAN900) were also explored as Zn-air battery catalyst.[91] Its ORR $E_{1/2}$ was measured at -0.188 V against silver chloride electrode (Ag/AgCl), comparable to Pt/C (-0.092 V). In OER testing, C-CoPAN900 displayed an E_{onset} of 0.64 V, better than 0.73 V of Pt/C. Zn-air battery equipped with C-CoPAN900 showcased a discharge potential of 1.26 V at 1 mA cm^{-2}, comparable to Pt/C. The charging potential of C-CoPAN900 (1.96 V) is significantly lower than Pt/C (2.09 V). The voltage gap of C-CoPAN900 only increased from 0.70 V to 0.78 V after 135 h of cycling, suggesting great durability. In contrast, Zn-air battery equipped with Pt/C experienced an increase of 0.26 V (from 0.83 V to 1.09 V) in voltage gap. Other Co_3O_4 nanomaterials including nanowires, nanoplates, and nanofilms have also been explored.[92-96]

Manganese oxide (MnO_x) is a particularly attractive ORR catalyst owing to its high abundance and low cost.[97] The ORR catalytic activity of MnO_x has been well documented in literature.[98-100] Mn_3O_4 NPs on Ti_3C_2 MXene (Mn_3O_4/MXene) with identical E_{onset} to Pt/C (0.89 V vs. RHE) was reported.[101] The Mn_3O_4/MXene exhibited peak power density of 150 mW cm^{-2}, higher than Pt/C (115 mW cm^{-2}).

MnO_x prepared via atomic layer deposition (ALD) displayed comparable E_{onset} to Pt/C and higher maximum current density.[102] The MnO_x had a peak power density of 184 mW cm^{-2}, higher than Pt/C (158 mW cm^{-2}). Zn-air batteries equipped with MnO_x nanowires demonstrated a peak power density of 190 mW cm^{-2} and discharge capacity of 300 mA h g^{-1}.[103] These performance values are comparable to what is observed for batteries based upon Pt/C.

Similar to CoO_x, iron and their oxides (FeO_x) have also shown promising bifunctional activity toward both ORR and OER.[104-106] High density iron NPs encapsulated in carbon shell (denoted as Fe@-C-700) with excellent bifunctional catalytic activity was reported.[107] Fe@-C-700 exhibited a superior (more positive) $E_{1/2}$ (0.83 V vs. Ag/AgCl) to Pt/C (0.82 V) while maintaining comparable limiting current density. The difference in ORR and OER E_{onset} of Fe@-C-700 was measured to be 0.88 V, much smaller than 1.21 V of Pt/C and 1.06 V of IrO_2. This indicates promising bifunctional activity of the iron catalyst. Zn-air battery equipped with Fe@-C-700 displayed a peak power density of 220 mW cm^{-2}, higher than Pt/C (192 mW cm^{-2}). Fe/Fe_2O_3 NPs on Fe-N-doped carbon nanosheets (Fe/Fe_2O_3@Fe-N-C-1000) also displayed excellent bifunctional activity in Zn-air batteries.[108] Fe/Fe_2O_3@Fe-N-C-1000 exhibited an ORR E_{onset} of 0.52 V (vs. Ag/AgCl), comparable to Pt/C (0.58 V). Its OER E_{onset} was measured at 0.69 V, comparable to

RuO_2 (0.59 V). Fe/Fe_2O_3@Fe-N-C-1000 also displayed a peak power density of 193 mW cm^{-2}, higher than Pt-RuO_2/C (173 mW cm^{-2}).

Ni and nickel oxides (NiO_x) have been used in a wide range of applications such as batteries, supercapacitors, and electrocatalysis.[109-111] Seaweed biomass derived (Ni, Co)/CNT aerogels (Ni/NiO/$NiCo_2O_4$/N-CNT-As) with bifunctional activity in Zn-air batteries have been reported.[112] Ni/NiO/$NiCo_2O_4$/N-CNT-As exhibited 1.43 V of OER E_{onset} vs. RHE, outperforming IrO_2/C. Its ORR E_{onset} was 0.89 V, very close to 0.92 V of Pt/C. Zn-air batteries equipped with Ni/NiO/$NiCo_2O_4$/N-CNT-As displayed initial charging and discharge potentials of 1.95 V and 1.20 V, respectively. After 70 cycles, the charging potential decreased to 1.94 V and the discharge potential only dropped to 1.14 V, indicating excellent durability. N-doped NiO nanosheets (N-NiO) synthesized via hydrothermal method were also studied.[113] The nanosheets exhibited small OER overpotential of 270 mV vs. RHE, outperforming Ir/C. The N-NiO also displayed satisfactory OER E_{onset} of 0.9 V vs. RHE. Zn-air battery equipped with N-NiO also exhibit high power density of 112.3 mW cm^{-2}.

1.3.3 Graphitic carbon nanomaterials

Carbon nanomaterials have been investigated extensively in recent years owing to their benefits such as low cost, high surface area, high conductivity, and

tailorability.[114, 115] Graphitic carbon is a class of carbon materials with multilayered sheets made up of sp^2 hybridized carbon atoms. The sheets are held together via van der Waals interactions.[116] Graphitic carbon nanomaterials such as carbon nanotubes (CNT) and graphene nanosheets are being investigated for applications in photonics, biosensors, transistors, telecommunications, fuel cells, batteries, and memory devices.[117-128]

Doped graphitic carbon nanomaterials have gained attention as ORR and OER catalysts. The introduction of heteroatoms induces charge and spin redistribution due to the differences in charge, size, and electronegativities between the carbon and dopant atoms.[116] Common dopants include nitrogen (N), oxygen (O), boron (B), sulfur (S), and phosphorus (P). It has been suggested that these dopants enhance the ORR catalytic activity to varying extents, with B > N > P > O > S.[129] Co-doped carbon nanomaterials that include more than one dopant type have shown enhanced catalytic activity beyond that of their counterparts with single dopants.[130, 131]

The ORR mechanism facilitated by heteroatom-doped carbons is commonly summarized as outlined in equations 1-22 through 1-26:[33]

$$O_2(g) + * \rightarrow O_2^* \quad (1\text{-}22)$$

$$O_2^* + H_2O(l) + e^- \rightarrow HOO^* + OH^- \quad (1\text{-}23)$$

$$HOO^* + e^- \rightarrow O^* + OH^- \quad (1\text{-}24)$$

$$O^* + H_2O(l) + e^- \rightarrow HO^* + OH^- \quad (1\text{-}25)$$

$$HO^* + e^- \rightarrow * + OH^- \quad (1\text{-}26)$$

where * represents active sites, and O^*, HOO^*, and HO^* represent the adsorbed intermediates. The OER mechanism that is believed to be active with heteroatom-doped carbons is similar to that of transition metals, described in Section 1.2.3.

N, P, F-codoped carbon nanoflowers (denoted as NPF@CNF-800) have been reported to show bifunctional activity for ORR and OER.[132] The NPF@CNF-800 exhibited an E_{onset} of 0.97 V and a $E_{1/2}$ of 0.85 V vs. RHE. Both values are comparable to those observed for Pt/C with E_{onset} of 1.01 V and $E_{1/2}$ of 0.86 V. Zn-air batteries equipped with the NPF@CNF-800 demonstrated a peak power density of 159 mW cm^{-2} that is significantly higher than the Pt/C (91 mW cm^{-2}) equivalent. NPF@CNF-800 was also cycled bifunctionally and displayed high initial efficiency of 62.3%, comparable to Pt/C+IrO_2 (64.8%). After over 810 cycles, NPF@CNF-800

maintained an efficiency of 58.1%. In contrast, the efficiency of Pt/C+IrO_2 plummeted to 54.1% after just 288 cycles. B, N co-doped graphene aerogel (BN-GAs-2) was also reported.[133] BN-GAs-2 demonstrated an E_{onset} of -0.05 V vs. Ag/AgCl for ORR, comparable to Pt/C (0.02 V). Its OER E_{onset} was measured at 0.37 V, lower than RuO_2. When incorporated into a battery, BN-GAs-2 exhibited 40 mW cm^{-2} in power density and superior stability to Pt/C+RuO_2.

Heteroatom-doped carbon has also been widely used as support for precious metal or transition metal catalysts. Fe-Co NPs embedded in a N-doped 3D carbon matrix (CoFe/N-GCT) were reported with ORR and OER activity.[134] CoFe/N-GCT exhibited a small E_{onset} difference of 0.88 V (vs. RHE), outperforming Pt/C (0.91 V). It was also incorporated into a Zn-air battery which demonstrated a peak power density of 203 mW cm^{-2}, almost double that of Pt/C+RuO_2 (107 mW cm^{-2}). The initial discharge and charging potentials of CoFe/N-GCT are 1.22 and 2.02 V, respectively. This corresponds to a voltage gap of 0.80 V. After 267 h (1600 cycles) of bifunctional cycling, the voltage gap only increased to 0.82 V. In contrast, Pt/C+RuO_2 experienced significant increase in voltage gap after just 240 cycles, indicating poor durability. Perovskite oxide NPs intertwined with CNT (IT-CCBC) were also reported.[135] The E_{onset} of IT-CCBC for ORR and OER were comparable to Pt/C and Ir/C, respectively. Zn-air battery equipped with IT-CCBC exhibited 1.02 V of discharge potential and 2.17 V of charging potential at 50 mA cm^{-2}. These values

were maintained after over 40 hours of bifunctional cycling (10 cycles). In contrast, Pt/C and Ir/C showed limited stability after just 15 h and 20 h of cycling, respectively.

1.3.4 Metal organic frameworks

Metal-organic frameworks (MOF), assembled using metal ions/clusters and multidentate organic linkers via coordination bonds, have gained considerable attention.[136, 137] MOFs have been investigated for applications in carbon capture, drug delivery, and catalysis because of their high surface area and tunable porosity.[138-141] MOFs have also become a popular precursor for heteroatom-doped porous carbon nanomaterials as they offer a convenient source of transition metals that can be incorporated into the carbon matrices.[142] In the context of Zn-air batteries, many MOFs have been used to synthesize high surface area hybrid electrocatalysts. Fe-based MOFs was used to derive N, S-codoped carbon matrices containing Fe_3C and Fe_3S NPs.[143] The E_{onset} for ORR of one of the hybrids investigated in this particular study (i.e., FeS/Fe_3C@NS-C-900) was measured at 1.03 V (vs. RHE) and was comparable to a Pt/C standard (1.05 V). In terms of OER, the Fe-MOF-900 demonstrated an E_{onset} of 120 mV vs. RHE, outperforming the performance of IrO_2/C (180 mV). With this in mind, the authors demonstrated a Zn-air battery equipped with Fe-MOF-900 that exhibited an initial efficiency of 58.1%. and that efficiency only dropped to 53.7% after 865 h (1730 cycles). In contrast, an equivalent battery with Pt/C+IrO_2 tested under the same conditions experienced a significant drop in

efficiency after just 80 h. MOF-derived 2D N-doped carbon nanosheets coupled with Co-Fe-P-Se (denoted as Co-Fe-P-Se/NC) were also developed.[144] Co-Fe-P-Se/NC exhibited an overpotential of (270 mV vs. RHE) for OER, lower than RuO_2 (290 mV). It also displayed a $E_{1/2}$ of 0.76 V, comparable to Pt/C. The peak power density of Co-Fe-P-Se/NC was measured at 104 mW cm^{-2}, very close to Pt/C+RuO_2 (108.5 mW cm^{-2}). After being cycled at 10 mA cm^{-2} for 40 h, the voltage gap of Co-Fe-P-Se/NC becomes smaller than that of Pt/C+RuO_2, suggesting its superior stability.

1.4 Materials Characterization

1.4.1 Scanning electron microscopy (SEM)

Scanning electron microscopy (SEM) is a common imaging technique used to evaluate nanomaterials. In SEM, a columnated monochromatic electron beam irradiates the specimen in vacuum. The collision between the incident electrons and specimen generates backscattered electrons, secondary electrons, and X-rays, which can provide crucial morphological, topographical, and compositional information about the specimen. Secondary electrons are the most commonly exploited in SEM imaging due to the rich morphological and topographical information they offer. The X-rays are characteristic to each element present in the specimen and provide qualitative and quantitative elemental composition. This is commonly referred to as energy dispersive X-ray spectroscopy (EDX/EDS).

1.4.2 Transmission electron microscopy and scanning transmission electron microscopy (TEM and STEM)

Transmission electron microscopy (TEM) is another imaging technique. It is performed by directing a beam of accelerated electrons at specimen. The transmitted electrons generate bright field (BR) TEM images, which provide information on morphology and thickness about the specimen. An advanced version of TEM, namely scanning transmission electron microscopy (STEM) uses a converged electron beam that is transmitted through a specimen, generating images with atomic resolution. It is important to note that neither TEM nor STEM provides definitive information on shapes as the images are a "shadow" of the specimen. High angle annular dark field (HAADF) STEM images are generated by collecting diffracted electrons. High resolution TEM (HRTEM) can be achieved through the interference between the transmitted and diffracted electrons. HRTEM provides crucial information on lattice spacing. Selected area electron diffraction (SAED) is performed using TEM in diffraction mode. The diffracted electron beams provide information on crystallinity and d-spacings of the sample. EDX/EDS is often incorporated into STEM instrument to perform elemental mapping at atomic resolution.

1.4.3 Powder X-ray diffraction (PXRD)

Powder X-ray diffraction (PXRD) is a common technique used to evaluate the structure of crystalline materials. PXRD is performed by radiating monochromatic X-rays onto a specimen and the reflected X-rays are collected. Constructive interference of the X-rays occurs when Bragg's Law is satisfied, shown below:

$$n\lambda = 2d\ sin\theta \tag{1-27}$$

where n is a positive integer, λ is the wavelength of incident X-ray, d is the spacing between specimen crystalline planes, and θ is the incident angle. The detector or the specimen is rotated, and the intensity of reflected X-ray is recorded as a function of associated incident angle (θ), generating a PXRD pattern. PXRD patterns are characteristic to different crystalline structures. Therefore, PXRD is commonly used to fingerprint and identify unknown crystalline materials.

1.4.4 X-ray photoelectron spectroscopy (XPS)

X-ray photoelectron spectroscopy (XPS) is a surface sensitive technique used to obtain elemental information. It is performed by irradiating a sample with monochromatic X-rays. When the X-rays collide with specimen surface, an inner electron is excited and leaves the specimen. The kinetic energy of the excited electron is measured and used to calculate the binding energy of the original inner electron using the following equation:

$$BE = h\nu - KE - \varphi \tag{1-28}$$

where BE is the binding energy, h is Planck's constant, ν is the frequency of incident X-ray, KE is the kinetic energy, and φ is the work function specific to the element. The intensity of the excited electrons is plotted against the BE, generating an XPS spectrum. XPS spectrum provides information regarding the chemical environment (e.g., oxidation state) and quantity of individual elements.

1.4.5 Brunauer–Emmett–Teller (BET) surface area analysis

In this work, BET analysis is performed by physical adsorption of nitrogen gas molecules onto the surface of materials of interest to probe properties such as specific surface area, average pore volume, and pore size distribution.[145, 146] The BET equation is shown below:

$$\frac{1}{\mathrm{v}(\frac{p_0}{p} - 1)} = \frac{c - 1}{\mathrm{v}_m c}\left(\frac{p}{p_0}\right) + \frac{1}{\mathrm{v}_m c} \tag{1-29}$$

where v is volume of adsorbed gas, p_0 is saturation pressure of adsorbates, p is equilibrium pressure of adsorbates, c is the BET constant, and v_m is the volume of adsorbed gas when surface is covered by a monolayer. The BET constant c is defined as:

$$c = e^{\frac{E_1 - E_L}{RT}} \tag{1-30}$$

where E_1 and E_L are the heat of adsorption for the first and next layers, respectively. R is the gas constant (8.314 J K^{-1} mol^{-1}) and T is temperature in Kelvin (K). Equation 1-29 is a linear function from which v_m and c can be extracted using the slope and y-intercept. The v_m is then used to calculate the specific surface area using the equations below:

$$S_{total} = \frac{v_m N s}{V} \tag{1-31}$$

$$S_{BET} = \frac{S_{total}}{m} \tag{1-32}$$

where S_{total} and S_{BET} are the total surface area and BET specific surface area, respectively. N is the Avogadro's number, m is mass of the material of interest, s is the adsorption cross section of the adsorbate (N_2), and V is the molar volume of the adsorbate.

1.5 Electrochemical Characterization

1.5.1 Cyclic voltammetry (CV)

Cyclic voltammetry (CV) is a common electrochemical technique used to probe electron transfer processes (i.e., reduction and oxidation). CV is performed by cycling potential sweep at working electrode within a particular voltage and monitoring the current passed. When investigating electron transfer processes, a background scan is usually performed, and a background current is collected. The

background current is often referred to as capacitive current, double-layer current, or non-faradaic current.[147] In the context of Zn-air batteries, CV is used to determine whether an electrocatalyst is active toward ORR or OER, by observing the increase in faradaic current within a potential window. CV is a well-established technique and in-depth details are discussed in literature.[148]

1.5.2 Linear sweep voltammetry (LSV)

Linear sweep voltammetry (LSV) is a preliminary technique used to compare catalytic activity of electrocatalysts. Like CV, LSV is performed by sweeping the potential on a catalyst-loaded working electrode linearly (a typical scan rate is 5 mV s^{-1}) through a potential window and collecting the current passed. Unlike CV, the scanning stops once the potential at the working electrode reaches a target value (i.e., it does not cycle back).

LSV is usually performed on a three-electrode cell that includes working, counter, and reference electrodes (Figure 1-5). The current flows between the counter electrode and working electrode, while the working electrode potential is measured against the reference electrode. This way, the potential at reference electrode is a constant value. The working electrode used in the three-electrode system is a piece of catalyst-loaded GDL (1×2 cm^2) with predetermined catalyst loading. The counter electrode is a platinum (Pt) wire. And the reference electrode

is Hg/HgO (0.098V vs. standard hydrogen electrode at 25˚C in 1M KOH). During a standard LSV testing, the electrolyte is always saturated with O_2 by continuously purging it with O_2 at a constant rate.

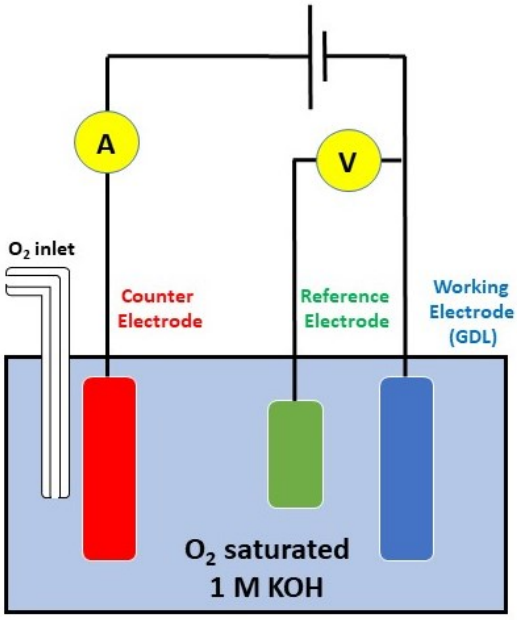

Figure 1-5. A pictorial representation of a three-electrode system.

The standard reduction potentials using standard hydrogen electrode (SHE) as reference are converted to values against Hg/HgO using the following equation:

$$E_{vs\ MMO} = E_{vs\ SHE} - 0.098\ V \tag{1-33}$$

where $E_{vs\ MMO}$ and $E_{vs\ SHE}$ are the equilibrium potentials vs. Hg/HgO and SHE reference electrodes, respectively. In 1 M KOH, the equilibrium potential of ORR/OER system is $E_{vs\ MMO} = 0.401 - 0.098\ V = 0.303\ V$. 1 M KOH is chosen

for standard LSV testing due to its high ionic conductivity and satisfactory O_2 solubility for stationary electrode voltammetry.[149, 150]

For ORR and OER, LSV was performed in potential windows of 0 V to -0.5 V and 0.2 V to 0.7 V vs. Hg/HgO, respectively. As mentioned in Section 1.3, onset potential (E_{onset}) is an essential feature in LSV testing. In this work, E_{onset} is defined as the potential at which the absolute value of current density surpasses 10 mA cm^{-2}. For electrocatalysts, the E_{onset} should be as close to the theoretical equilibrium potentials as possible. In other words, good ORR catalysts have relatively positive (close to 0.303 V vs. Hg/HgO) E_{onset}, whereas OER catalyst have relatively negative (close to 0.303 V vs. Hg/HgO) E_{onset}. Maximum current density (j_{max}) obtained in LSV is also of interest as it can provide qualitative information on the electric conductivity and the associated electrochemical surface area of the catalyst of interest.

1.5.3 Rotating disk electrode (RDE)

Rotating disk electrode (RDE) is a special form of LSV commonly used to evaluate electron-transfer kinetics of redox reactions. The cell setup is very similar to regular LSV, using the three-electrode system with Hg/HgO and Pt wire as reference and counter electrodes, respectively. The cell is also constantly purged with O_2 to maintain an O_2-saturated KOH electrolyte. In regular LSV, the mass

transfer processes take place in the form of diffusion, convection, and migration through porous GDL with complex structures.[151] In RDE, a rotating electrode with a flat glassy carbon (GC) surface is used as the working electrode instead, shown in Figure 1-6. The catalyst is coated on the flat surface of the rotating GC to ensure that mass transport is only caused by convection, which is in turn dictated by the rotating speed of GC.

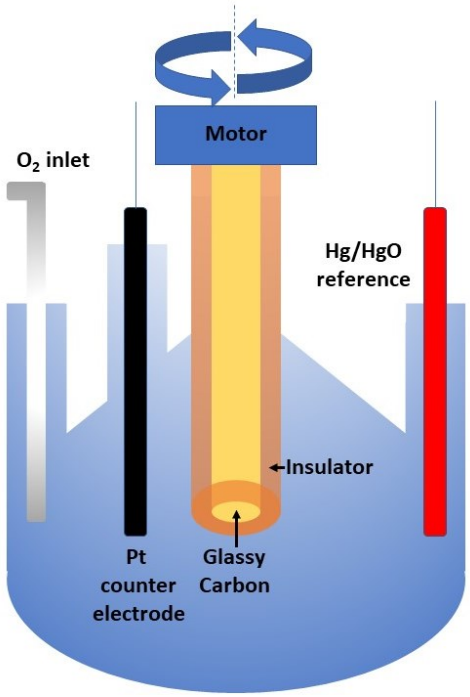

Figure 1-6. Pictorial representation of a standard RDE apparatus.

In RDE, the collected LSV curve can be divided into three regions (Fig. 1-7). At low overpotential (kinetic region), the reaction rate is limited by the sluggish kinetics of ORR and the measured current density is dictated by the activation energy barrier. At moderate overpotential (mixed region), the reaction rate and the

associated current density are influenced by both the reaction kinetics and mass transport (convection) of the active species. At high overpotential, indicated by the diffusion region, the active species react as soon as they come in contact with the catalyst coated electrode. In this region, the current density depends entirely on the mass transport. As mass transport only takes place in the form of convection in RDE, the observed limiting current density is a function of the rotating speed of the working electrode.

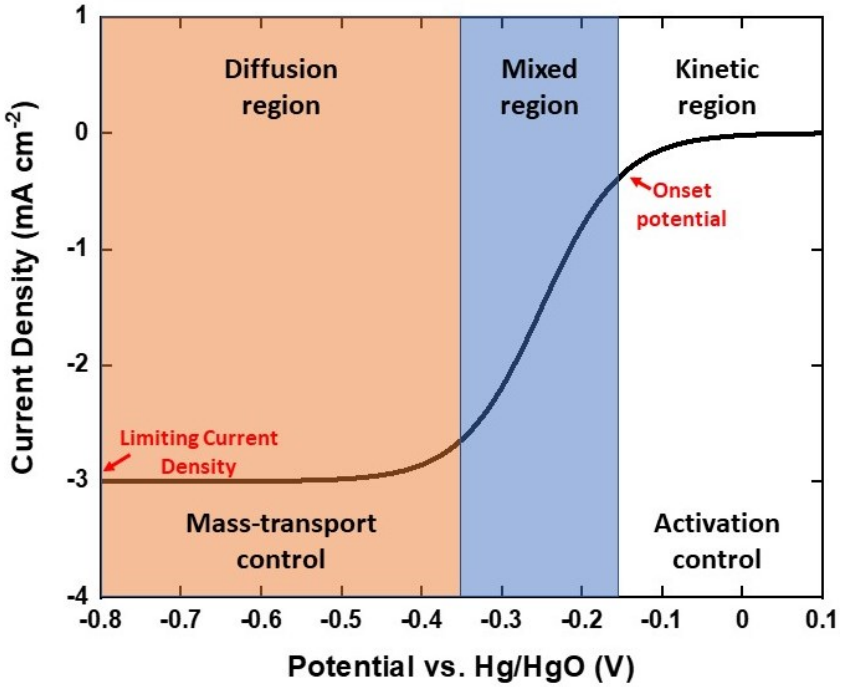

Figure 1-7. Typical ORR LSV curve from RDE.[152]

The measured current density can be calculated using the Koutecký–Levich equation:[153]

$$\frac{1}{|j_{measured}|} = \frac{1}{|j_L|} + \frac{1}{|j_K|} = \frac{1}{B\omega^{0.5}} + \frac{1}{|j_K|} \quad (1\text{-}34)$$

$$j_k = nFkC_{O_2} \quad (1\text{-}35)$$

$$B = 0.62nFC_{O_2}v^{-\frac{1}{6}}D_0^{\frac{2}{3}} \quad (1\text{-}36)$$

where $j_{measured}$, j_L, and j_K are the measured current density, diffusion-limiting current density, and kinetic-limiting current density, respectively. ω is the rotating speed (rad s^{-1}). n is the electron transfer number, F is the faradaic constant (96485 C mol^{-1}, k is the electron transfer rate constant, C_{O2} is the bulk O_2 concentration, ν is the kinematic viscosity of the electrolyte, and D_0 is the diffusion coefficient of the electrolyte. 0.1 M KOH is commonly used for RDE testing as its high O_2 solubility compensates for the low surface area of the working electrode.[51] In 0.1 M KOH, the above constants are 1.2×10^{-6} mol cm^{-3} (C_0), 1.9×10^{-5} cm^2 s^{-1} (D_0), and 0.01 cm^2 s^{-1} (υ), respectively. By using RDE, one can calculate the electron transfer number for the reaction of interest. As mentioned in Section 1.2.3, ORR can proceed through a two or four-electron pathway, and the four-electron pathway is generally preferred. In RDE, an electron-transfer number (n) close to the value of 4 is a good indication

that ORR takes place via the preferred four-electron pathway using the catalyst of interest.

1.5.4 Galvanostatic full cell testing

Galvanostatic testing is an electrochemical method for battery evaluation. It is performed by collecting the battery potential while maintaining a constant current density through the battery. In Zn-air battery applications, galvanostatic rate test and discharge/charge cycling are often performed to evaluate the electrocatalysts. In this work, a vertical cell design is used for galvanostatic rate test as it minimizes the noise signal from bubbles (Fig. 1-8). A horizontal cell is used for discharge/charge cycling to prevent flooding (Fig. 1-9).

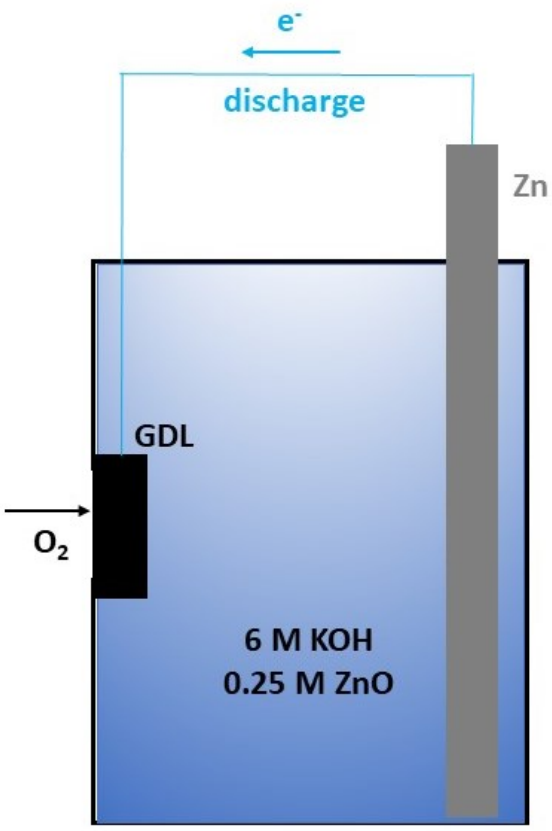

Figure 1-8. Pictorial representation of a vertical prototype Zn-air battery cell.

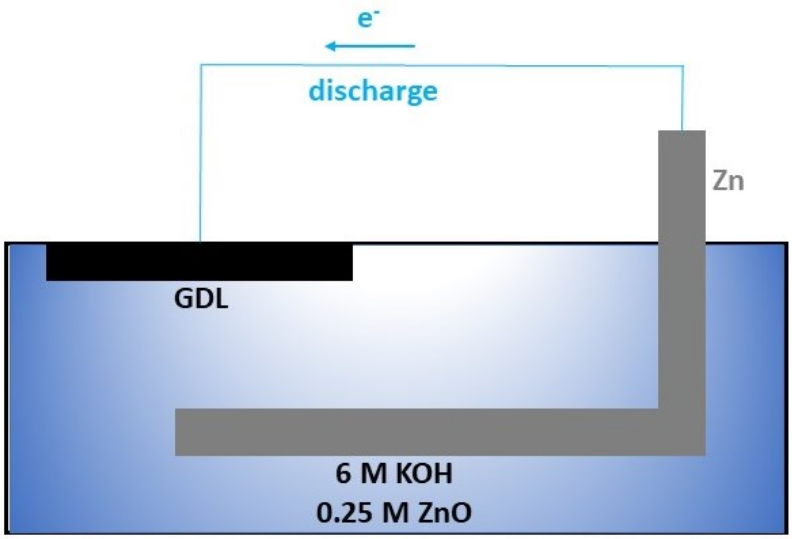

Figure 1-9. Schematic of a horizontal prototype Zn-air battery cell.

In galvanostatic discharge rate test, discharge current densities of 2, 5, 10 and 20 mA cm^{-2} are maintained for 10 min, while the discharge potential of the battery is collected as a function of time (min). As mentioned in Section 1.2.2 and 1.3, the discharge potential is greatly reduced by overpotential. Overpotential can be visualized as a charge-transfer resistance. This relationship is shown in the following equation:

$$E_{discharge} = E_{OC} - iR_{CT} - iR_{ohmic} \quad (1\text{-}37)$$

where $E_{discharge}$ and E_{OC} represent the measured discharge potential and open-circuit potential of the battery, respectively. i is the current, R_{CT} is charge-transfer resistance, and R_{ohmic} is the ohmic resistance from the circuit. An ORR electrocatalyst can reduce the overpotential and R_{CT}, resulting in a higher discharge potential from the battery.

In a galvanostatic charge rate test, charging current of same current densities were maintained for 10 min each and the charging potentials are measured as a function of time. Overpotential drastically increases the necessary charging potential to deliver the charging current via the following equation:

$$E_{charge} = E_{OC} + iR_{CT} + iR_{ohmic} \quad (1\text{-}38)$$

where E_{charge} represents required charging potential and other terms are identical to in Eqn. 1-37. In this case, an OER catalyst can reduce the charging potential by minimizing the OER overpotential and its associated R_{CT}.

Discharge/charge cycling is performed by discharging a prototype Zn-air battery at a predetermined current density (e.g., 10 mA cm^{-2}) for 10 min and resting the battery for 5 min, followed by a charging process at the same current density (current of opposite direction) for another 10 min and resting the battery for 5 min. One discharge process combined with one charging process are referred to as one cycle (30 min). This cycle is then repeated for an extended period of time. As mentioned in Section 1.3, Zn-air battery efficiency can be obtained by dividing the $E_{discharge}$ with $E_{charging}$ (Eqn. 1-15). The battery efficiency is an essential indicator for catalyst stability. It is calculated before and after cycling. Higher efficiency, especially after long-term cycling, suggests a stable electrocatalyst for Zn-air battery.

In galvanostatic testing, 6 M KOH combined with 0.25 M ZnO is used as electrolyte. The highly concentration KOH provides high ionic conductivity to the battery.[154] The presence of ZnO in the electrolyte suppresses a side reaction: hydrogen evolution reaction (HER).[155]

1.5.5 Electrochemical impedance spectroscopy (EIS)

Electrochemical impedance spectroscopy (EIS) is performed by applying an alternating potential wave to the working electrode and recording the resulting current. The function of the alternating potential is expressed in Eqn. 1-39 below[156]:

$$E_t = E_0 \sin(\omega t) \tag{1-39}$$

$$\omega = 2\pi f \tag{1-40}$$

where E_t is the applied potential at time t, E_0 is the maximum potential (amplitude), ω is radial frequency, and f is applied frequency. The alternating potential results in an alternating current shifted in phase Φ, shown below:

$$I_t = I_0 \sin(\omega t + \Phi) \tag{1-41}$$

where I_t is the current at time t, I_0 is the maximum current (amplitude), and Φ is the phase shift. The overall impedance (Z) of the circuit is calculated from the equation below:

$$Z = \frac{E}{I} = Z_0 e^{i\Phi} = Z_0(\cos\Phi + i\sin\Phi) \tag{1-42}$$

where Z_0 is the amplitude of the overall impedance and i is the imaginary number. When the imaginary part (Z_i) is plotted against the real part (Z_r), a Nyquist plot is generated. The x-intercepts of the Nyquist plot provide quantitative information regarding ohmic resistance and charge-transfer resistance.[157, 158]

1.6 Scope of The Thesis

The work outlined in this thesis describes the synthesis and characterization of a wide range of affordable precious-metal-free Zn-air battery catalysts. Chapter 2 presents hollow mesoporous carbon (HMC) nanospheres decorated with Mn_3O_4 nanoparticles (NP) as an efficient ORR catalyst. This was the first time HMC was combined with transition metal oxide NPs and is a proof of concept for using HMC as a porous carbon support. The hybrid exhibited excellent ORR catalytic activity and outperformed commercial benchmark Pt-Ru (30% Pt and 15% RuO_2 on carbon black) in all testing environments.

Chapter 3 expands on the foundation of Chapter 2, by incorporating a large selection of transition metal oxides into HMC. Among the catalysts of interest, some exhibited outstanding ORR performance (e.g., $MnCo_2O_4$@HMC) while others displayed excellent OER activity (e.g., 'CoFeNiO'@HMC). Most interestingly, Co_3O_4@HMC demonstrated superior bifunctional activity toward both ORR and OER to Pt-Ru. The hybrid also exhibited excellent durability, outperforming Pt-Ru in long-term bifunctional cycling.

Chapter 4 steps away from HMC synthesized via hydrofluoric acid etching and move toward hollow carbon cubes (HCC), prepared using thermally unstable ZIF-67 as a sacrificial template. By utilizing the thermal instability of ZIF-67,

carbonization, template removal, and metal (e.g., CoNi) introduction were accomplished in one single step, dramatically simplifying the synthesis. CoNi@HCC exhibited promising ORR and OER performance, as well as good durability after long term cycling.

Chapter 5 summarizes the thesis and provides insights into the contribution from this work to Zn-air battery community. It also proposes alternative applications of the materials discussed in this work and potential future projects.

1.7 References

(1) Al-mulali, U.; Sab, C. N. B. C.; Fereidouni, H. G. *Energy* **2012**, *46* (1), 156-167.
(2) Waheed, R.; Chang, D. F.; Sarwar, S.; Chen, W. *J. Clean. Prod.* **2018**, *172*, 4231-4238.
(3) Peters, G. P.; Andrew, R. M.; Canadell, J. G.; Friedlingstein, P.; Jackson, R. B.; Korsbakken, J. I.; Le Quere, C.; Peregon, A. *Nat. Clim. Change.* **2020**, *10* (1), 3-6.
(4) Kweku, D.; Bismark, O.; Maxwell, A.; Desmond, K.; Danso, K.; Oti-Mensah, E.; Quachie, A.; Adormaa, B. *JSRR* **2017**, *17* (6), 1-9.
(5) Gielen, D.; Boshell, F.; Saygin, D.; Bazilian, M. D.; Wagner, N.; Gorini, R. *Energy Strateg. Rev.* **2019**, *24*, 38-50.
(6) Le, T. H.; Chang, Y.; Park, D. *Energ J.* **2020**, *41* (2), 73-92.
(7) Panwar, N. L.; Kaushik, S. C.; Kothari, S. *Renew. Sust. Energ. Rev.* **2011**, *15* (3), 1513-1524.
(8) Sinsel, S. R.; Riemke, R. L.; Hoffmann, V. H. *Renew. Energ.* **2020**, *145*, 2271-2285.
(9) Notton, G.; Nivet, M. L.; Voyant, C.; Paoli, C.; Darras, C.; Motte, F.; Fouilloy, A. *Renew. Sust. Energ. Rev.* **2018**, *87*, 96-105.
(10) Grubler, A.; Wilson, C.; Bento, N.; Boza-Kiss, B.; Krey, V.; McCollum, D. L.; Rao, N. D.; Riahi, K.; Rogelj, J.; De Stercke, S.; Cullen, J.; Frank, S.; Fricko, O.; Guo, F.; Gidden, M.; Havlik, P.; Huppmann, D.; Kiesewetter, G.; Rafaj, P.; Schoepp, W.; Valin, H. *Nat. Energy* **2018**, *3* (6), 515-527.

(11) Zhang, C.; Wei, Y. L.; Cao, P. F.; Lin, M. C. *Renew. Sust. Energ. Rev.* **2018**, *82*, 3091-3106.
(12) Soloveichik, G. L. *Annu. Rev. Chem. Biomol.* **2011**, *2*, 503-527.
(13) Chen, T.; Jin, Y.; Lv, H.; Yang, A.; Liu, M.; Chen, B.; Xie, Y.; Chen, Q. *Trans. Tianjin Univ.* **2020**, *26* (3), 208-217.
(14) Van Noorden, R. *Nature* **2014**, *507* (7490), 26-28.
(15) Zhang, J.; Zhou, Q. X.; Tang, Y. W.; Zhang, L.; Li, Y. G. *Chem. Sci.* **2019**, *10* (39), 8924-8929.
(16) Lee, J. S.; Kim, S. T.; Cao, R.; Choi, N. S.; Liu, M.; Lee, K. T.; Cho, J. *Adv. Energy Mater.* **2011**, *1* (1), 34-50.
(17) Li, Y. G.; Dai, H. J. *Chem. Soc. Rev.* **2014**, *43* (15), 5257-5275.
(18) Fu, J.; Cano, Z. P.; Park, M. G.; Yu, A. P.; Fowler, M.; Chen, Z. W. *Adv. Mater.* **2017**, *29* (7), 1604685.
(19) Wang, K.; Pei, P.; Zuo, Y.; Wei, M.; Wang, H.; Zhang, P.; Chen, Z.; Shang, N. *Iscience* **2022**, *25* (2), 103837.
(20) Zhang, W.; Lai, W. Z.; Cao, R. *Chem. Rev.* **2017**, *117* (4), 3717-3797.
(21) Zalka, D.; Peter, L. *J. Solid State Electr.* **2020**, *24* (11-12), 2595-2602.
(22) Kissinger, P. T. *Curr. Sep.* **2002**, *20* (2), 51-53.
(23) Hoyt, N. C.; Savinell, R. F.; Wainright, J. S. *Chem. Eng. Sci.* **2016**, *144*, 288-297.
(24) Mandin, P.; Derhoumi, Z.; Roustan, H.; Rolf, W. *Electrochim. Acta.* **2014**, *128*, 248-258.
(25) Norskov, J. K.; Rossmeisl, J.; Logadottir, A.; Lindqvist, L.; Kitchin, J. R.; Bligaard, T.; Jonsson, H. *J. Phys. Chem. B* **2004**, *108* (46), 17886-17892.
(26) Zhou, R. F.; Zheng, Y.; Jaroniec, M.; Qiao, S. Z. *ACS Catal.* **2016**, *6* (7), 4720-4728.
(27) Qiu, K. P.; Chai, G. L.; Jiang, C. R.; Ling, M.; Tang, J. W.; Guo, Z. X. *ACS Catal.* **2016**, *6* (6), 3558-3568.
(28) Wiggins-Camacho, J. D.; Stevenson, K. J. *J. Phys. Chem. C* **2011**, *115* (40), 20002-20010.
(29) Peng, L. S.; Shang, L.; Zhang, T. R.; Waterhouse, G. I. N. *Adv. Energy Mater.* **2020**, *10* (48), 2003018.
(30) Stephens, I. E. L.; Bondarenko, A. S.; Gronbjerg, U.; Rossmeisl, J.; Chorkendorff, I. *Energ. Environ. Sci.* **2012**, *5* (5), 6744-6762.
(31) Dau, H.; Limberg, C.; Reier, T.; Risch, M.; Roggan, S.; Strasser, P. *Chemcatchem* **2010**, *2* (7), 724-761.
(32) Suen, N. T.; Hung, S. F.; Quan, Q.; Zhang, N.; Xu, Y. J.; Chen, H. M. *Chem. Soc. Rev.* **2017**, *46* (2), 337-365.
(33) Zhu, X. F.; Hu, C. G.; Amal, R.; Dai, L. M.; Lu, X. Y. *Energ. Environ. Sci.* **2020**, *13* (12), 4536-4563.

(34) Fu, J.; Liang, R. L.; Liu, G. H.; Yu, A. P.; Bai, Z. Y.; Yang, L.; Chen, Z. W. *Adv. Mater.* **2019**, *31* (31), 1805230.
(35) Jung, C. Y.; Kim, T. H.; Kim, W. J.; Yi, S. C. *Energy* **2016**, *102*, 694-704.
(36) Shen, Y. W.; Kordesch, K. *J. Power Sources* **2000**, *87* (1-2), 162-166.
(37) Wang, R. Y.; Kirk, D. W.; Zhang, G. X. *J. Electrochem. Soc.* **2006**, *153* (5), C357-C364.
(38) Lee, T. S. *J. Electrochem. Soc.* **1971**, *118* (8), 1278.
(39) Huang, J. H.; Yang, Z. H.; Wang, R. J.; Zhang, Z.; Feng, Z. B.; Xie, X. E. *J. Mater. Chem. A* **2015**, *3* (14), 7429-7436.
(40) Lee, D. U.; Fu, J.; Park, M. G.; Liu, H.; Kashkooli, A. G.; Chen, Z. W. *Nano Lett.* **2016**, *16* (3), 1794-1802.
(41) Li, H. F.; Xu, C. J.; Han, C. P.; Chen, Y. Y.; Wei, C. G.; Li, B. H.; Kang, F. Y. *J. Electrochem. Soc.* **2015**, *162* (8), A1439-A1444.
(42) Parker, J. F.; Chervin, C. N.; Nelson, E. S.; Rolison, D. R.; Long, J. W. *Energ. Environ. Sci.* **2014**, *7* (3), 1117-1124.
(43) Yi, J.; Liang, P. C.; Liu, X. Y.; Wu, K.; Liu, Y. Y.; Wang, Y. G.; Xia, Y. Y.; Zhang, J. J. *Energ. Environ. Sci.* **2018**, *11* (11), 3075-3095.
(44) Zhao, Z. Q.; Fan, X. Y.; Ding, J.; Hu, W. B.; Zhong, C.; Lu, J. *ACS Energy Lett.* **2019**, *4* (9), 2259-2270.
(45) Pei, P. C.; Wang, K. L.; Ma, Z. *Appl. Energ.* **2014**, *128*, 315-324.
(46) Mainar, A. R.; Iruin, E.; Colmenares, L. C.; Kvasha, A.; de Meatza, I.; Bengoechea, M.; Leonet, O.; Boyano, I.; Zhang, Z. C.; Blazquez, J. A. *J. Energy Storage* **2018**, *15*, 304-328.
(47) Chen, P.; Zhang, K. Y.; Tang, D. J.; Liu, W. L.; Meng, F. C.; Huang, Q. W.; Liu, J. H. *Front. Chem.* **2020**, *8*, 372.
(48) Mainar, A. R.; Leonet, O.; Bengoechea, M.; Boyano, I.; de Meatza, I.; Kvasha, A.; Guerfi, A.; Blazquez, J. A. *Int. J. Energ. Res.* **2016**, *40* (8), 1032-1049.
(49) Sapkota, P.; Kim, H. *J. Ind. Eng. Chem.* **2009**, *15* (4), 445-450.
(50) See, D. M.; White, R. E. *J. Chem. Eng. Data* **1997**, *42* (6), 1266-1268.
(51) Qiao, J. L.; Xu, L.; Ding, L.; Shi, P. H.; Zhang, L.; Baker, R.; Zhang, J. J. *Int. J. Electrochem. Sc.* **2013**, *8* (1), 1189-1208.
(52) Lapicque, F.; Belhadj, M.; Bonnet, C.; Pauchet, J.; Thomas, Y. *J. Power Sources* **2016**, *336*, 40-53.
(53) Lim, C.; Wang, C. Y. *Electrochim. Acta.* **2004**, *49* (24), 4149-4156.
(54) Ralph, T. R.; Hards, G. A.; Keating, J. E.; Campbell, S. A.; Wilkinson, D. P.; Davis, M.; StPierre, J.; Johnson, M. C. *J. Electrochem. Soc.* **1997**, *144* (11), 3845-3857.
(55) Benziger, J.; Nehlsen, J.; Blackwell, D.; Brennan, T.; Itescu, J. *J. Membrane Sci.* **2005**, *261* (1-2), 98-106.
(56) Bhattacharya, P. K. *Directions* **2015**, *15*, 24-33.

(57) Li, H.; Tang, Y. H.; Wang, Z. W.; Shi, Z.; Wu, S. H.; Song, D. T.; Zhang, J. L.; Fatih, K.; Zhang, J. J.; Wang, H. J.; Liu, Z. S.; Abouatallah, R.; Mazza, A. *J. Power Sources* **2008**, *178* (1), 103-117.
(58) Cindrella, L.; Kannan, A. M.; Lin, J. F.; Saminathan, K.; Ho, Y.; Lin, C. W.; Wertz, J. *J. Power Sources* **2009**, *194* (1), 146-160.
(59) Gostick, J. T.; Ioannidis, M. A.; Fowler, M. W.; Pritzker, M. D. *Electrochem. Commun.* **2009**, *11* (3), 576-579.
(60) Omrani, R.; Shabani, B. *Int. J. Hydrogen Energ.* **2017**, *42* (47), 28515-28536.
(61) Schweiss, R.; Steeb, M.; Wilde, P. M. *Fuel Cells* **2010**, *10* (6), 1176-1180.
(62) Chen, J.; Xu, H.; Zhang, H.; Yi, B. *J. Power Sources* **2008**, *182* (2), 531-539.
(63) Fluckiger, R.; Freunberger, S. A.; Kramer, D.; Wokaun, A.; Scherer, G. G.; Buchi, F. N. *Electrochim. Acta.* **2008**, *54* (2), 551-559.
(64) Kang, S.; Yu, J. S.; Kruk, M.; Jaroniec, M. *Chem. Commun.* **2002**, (16), 1670-1671.
(65) Liu, D. L.; Tong, Y. Y.; Yan, X.; Liang, J.; Dou, S. X. *Batteries Supercaps* **2019**, *2* (9), 743-765.
(66) Zhong, Y. J.; Xu, X. M.; Wang, W.; Shao, Z. P. *Batteries Supercaps* **2019**, *2* (4), 272-289.
(67) Perez, G.; Pastor, E.; Zinola, C. F. *Int. J. Hydrogen Energ.* **2009**, *34* (23), 9523-9530.
(68) Favaro, M.; Valero-Vidal, C.; Eichhorn, J.; Toma, F. M.; Ross, P. N.; Yano, J.; Liu, Z.; Crumlin, E. J. *J. Mater. Chem. A* **2017**, *5* (23), 11634-11643.
(69) Tenkortenaar, M. V.; Vente, J. F.; Ijdo, D. J. W.; Muller, S.; Kotz, R. *J. Power Sources* **1995**, *56* (1), 51-60.
(70) Petrykin, V.; Macounova, K.; Shlyakhtin, O. A.; Krtil, P. *Angew. Chem. Int. Edit.* **2010**, *49* (28), 4813-4815.
(71) Labata, M. F.; Li, G. F.; Ocon, J.; Chuang, P. Y. A. *J. Power Sources* **2021**, *487*, 229356.
(72) Roduner, E. *Chem. Soc. Rev.* **2006**, *35* (7), 583-592.
(73) Wang, X. Q.; Li, Z. J.; Qu, Y. T.; Yuan, T. W.; Wang, W. Y.; Wu, Y.; Li, Y. D. *Chem* **2019**, *5* (6), 1486-1511.
(74) Liang, H. W.; Cao, X. A.; Zhou, F.; Cui, C. H.; Zhang, W. J.; Yu, S. H. *Adv. Mater.* **2011**, *23* (12), 1467-1471.
(75) Laha, S.; Lee, Y.; Podjaski, F.; Weber, D.; Duppel, V.; Schoop, L. M.; Pielnhofer, F.; Scheurer, C.; Muller, K.; Starke, U.; Reuter, K.; Lotsch, B. V. *Adv. Energy Mater.* **2019**, *9* (15), 1803795.
(76) Ding, J. B.; Shao, Q.; Feng, Y. G.; Huang, X. Q. *Nano Energy* **2018**, *47*, 1-7.
(77) Hornberger, E.; Mastronardi, V.; Brescia, R.; Pompa, P. P.; Klingenhof, M.; Dionigi, F.; Moglianetti, M.; Strasser, P. *ACS Appl. Energ. Mater.* **2021**, *4* (9), 9542-9552.

(78) Mahata, A.; Rawat, K. S.; Choudhuri, I.; Pathak, B. *J. Mater. Chem. A* **2016**, *4* (33), 12756-12767.
(79) Wang, G. Z.; Chang, J. F.; Koul, S.; Kushima, A.; Yang, Y. *J. Am. Chem. Soc.* **2021**, *143* (30), 11595-11601.
(80) li, Z.; Niu, W. H.; Yang, Z. Z.; Zaman, N.; Samarakoon, W.; Wang, M. Y.; Kara, A.; Lucero, M.; Vyas, M. V.; Chao, H.; Zhou, H.; Sterbinsky, G. E.; Feng, Z. X.; Du, Y. G.; Yang, Y. *Energ. Environ. Sci.* **2020**, *13* (3), 884-895.
(81) Behm, K.; McIntosh, R. D. *Chempluschem* **2020**, *85* (12), 2611-2618.
(82) Hansen, H. A.; Viswanathan, V.; Norskov, J. K. *J. Phys. Chem. C* **2014**, *118* (13), 6706-6718.
(83) Wang, H. Y.; Weng, C. C.; Yuan, Z. Y. *J. Energy Chem.* **2021**, *56*, 470-485.
(84) Davis, D. J.; Lambert, T. N.; Vigil, J. A.; Rodriguez, M. A.; Brumbach, M. T.; Coker, E. N.; Limmer, S. J. *J. Phys. Chem. C* **2014**, *118* (31), 17342-17350.
(85) Zhan, Y.; Xu, C. H.; Lu, M. H.; Liu, Z. L.; Lee, J. Y. *J. Mater. Chem. A* **2014**, *2* (38), 16217-16223.
(86) Wang, Y.; Li, J.; Wei, Z. D. *J. Mater. Chem. A* **2018**, *6* (18), 8194-8209.
(87) Saddeler, S.; Bendt, G.; Salamon, S.; Haase, F. T.; Landers, J.; Timoshenko, J.; Rettenmaier, C.; Jeon, H. S.; Bergmann, A.; Wende, H.; Cuenya, B. R.; Schulz, S. *J. Mater. Chem. A* **2021**, *9* (45), 25381-25390.
(88) Liu, J.; Bao, H. L.; Zhang, B. S.; Hua, Q. F.; Shang, M. F.; Wang, J. Q.; Jiang, L. H. *ACS Appl. Mater. Inter.* **2019**, *11* (13), 12525-12534.
(89) He, X. B.; Yin, F. X.; Li, G. R. *Int. J. Hydrogen Energ.* **2015**, *40* (31), 9713-9722.
(90) Guan, C.; Sumboja, A.; Wu, H. J.; Ren, W. N.; Liu, X. M.; Zhang, H.; Liu, Z. L.; Cheng, C. W.; Pennycook, S. J.; Wang, J. *Adv. Mater.* **2017**, *29* (44).
(91) Li, B.; Ge, X. M.; Goh, F. W. T.; Hor, T. S. A.; Geng, D. S.; Du, G. J.; Liu, Z. L.; Zhang, J.; Liu, X. G.; Zong, Y. *Nanoscale* **2015**, *7* (5), 1830-1838.
(92) Zhao, J.; He, Y.; Chen, Z. L.; Zheng, X. R.; Han, X. P.; Rao, D. W.; Zhong, C.; Hu, W. B.; Deng, Y. D. *ACS Appl. Mater. Inter.* **2019**, *11* (5), 4915-4921.
(93) Lee, D. U.; Choi, J. Y.; Feng, K.; Park, H. W.; Chen, Z. W. *Adv. Energy Mater.* **2014**, *4* (6).
(94) Da, P. F.; Wu, M. Y.; Qiu, K. W.; Yan, D. Y.; Li, Y. J.; Mao, J.; Dong, C. K.; Ling, T.; Qiao, S. Z. *Chem. Eng. Sci.* **2019**, *194*, 127-133.
(95) Xu, L.; Wang, C.; Deng, D. J.; Tian, Y. H.; He, X. Y.; Lu, G. F.; Qian, J. C.; Yuan, S. Q.; Li, H. N. *ACS Sustain. Chem. Eng.* **2020**, *8* (1), 343-350.
(96) He, Y.; Zhang, J. F.; He, G. W.; Han, X. P.; Zheng, X. R.; Zhong, C.; Hu, W. B.; Deng, Y. D. *Nanoscale* **2017**, *9* (25), 8623-8630.
(97) Lee, J. S.; Lee, T.; Song, H. K.; Cho, J.; Kim, B. S. *Energ. Environ. Sci.* **2011**, *4* (10), 4148-4154.

(98) Gorlin, Y.; Lassalle-Kaiser, B.; Benck, J. D.; Gul, S.; Webb, S. M.; Yachandra, V. K.; Yano, J.; Jaramillo, T. F. *J. Am. Chem. Soc.* **2013**, *135* (23), 8525-8534.
(99) Liu, B.; Sun, Y. L.; Liu, L.; Xu, S.; Yan, X. B. *Adv. Funct. Mater.* **2018**, *28* (15).
(100) Tang, Q.; Jiang, L.; Liu, J.; Wang, S.; Sun, G. *ACS Catal.* **2014**, *4* (2), 457-463.
(101) Xue, Q.; Pei, Z. X.; Huang, Y.; Zhu, M. S.; Tang, Z. J.; Li, H. F.; Huang, Y.; Li, N.; Zhang, H. Y.; Zhi, C. Y. *J. Mater. Chem. A* **2017**, *5* (39), 20818-20823.
(102) Clark, M. P.; Xiong, M.; Cadien, K.; Ivey, D. G. *ACS Appl. Energ. Mater.* **2020**, *3* (1), 603-613.
(103) Lee, J. S.; Park, G. S.; Lee, H. I.; Kim, S. T.; Cao, R. G.; Liu, M. L.; Cho, J. *Nano Lett.* **2011**, *11* (12), 5362-5366.
(104) Jia, Q. Y.; Ramaswamy, N.; Tylus, U.; Strickland, K.; Li, J. K.; Serov, A.; Artyushkova, K.; Atanassov, P.; Anibal, J.; Gumeci, C.; Barton, S. C.; Sougrati, M. T.; Jaouen, F.; Halevi, B.; Mukerjee, S. *Nano Energy* **2016**, *29*, 65-82.
(105) Ferrandon, M.; Kropf, A. J.; Myers, D. J.; Artyushkova, K.; Kramm, U.; Bogdanoff, P.; Wu, G.; Johnston, C. M.; Zelenay, P. *J. Phys. Chem. C* **2012**, *116* (30), 16001-16013.
(106) Zhang, Z. P.; Sun, J. T.; Wang, F.; Dai, L. M. *Angew. Chem. Int. Edit.* **2018**, *57* (29), 9038-9043.
(107) Wang, J.; Wu, H. H.; Gao, D. F.; Miao, S.; Wang, G. X.; Bao, X. H. *Nano Energy* **2015**, *13*, 387-396.
(108) Zang, Y. P.; Zhang, H. M.; Zhang, X.; Liu, R. R.; Liu, S. W.; Wang, G. Z.; Zhang, Y. X.; Zhao, H. J. *Nano Res.* **2016**, *9* (7), 2123-2137.
(109) Kuhlenbeck, H.; Shaikhutdinov, S.; Freund, H. J. *Chem. Rev.* **2013**, *113* (6), 3986-4034.
(110) Lu, Q.; Lattanzi, M. W.; Chen, Y. P.; Kou, X. M.; Li, W. F.; Fan, X.; Unruh, K. M.; Chen, J. G. G.; Xiao, J. Q. *Angew. Chem. Int. Edit.* **2011**, *50* (30), 6847-6850.
(111) Liu, H.; Wang, G. X.; Liu, J.; Qiao, S. Z.; Ahn, H. J. *J. Mater. Chem.* **2011**, *21* (9), 3046-3052.
(112) Ma, N.; Jia, Y.; Yang, X. F.; She, X. L.; Zhang, L. Z.; Peng, Z.; Yao, X. D.; Yang, D. J. *J. Mater. Chem. A* **2016**, *4* (17), 6376-6384.
(113) Qian, J. M.; Bai, X. W.; Xi, S. B.; Xiao, W.; Gao, D. Q.; Wang, J. L. *ACS Appl. Mater. Inter.* **2019**, *11* (34), 30865-30871.
(114) Vasilescu, A.; Hayat, A.; Gaspar, S.; Marty, J. L. *Electroanal.* **2018**, *30* (1), 2-19.
(115) Zhu, J.; Holmen, A.; Chen, D. *Chemcatchem* **2013**, *5* (2), 378-401.
(116) Hu, C. G.; Dai, L. M. *Adv. Mater.* **2019**, *31* (7), 1804672.

(117) Das, A.; Pisana, S.; Chakraborty, B.; Piscanec, S.; Saha, S. K.; Waghmare, U. V.; Novoselov, K. S.; Krishnamurthy, H. R.; Geim, A. K.; Ferrari, A. C.; Sood, A. K. *Nat. Nanotechnol.* **2008**, *3* (4), 210-215.
(118) Antolini, E. *Appl. Catal. B-Environ.* **2012**, *123*, 52-68.
(119) Bonaccorso, F.; Sun, Z.; Hasan, T.; Ferrari, A. C. *Nat. Photonics* **2010**, *4* (9), 611-622.
(120) Chung, C.; Kim, Y. K.; Shin, D.; Ryoo, S. R.; Hong, B. H.; Min, D. H. *Accounts Chem. Res.* **2013**, *46* (10), 2211-2224.
(121) Pyatkov, F.; Futterling, V.; Khasminskaya, S.; Flavel, B. S.; Hennrich, F.; Kappes, M. M.; Krupke, R.; Pernice, W. H. P. *Nat. Photonics* **2016**, *10* (6), 420-+.
(122) Flavel, B. S.; Yu, J. X.; Shapter, J. G.; Quinton, J. S. *J. Mater. Chem.* **2007**, *17* (45), 4757-4761.
(123) Steiner, M.; Engel, M.; Lin, Y. M.; Wu, Y. Q.; Jenkins, K.; Farmer, D. B.; Humes, J. J.; Yoder, N. L.; Seo, J. W. T.; Green, A. A.; Hersam, M. C.; Krupke, R.; Avouris, P. *Appl. Phys. Lett.* **2012**, *101* (5).
(124) Varga, A.; Pfohl, M.; Brunelli, N. A.; Schreier, M.; Giapis, K. P.; Haile, S. M. *Phys. Chem. Chem. Phys.* **2013**, *15* (37), 15470-15476.
(125) Landi, B. J.; Ganter, M. J.; Cress, C. D.; DiLeo, R. A.; Raffaelle, R. P. *Energ. Environ. Sci.* **2009**, *2* (6), 638-654.
(126) Tatsuura, S.; Furuki, M.; Sato, Y.; Iwasa, I.; Tian, M. Q.; Mitsu, H. *Adv. Mater.* **2003**, *15* (6), 534-537.
(127) Engel, M.; Moore, K. E.; Alam, A.; Dehm, S.; Krupke, R.; Flavel, B. S. *ACS Nano* **2014**, *8* (9), 9324-9331.
(128) Avouris, P.; Freitag, M.; Perebeinos, V. *Nat. Photonics* **2008**, *2* (6), 341-350.
(129) Jiao, Y.; Zheng, Y.; Jaroniec, M.; Qiao, S. Z. *J. Am. Chem. Soc.* **2014**, *136* (11), 4394-4403.
(130) You, C. H.; Liao, S. J.; Li, H. L.; Hou, S. Y.; Peng, H. L.; Zeng, X. Y.; Liu, F. F.; Zheng, R. P.; Fu, Z. Y.; Li, Y. W. *Carbon* **2014**, *69*, 294-301.
(131) Zhang, J. T.; Qu, L. T.; Shi, G. Q.; Liu, J. Y.; Chen, J. F.; Dai, L. M. *Angew. Chem. Int. Edit.* **2016**, *55* (6), 2230-2234.
(132) Zheng, Y.; Chen, S.; Zhang, K. A. I.; Zhu, J. X.; Xu, J. S.; Zhang, C.; Liu, T. X. *ACS Appl. Mater. Inter.* **2021**, *13* (11), 13328-13337.
(133) Chen, W.; Xu, L.; Tian, Y. H.; Li, H. A.; Wang, K. *Carbon* **2018**, *137*, 458-466.
(134) Liu, X.; Wang, L.; Yu, P.; Tian, C. G.; Sun, F. F.; Ma, J. Y.; Li, W.; Fu, H. G. *Angew. Chem. Int. Edit.* **2018**, *57* (49), 16166-16170.
(135) Lee, D. U.; Park, H. W.; Park, M. G.; Ismayilov, V.; Chen, Z. W. *ACS Appl. Mater. Inter.* **2015**, *7* (1), 902-910.
(136) Zhou, H. C.; Kitagawa, S. *Chem. Soc. Rev.* **2014**, *43* (16), 5415-5418.

(137) Lee, Y. R.; Kim, J.; Ahn, W. S. *Korean J. Chem. Eng.* **2013**, *30* (9), 1667-1680.
(138) Aguado, S.; Canivet, J.; Farrusseng, D. *J. Mater. Chem.* **2011**, *21* (21), 7582-7588.
(139) Chen, X. R.; Tong, R. L.; Shi, Z. Q.; Yang, B.; Liu, H.; Ding, S. P.; Wang, X.; Lei, Q. F.; Wu, J.; Fang, W. J. *ACS Appl. Mater. Inter.* **2018**, *10* (3), 2328-2337.
(140) Ding, M. L.; Flaig, R. W.; Jiang, H. L.; Yaghi, O. M. *Chem. Soc. Rev.* **2019**, *48* (10), 2783-2828.
(141) Ding, M. L.; Cai, X. C.; Jiang, H. L. *Chem. Sci.* **2019**, *10* (44), 10209-10230.
(142) Shen, K.; Chen, X. D.; Chen, J. Y.; Li, Y. W. *ACS Catal.* **2016**, *6* (9), 5887-5903.
(143) Li, Y. W.; Zhang, W. J.; Li, J.; Ma, H. Y.; Du, H. M.; Li, D. C.; Wang, S. N.; Zhao, J. S.; Dou, J. M.; Xu, L. Q. *ACS Appl. Mater. Inter.* **2020**, *12* (40), 44710-44719.
(144) Wu, H. B.; Wang, J.; Yan, J.; Wu, Z. X.; Jin, W. *Nanoscale* **2019**, *11* (42), 20144-20150.
(145) Dogan, A. U.; Dogan, M.; Onal, M.; Sarikaya, Y.; Aburub, A.; Wurster, D. E. *Clay. Clay Miner.* **2006**, *54* (1), 62-66.
(146) Tarleton, E.; Tarleton, E. S.; Elsevier. *Progress in filtration and separation*; Academic Press, 2015.
(147) Elgrishi, N.; Rountree, K. J.; McCarthy, B. D.; Rountree, E. S.; Eisenhart, T. T.; Dempsey, J. L. *J. Chem. Educ.* **2018**, *95* (2), 197-206.
(148) Bard, A. J. *ELECTROCHEMICAL METHODS*; 1980.
(149) Sapkota, P.; Kim, H. *J. Ind. Eng. Chem.* **2010**, *16* (1), 39-44.
(150) Davis, R. E.; Horvath, G. L.; Tobias, C. W. *Electrochim. Acta.* **1967**, *12* (3), 287-297.
(151) Nikolic, J.; Exposito, E.; Iniesta, J.; Gonzalez-Garcia, J.; Montiel, V. *J. Chem. Educ.* **2000**, *77* (9), 1191-1194.
(152) Chen, W. L.; Xiang, Q.; Peng, T.; Song, C. Y.; Shang, W.; Deng, T.; Wu, J. B. *Iscience* **2020**, *23* (10), 101532.
(153) Vayner, E.; Sidik, R. A.; Anderson, A. B.; Popov, B. N. *J. Phys. Chem. C* **2007**, *111* (28), 10508-10513.
(154) Gilliam, R. J.; Graydon, J. W.; Kirk, D. W.; Thorpe, S. J. *Int. J. Hydrogen Energ.* **2007**, *32* (3), 359-364.
(155) Shivkumar, R.; Kalaignan, G. P.; Vasudevan, T. *J. Power Sources* **1995**, *55* (1), 53-62.
(156) Zia, A. I.; Mukhopadhyay, S. C. *Electrochemical Sensing: Carcinogens in Beverages*; Springer International Publishing, 2016.

(157) Bredar, A. R. C.; Chown, A. L.; Burton, A. R.; Farnum, B. H. *ACS Appl. Energ. Mater.* **2020**, *3* (1), 66-98.
(158) Park, S. M.; Yoo, J. S. *Anal. Chem.* **2003**, *75* (21), 455a-461a.

Chapter 2: Mn_3O_4 Nanoparticle-Decorated Hollow Mesoporous Carbon Spheres as an Efficient Catalyst for Oxygen Reduction Reaction in Zn-Air Batteries

A version of this chapter was published as:

He, Y.; Aasen, D.; Yu, H.; Labbe, M.; Ivey, D. G.; Veinot, J. G. C. *Nanoscale Adv*. **2020**, *2*, 3367–3374.

2.1 Introduction

Society's seemingly insatiable demand for energy and the associated environmental impact of fossil fuel use have led to calls for a global transition to renewable energy sources that include wind and solar power.[1] Despite maturing technologies and declining cost, the intrinsic intermittency of renewable energy production remains a challenge for large scale commercialization and implementation.[1, 2] One approach toward mitigating this important issue is employing energy storage units that can provide better alignment of energy supply and demand timing.[3, 4] Clearly, developing efficient and cost-effective cyclable energy storage technologies, like batteries, is of nascent importance.[5]

Among the many technologies that have appeared, metal-air batteries have attracted substantial attention in part because of their comparatively high energy density.[6-10] Aqueous Zn-air batteries are particularly attractive for stationary energy storage because they are based upon earth abundant, non-toxic elements (i.e., Zn) and have a high theoretical energy density (1086 kW kg^{-1}) which is four times that of current Li-ion batteries.[11] Despite these advantages, further advances are required if Zn-air batteries are to realize their full potential. The most substantial benefits will come from the development of efficient precious metal-free catalysts that facilitate reactions at the air electrode.[12]

The oxygen reduction and evolution reactions (i.e., ORR and OER, respectively) occur at the air electrode and are crucial to battery performance (Fig. 2-1). When the battery is discharging, the ORR reaction is active, and oxygen is reduced to form hydroxide anions at the air electrode. Upon charging, this process is reversed and oxygen is regenerated via the OER. While ORR is thermodynamically favorable under operational conditions, both the ORR and OER are kinetically hindered.[13] As a result, electrocatalysts are essential to realizing functional/cyclable batteries. Conventional ORR and OER catalysts rely on precious metals and their oxides.[14] The high cost of these metals/metal oxides potentially limits the economic viability of their large-scale application.

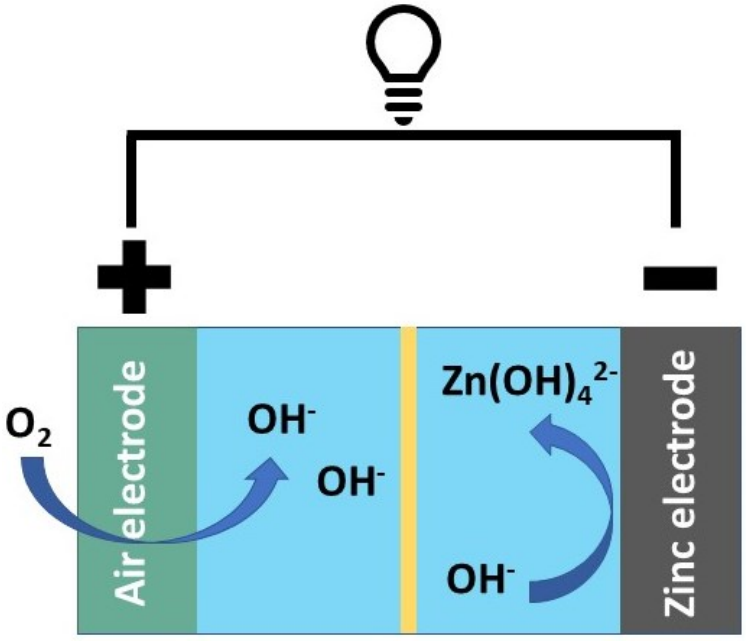

Figure 2-1. A pictorial representation of a Zn-air battery and its associated processes.

Precious-metal free systems are being aggressively explored in efforts to find alternative, efficient catalysts. Of late, a variety of carbon nanomaterials (e.g., N-doped carbon nanotubes (CNTs), carbon nanoribbons, and graphene nanosheets) have shown excellent ORR and/or OER catalytic activity.[15-18] Transition metal oxide nanoparticles (e.g., MnO_x, CoO_x) also exhibit promising performance.[19, 20] There have even been reports of synergistic effects when these materials are combined, however its chemical origin was not identified.[21] Previously we demonstrated that N-doped hollow mesoporous carbon (HMC) nanospheres for their catalytic activity.[22]

Here, we report a new precious-metal free hybrid that combines the favorable ORR properties of N-doped HMCs with those of earth abundant Mn_3O_4 nanoparticles. The hybrid exhibits enhanced catalytic ORR performance when compared with the individual components, as well as benchmark Pt-Ru catalysts. Further adding to the appeal of this new catalyst, its stability exceeds that of Pt-Ru standards when incorporated into prototype Zn-air batteries.

2.2 Experimental Section

2.2.1 Chemicals

Dopamine hydrochloride, pluronic F127, tris(hydroxymethyl)amino-methane (Tris), tetraethoxysilane (TEOS) (≥99%), 2-propanol, and anhydrous ethanol (≤

0.005% water) were obtained from Sigma-Aldrich. Ammonium hydroxide (NH_4OH; 28 - 30%) was acquired from Caledon Laboratory Chemicals. Hydrofluoric acid (HF, electronic grade, 48-50%) and sodium hydroxide (NaOH, pellets) were purchased from Fisher Scientific. Manganese acetate tetrahydrate ($Mn(CH_3COO)_2 \cdot 4H_2O$, powder) was obtained from Matheson Colman & Bell. Pt-Ru powder (30% Pt and 15% RuO_2 on carbon black) and Nafion solution (D521, 5% w/w in water) were purchased from Alfa Aesar. Teflon-coated porous carbon paper (SGL 39BC gas diffusion layer; GDL) was acquired from the Fuel Cell Store. All reagents were used as received unless otherwise specified.

2.2.2 Synthesis of Stöber SiO_2 nanoparticles (SiO_2 NPs)

Stöber SiO_2 NPs were prepared using a modified literature procedure.[23] Briefly, TEOS (3.575 mL) was added to a mixture of deionized water (80 mL) and anhydrous ethanol (156 mL), followed by the addition of NH_4OH (8 mL). The reaction mixture was stirred at 500 rpm for 3 h at room temperature (25°C). Subsequently, the SiO_2 NPs were isolated upon centrifugation at 12000 rpm for 30 min. They were then re-dispersed in anhydrous ethanol and purified by centrifugation. The dispersion/isolation process was repeated twice. The purified SiO_2 NPs were dried in ambient conditions (in air at 25°C) for 16 h, after which they were transferred to a sealed glass vial and stored at room temperature (25°C) and under ambient light until needed.

2.2.3 Synthesis of SiO_2@C nanoparticles (NPs)

The SiO_2 NPs (0.700 g) were dispersed in 187 mL deionized water with exposure to a bath sonicator for 10 min. Triblock copolymer pluronic F127 (0.350 g), Tris (0.210 g), and dopamine hydrochloride (0.700 g) were added as powders to the SiO_2 NP suspension. The mixture was magnetically stirred at 500 rpm for 24 h at room temperature (25°C). The resulting polydopamine coated SiO_2 NPs (SiO_2@PDA) were isolated via centrifugation at 12000 rpm for 30 min. Subsequently, the SiO_2@PDA were re-dispersed in DI water with sonication and recovered via centrifugation. This process was repeated twice, replacing water with anhydrous ethanol. The purified SiO_2@PDA was dried in air at 25°C for 16 h. The SiO_2@PDA was then transferred to a quartz boat, placed in a standard tube furnace and carbonized under flowing Ar atmosphere. The furnace was heated to 400°C (heating rate of 1°C min^{-1}) and maintained at 400°C for 2 h before the heating to 800°C (heating rate of 5°C min^{-1}) for 3 h. Finally, the furnace was cooled to 25°C and SiO_2@C NPs were obtained as a black solid.

2.2.4. Synthesis of hollow mesoporous carbon spheres (HMCs)

The as-synthesized SiO_2@C (0.600 g) was dispersed in anhydrous ethanol (6 mL) and DI water (6 mL) via magnetic stirring (10 min at 500 rpm) followed by sonication (10 min) in a polyethylene terephthalate (PET) beaker. HF (49 %, 6 mL)

was added to the mixture, which was magnetically stirred at 25°C for 1 h. The HF dissolved the SiO_2 core without damaging the carbon shell, yielding hollow mesoporous carbon spheres (HMCs). The HMCs were collected via vacuum filtration using a Teflon funnel and filter flask and washed with 60 mL of DI water and anhydrous ethanol (Caution! HF must be handled with extreme care and in accordance with local regulations).

2.2.5 Synthesis of Mn_3O_4@HMC

The hybrid material was synthesized according to a modified literature procedure.[21] The purified HMCs (50 mg) were dispersed in anhydrous ethanol (10 mL) and magnetically stirred for 10 min at 500 rpm. Subsequently, $Mn(CH_3CO_2)_2 \cdot 4H_2O$ (250 mg) and NaOH (100 mg) were added to the HMC ethanol suspension. The mixture was transferred to a sealed glass reaction vessel and exposed to a bath sonicator for 2.5 h. The water bath was replenished with cold water and the sonication was continued for an additional 2.5 h. The final product (Mn_3O_4@HMC) was isolated via centrifugation at 12000 rpm for 30 min. It was then re-suspended in anhydrous ethanol and centrifuged. The process was repeated three times. The centrifuged Mn_3O_4@HMC was again re-dispersed in anhydrous ethanol and filtered via vacuum filtration.

2.2.6 Synthesis of freestanding Mn_3O_4

Freestanding Mn_3O_4 NPs were synthesized for comparison. The preparation was identical to that for Mn_3O_4@HMC; however, no HMC was added to the reaction mixture. $Mn(CH_3CO_2)_2 \cdot 4H_2O$) (250 mg) and NaOH (100 mg) were added to ethanol (10 mL), followed by sonication (5 h) in a bath sonicator.

2.2.7 Material characterization

Fourier-transform infrared (FTIR) spectra were obtained with a Nicolet 8700 (Thermo Fischer, USA) FT-IR spectrometer. FTIR samples were prepared by mixing the material of interest (~1 mg) and potassium bromide fine powder (KBr, 150 mg). The powder mixture was then pressed into a pellet using a hand press (Specac Ltd).

Scanning electron microscopy (SEM) was performed using a Zeiss Sigma 300 VP-FESEM (accelerating voltage of 5-20 kV) equipped with secondary and backscattered electron detectors and an in-lens detector. Samples were prepared by placing a drop of ethanol suspension of the material of interest onto an Al stub and was subsequently air dried for 1 h at room temperature (25°C). Transmission electron microscopy (TEM) was performed with a JEOL JEM-ARM200CF TEM/STEM (accelerating voltage of 200 kV) equipped with energy dispersive X-ray (EDX) spectrometer. High resolution TEM (HRTEM) images were processed

using Gatan Digital Micrograph software (Version 3.22.1461.0) and ImageJ (Version 1.52A). TEM samples were prepared by dispersing the purified sample in anhydrous ethanol, which was then drop cast onto a holy/lacey carbon coated Cu grid (Electron Microscopy Inc.) and dried under vacuum for at least 16 h. At least 300 nanoparticles were used for determination of thickness and diameter of the purified materials. EDX maps of several representative regions were also obtained.

X-ray photoelectron spectroscopy (XPS) was performed with a Kratos Axis 165 Ultra X-ray spectrometer operating in energy spectrum mode under ultra-high vacuum. A monochromatic Al K source (λ = 8.34 Å) was used as the X-ray source. The samples were prepared by drop-casting an ethanol suspension of material of interest onto a Cu foil that was air dried for at least 16 h at room temperature (25°C). The take-off angle was 90°. CasaXPS software (VAMAS) was used to analyze the obtained data. In general, a Shirley-type background was subtracted.[24] The spectra were calibrated by setting the deconvoluted adventitious C 1s peak to 284.8 eV.

Powder X-ray diffraction (PXRD) was conducted by placing purified samples on a zero-background Si wafer. PXRD patterns were collected using a Rigaku Ultima IV XRD system equipped with a Cu Kα radiation source.

Nitrogen adsorption-desorption isotherms were obtained with a Quantachrome Autosorb-iQ-XR system at -196°C. Before measurements, samples

were outgassed at 150°C under vacuum for 3 h. Data was analyzed using Brunauer-Emmett-Teller (BET) theory. The BET specific surface area was extrapolated from the linear region of the BET graph and the total pore volume was obtained from the data point at around $P/P_0 = 0.992$.

2.2.8 Electrochemical testing

The electrochemical performance of candidate catalysts was evaluated using linear sweep voltammetry (LSV). Measurements were performed in O_2 saturated 1 M KOH with a potentiostat (VSP-100) using a three-electrode cell and at a scan rate of 5 mV s^{-1}. The KOH solution was purged with O_2 gas and was stirred constantly during testing. The working electrode was prepared as follows. An ethanol suspension was prepared by dispersing 50 mg of sample of interest in 15 mL of anhydrous ethanol and 1 mL of 5% Nafion. A pre-cut piece of GDL (circular, diameter = 4.5 cm) was soaked and sonicated in the ethanol suspension for 20 min, before it was dried in air at 25°C for 15 min. Subsequently, the ethanol suspension (3 mL) was passed through the GDL via vacuum filtration, producing an impregnated GDL with a mass loading of ~2 mg cm^{-2}. For comparison, a Pt-Ru sample was prepared by spray coating an ink consisting of Pt-Ru (50 mg), deionized water (1 mL), ethanol (2 mL), and 5% Nafion (0.1 mL) onto the GDL. The impregnated or sprayed GDL samples were used as the working electrode. A platinum wire and Hg/HgO (0.098 V vs. SHE) were used as counter electrode and

reference electrode, respectively. The reported current densities were normalized to the exposed surface area of the working electrode. All reported potentials were IR compensated (Ru = 2-4 Ω). Experimental errors are not reported due to the variability of the complex device structure.

2.2.9 Prototype Zn-air battery assembly

Prototype Zn-air battery testing was performed in both vertical and horizontal home-made cells. The vertical cell had a two-electrode setup whereas the horizontal cell had a tri-electrode configuration (decoupled electrodes for ORR and OER).[25] In both configurations, the electrolyte consisted of 6 M KOH and 0.25 M ZnO. In the vertical cell, zinc sheet (8 g) and catalyst loaded GDL were used as zinc and air electrodes. Discharge rate test and power density curves were obtained using this configuration. The horizontal cell consisted of zinc sheet (8 g), catalyst loaded GDL, and Ni foam as zinc, ORR, and OER electrodes respectively. Electrochemical impedance spectra (EIS) and discharge and charge cycling were performed using this setup. For comparison, Pt-Ru spray-coated GDL was used as the air electrode in the vertical cell and ORR electrode in the horizontal cell. Discharge and charge cycling were performed at 20 mA cm^{-2} and 30 min per cycle. Experimental errors are not reported due to the variability of the complex device structure.

2.2.10 Rotating disk electrode (RDE) testing

Cyclic voltammetry (CV) and linear sweep voltammetry (LSV) were also performed using a glassy carbon rotating disk electrode (RDE) (Pine instruments Co). An ink was prepared by combining 4 mg of the Mn_3O_4@HMC, 0.25 mL Nafion solution, and 0.75 mL 2-propanol. The ink was sonicated for 1 h in a bath ultrasonicator filled with ice-water. The dispersed ink was immediately drop-cast (0.005 mL aliquot) onto a polished and cleaned RDE electrode. The electrode was then dried under a heat lamp (20 W) for 1 h (mass loading 0.1 mg cm^{-2}). A three-electrode cell was used, with the catalyst coated RDE, Pt coil, and Hg/HgO as working, counter, and reference electrodes, respectively. 0.1 M KOH aqueous solution was used as the electrolyte. CV and LSV were performed at a scan rate of 20 and 5 mV s^{-1}, respectively, in O_2-saturated electrolyte. O_2-saturated electrolytes were prepared by purging 0.1 M KOH with high purity O_2 for at least 25 min at a rate of 0.04 standard liters per minute (SLPM).

2.3 Results and Discussion

HMCs were prepared using a method developed in our laboratory.[22] Silica (SiO_2) nanoparticles (NPs) were synthesized via the Stöber method and used as a sacrificial template. The as-synthesized SiO_2 NPs were coated with dopamine and pluronic F127. The coating was polymerized under basic conditions, after which the

polymer shell was carbonized. The SiO_2 core was removed via alcoholic hydrofluoric acid (HF) etching to yield the HMCs on/in which, Mn_3O_4 NPs were deposited.[21]

Figures 2-2A and B show electron microscopy images of as-synthesized HMCs. It is clear that HF etching removes the SiO_2 core to yield a hollow structure that retains a spherical morphology with a diameter of 98±20 nm and a shell thickness of 3.8±0.4 nm (Figs. 2-3 and 2-4). After addition of $Mn(CH_3CO_2)_2$ and NaOH followed by 5 h of sonication, the morphology of the HMCs remained intact (Fig. 2-2C). The SEM image reveals a rough surface on the modified HMCs that presumably arises from the deposition of NPs. Higher magnification inspection using TEM (Fig. 2-2D) reveals Mn_3O_4 NPs on the surfaces and within the HMCs. The average NP size was determined to be 3.8±0.5 nm (Fig. 2-5). The crystallinity of the Mn_3O_4 NPs is clear from the selected area electron diffraction (SAED) pattern (Fig. 2-6A), which shows rings with d-spacings of 0.312, 0.282, 0.251, 0.204, 0.182, and 0.155 nm, that we confidently assigned to (112), (103), (211), (220), (105), and (224) planes, respectively, of hausmannite Mn_3O_4 (JCPDS CARD 24-0734).[25, 26] These d-spacings were also directly observed via HRTEM (Fig. 2-6B). PXRD analysis (Fig. 2-6C) further confirms the reflections are readily indexed to hausmannite Mn_3O_4.[26]

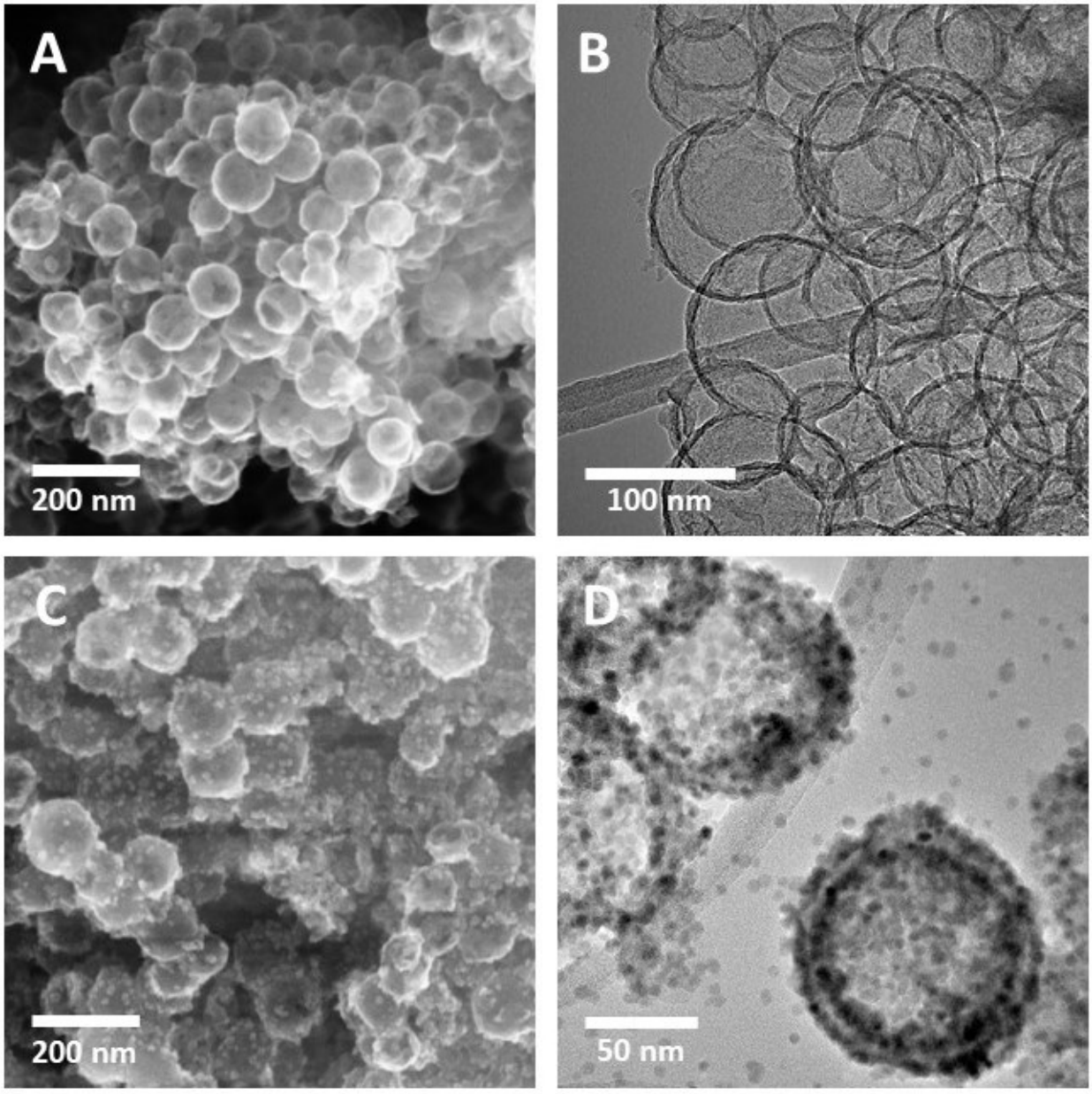

Figure 2-2. Representative SEM secondary electron (SE) (A) and TEM bright field (BF) (B) images of HMC; SEM SE (C) and TEM BF (D) images of Mn_3O_4@HMC.

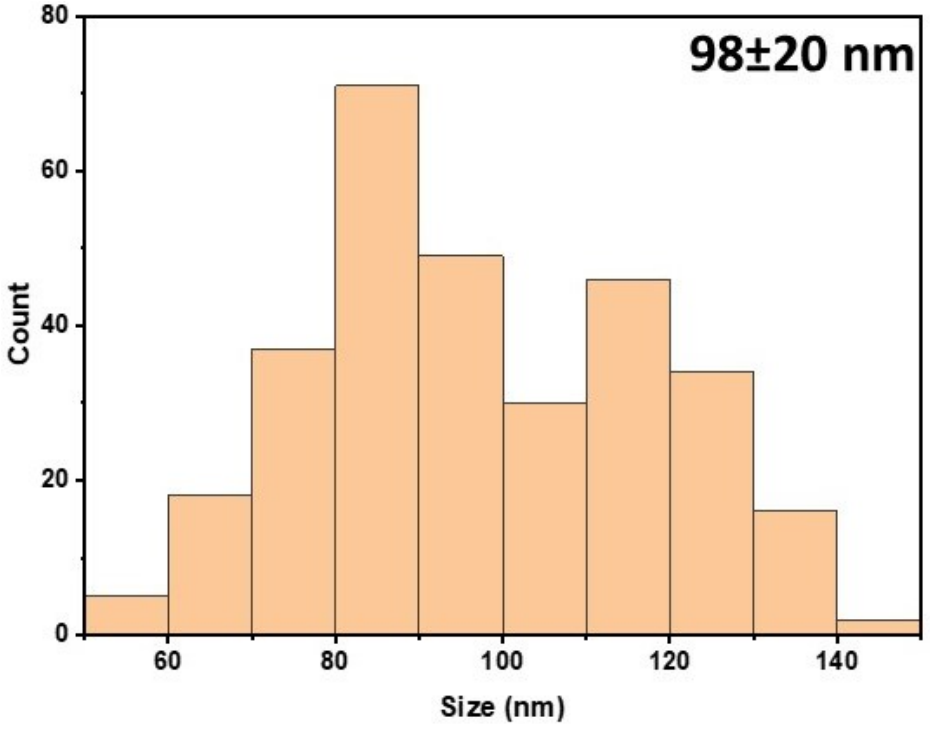

Figure 2-3. Size distribution of HMCs determined from TEM.

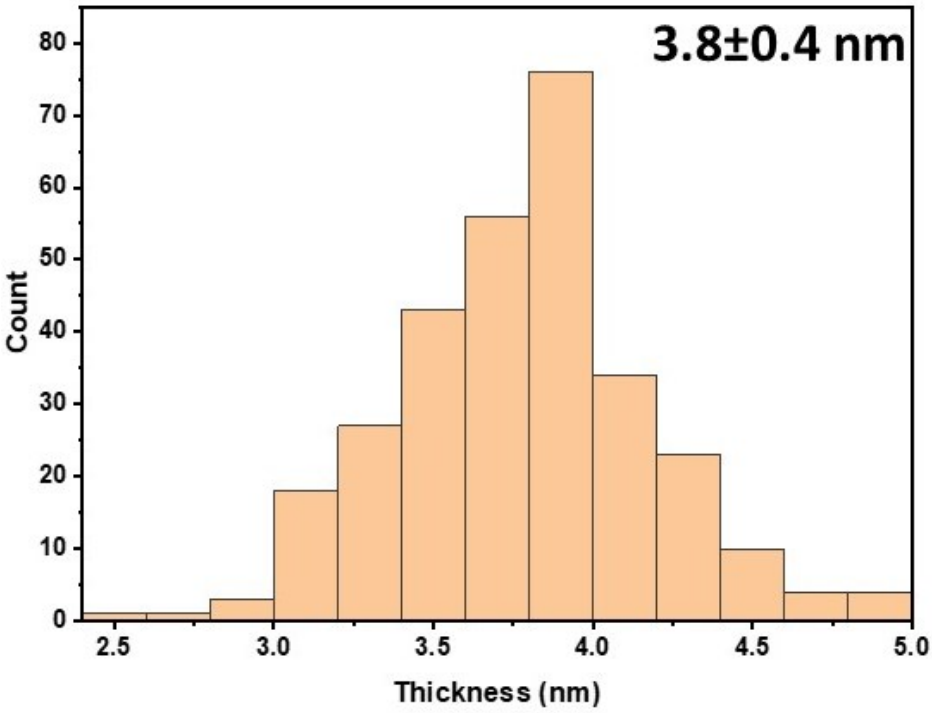

Figure 2-4. Thickness distribution of HMCs determined from TEM.

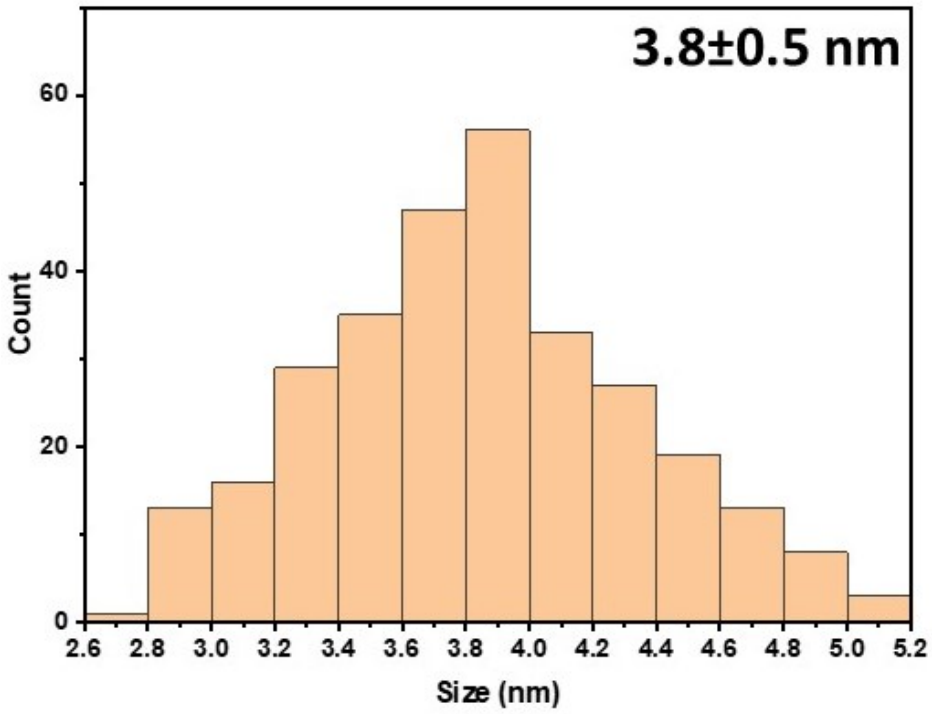

Figure 2-5. Size distribution of Mn_3O_4 nanoparticles determined from TEM.

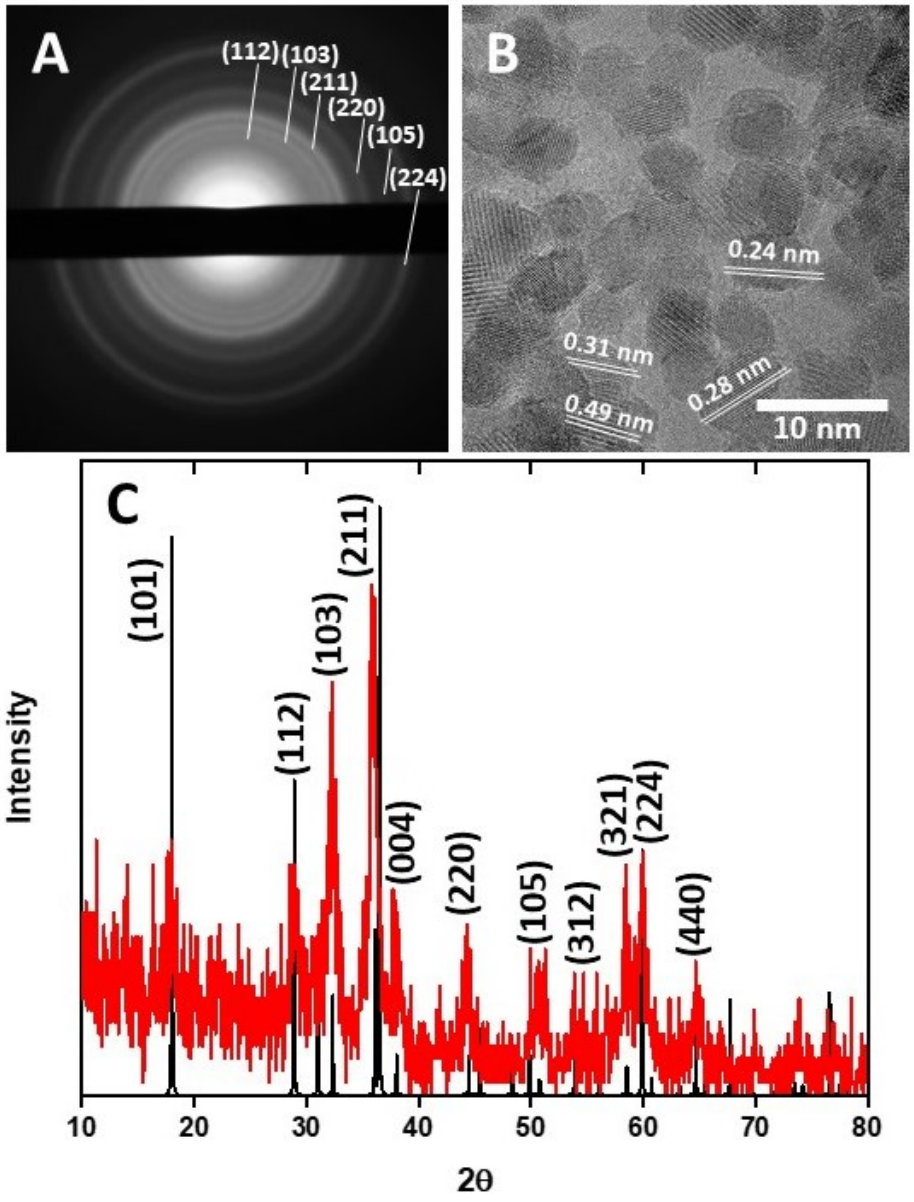

Figure 2-6. Selected area electron diffraction pattern (A), HRTEM image (B), and PXRD pattern (C) for Mn_3O_4@HMC.

EDX mapping of the HMCs (Fig. 2-7) shows the N signal overlaps with the bright field image, which is consistent with N being incorporated into the carbon matrix. The oxygen present in the carbon matrix can be reasonably attributed to

residual oxygen remaining after the pyrolysis of polydopamine. Figure 2-8 shows EDX mapping for the Mn_3O_4@HMC. The C, Mn, and O signals all overlap with the S/TEM HAADF image. EDX analysis shows that the NPs are uniformly distributed and have a composition consistent with Mn_3O_4.

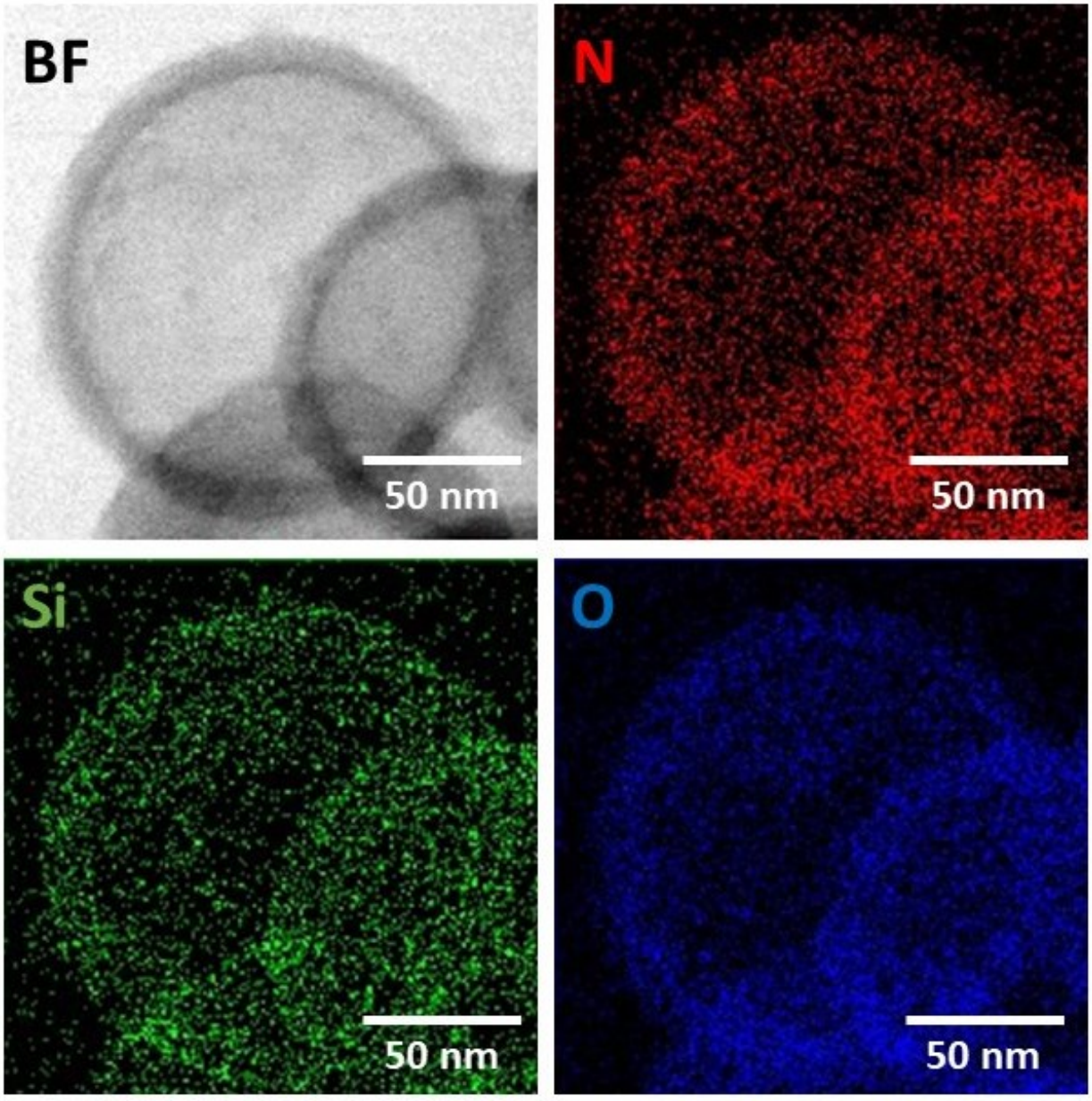

Figure 2-7. Elemental mapping of HMCs.

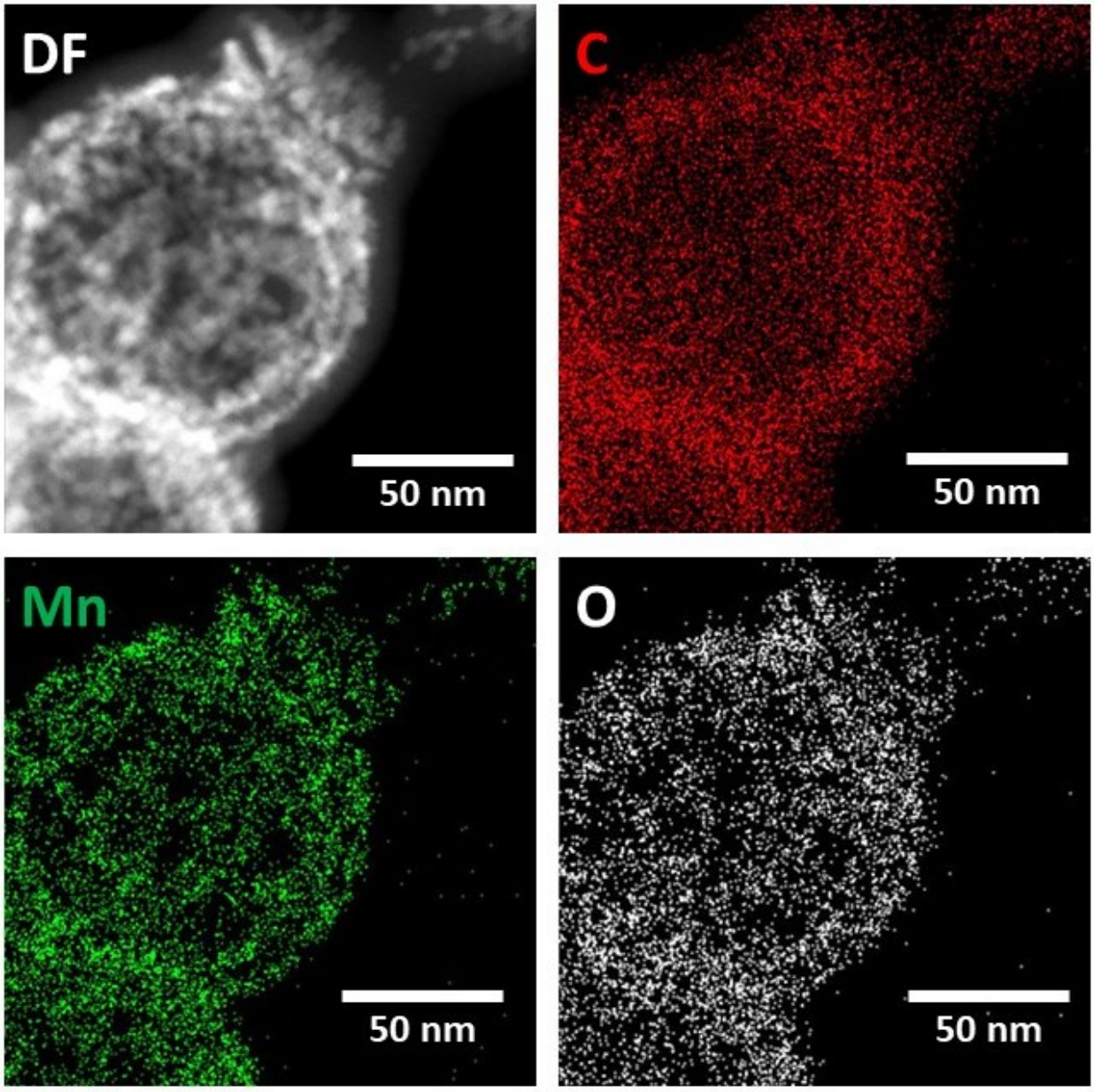

Figure 2-8. EDX mapping of Mn_3O_4@HMC showing uniform distribution of Mn and O.

The Mn_3O_4@HMC hybrid was also characterized using XP and FTIR spectroscopy. As expected, the XP survey spectrum (Fig. 2-9) shows emissions associated with Mn, C, N, and O. In the deconvoluted C 1s spectrum (Fig. 2-10), the

C=O emission shifted to a higher binding energy and merged with the O-C=O feature, consistent with the C=O species interacting with the Mn_3O_4 surface through the oxygen. The deconvoluted Mn 2p spectrum (Fig. 2-11) of the hybrids shows Mn $2p_{3/2}$ at 641.4 eV, confidently assigned to Mn_3O_4.[27] A satellite peak corresponding to Mn_3O_4 was also observed at 649.2 eV. The Mn 3s spectrum (Fig. 2-12) shows a signature 5.4 eV splitting of the 3s emission that is commonly attributed to the presence of Mn^{3+}.[27-29]

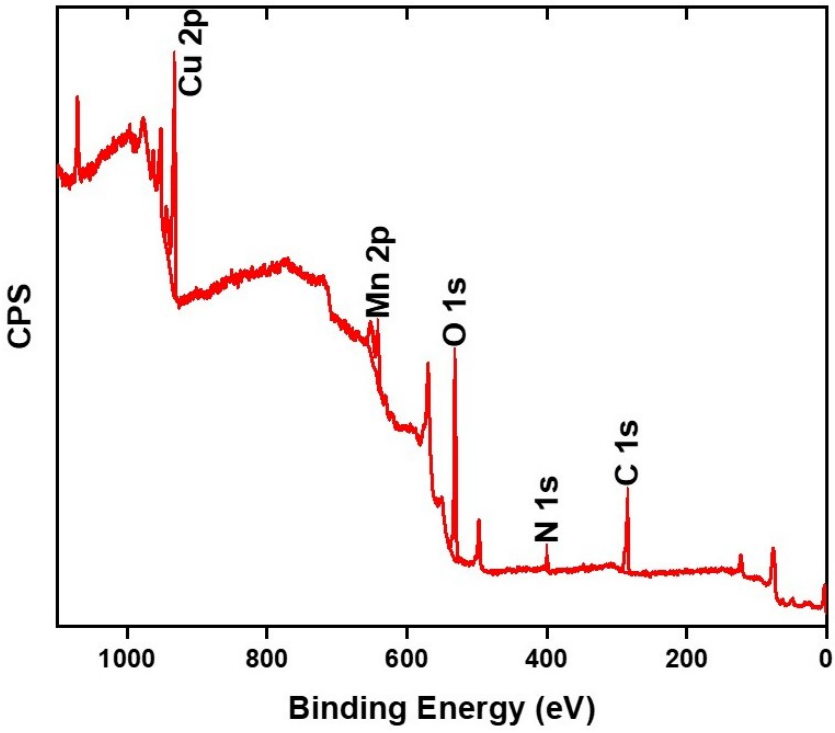

Figure 2-9. XP survey spectrum for Mn_3O_4@HMC.

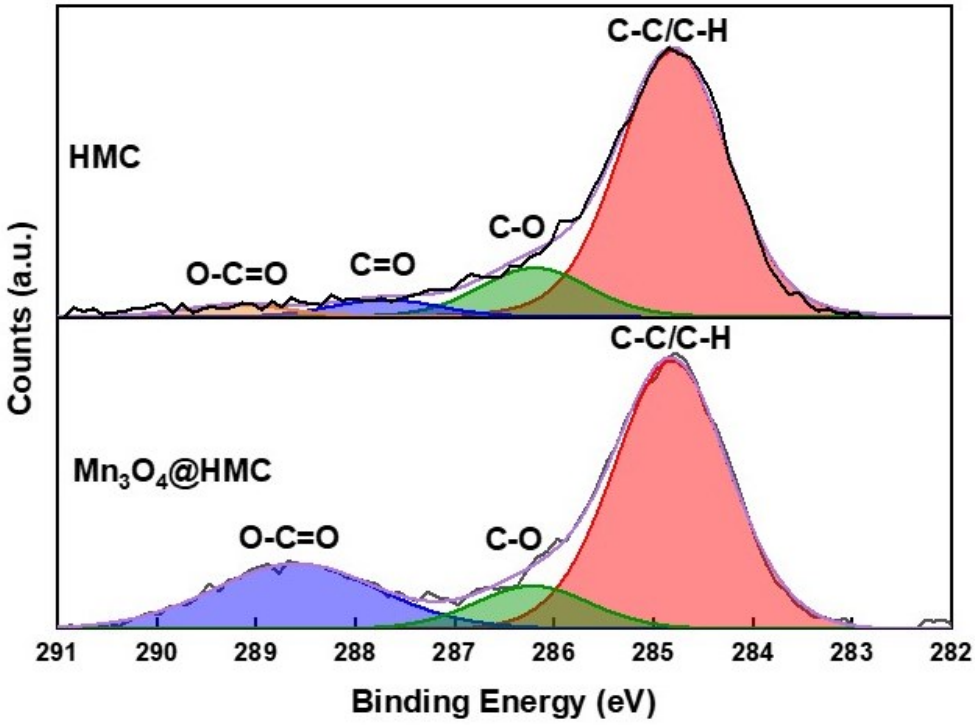

Figure 2-10. High resolution XP spectra for C 1s region.

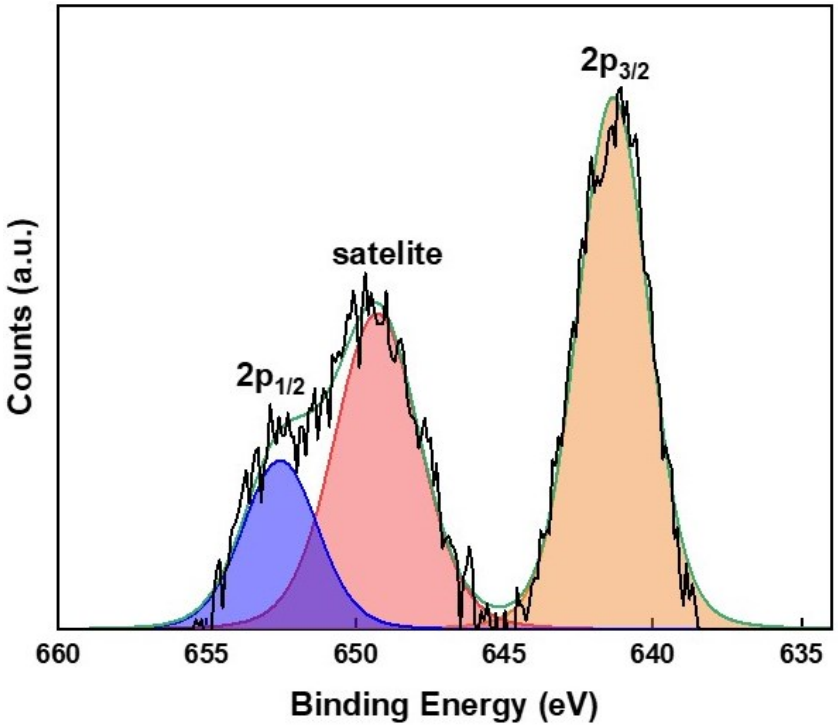

Figure 2-11. High resolution XP spectra Mn 2p region.

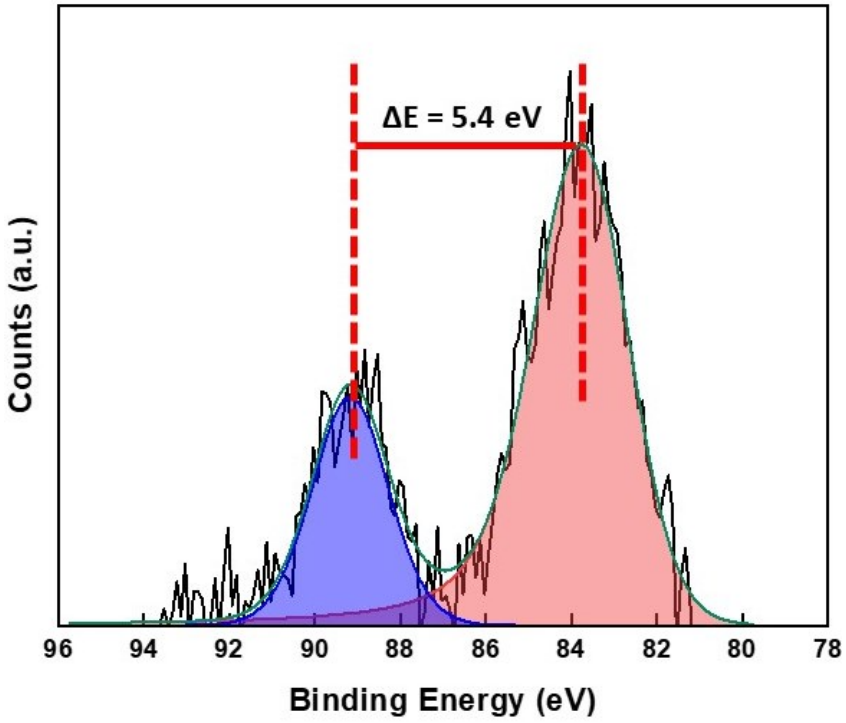

Figure 2-12. High resolution XP spectra Mn 3s region.

FTIR spectra for HMC and Mn_3O_4@HMC are shown in Figure 2-13. The HMC spectrum shows an absorption at 3434 cm^{-1} that is attributed to surface O-H and N-H stretching.[30] The feature at 2925 cm^{-1} arises from C-H stretching.[30] Features at 1585 and 1435 cm^{-1} correspond to C-N bending and heterocyclic stretching, respectively, and the feature at 1172 cm^{-1} is assigned to heterocyclic N-H in-plane deformation breathing.[30] In addition to all the HMC spectral features, the Mn_3O_4@HMC spectrum shows an absorption at 524 cm^{-1} corresponding to Mn-O bonding.[31] The C-N bending and heterocyclic stretching features in the HMC spectrum are qualitatively sharper and located at lower energy (i.e., 1556 and 1410

cm^{-1}, respectively) for the hybrid, which is consistent with HMC-NP interactions suggested by the N-region of the XP spectra.

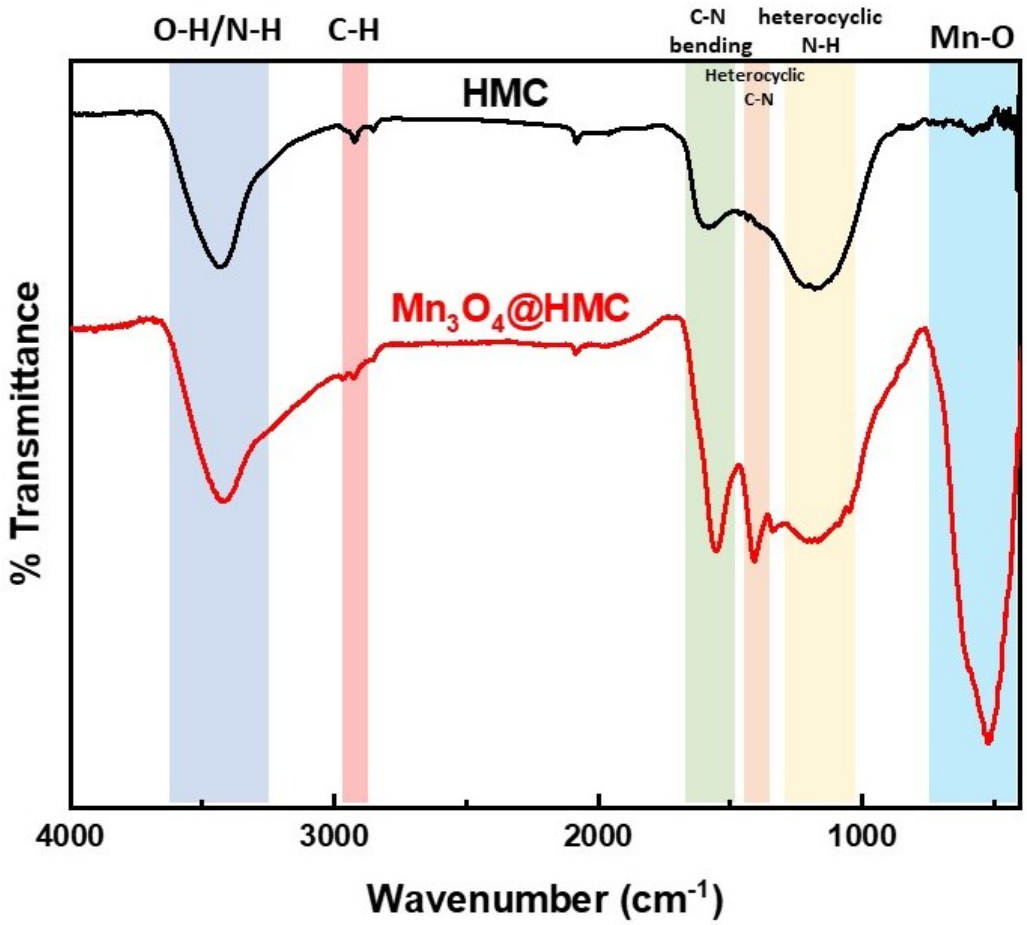

Figure 2-13. FTIR spectra for HMC and Mn_3O_4@HMC.

The textural properties of the pristine HMC and Mn_3O_4@HMC were evaluated by nitrogen sorption analysis. BET surface area, pore diameter, and pore volume were acquired (Table 2-1). Isotherms (Fig. 2-14) show a distinct hysteresis loop was observed at high relative pressure for the pristine HMCs giving an average pore diameter is 29 nm, consistent with a mesoporous material.[22] In addition, they

exhibit a BET surface area of 498 cm^2 g^{-1}. After incorporation of Mn_3O_4 NPs, the BET surface area and pore volume drop to 201 cm^2 g^{-1} and 1.28 cm^3 g^{-1}, respectively. This observation can be attributed to Mn_3O_4 NPs occupying the space inside the HMCs.

Table 2-1. HMC and Mn_3O_4@HMC textural properties.

Catalyst	BET surface area (m^2 g^{-1})	Pore diameter (nm)	Pore Volume (cm^3 g^{-1})
Pristine HMC	498	29	3.33
Mn_3O_4@HMC	201	24	1.28

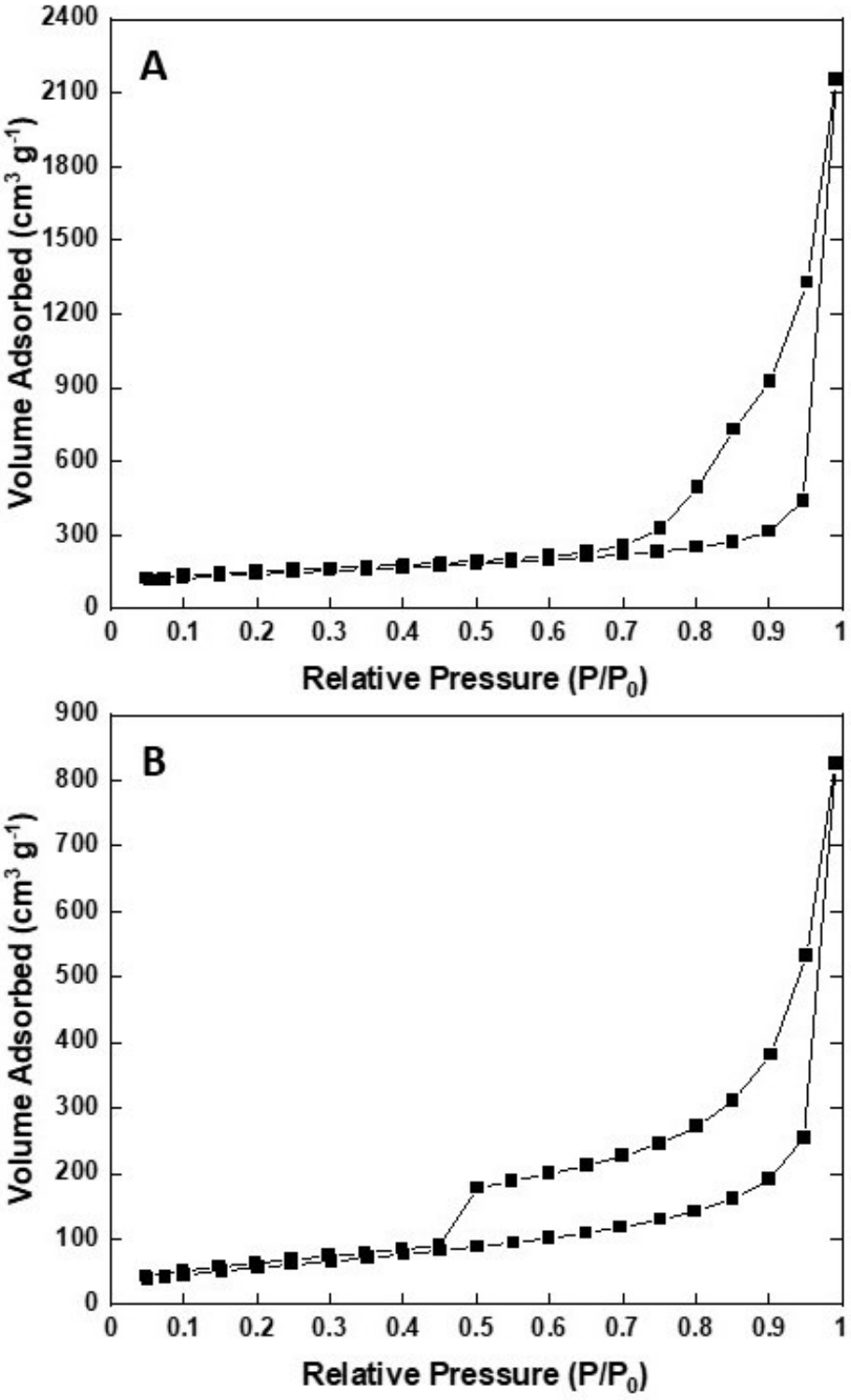

Figure 2-14. Nitrogen adsorption-desorption isotherms for (A) purified HMC and (B) Mn_3O_4@HMC.

The ORR activity of Mn_3O_4@HMC was first assessed using cyclic voltammetry (CV) in both Ar- and O_2- saturated 0.1 M KOH aqueous solution using a rotating disk electrode (Fig. 2-15A). For these measurements, a 0.1 M KOH aqueous electrolyte was used to maximize O_2 solubility and minimize background current.[32] The Ar-saturated cyclic voltammogram is featureless and only shows capacitive current; in contrast, the cyclic voltammogram from the O_2-saturated system shows a cathodic current at -0.17 V. This observation indicates that the ORR reaction occurs on the Mn_3O_4@HMC. The ORR performance was subsequently evaluated using standard linear sweep voltammetry (LSV) in 1 M KOH aqueous electrolyte. Electrodes were prepared by impregnating a circular GDL with pristine HMC or Mn_3O_4@HMC. LSV curves of pristine HMC, Mn_3O_4 NPs, Mn_3O_4@HMCs, and Pt-Ru are shown in Figure 2-15B. The onset potential (defined as the potential at which the current density reaches 10 mA cm^{-2}) for the hybrid material was improved from -0.156 V for the pristine HMC to -0.082 V; this suggests synergistic effects resulting from the combination of HMCs with Mn_3O_4 NPs. This performance is comparable to that of Pt-Ru (-0.077 V). In addition, the maximum current density obtained for Mn_3O_4@HMC is 198.1 mA cm^{-2} and exceeds that of pristine HMC (i.e., 167.6 mA cm^{-2}); it is comparable to that of the Pt-Ru (i.e., 196.5 mA cm^{-2}). Based upon these observations, Mn_3O_4@HMC exhibits improved catalytic activity relative to pristine HMC and meets the performance of our Pt-Ru benchmark.

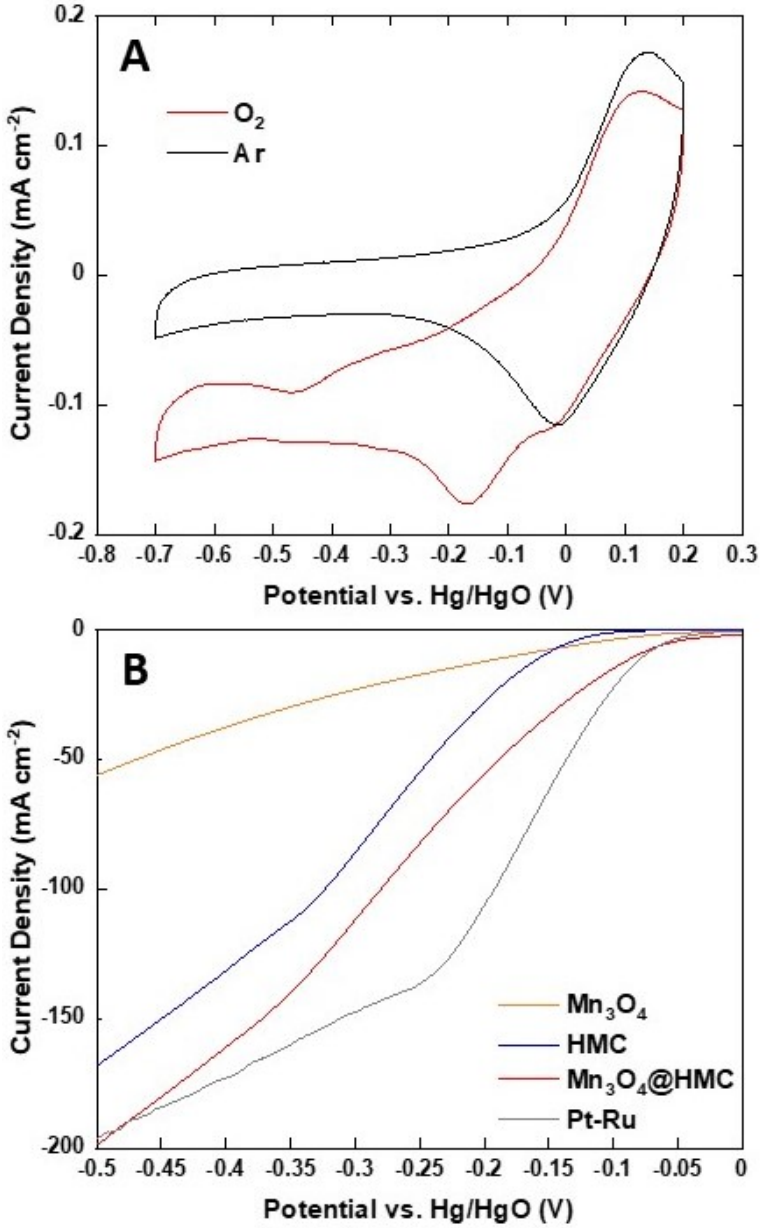

Figure 2-15. (A) Cyclic voltammograms for Mn_3O_4@HMC in Ar- and O_2-saturated 0.1 M KOH at a scan rate of 5 mV s^{-1}; (B) LSV curves obtained in O_2-saturated 1 M KOH aqueous solution at a scan rate of 5 mV s^{-1}.

To investigate the kinetics and catalytic mechanism, LSV was also performed using a Mn_3O_4@HMC-coated rotating disk electrode (RDE) at a scan rate of 5 mV

s^{-1} and predefined rotation rates (i.e., 225, 400, 625, 900, 1225, and 1600 rpm) in O_2-saturated 0.1 M KOH electrolyte (Fig. 2-16A). In Figure 2-16A, kinetically controlled (0 to -0.1 V), kinetic-diffusion controlled (-0.1 to -0.3 V), and diffusion controlled (-0.3 to -0.7 V) regions were observed. The Koutecky-Levich (K-L) equation (1) was used to determine the number of electrons transferred:

$$\frac{1}{|i|} = \frac{1}{|i_L|} + \frac{1}{|i_K|} = \frac{1}{B\omega^{0.5}} + \frac{1}{|i_K|} \tag{2-1}$$

$$i_K = nFAkC_{O_2} \tag{2-2}$$

$$B = 0.62nAFC_{O_2}v^{-\frac{1}{6}}D_0^{\frac{2}{3}} \tag{2-3}$$

where the measured current (i) is related to the kinetic current (i_K) and the diffusion-limiting current (i_L). ω is the angular velocity of the RDE, n is the number of electrons transferred per O_2 molecule, F is the Faraday constant (96485 C mol^{-1}), A is the electrode area (cm^2), k is the electron rate transfer constant, C_{O2} is the saturated O_2 concentration of the electrolyte (1.2 x 10^{-6} mol cm^{-3}), ν is the kinematic viscosity of the 0.1 M KOH solution (0.01 cm^2 s^{-1}), and D_0 is the diffusion coefficient of O_2 in the electrolyte (1.9 x 10^{-5} cm^2 s^{-1}).[33, 34] As the rotation rate was increased, higher (more negative) current densities were observed as a result of faster O_2 flux to the electrode surface. K-L plots were constructed by plotting i^{-1} against $\omega^{-0.5}$ (Fig. 2-16B). The number of electrons transferred per O_2 molecule was obtained from the

slope of the fitted lines. The average n value in the potential window 0.3-0.7 V is 3.95, suggesting that the Mn_3O_4@HMC catalyst predominantly proceeds via the four-electron pathway (Eqn. 2-6) rather than the competing alternative two-electron pathway (Eqn. 2-4 and 2-5).[35]

$$O_2 + H_2O + 2e^- \rightarrow HO_2^- + OH^- \quad (2\text{-}4)$$

$$2HO_2^- \rightarrow 2OH^- + O_2 \quad (2\text{-}5)$$

$$O_2 + 2H_2O + 4e^- \rightarrow 4OH^- \quad (2\text{-}6)$$

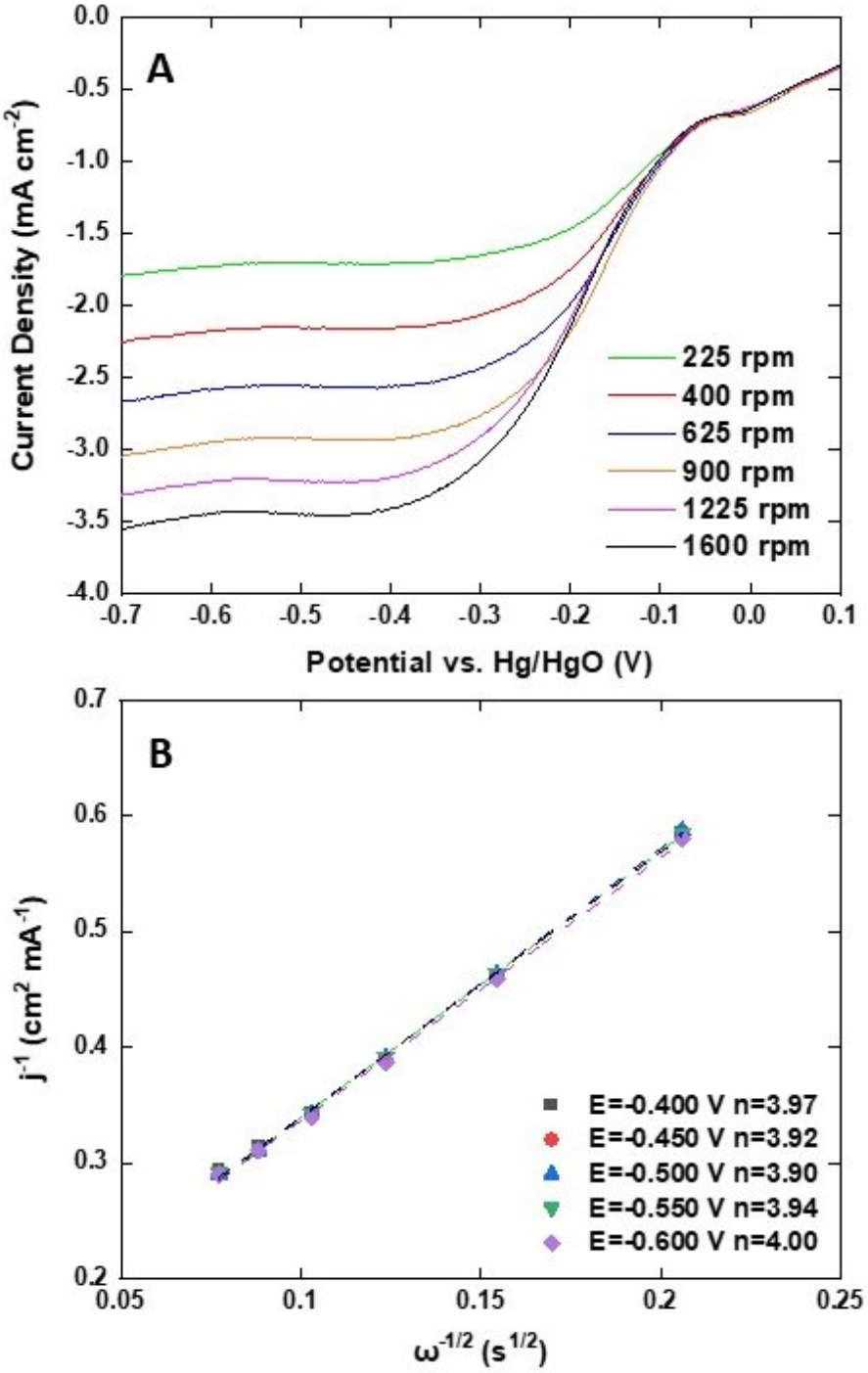

Figure 2-16. (A) ORR LSV curves for Mn_3O_4@HMC in O_2-saturated 0.1 M KOH at scan rate of 5 mV s^{-1} using RDE; (B) K-L plots for Mn_3O_4@HMC extrapolated in the potential range of 0.4-0.6 V.

Mn_3O_4@HMC and pristine HMC were incorporated into separate primary Zn-air batteries as the air electrode catalyst to evaluate their performance. Discharge rate tests were performed at predefined current densities (2, 5, 10, and 20 mA cm^{-2}). In all cases, the rate discharge curves (Fig. 2-17A) show the discharge potential of the Mn_3O_4@HMC was markedly better compared with pristine HMC. Mn_3O_4@HMC is also comparable to Pt-Ru at the tested current densities, indicating its promising ORR catalytic activity. At 10 and 20 mA cm^{-2}, the discharge potentials were 1.26 and 1.22 V, respectively for Mn_3O_4@HMC. Our benchmark Pt-Ru catalyst only exhibited 1.25 and 1.20 V discharge potential at 10 and 20 mA cm^{-2}, respectively. Furthermore, the performance of the present Mn_3O_4@HMC outperforms many transition metal oxide and carbon nanomaterial hybrids (Table 2-2). This is also the first time N-doped hollow carbon nanospheres have been combined with transition metal oxide nanoparticles as a Zn-air battery catalyst. Conventional transition metal nanoparticle synthesis often involves high temperature annealing (>300°C), which is likely to destroy the delicate feature of the HMC (average thickness = 3.8 nm).[36-38] By implementing the sonication procedure, the potential damage to the HMC active sites was avoided.

Polarization and power density curves are shown in Figure 2-17B. They highlight that the maximum power density was improved from 158 mW cm^{-2} to 183 mW cm^{-2} after the incorporation of Mn_3O_4 NPs. The maximum power density is

higher than the value obtained for our Pt-Ru benchmark (158 mW cm^{-2}) under the same conditions. The hybrid catalyst also exhibits a lower charge-transfer resistance, evidenced by the smaller size of the semi-circular region of EIS Nyquist plot (Fig. 2-18). The excellent catalytic performance can be attributed to the exterior and interior surfaces of the HMCs being decorated with Mn_3O_4 NPs. The number of active sites was maximized and any synergistic effects were amplified.

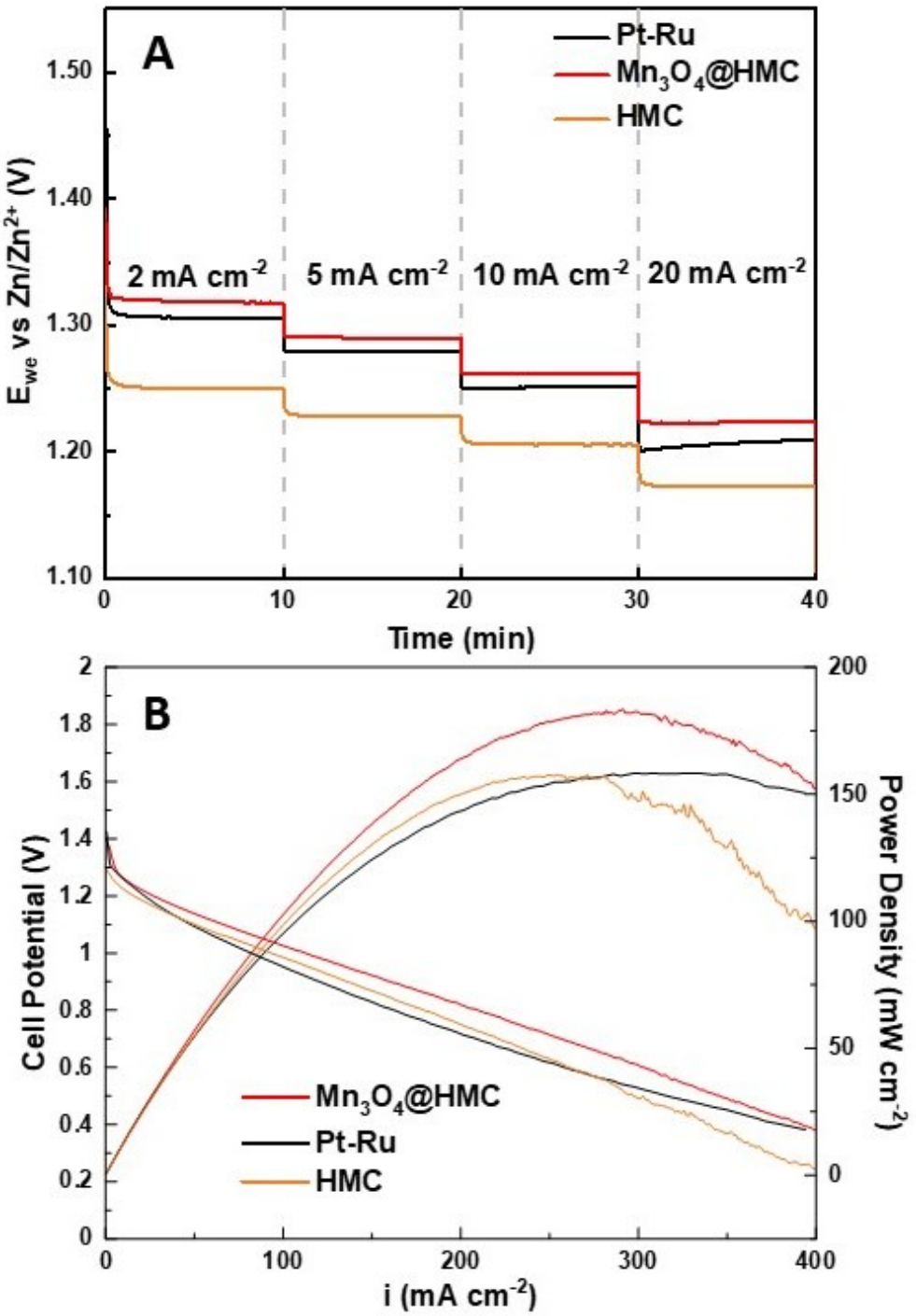

Figure 2-17. (A) Rate discharge curves; (B) polarization and power density curves for a primary Zn-air battery using Mn_3O_4@HMC, pristine HMC, and Pt-Ru as ORR catalysts.

Table 2-2. Performance Comparison of Mn_3O_4@HMC with Other Zn-Air Battery Catalyst in Literature

Notable Catalyst from Literature	**Discharge Potential (V) @ i (mA cm^{-2})**	**Cyclability**	**Ref**
Mn_3O_4@HMC	1.22@20	40 mV drop, 235 cycles, 20 mA cm^{-2}	This work
Mn_3O_4/N-CNT	1.21@20	100 mV drop, 100 cycles, 10 mA cm^{-2}	[39]
Mn_3O_4 QD/N-p-MCNT	~1.1@20	Stable, 100 h, 20 mA cm^{-2}	[40]
Co_3O_4/N-CNT on Stainless Steel Mesh	1.2@25	Stable, 60 cycles, 25 mA cm^{-2}	[41]
$Fe_{0.5}Co_{0.5}O_x$/N-rGO	1.21@10	50 mV drop, 60 cycles, 10 mA cm^{-2}	[42]
Fe-N-CNN	1.21@20	N/A – Not cycled	[43]
$MnCo_2O_4$/CNT	1.20@10	200 mV drop, 70 cycles, 15 mA cm^{-2}	[44]
MnO_2 on Carbon Paper	1.20@15	20 mV drop, 350 cycles, 15 mA cm^{-2}	[45]
Co_4N/CNW/CC	1.15@10	Stable over 400 cycles	[46]
Fe@N-C	1.25@10	125 mV drop, 200 cycles, 10 mA cm^{-2}	[38]

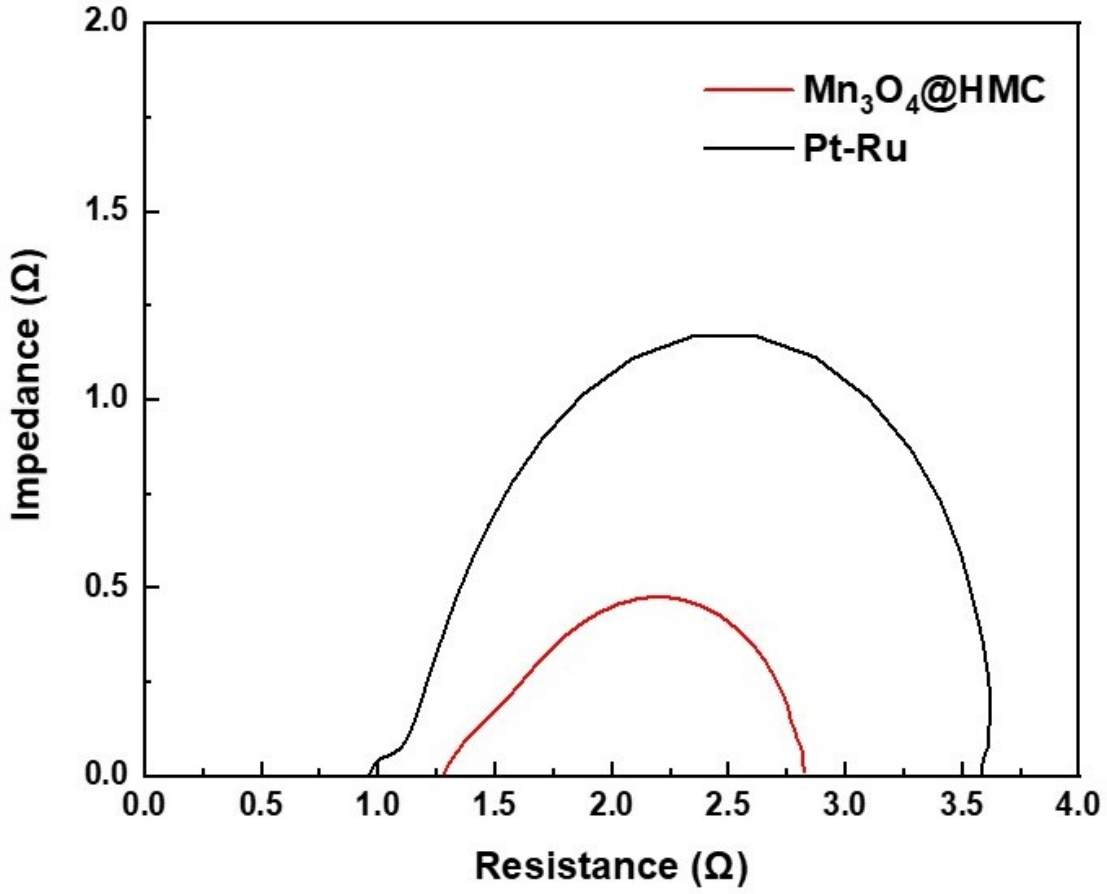

Figure 2-18. Electrochemical impedance spectra of Mn_3O_4@HMC and Pt-Ru.

The stability of the as-synthesized hybrid material was further investigated by cycling a rechargeable Zn-air battery at 20 mA cm^{-2} using Mn_3O_4@HMC on GDL as the ORR electrode. Each cycle was 30 min and 235 cycles (117.5 h) were performed. Ni foam was used as the OER electrode due to its high surface area, good OER catalytic activity, and stability.[47] A tri-electrode configuration was utilized so that the ORR performance could be evaluated independently of the OER performance. As shown in the discharge/charge curves (Fig. 2-19A), the HMC hybrid initially exhibits a discharge potential of 1.21 V. After 117.5 h of cycling

(235 cycles), the discharge potential decreased slightly to 1.17 V corresponding to a 3.3% loss. A similar tri-electrode battery, using Pt-Ru on GDL as the ORR electrode and Ni foam as OER electrode, was tested under the same conditions (Fig. 2-19B). The discharge potential for Pt-Ru decreased from 1.19 to 1.14 V, after 117.5 h of cycling, corresponding to a 4.2% change. This shows the comparable long-term durability of the Mn_3O_4@HMC compared with Pt-Ru. The morphology of the HMC hybrid was not evaluated after cycling due to the difficulty in separating the hybrid from the GDL.

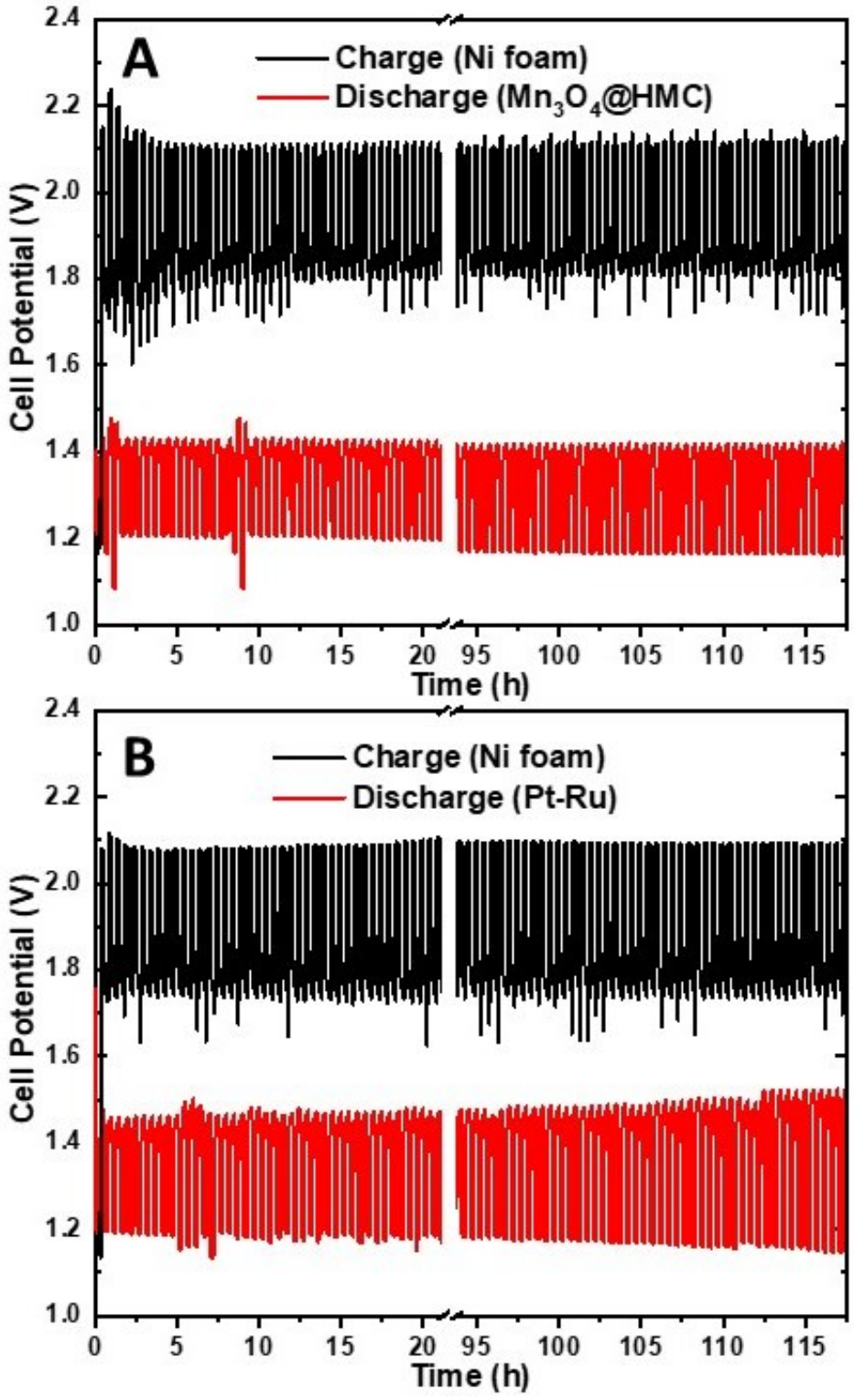

Figure 2-19. (A) Discharge/charge cycling curves for a three-electrode Zn-air battery using Mn_3O_4@HMC on GDL and Ni foam as ORR and OER electrodes,

respectively. (B) Discharge/charge cycling curves for a three-electrode Zn-air battery using Pt-Ru on GDL and Ni foam as ORR and OER electrodes, respectively.

2.4 Conclusions

Mn_3O_4 decorated N-doped hollow mesoporous carbon nanospheres were prepared using a straightforward templated growth/sonication approach. Comparing performance of the hybrid with that of pristine HMCs, we note improved catalytic ORR activity in primary and secondary Zn-air batteries. This synergistic effect, that can reasonably be attributed to Mn-O-C interaction that manifest in the presented XPS analysis, opens the door to the potential of exquisite tuning of catalytic response that could lead to next-generation systems. The primary battery fabricated using Mn_3O_4@HMC generated a maximum power density of 183 mW cm^{-2} at a current density of 291 mA cm^{-2}. The secondary battery with a three-electrode configuration exhibited a small discharge potential drop from 1.21 to 1.17 V after over 117.5 h of cycling at 20 mA cm^{-2}, displaying excellent durability.

2.5 References

(1) Chu, S.; Cui, Y.; Liu, N. *Nat. Mater.* **2017**, *16* (1), 16-22.
(2) Roger, I.; Shipman, M. A.; Symes, M. D. *Nat. Rev. Chem.* **2017**, *1* (1), 0003.
(3) Cano, Z. P.; Banham, D.; Ye, S. Y.; Hintennach, A.; Lu, J.; Fowler, M.; Chen, Z. W. *Nat. Energy* **2018**, *3* (4), 279-289.

(4) Sui, S.; Wang, X. Y.; Zhou, X. T.; Su, Y. H.; Riffatc, S.; Liu, C. J. *J. Mater. Chem. A* **2017**, *5* (5), 1808-1825.
(5) Zuo, W. H.; Li, R. Z.; Zhou, C.; Li, Y. Y.; Xia, J. L.; Liu, J. P. *Adv. Sci.* **2017**, *4* (7).
(6) Wang, Y. X.; Liu, B.; Li, Q. Y.; Cartmell, S.; Ferrara, S.; Deng, Z. Q. D.; Xiao, J. *J. Power Sources* **2015**, *286*, 330-345.
(7) Girishkumar, G.; McCloskey, B.; Luntz, A. C.; Swanson, S.; Wilcke, W. *J. Phys. Chem. Lett.* **2010**, *1* (14), 2193-2203.
(8) Liu, X.; Huang, J. Q.; Zhang, Q.; Mai, L. Q. *Adv. Mater.* **2017**, *29* (20), 1601759.
(9) Hwang, J. Y.; Myung, S. T.; Sun, Y. K. *Chem. Soc. Rev.* **2017**, *46* (12), 3529-3614.
(10) Fu, J.; Cano, Z. P.; Park, M. G.; Yu, A. P.; Fowler, M.; Chen, Z. W. *Adv. Mater.* **2017**, *29* (7), 1604685.
(11) Pan, J.; Xu, Y. Y.; Yang, H.; Dong, Z. H.; Liu, H. F.; Xia, B. Y. *Adv. Sci.* **2018**, *5* (4), 1700691
(12) Li, Y. G.; Lu, J. *ACS Energy Lett.* **2017**, *2* (6), 1370-1377.
(13) Zhang, W.; Lai, W. Z.; Cao, R. *Chem. Rev.* **2017**, *117* (4), 3717-3797.
(14) Cheng, F. Y.; Chen, J. *Chem. Soc. Rev.* **2012**, *41* (6), 2172-2192.
(15) Ren, M. Q.; Zhang, J. B.; Tour, J. M. *ACS Appl. Energ. Mater.* **2019**, *2* (2), 1460-1468.
(16) Qu, L. T.; Liu, Y.; Baek, J. B.; Dai, L. M. *ACS Nano* **2010**, *4* (3), 1321-1326.
(17) Wang, H. P.; Keum, J. K.; Hiltner, A.; Baer, E.; Freeman, B.; Rozanski, A.; Galeski, A. *Science* **2009**, *323* (5915), 757-760.
(18) Liu, M. K.; Song, Y. F.; He, S. X.; Tjiu, W. W.; Pan, J. S.; Xia, Y. Y.; Liu, T. X. *ACS Appl. Mater. Inter.* **2014**, *6* (6), 4214-4222.
(19) Koza, J. A.; He, Z.; Miller, A. S.; Switzer, J. A. *Chem. Mater.* **2012**, *24* (18), 3567-3573.
(20) Cheng, F. Y.; Su, Y.; Liang, J.; Tao, Z. L.; Chen, J. *Chem. Mater.* **2010**, *22* (3), 898-905.
(21) Li, L. Q.; Yang, J.; Yang, H. B.; Zhang, L. P.; Shao, J. J.; Huang, W.; Liu, B.; Dong, X. C. *ACS Appl. Energ. Mater.* **2018**, *1* (3), 963-969.
(22) Hadidi, L.; Davari, E.; Iqbal, M.; Purkait, T. K.; Ivey, D. G.; Veinot, J. G. C. *Nanoscale* **2015**, *7* (48), 20547-20556.
(23) Dasog, M.; Smith, L. F.; Purkait, T. K.; Veinot, J. G. C. *Chem. Commun.* **2013**, *49* (62), 7004-7006.
(24) Shirley, D. A. *Phys. Rev. B* **1972**, *5* (12), 4709-4714.
(25) Xiong, M.; Clark, M. P.; Labbe, M.; Ivey, D. G. *J. Power Sources* **2018**, *393*, 108-118.
(26) Wu, T. H.; Hesp, D.; Dhanak, V.; Collins, C.; Braga, F.; Hardwick, L. J.; Hu, C. C. *J. Mater. Chem. A* **2015**, *3* (24), 12786-12795.

(27) Lee, J. W.; Hall, A. S.; Kim, J. D.; Mallouk, T. E. *Chem. Mater.* **2012**, *24* (6), 1158-1164.
(28) Chigane, M.; Ishikawa, M.; Izaki, M. *J. Electrochem. Soc.* **2001**, *148* (7), D96-D101.
(29) Gorlin, Y.; Jaramillo, T. F. *J. Am. Chem. Soc.* **2010**, *132* (39), 13612-13614.
(30) Yu, X.; Fan, H. L.; Liu, Y.; Shi, Z. J.; Jin, Z. X. *Langmuir* **2014**, *30* (19), 5497-5505.
(31) Dubal, D. P.; Dhawale, D. S.; Salunkhe, R. R.; Pawar, S. M.; Lokhande, C. D. *Appl. Surf. Sci.* **2010**, *256* (14), 4411-4416.
(32) Xing, W.; Yin, G.; Zhang, J.; Elsevier. *Rotating electrode methods and oxygen reduction electrocatalysts*; Elsevier, 2014.
(33) Paulus, U. A.; Schmidt, T. J.; Gasteiger, H. A.; Behm, R. J. *J. Electroanal. Chem.* **2001**, *495* (2), 134-145.
(34) Zhang, J. T.; Zhao, Z. H.; Xia, Z. H.; Dai, L. M. *Nat. Nanotechnol.* **2015**, *10* (5), 444-452.
(35) Wu, Z. S.; Yang, S. B.; Sun, Y.; Parvez, K.; Feng, X. L.; Mullen, K. *J. Am. Chem. Soc.* **2012**, *134* (22), 9082-9085.
(36) Chen, L.; Sun, L. J.; Luan, F.; Liang, Y.; Li, Y.; Liu, X. X. *J. Power Sources* **2010**, *195* (11), 3742-3747.
(37) Vijayakumar, S.; Ponnalagi, A. K.; Nagamuthu, S.; Muralidharan, G. *Electrochim. Acta.* **2013**, *106*, 500-505.
(38) Laurent, S.; Forge, D.; Port, M.; Roch, A.; Robic, C.; Elst, L. V.; Muller, R. N. *Chem. Rev.* **2008**, *108* (6), 2064-2110.
(39) Aasen, D.; Clark, M.; Ivey, D. G. *Batteries Supercaps* **2019**, *2* (10), 882-893.
(40) Huang, Z. X.; Qin, X. P.; Gu, X. F.; Li, G. Z.; Mu, Y. C.; Wang, N. G.; Ithisuphalap, K.; Wang, H. X.; Guo, Z. P.; Shi, Z. C.; Wu, G.; Shao, M. H. *ACS Appl. Mater. Inter.* **2018**, *10* (28), 23900-23909.
(41) Fu, J.; Hassan, F. M.; Li, J. D.; Lee, D. U.; Ghannoum, A. R.; Lui, G.; Hoque, M. A.; Chen, Z. W. *Adv. Mater.* **2016**, *28* (30), 6421-6428.
(42) Wei, L.; Karahan, H. E.; Zhai, S. L.; Liu, H. W.; Chen, X. C.; Zhou, Z.; Lei, Y. J.; Liu, Z. W.; Chen, Y. *Adv. Mater.* **2017**, *29* (38), 1701410.
(43) Li, F. Y.; Li, H.; Liu, X. X.; Wang, L. B.; Lu, Y.; Hu, X. L. *Chem-Eur. J.* **2019**, *25* (2), 635-641.
(44) Ge, X. M.; Liu, Y. Y.; Goh, F. W. T.; Hor, T. S. A.; Zong, Y.; Xiao, P.; Zhang, Z.; Lim, S. H.; Li, B.; Wang, X.; Liu, Z. L. *ACS Appl. Mater. Inter.* **2014**, *6* (15), 12684-12691.
(45) Sumboja, A.; Ge, X. M.; Goh, F. W. T.; Li, B.; Geng, D. S.; Hor, T. S. A.; Zong, Y.; Liu, Z. L. *Chempluschem* **2015**, *80* (8), 1341-1346.
(46) Meng, F. L.; Zhong, H. X.; Bao, D.; Yan, J. M.; Zhang, X. B. *J. Am. Chem. Soc.* **2016**, *138* (32), 10226-10231.

(47) Zhang, W.; Li, D. H.; Zhang, L. Z.; She, X. L.; Yang, D. J. *J. Energy Chem.* **2019**, *39*, 39-53.

Chapter 3: Hollow Mesoporous Carbon Nanospheres Decorated with Metal Oxide Nanoparticles as Efficient Earth-Abundant Zinc-Air Battery Catalysts

A version of this chapter was published as:

He, Y.; Aasen, D.; McDougall, A.; Yu, H.; Labbe, M.; Ni, C.; Milliken, S.; Ivey, D. G.; Veinot, J. G. C. *ChemElectrochem* **2021**, *8* (8), 1455–1463.

3.1 Introduction

The ever-rising global energy consumption and increasing awareness of climate change have seen many nations begin to shift away from fossil fuel-based economies and embrace renewable energy options.[1, 2] Even though these alternative energy sources are more sustainable and environmentally 'friendly', they are often intermittent and their energy output depends greatly on time and location.[3] This factor alone creates an imbalance between energy supply and demand that must be mitigated/managed.[4] Efficient and cost-effective energy storage technologies are urgently needed to address this important challenge.

Zinc-air batteries (Zn-air) have gained much attention as stationary energy storage systems because of their established advantages over traditional Li-ion batteries.[5] First and foremost, Zn-air batteries have a theoretical energy density of 1086 Wh kg^{-1}; this exceeds the energy density of current Li-ion batteries (220 Wh kg^{-1}) by almost five times.[6, 7] Zn is also a more abundant and cost effective raw material than Li that results in a lower cost per unit energy for Zn-air batteries (currently ~\$65-135 kW^{-1} h^{-1} and potentially < \$10 kW^{-1} h^{-1}) versus Li-ion batteries (~\$150 kW^{-1} h^{-1}).[8-11] Finally and equally important, Zn-air batteries use aqueous electrolytes, which eliminates risks of fire and explosion that exist for Li-ion batteries.[11]

Despite these important and obvious advantages, Zn-air battery development still faces challenges. The biggest hurdle facing Zn-air batteries is a lack of efficient and cost-effective catalysts for the oxygen-based reactions that occur at the air electrode.[12] Figure 3-1 shows a depiction of a Zn-air battery and summarizes the electrochemical reactions responsible for its operation. During battery discharge, oxygen gas is reduced to hydroxide anions at the air electrode -- this is commonly termed the oxygen reduction reaction (ORR), while the metallic Zn is oxidized to zincate anions.[13] When the battery is being recharged, hydroxide and zincate anions are converted back to oxygen and Zn, respectively - the former case is termed the oxygen evolution reaction (OER). It is well established that ORR and OER occurring at the air electrode are kinetically sluggish.[14] These low rates of reaction diminish the discharge potential and increase the charge potential of the Zn-air battery resulting in a lowering/limiting of its overall efficiency.[15] This apparent barrier to realizing optimal Zn-air battery efficiency can be overcome with the design and implementation of bifunctional electrocatalysts that promote both the ORR and OER reactions.

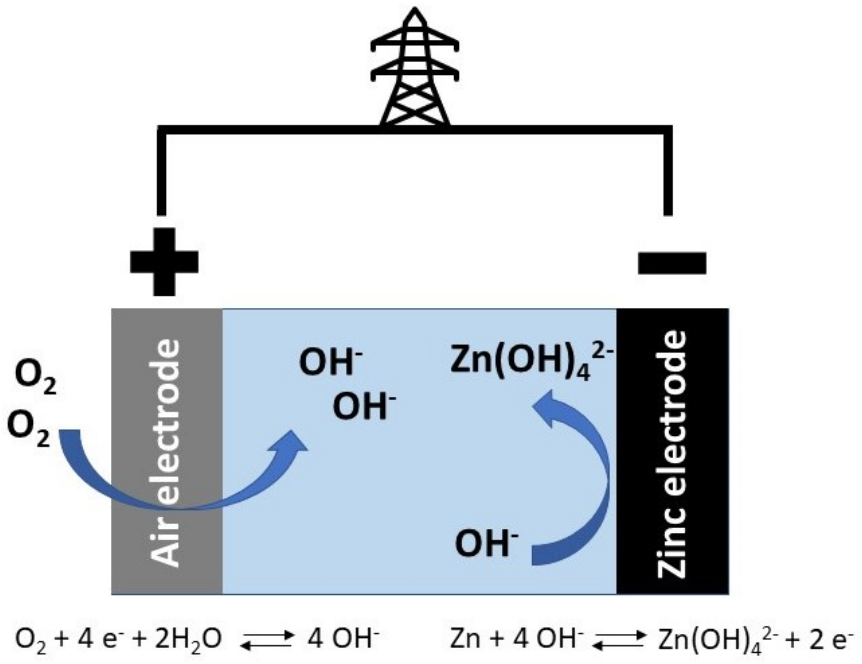

Figure 3-1. A pictorial presentation of the electrochemical reactions inside a Zn-air battery.

Traditional bifunctional catalysts typically consist of physical mixtures containing platinum (Pt), ruthenium oxide (RuO_2), and iridium oxide (IrO_2) powders.[16] These costly precious metal containing systems ultimately limit the wide spread commercial implementation of Zn-air battery technologies. Furthermore, while precious metal-based bifunctional catalysts promote the ORR and OER reactions, they suffer from poor stability during battery cycling.[17] Clearly, more stable, cost-effective, and efficient bifunctional ORR/OER catalysts are urgently needed if Zn-air batteries are to realize wide spread adoption. Of late, a variety of materials have been investigated as alternative catalysts. Heteroatom-doped carbon

nanomaterials such as N-doped hollow mesoporous carbon nanospheres (HMC) and Fe/N-doped graphene nanosheets have shown excellent catalytic activities toward ORR and OER.[18, 19] Transition metal oxides, phosphates and sulfides have also exhibited promising performance in Zn-air batteries.[20-25] In addition, a variety of metal oxide nanoparticles have been interfaced with HMC with varying degrees of success.[26, 27] Most recently, metal-organic-frameworks (MOFs) have also been studied as a precursor to form metal oxide/carbon nanomaterial hybrids that act as bifunctional catalysts for ORR/OER.[28]

In this work, we report the synthesis and testing of hybrid catalysts that combine nitrogen-doped hollow mesoporous carbon (HMC) nanospheres with transition metal oxide (i.e., Co_3O_4, $MnCo_2O_4$, 'CoFeNiO') nanoparticles. By combining transition metal oxides and HMC, we were successful in preparing catalysts using earth abundant elements that provide excellent ORR and OER activities when compared to costly benchmark catalyst 30% Pt and 15% RuO_2 on carbon black (denoted as Pt-Ru). Co_3O_4@HMC and $MnCo_2O_4$@HMC exhibit onset potentials of -0.076 and -0.060 V (vs. Hg/HgO) respectively, comparable to Pt-Ru (-0.077 V). Co_3O_4@HMC and $MnCo_2O_4$@HMC show discharge potentials of 1.26 and 1.28 V, respectively, at 10 mA cm^{-2} that exceed the 1.25 V of Pt-Ru. 'CoFeNiO'@HMC displays an OER onset potential of 0.587 V, comparable to Pt-

Ru (0.576 V). It also exhibits a charging potential of 1.96 V at 10 mA cm^{-2}, which is lower than 2.01 V for Pt-Ru.

3.2 Experimental Section

3.2.1 Materials and reagents

Dopamine hydrochloride, pluronic F127, tris(hydroxymethyl)amino-methane (Tris), tetraethoxysilane (TEOS) (≥99 %), 2-propanol, anhydrous ethanol (≤0.005 % water), cobalt acetate ($Co(CH_3COO)_2$), manganese acetate ($Mn(CH_3COO)_2$), iron(II) sulfate heptahydrate ($FeSO_4 \cdot 7H_2O$), and nickel(II) sulfate heptahydrate ($NiSO_4 \cdot 7H_2O$) were purchased from Sigma-Aldrich. Ammonium hydroxide (NH_4OH; 28-30%) was obtained from Caledon Laboratory Chemicals. Hydrofluoric acid (HF, electronic grade, 48-50%) was acquired from Fisher Scientific. Pt-Ru powder (30% Pt and 15% RuO_2 on carbon black) and Nafion solution (D521, 5% w/w in water) were obtained from Alfa Aesar. Teflon-coated porous carbon paper (SGL 39BC gas diffusion layer; GDL) was purchased from the Fuel Cell Store. All reagents were used as received unless otherwise specified.

3.2.2 Synthesis of Stöber SiO_2 nanoparticles

Stöber SiO_2 nanoparticles (NPs) were synthesized via a modified literature procedure.[29] In brief, aqueous NH_4OH (8 mL) was added to a mixture of deionized

water (80 mL) and anhydrous ethanol (156 mL) under magnetic stirring (900 rpm). Subsequently, TEOS (3.575 mL) was added to the basic water/ethanol mixture and the entire mixture was stirred at 900 rpm for 3 h at room temperature (25 °C). The resulting SiO_2 NPs were collected using centrifugation at 11400 rpm for 35 min. The NPs were then re-dispersed in deionized water via sonication and purified by centrifugation. The purification process was repeated twice with anhydrous ethanol. The purified SiO_2 NPs were dried under vacuum for 5 h before being transferred to a sealed glass vial until use.

3.2.3 Synthesis of SiO_2@C nanoparticles (NPs)

The SiO_2 NPs (0.7 g) were ground into fine powder before being dispersed in 187 mL of deionized water via sonication (10 min). Triblock copolymer pluronic F127 (0.35 g), Tris (0.21 g), and dopamine hydrochloride (0.7 g) were added to the SiO_2 aqueous suspension. The mixture was magnetically stirred at 900 rpm at room temperature (25 °C) for 24 h, resulting in a dark aqueous suspension of polydopamine coated SiO_2 NPs (SiO_2@PDA). The SiO_2@PDA NPs were collected by centrifugation at 11400 rpm for 35 min. Subsequently, the SiO_2@PDA NPs were re-dispersed in anhydrous ethanol via sonication and purified with centrifugation. The purification process was repeated twice. The SiO_2@PDA NPs were then dried under vacuum for 5 h before being transferred to a quartz boat. The boat containing SiO_2@PDA NPs was placed in a tube furnace under flowing Ar atmosphere. The

furnace was heated to 400 °C (heating rate of 1 °C min^{-1}) and maintained at 400 °C for 2 h. The furnace was then heated to 800 °C (heating rate of 5 °C min^{-1}) and maintained at 800 °C for 3 h. Finally, the furnace was cooled to room temperature (25 °C) and SiO_2@C NPs were collected as a black solid.

3.2.4 Synthesis of hollow mesoporous carbon spheres (HMCs)

The SiO_2@C (0.6 g) was ground to a fine powder using an agate mortar and pestle, placed in a polyethylene terephthalate (PET) beaker, and dispersed in a mixture of anhydrous ethanol (6 mL) and deionized (DI) water (6 mL) upon sonication using a standard bath sonicator (10 min). HF (49 wt%, 6 mL) was added and the mixture was magnetically stirred at 25 °C for 1 h. The inherent porosity of the carbon shell made it possible to remove the SiO_2 core to yield HMCs. The HMCs were isolated from the mixture via vacuum filtration using a Teflon funnel and filter flask and were subsequently washed with DI water (60 mL) and anhydrous ethanol (60 mL). Finally, the purified HMCs were dried under vacuum for 5 h and transferred to a sealed glass vial and stored in ambient conditions. (Caution! HF must be handled with extreme care and in accordance with local regulations/guidelines)

3.2.5 Synthesis of transition metal oxide nanoparticle-decorated HMCs ('MO'@HMC)

Transition metal oxide nanoparticles were added to the HMC surfaces using a modified literature method.[30] Briefly, the purified HMCs (50 mg) was dispersed in anhydrous ethanol (20 mL) via sonication (10 min), after which NH4OH (1 mL) and DI H_2O (2 mL) were added to the HMC suspension. Transition metal precursors (powder, 8.4×10^{-4} mol total) were then added to the mixture. A summary of the conditions is provided in Table 3-1. The reaction mixture was sealed in a glass reaction vessel and heated to 80 °C for 20 h. The 'MO'@HMCs were collected via centrifugation at 11400 rpm for 35 min. The HMCs were then re-dispersed in anhydrous ethanol via sonication and purified by centrifugation. The purification was repeated twice. Finally, the purified 'MO'@HMCs were dried in vacuo for 5 h.

Table 3-1. Metal precursor content during synthesis for each hybrid.

Hybrids	$Co(CH_3CO_2)_2$	$FeSO_4 \cdot 7H_2O$	$Mn(CH_3CO_2)_2$	$NiSO_4 \cdot 7H_2O$
Co_3O_4 @HMC	8.4×10^{-4} mol	-	-	-
$MnCo_2O_4$ @HMC	4.2×10^{-4} mol	-	4.2×10^{-4} mol	-
'CoFeNiO' @HMC	2.8×10^{-4} mol	2.8×10^{-4} mol	-	2.8×10^{-4} mol
'FeMnNiO' @HMC	-	2.8×10^{-4} mol	2.8×10^{-4} mol	2.8×10^{-4} mol
'CoFeMnO' @HMC	2.8×10^{-4} mol	2.8×10^{-4} mol	2.8×10^{-4} mol	-

3.2.6 Material characterization

Scanning electron microscopy (SEM) was performed on a Zeiss Sigma 300 VP-FESEM (accelerating voltage of 5-20 kV) equipped with secondary and backscattered electron detectors and an in-lens detector. SEM samples were prepared by drop-coating an ethanol suspension of material of interest onto an aluminum (Al) stub. The coated stub was subsequently air dried for 1 h at room temperature (25 °C). Transmission/scanning transmission electron microscopy (TEM/STEM) was performed on a JEOL JEM-ARM200CF TEM/STEM (accelerating voltage of 200 kV) equipped with energy dispersive X-ray (EDX)

spectrometer. High resolution TEM (HRTEM) images were processed using Gatan Digital Micrograph software (Version 3.22.1461.0) and ImageJ (Version 1.52 A). TEM samples were prepared by placing a drop of ethanol suspension of material of interest onto a holy/lacey carbon coated Cu grid (Electron Microscopy Inc.). The coated carbon grid was subsequently dried under vacuum for at least 16 h.

X-ray photoelectron spectroscopy (XPS) was performed on a Kratos Axis 165 Ultra X-ray spectrometer operating in energy spectrum mode under ultra-high vacuum. Samples were prepared by placing a drop of ethanol suspension of material of interest onto a Cu foil. This substrate was subsequently dried in vacuum for at least 16 h. A monochromatic Al K source (λ = 8.34 Å) was used as the X-ray source with a take-off angle of 90° and a charge neutralizer was used when necessary. CasaXPS software (VAMAS) was used to process data. A Shirley-type function was subtracted to account for the intrinsic loss background and spectra were calibrated by setting the deconvoluted adventitious C 1s peak to 284.8 eV. All high resolution XP spectra were deconvoluted using literature methods.[31, 32]

Powder X-ray diffraction (PXRD) patterns were collected by placing a ground and purified sample on a zero-background Si wafer. The measurement was performed on a Bruker D8 Discovery diffraction system equipped with Cu Kα radiation source (λ = 1.5406 Å) and high throughput LynxEYE 1-dimensional detector.

3.2.7 Electrochemical testing

The electrochemical performances of candidate catalysts were examined via linear sweep voltammetry (LSV). LSV was performed using a potentiostat (VSP) equipped with a three-electrode cell and O_2-saturated 1 M KOH electrolyte at a scan rate of 5 mV s^{-1}. The KOH solution was continuously purged with O_2 gas during testing. The working electrode was prepared as follows. The candidate catalyst (50 mg) of interest was dispersed in 15 mL of anhydrous ethanol via sonication for 2 h. Subsequently, 1 mL of 5 % Nafion was added to this ethanol suspension. A pre-cut piece of GDL (circular, diameter = 4.5 cm) was soaked and sonicated in the ethanol suspension for 20 min, before it was removed from the suspension and dried in air at 25 °C for 15 min. After that, 5 mL of the ethanol suspension was passed through the GDL via vacuum filtration, producing an impregnated GDL with a mass loading of ~2 mg cm^{-2} (±10 %). For comparison, a Pt-Ru sample was prepared by spray coating an ink consisting of Pt-Ru (50 mg), deionized water (1 mL), ethanol (2 mL), and 5 % Nafion (0.1 mL) onto the GDL. The impregnated/sprayed GDL samples were cut into rectangular pieces (1 cm×2 cm) and used as the working electrode, ensuring an exposed surface area of 1 cm^2. Hg/HgO (0.098 V vs. SHE) and a platinum wire were employed as reference and counter electrodes, respectively. The reported current densities were normalized to the exposed surface area of the working electrode (1 cm^2). All reported potentials were IR compensated (Ru = 2-4

Ω). Experimental errors are not reported due to the variability of the complex device structure.

3.2.8 Prototype Zn-Air battery assembly

Prototype Zn-air battery testing was performed in both vertical and horizontal home-made cells. In both cell orientations, a zinc sheet (8 g) and catalyst loaded GDL were used as zinc and air electrodes, respectively. The electrolyte of choice was an aqueous mixture of 6 M KOH and 0.25 M ZnO. Rate tests were obtained using the vertical cell and bifunctional cycling was performed in the horizontal cell. Pt-Ru spray-coated GDL was tested as the air electrode for comparison. Bifunctional cycling was performed at 10 mA cm^{-2}, with 10 min discharging and 5 min resting, followed by 10 min recharging and 5 min resting (30 min/cycle). The cycling was continued for 100 h (i.e., 200 cycles). Experimental errors are not reported due to the variability of the complex device structure.

3.3. Results and Discussion

Transition metal oxide nanoparticles ('MO'NPs) were deposited onto the surfaces of HMC substrates using solution-based methods to yield 'MO'@HMC hybrids.[30] Secondary electron scanning electron microscopy (SEM) images of pristine HMCs and those decorated with the indicated nanoparticles are shown in Figure 3-2. It is clear that pristine HMCs possess a spherical morphology and smooth

exterior surfaces (Fig. 3-2A). Following deposition of ‘MO’NPs, the general HMC spherical morphology remains intact; however, particle surfaces possess a rough coating consistent with the presence of NPs (Fig. 3-2B to F). In fact, NPs (i.e., individual and clusters) are readily observed on the HMC surfaces in all presented SEM images. Bright field transmission electron microscopy (TEM) imaging reveals complementary structural information and shows pristine HMCs are hollow with a shell thickness of 7±1 nm (Fig. 3-3A). Consistent with the SEM imaging, the ‘MO‘@HMCs are generally spherical; however, the apparent mean shell thickness increases to 10±1 nm as a result of the NP coatings that are clearly evident (Fig. 3-3B to F).

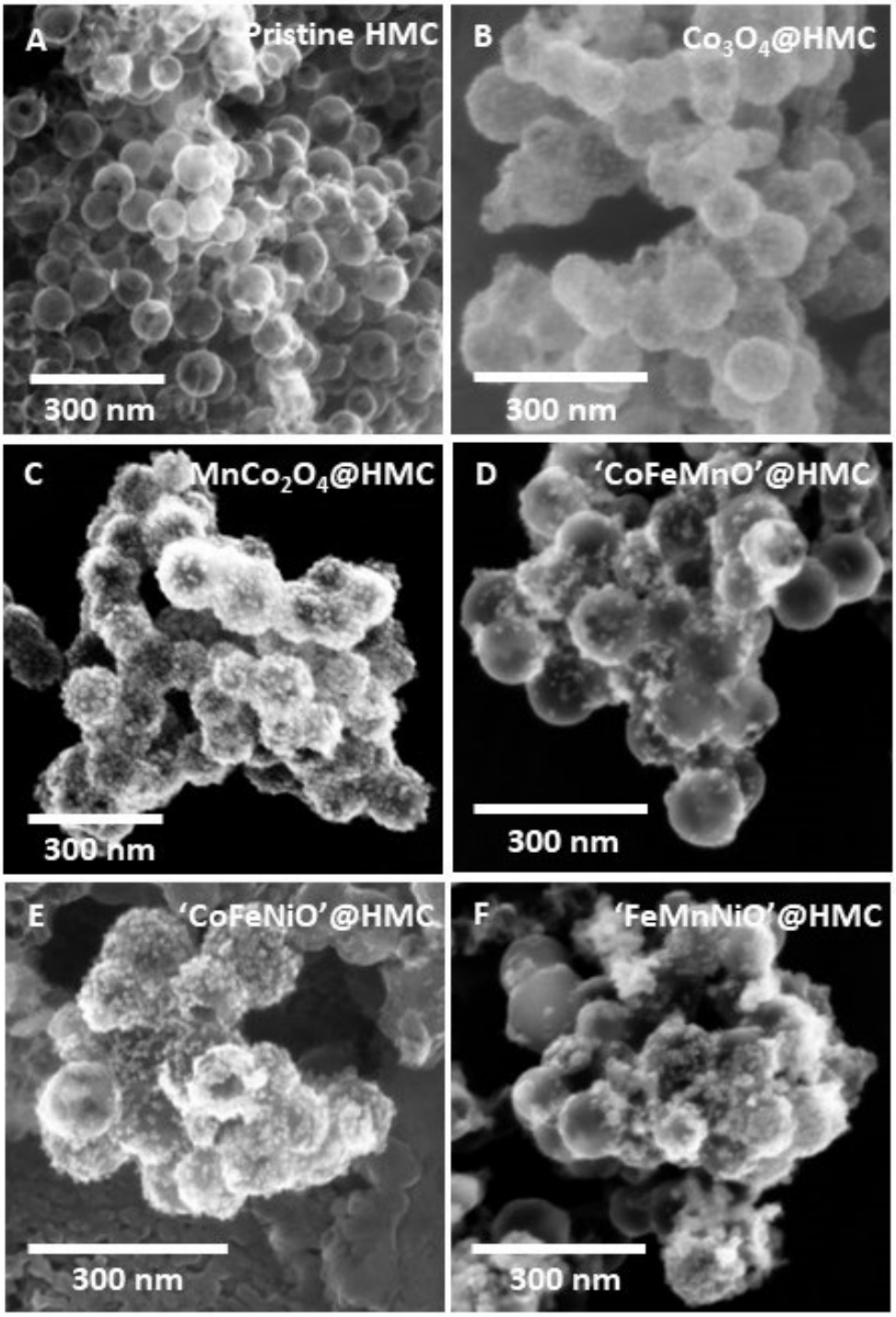

Figure 3-2. Secondary electron scanning electron microscopy images of (A) pristine HMC; (B) Co_3O_4@HMC; (C) $MnCo_2O_4$@HMC; (D) 'CoFeMnO'@HMC; (E) 'CoFeNiO'@HMC; and (F) 'FeMnNiO'@HMC.

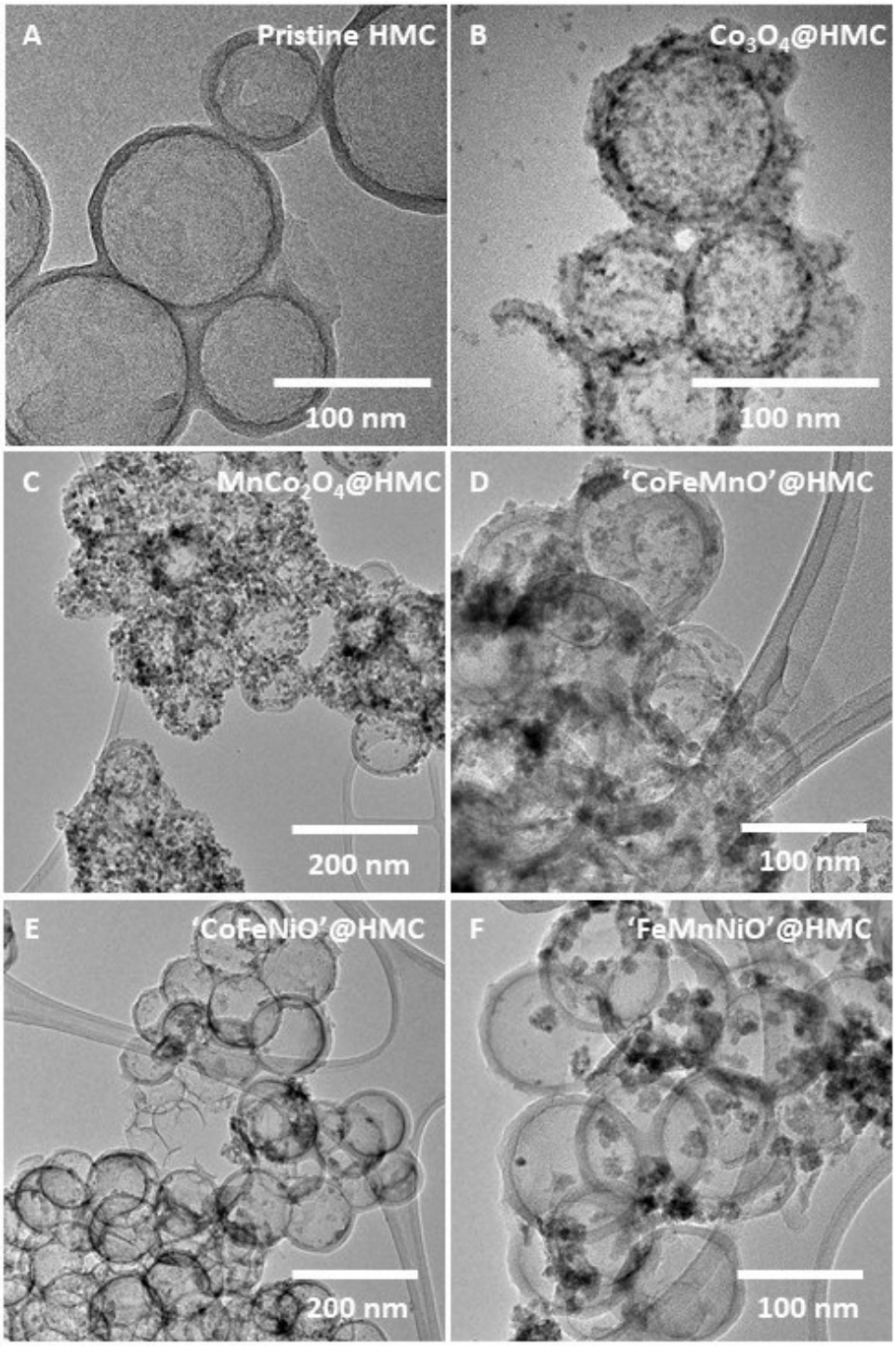

Figure 3-3. Bright field transmission electron microscopy images of (A) pristine HMC; (B) Co_3O_4@HMC; (C) $MnCo_2O_4$@HMC; (D) 'CoFeMnO'@HMC; (E) 'CoFeNiO'@HMC; and (F) 'FeMnNiO'@HMC.

High-resolution TEM (HRTEM) imaging and powder X-ray diffraction (PXRD) were used to probe the local and bulk crystallinity of the 'MO'NPs on the hybrids. For Co_3O_4@HMC, d-spacings of 2.8 and 2.4 Å, corresponding to (220) and (311) crystalline planes, were observed in the HRTEM image (Fig. 3-4). Consistent with these observations, the PXRD pattern of Co_3O_4@HMC matches that of Co_3O_4 (Fig. 3-5).[33] In the case of $MnCo_2O_4$@HMC, d-spacings of 4.9, 2.9, 2.4, and 2.2 Å were detected in the HRTEM image (Fig. 3-6), corresponding to (111), (220), (222), and (400) crystalline planes in $MnCo_2O_4$. Its PXRD pattern is also consistent with $MnCo_2O_4$ (Fig. 3-7).[34] For the ternary metal oxide nanoparticle decorated HMCs, lattices with various d-spacings were observed (Figs. 3-8 to 3-10). Although their PXRD patterns suggest some crystallinity, fingerprinting is not straightforward due to the large presence of amorphous components and the complex nature of the mixed metal oxide NPs (Fig. 3-11). Selected area electron diffraction (SAED -- not shown) is consistent with largely amorphous materials.

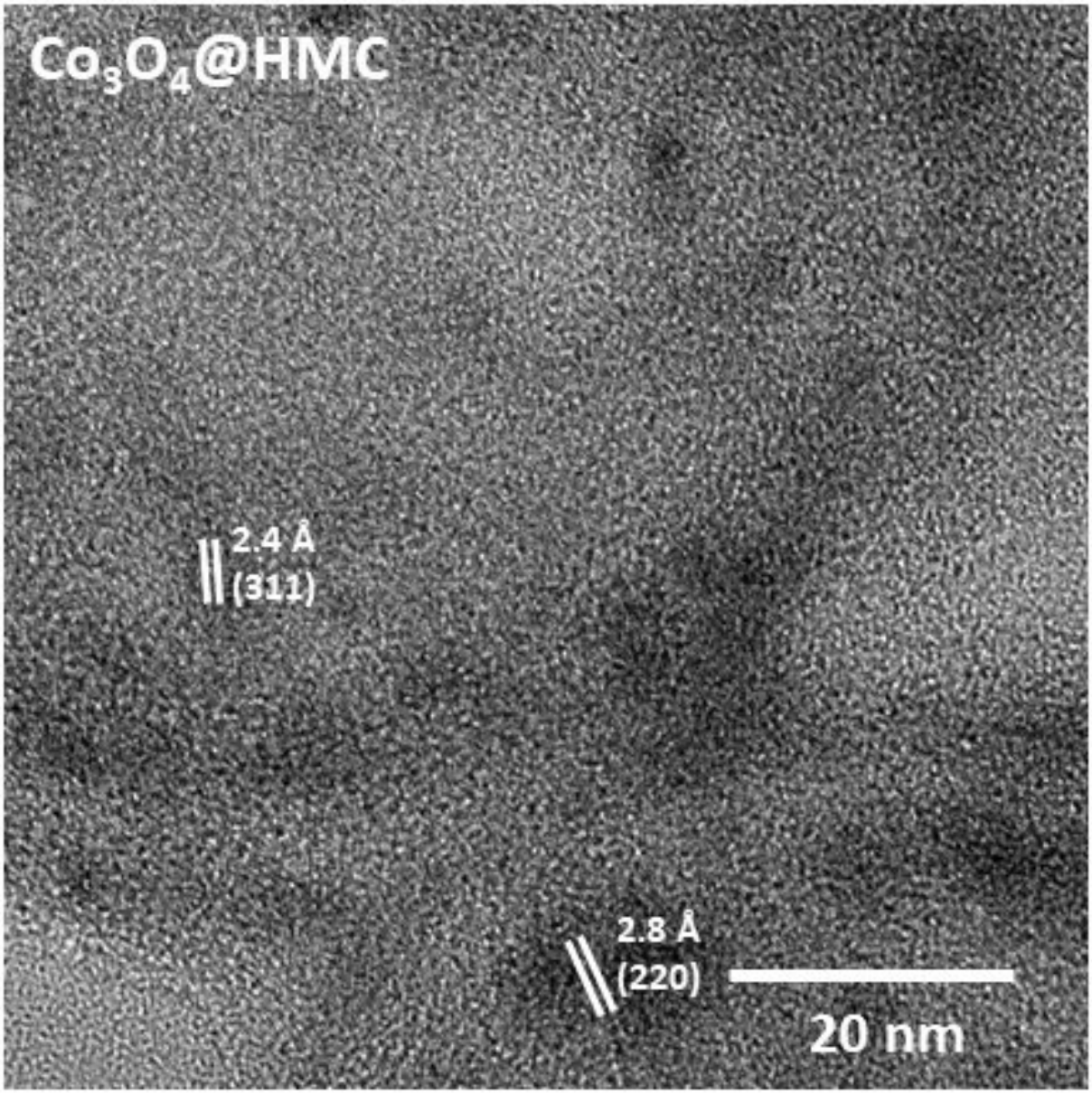

Figure 3-4. High resolution transmission electron microscopy (HRTEM) image of Co_3O_4@HMC. d-spacings of 2.4 and 2.8 Å were observed, corresponding to (311) and (220) crystalline planes in Co_3O_4.

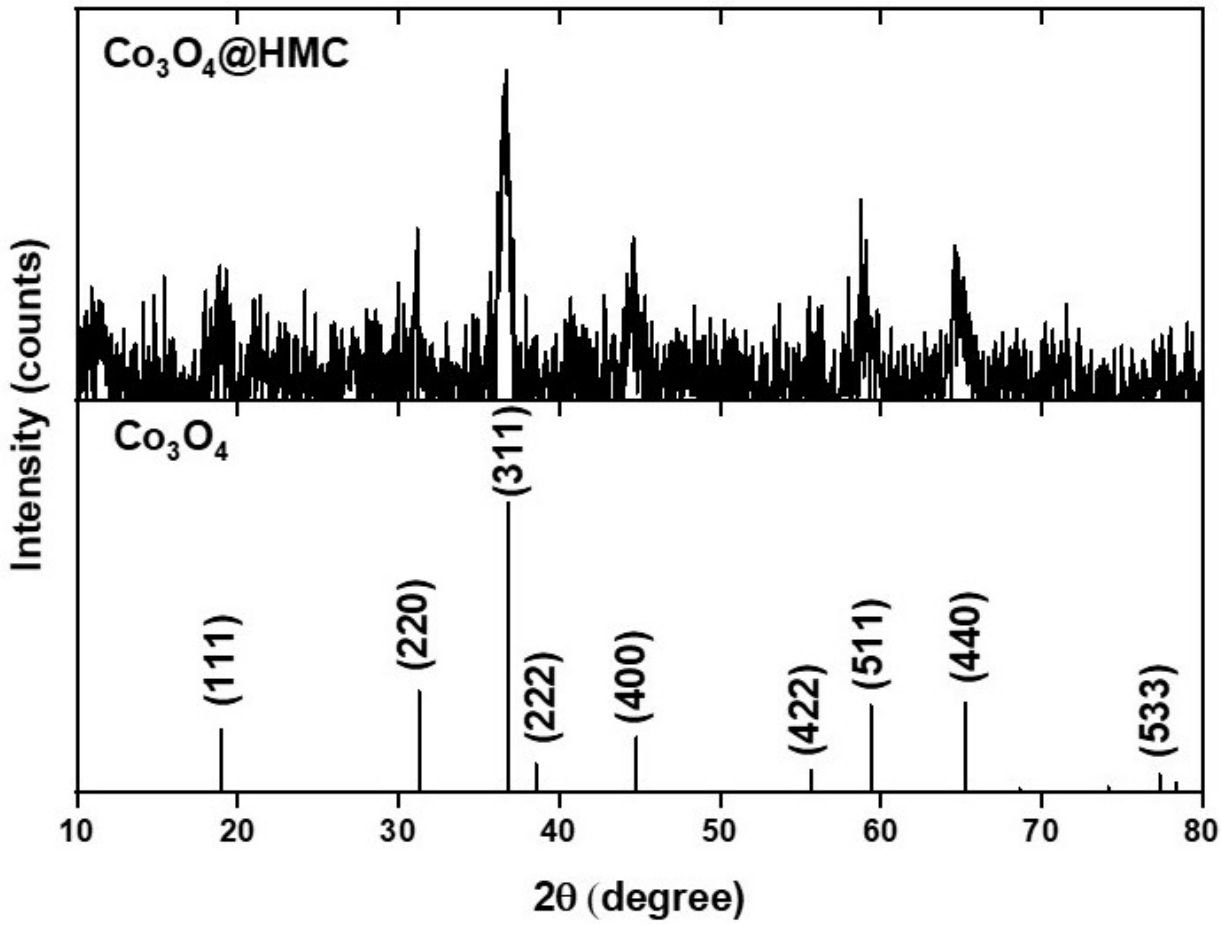

Figure 3-5. Powder X-ray diffraction (PXRD) pattern of Co_3O_4@HMC and standard cubic Co_3O_4 crystalline PXRD pattern (JCPDS card 42-1467).

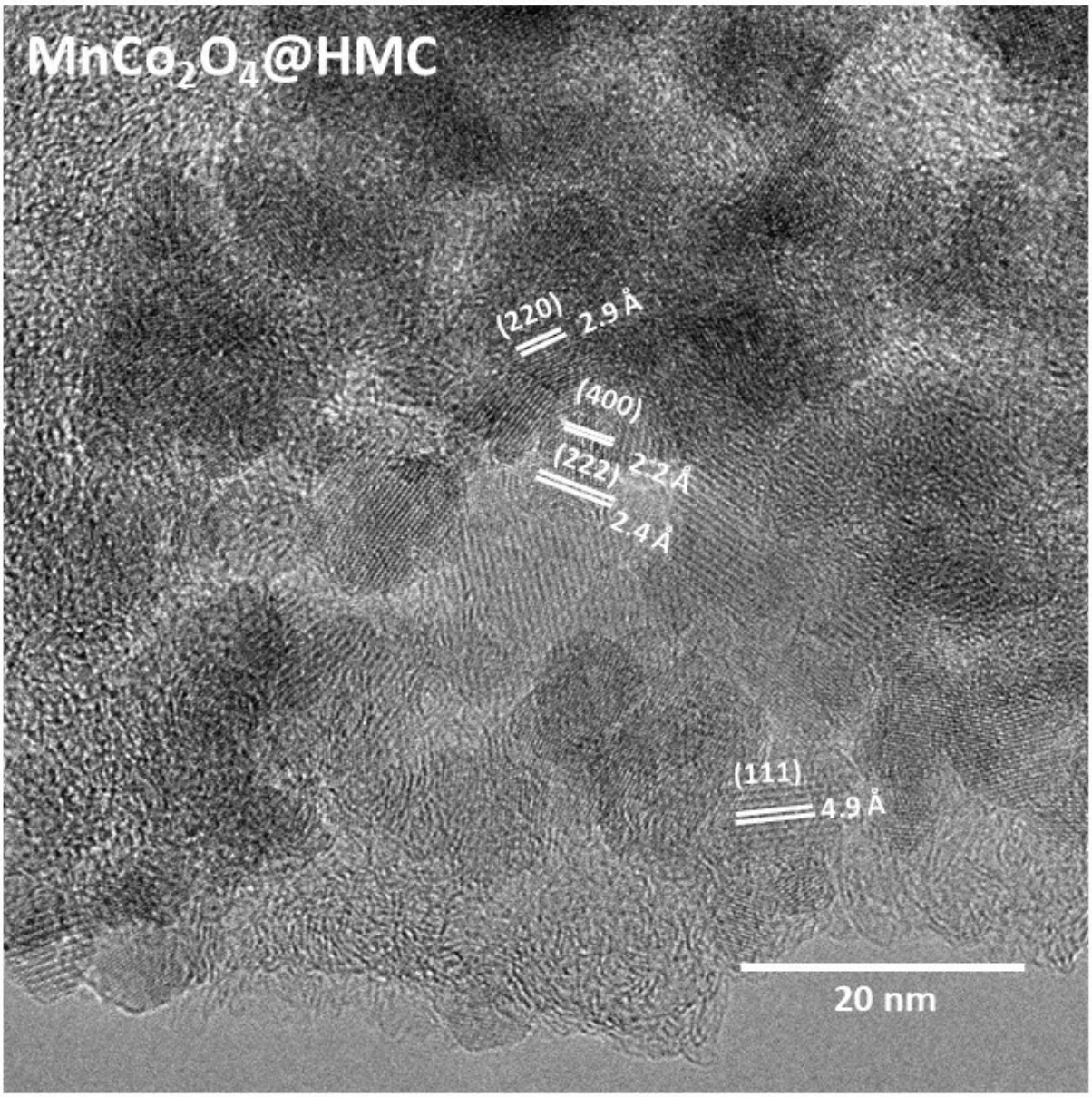

Figure 3-6. High resolution transmission electron microscopy (HRTEM) image of $MnCo_2O_4$@HMC. d-spacings of 2.2, 2.4, 2.9 and 4.9 Å were observed, corresponding to (400), (222), (220), and (111) crystalline planes in $MnCo_2O_4$.

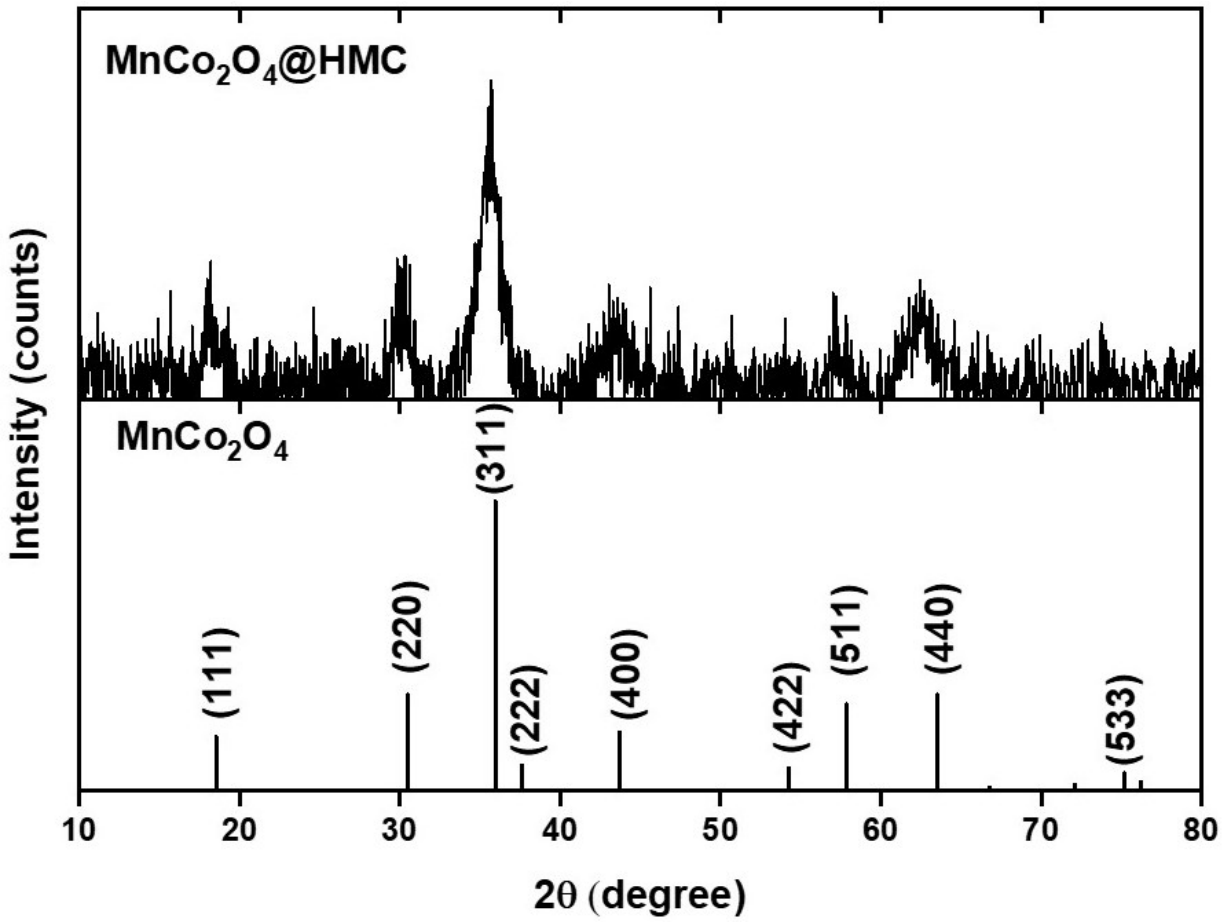

Figure 3-7. Powder X-ray diffraction (PXRD) pattern of $MnCo_2O_4$@HMC and standard cubic $MnCo_2O_4$ crystalline PXRD pattern (JCPDS card 23-1237).

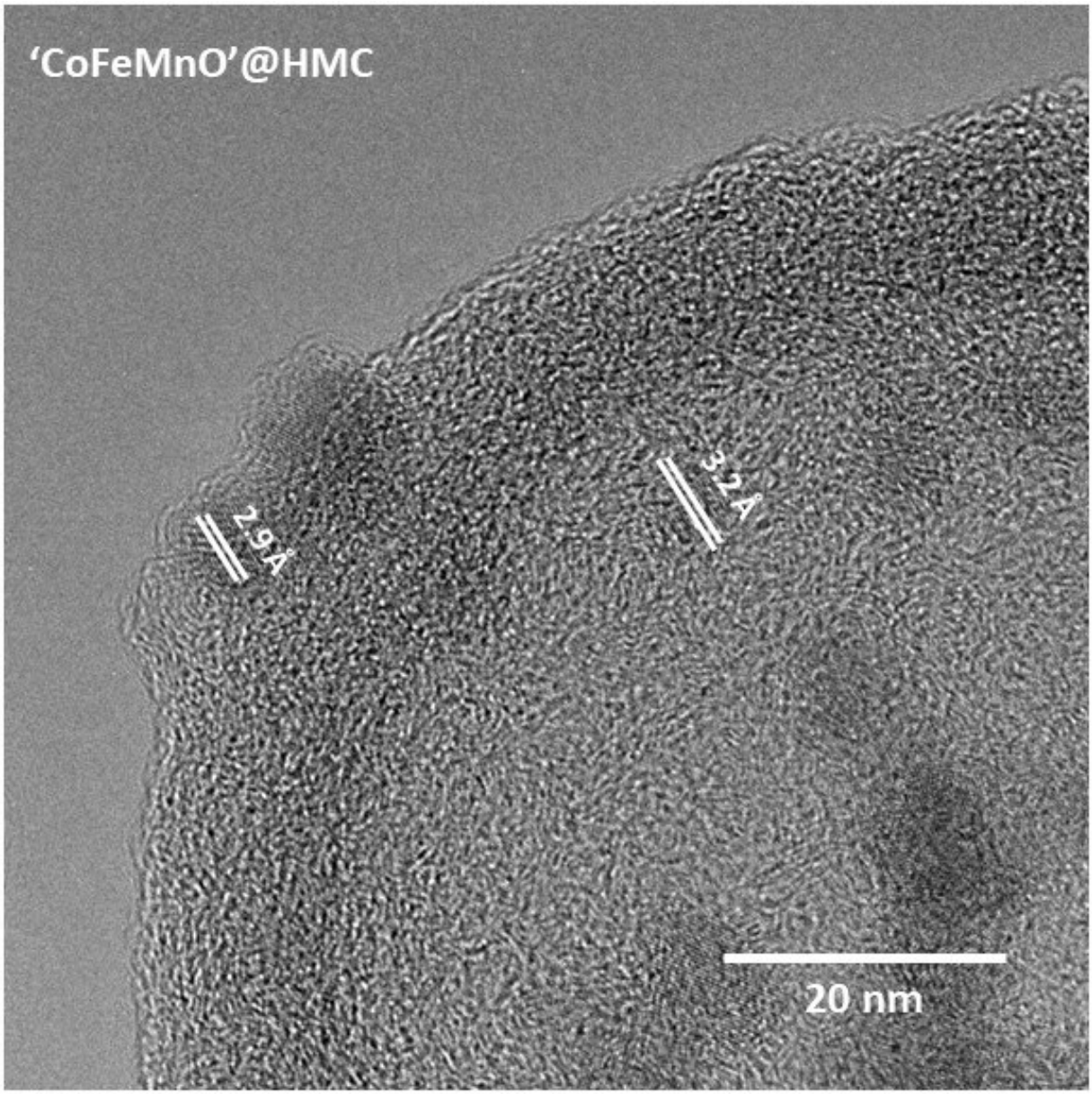

Figure 3-8. High resolution transmission electron microscopy (HRTEM) image of 'CoFeMnO'@HMC. d-spacings of 2.9 and 3.2 Å were observed.

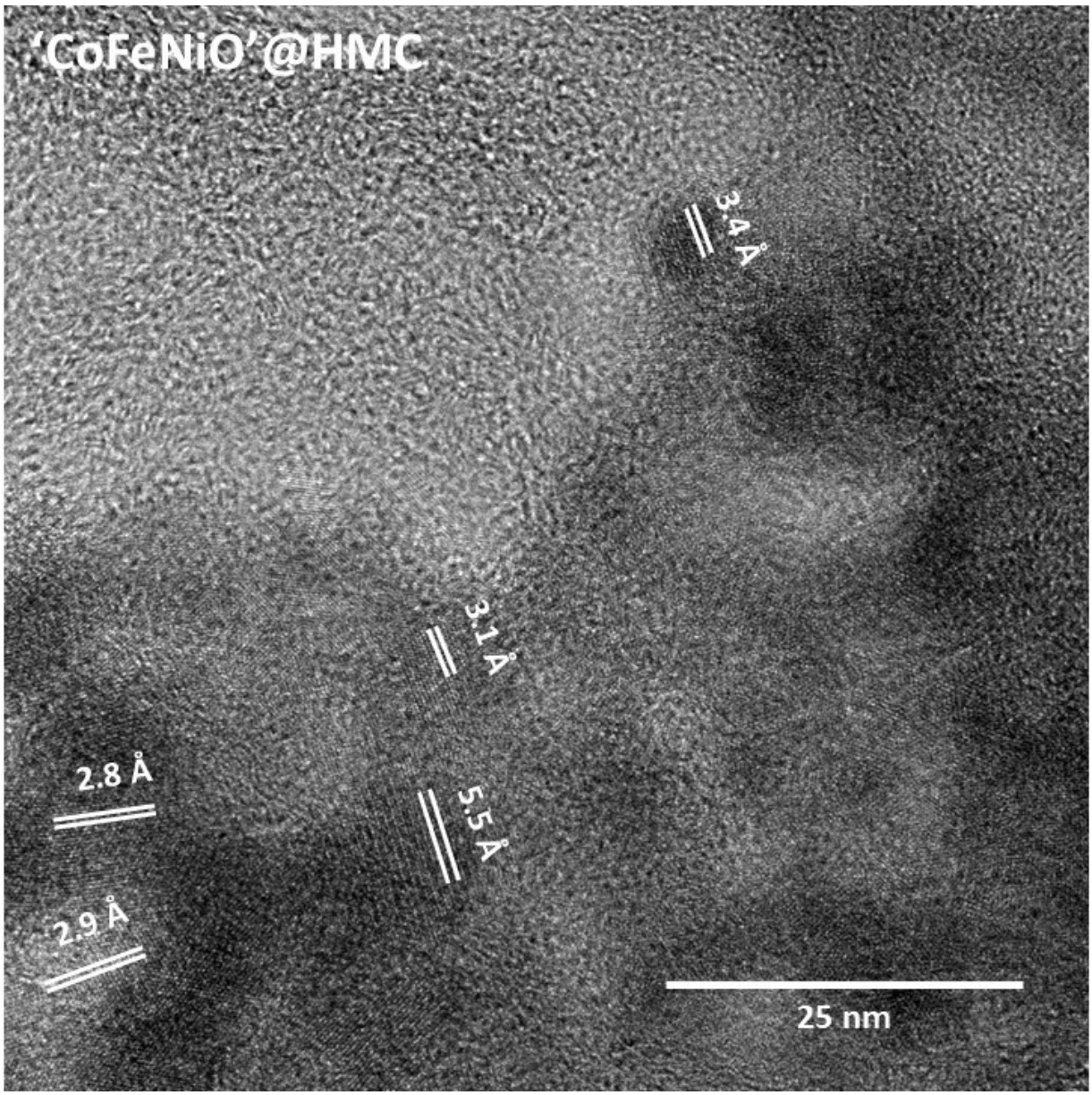

Figure 3-9. High resolution transmission electron microscopy (HRTEM image) of 'CoFeNiO'@HMC. d-spacings of 2.8, 2.9, 3.1, 3.4, and 5.5 Å were observed.

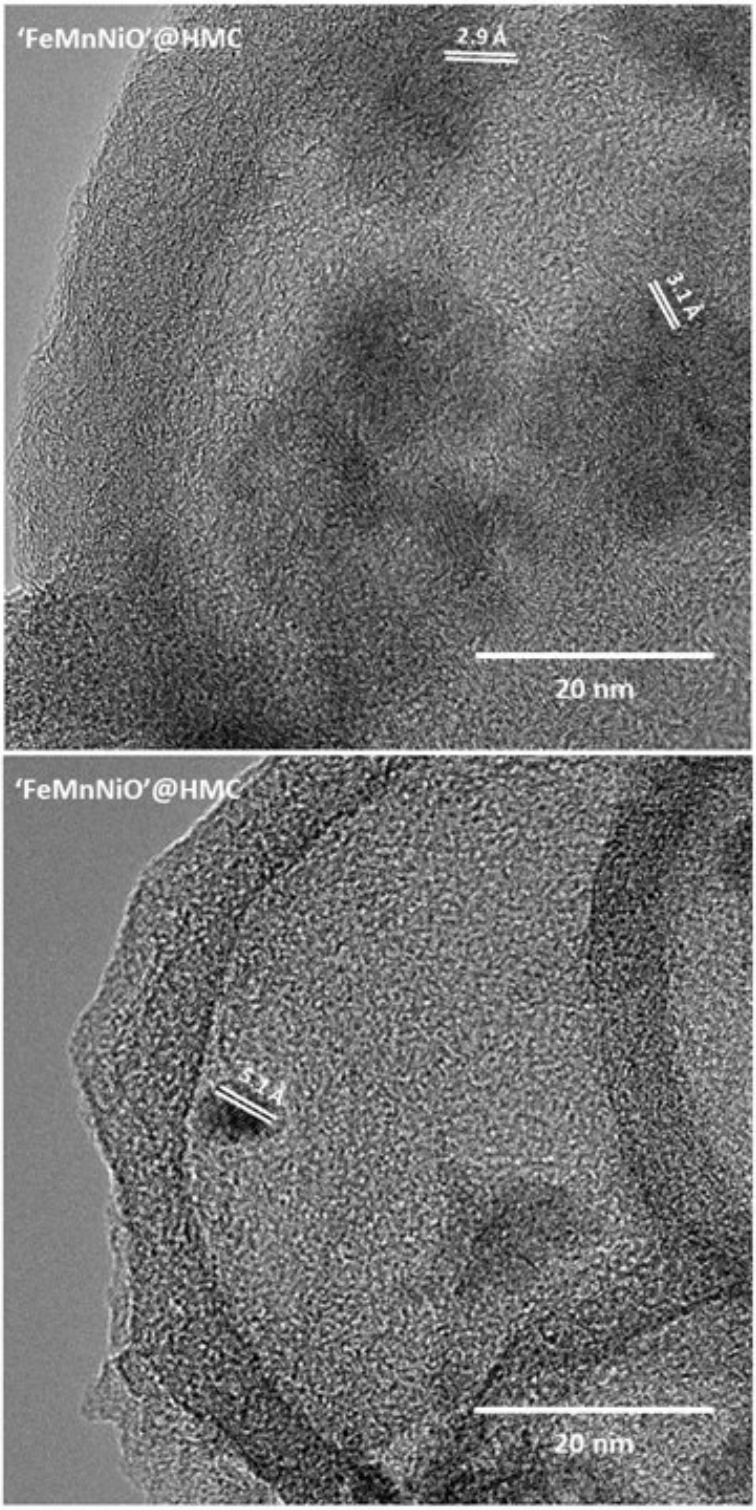

Figure 3-10. High resolution transmission electron microscopy (HRTEM images) of 'FeMnNiO'@HMC. d-spacings of 2.9, 3.1, and 5.1 Å were observed.

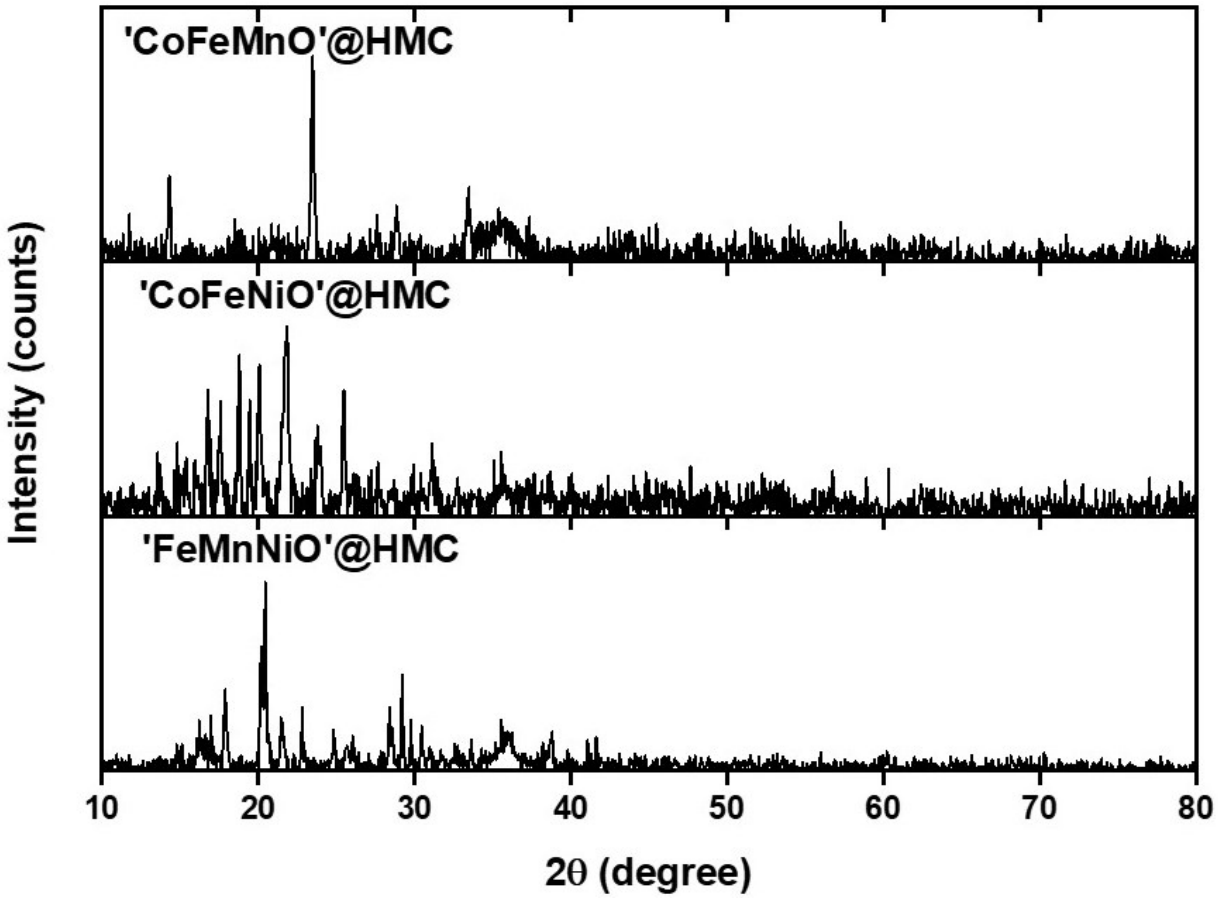

Figure 3-11. Powder X-ray diffraction (PXRD patterns) of 'CoFeMnO'@HMC, 'CoFeNiO'@HMC, and 'FeMnNiO'@HMC.

Energy dispersive X-ray (EDX) mapping gives insight into the nanoscale distribution of the constituent elements in the hybrids. Images of pristine HMCs reveal overlap of the bright field TEM and the C and N emissions consistent with successful and uniform N-doping (Fig. 3-12). As expected, all metal oxide decorated HMCs show co-localization with the C emission arising from the HMC component and the expected metal and oxygen emissions from the corresponding 'MO'NPs (Fig. 3-13 to 3-17).

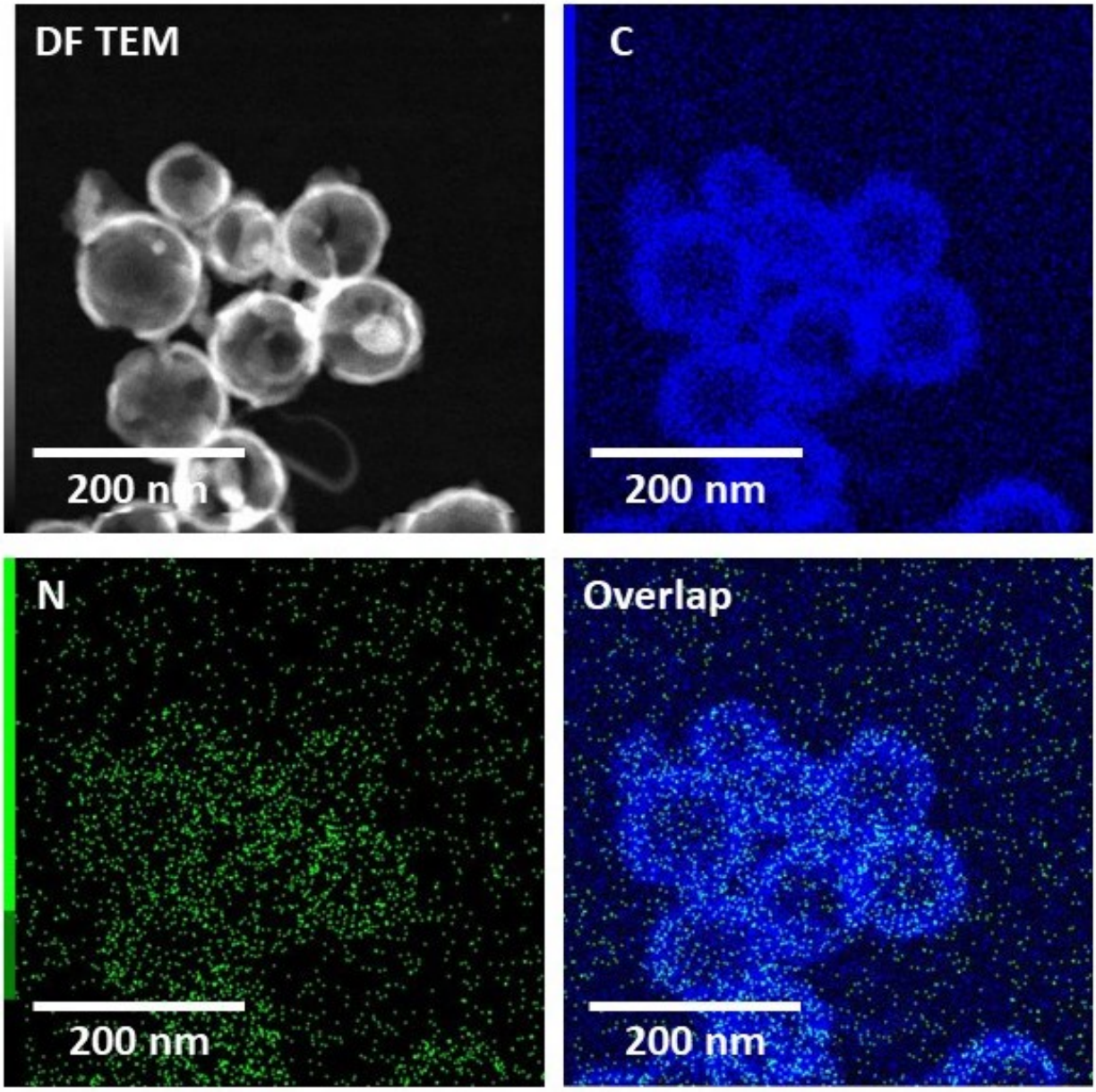

Figure 3-12. Energy dispersive X-ray (EDX) spectroscopy composition mapping of pristine HMC.

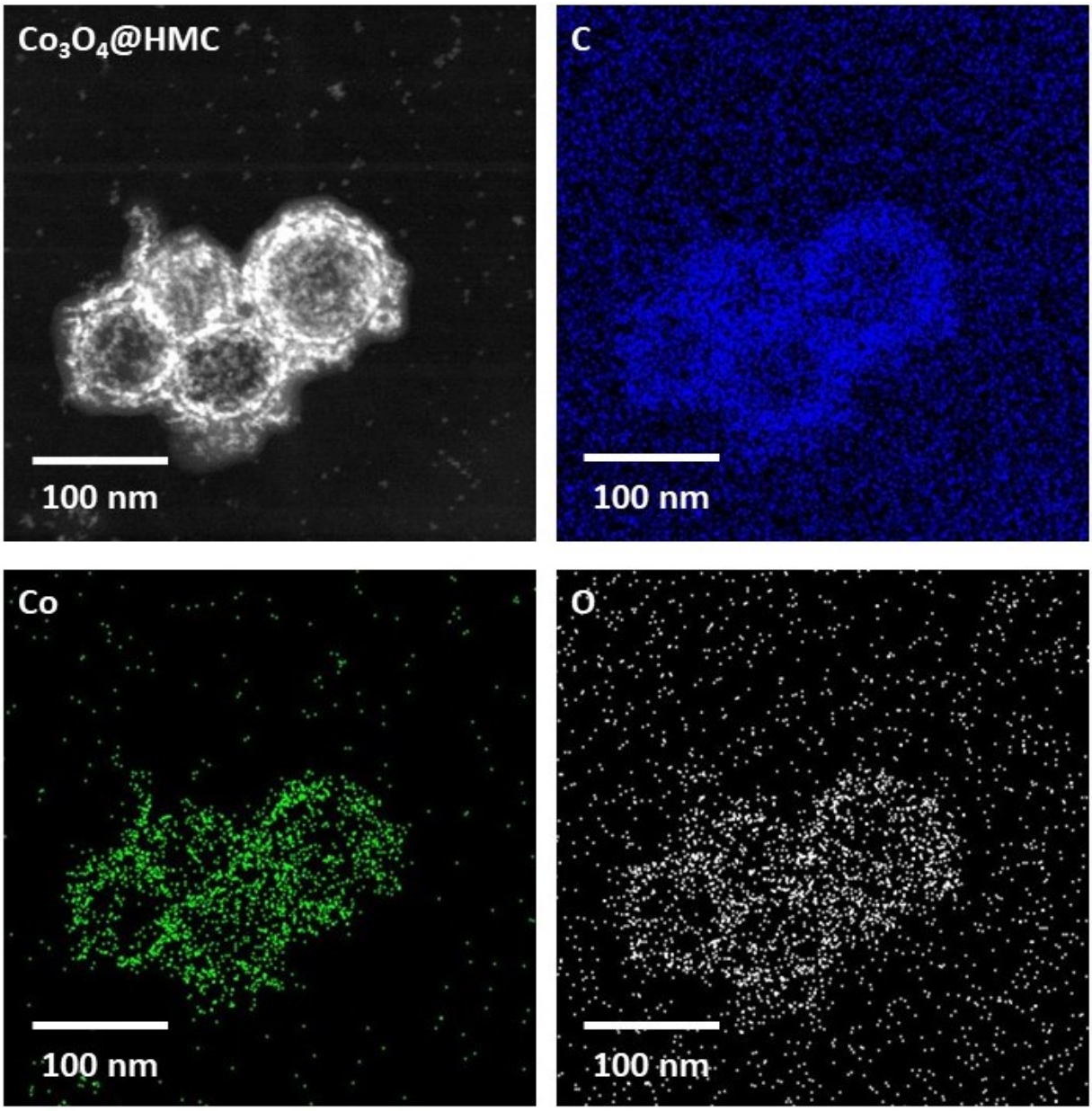

Figure 3-13. Annular dark-field STEM images and EDX mapping of Co_3O_4@HMC.

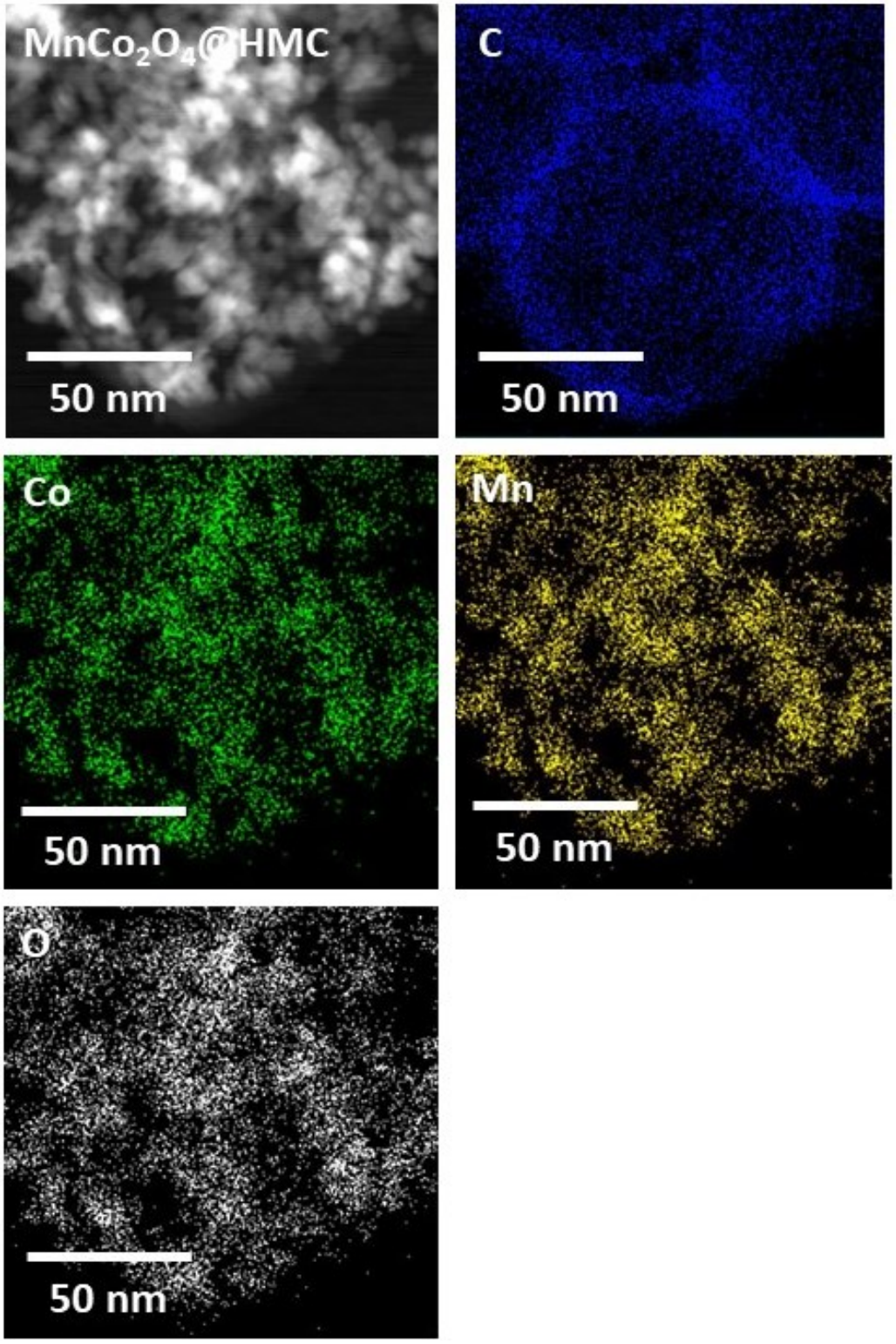

Figure 3-14. Annular dark-field STEM images and EDX mapping of $MnCo_2O_4$@HMC.

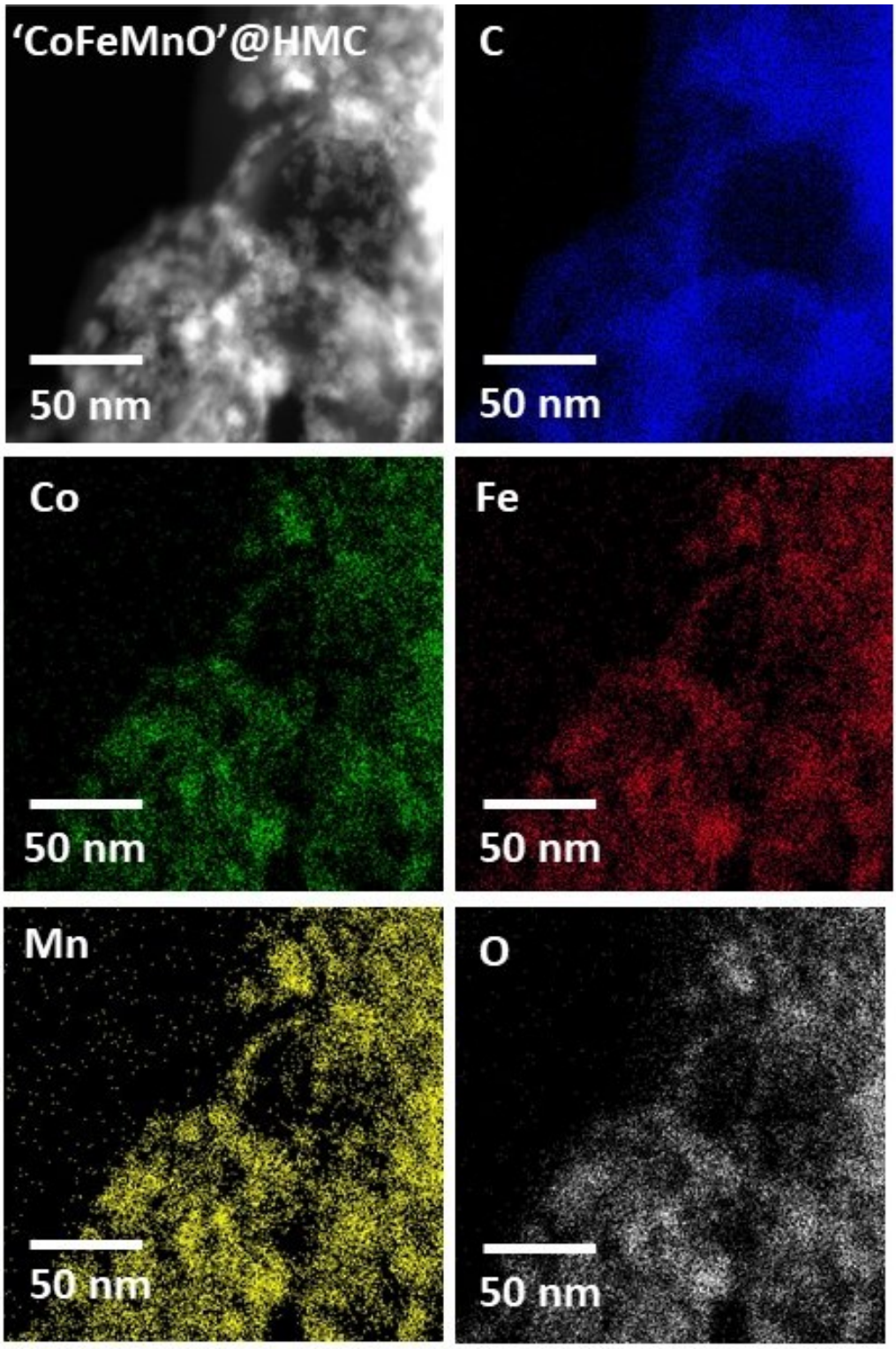

Figure 3-15. Annular dark-field STEM images and EDX mapping of 'CoFeMnO'@HMC.

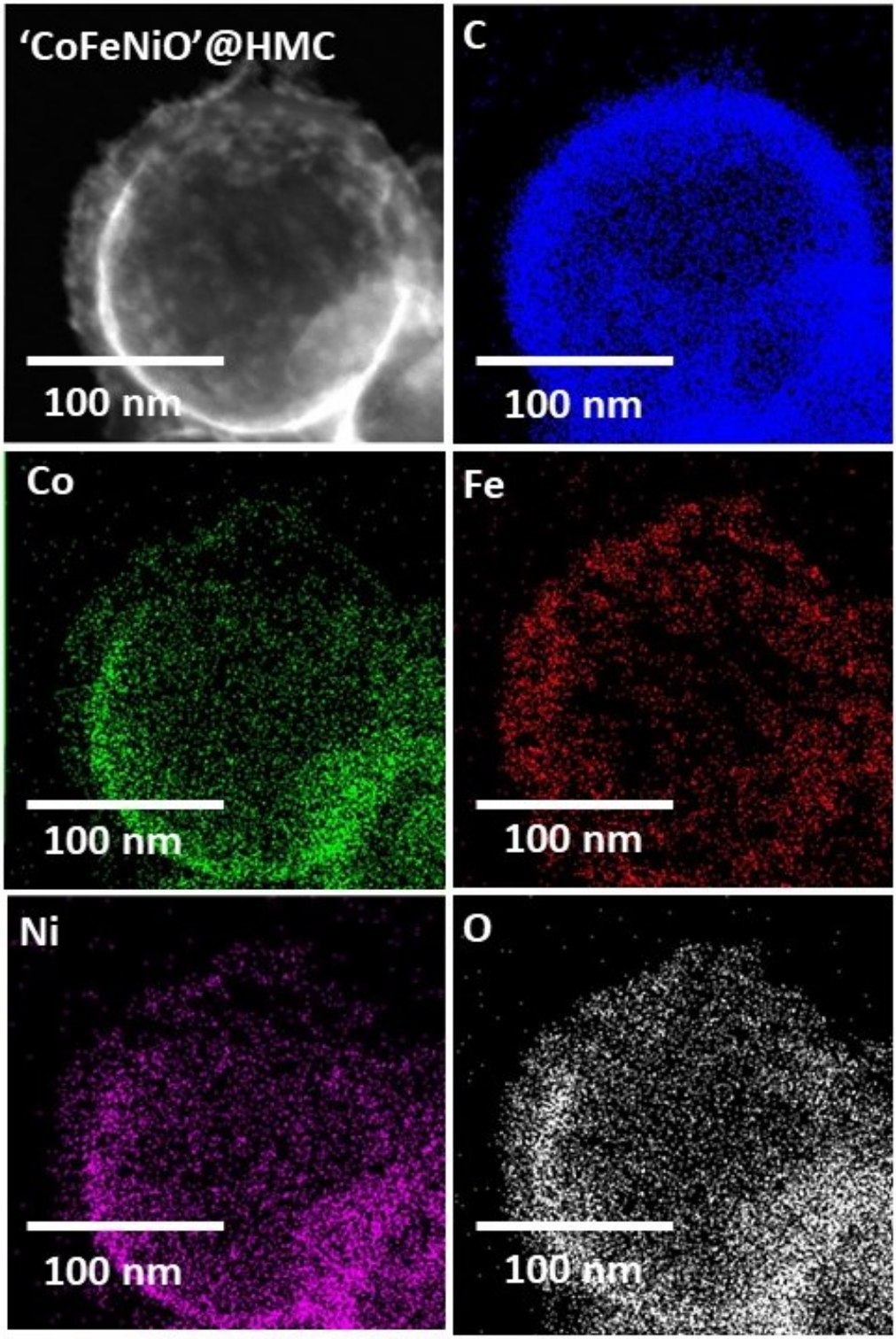

Figure 3-16. Annular dark-field STEM images and EDX mapping of 'CoFeNiO'@HMC.

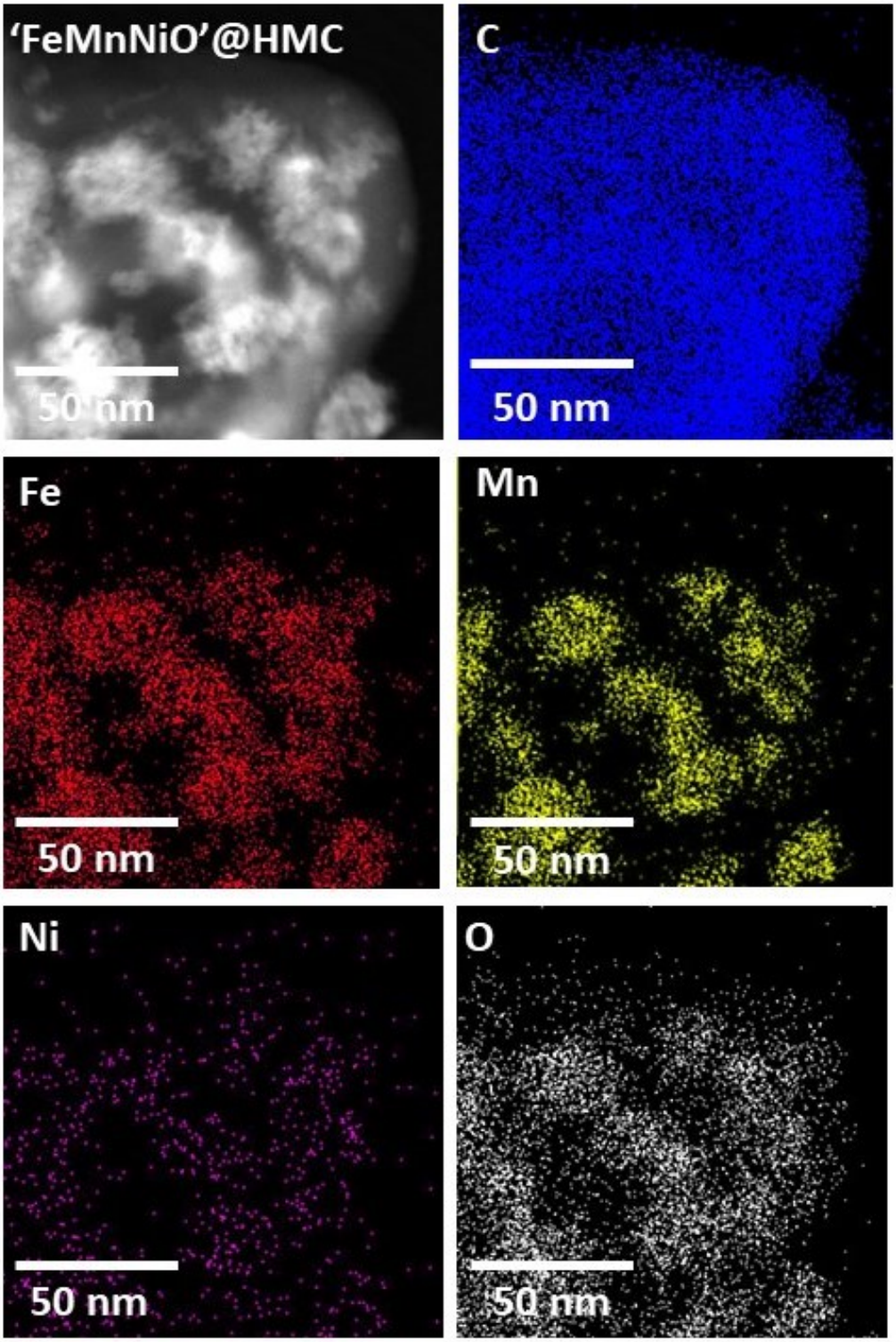

Figure 3-17. Annular dark-field STEM images and EDX mapping of 'FeMnNiO'@HMC.

X-ray photoelectron spectroscopy (XPS) compliments EDX mapping and provides compositional information as well as speciation (i.e., oxidation states) of the elements that are present. As expected, survey XP spectra of all decorated HMCs confirm C, N, O, and the expected metal elements are present at the sensitivity of the method (Fig. 3-18 to 3-22). Deconvolution of the metal 2p regions of the high-resolution XP spectra are shown in Figure 3-23 to 3-27 and the metal oxidation states as well as their corresponding percentages are summarized in Table 3-2. For Co_3O_4@HMC and $MnCo_2O_4$@HMC, Co is present as Co (II) and Co (III). In 'CoFeNiO'@HMC and 'CoFeMnO'@HMC; however, Co exclusively exists as Co (II). All Mn-containing hybrids contain a mixture of Mn (II), Mn (III), and Mn (IV) oxidation states. Mn 3s spectra were also acquired to assist in the identification of the oxidation state (Fig 3-28 to 3-30) and revealed a 3s splitting energy consistent with the results summarized in Table 3-2. Finally, Fe and Ni exist primarily as Fe (III) and Ni (II) in their corresponding hybrids, respectively.

Table 3-2. Metal oxidation states and their corresponding XPS-derived percentages within indicated hybrids.

	Co (II)	Co (III)	Fe (II)	Fe (III)	Mn (II)	Mn (III)	Mn (IV)	Ni (II)	Ni (III)
Co_3O_4 @HMC	43.7%	56.3%	-	-	-	-	-	-	-
$MnCo_2O_4$ @HMC	54.6%	45.4%	-	-	4.8%	75.9%	19.3%	-	-
'CoFeMnO' @HMC	100%	0%	25.6%	74.4%	69.9%	29.2%	0.9%	-	-
'CoFeNiO' @HMC	100%	0%	6.5%	93.5%	-	-	-	100%	0%
'FeMnNiO' @HMC	-	-	8.5%	91.5%	69.1%	13.5%	17.4%	92.7%	7.3%

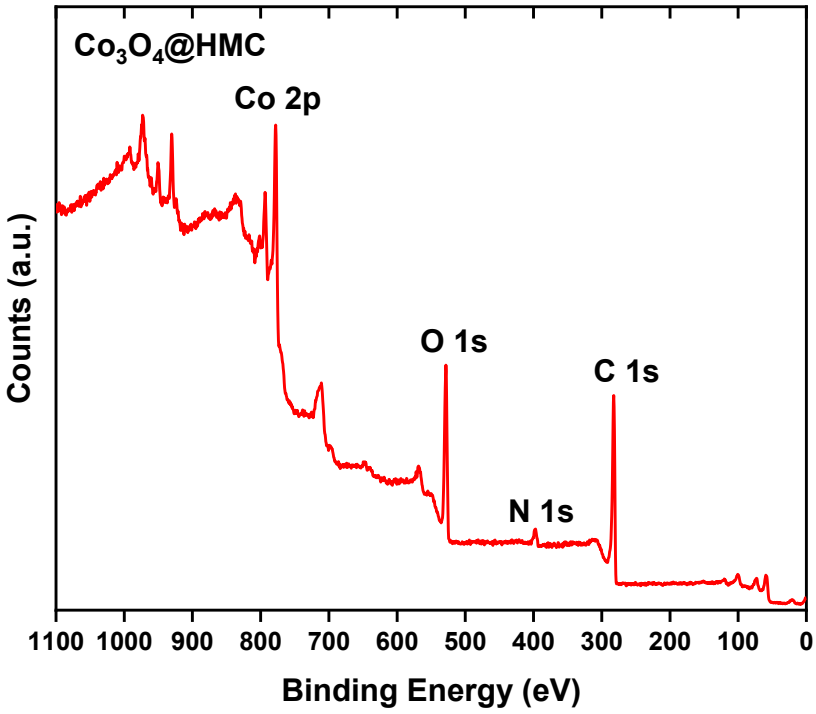

Figure 3-18. X-ray photoelectron (XP) survey spectrum of Co_3O_4@HMC.

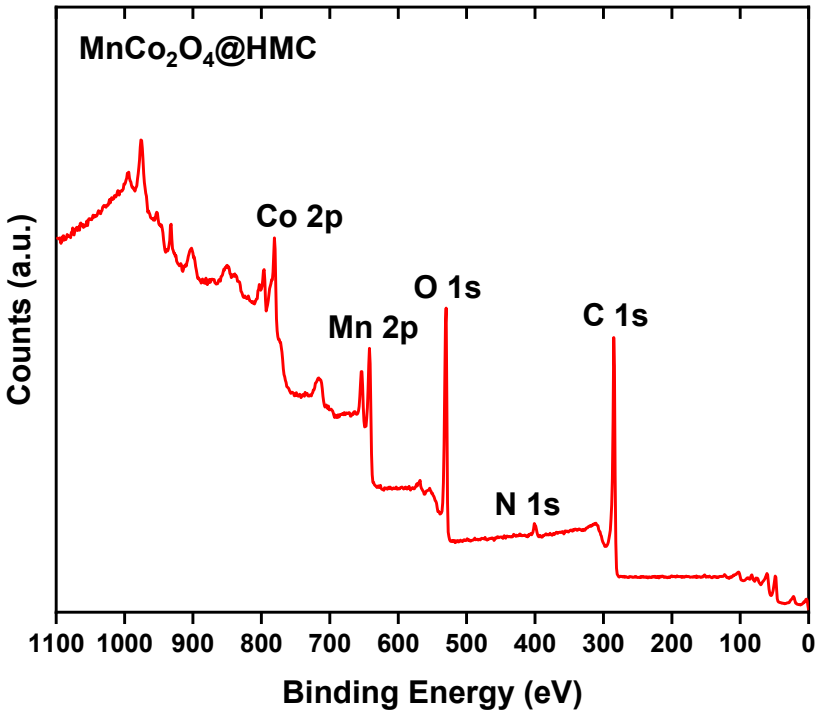

Figure 3-19. X-ray photoelectron (XP) survey spectrum of $MnCo_2O_4$@HMC.

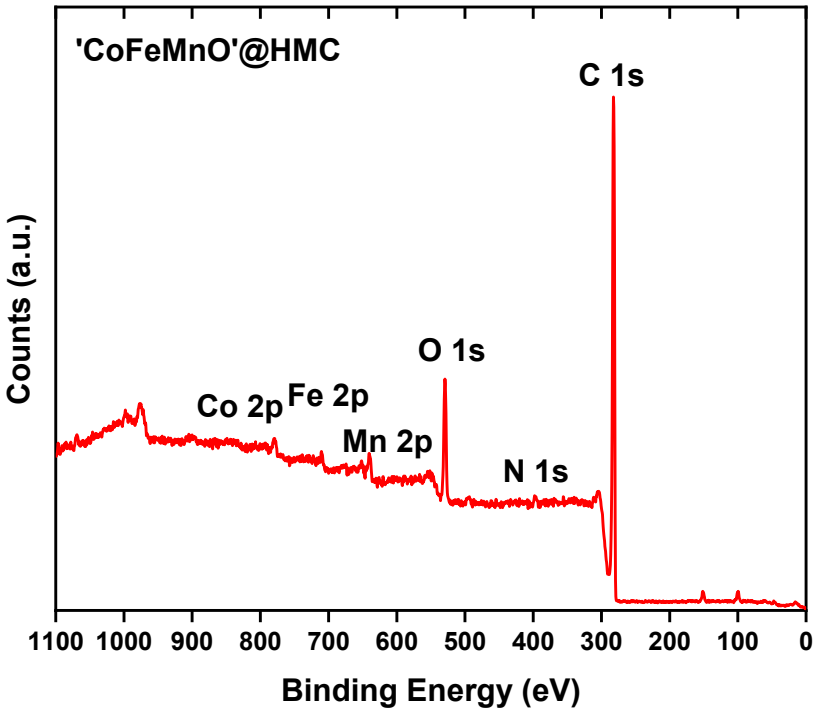

Figure 3-20. X-ray photoelectron (XP) survey spectrum of 'CoFeMnO'@HMC.

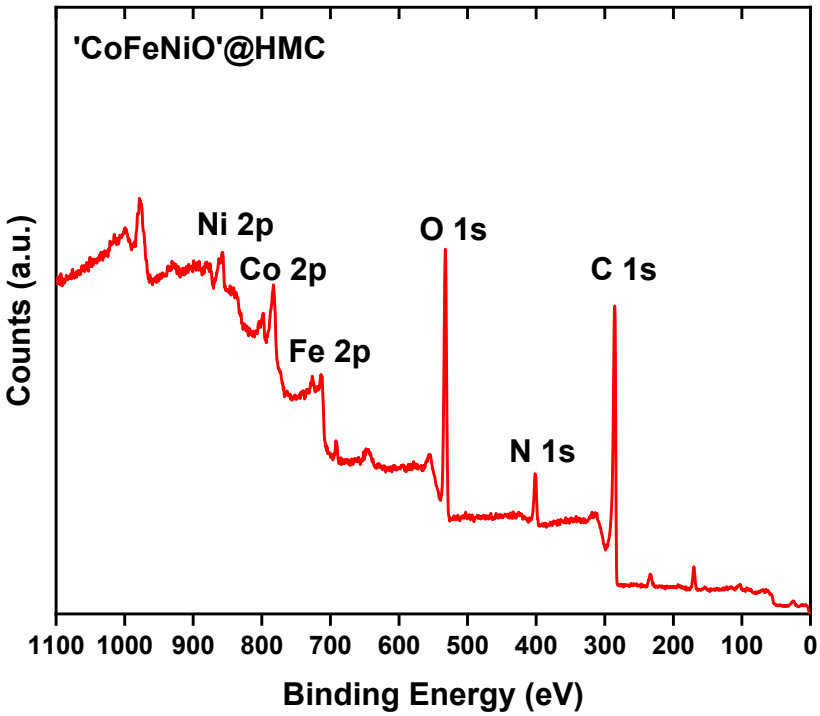

Figure 3-21. X-ray photoelectron (XP) survey spectrum of 'CoFeNiO'@HMC.

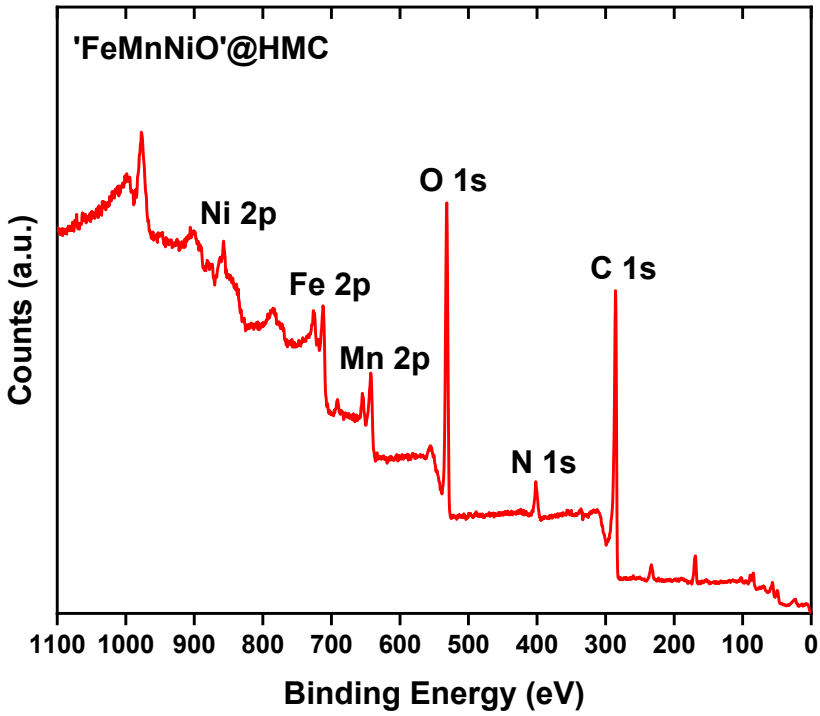

Figure 3-22. X-ray photoelectron (XP) survey spectrum of 'FeMnNiO'@HMC.

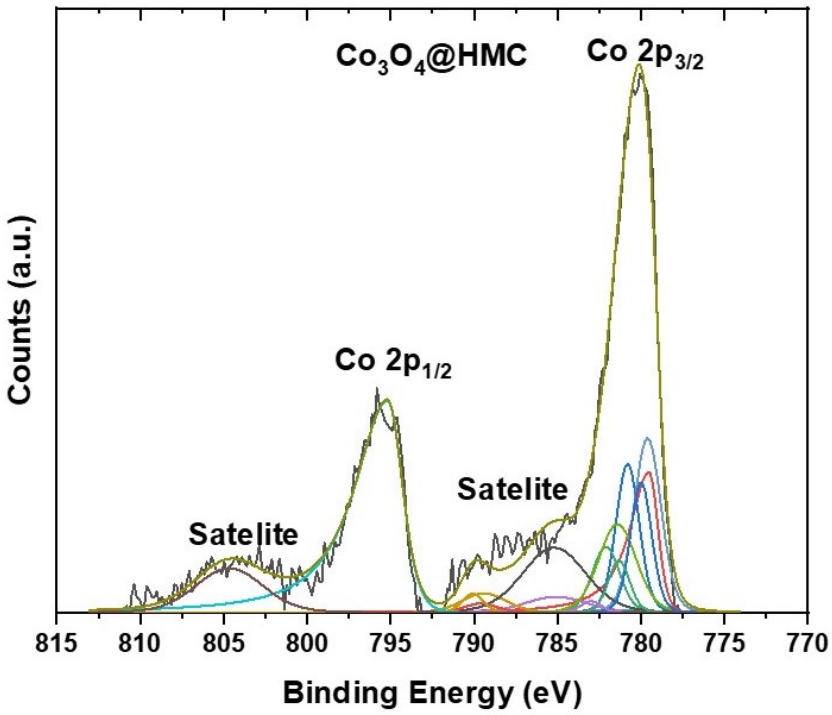

Figure 3-23. Deconvoluted Co 2p XP spectrum of Co_3O_4@HMC.

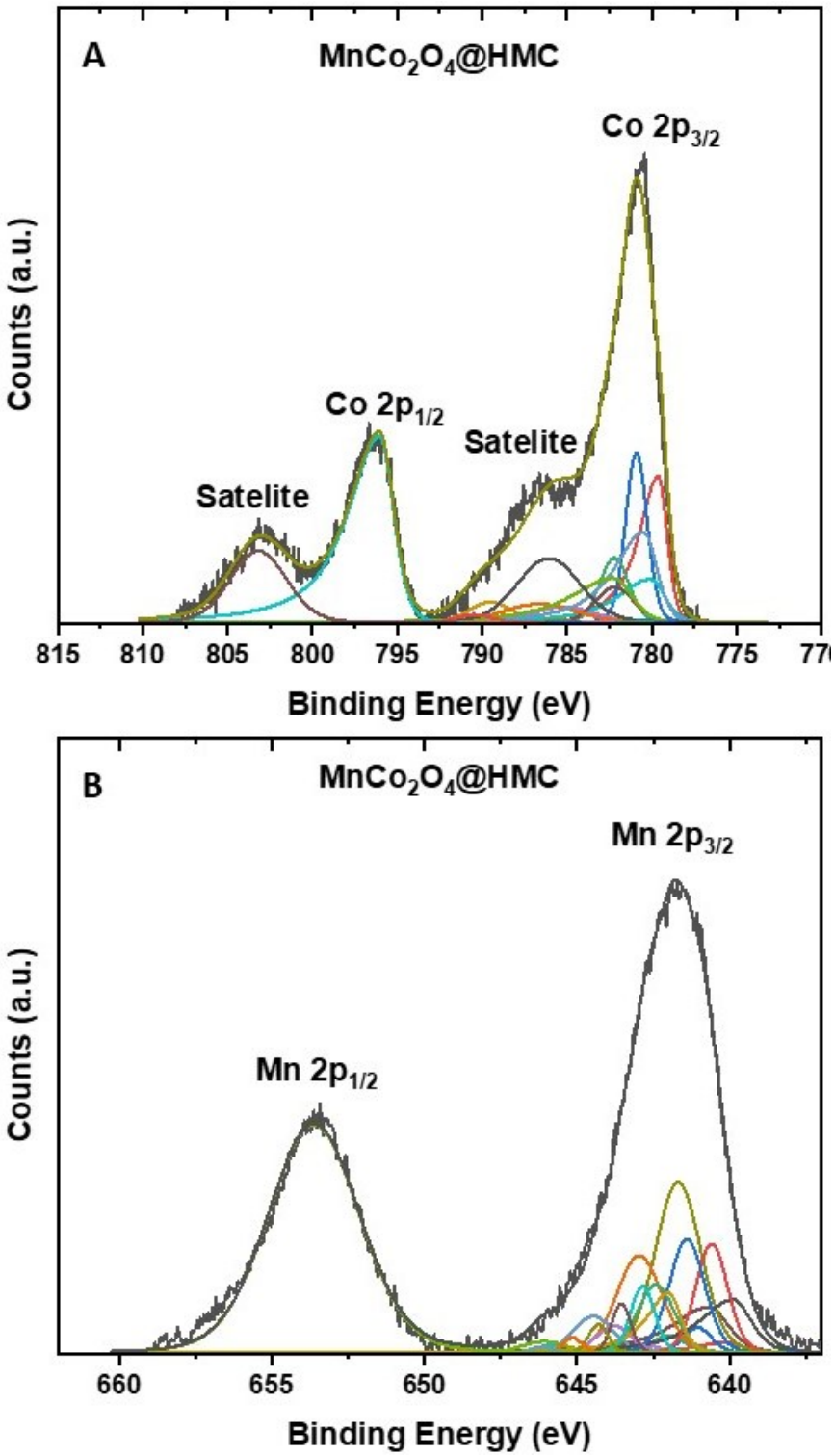

Figure 3-24. Deconvoluted (A) Co 2p and (B) Mn 2p XP spectra of $MnCo_2O_4$@HMC.

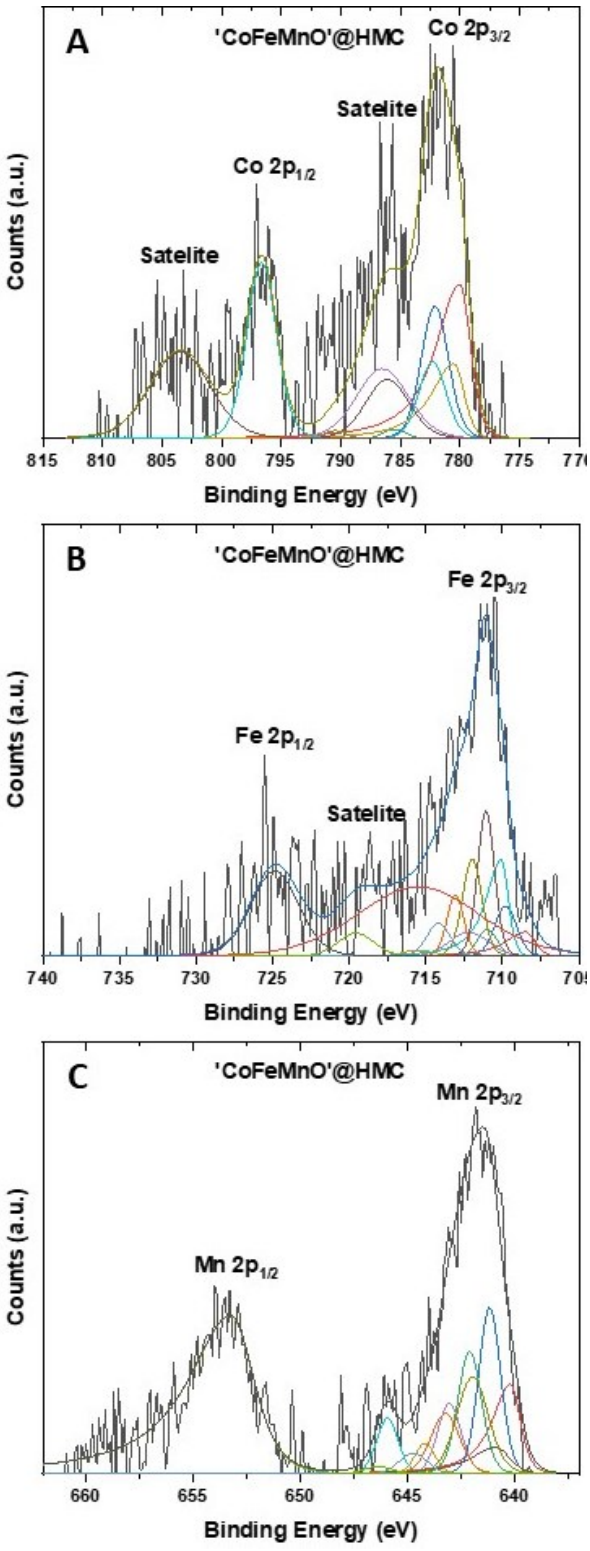

Figure 3-25. Deconvoluted (A) Co 2p; (B) Fe 2p; and (C) Mn 2p XP spectra of 'CoFeMnO'@HMC.

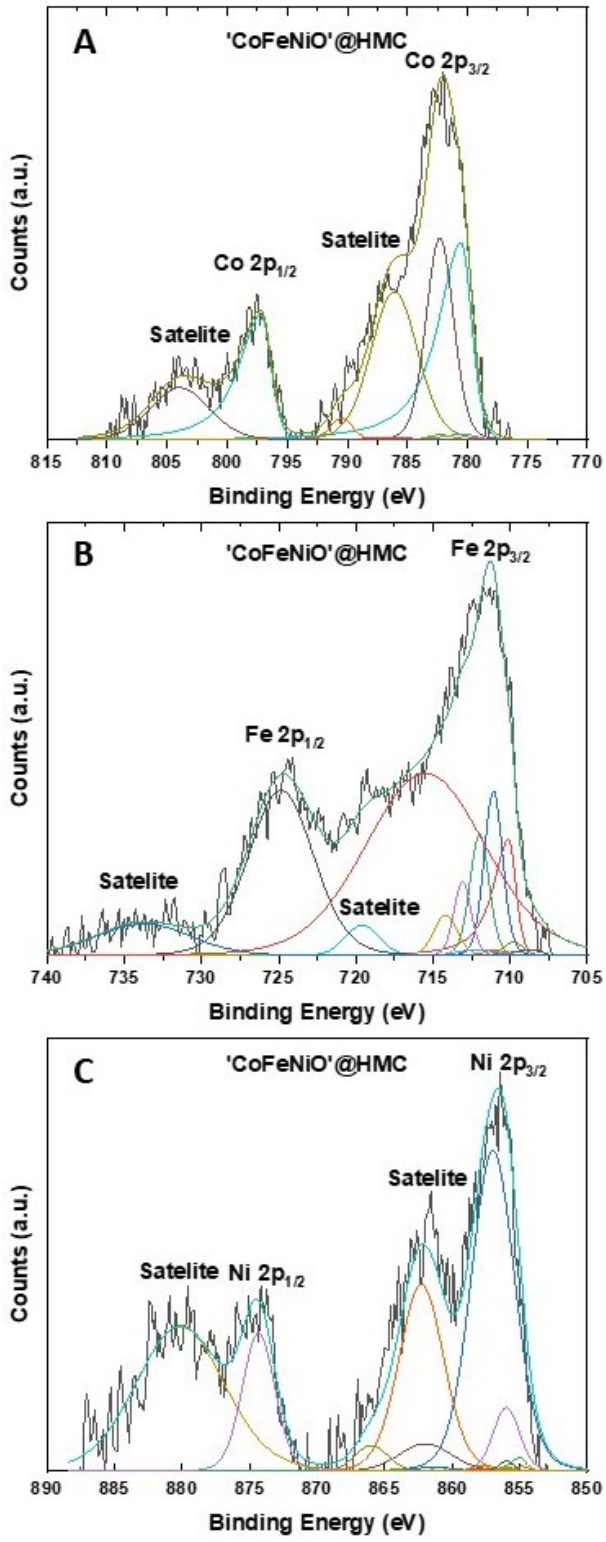

Figure 3-26. Deconvoluted (A) Co 2p; (B) Fe 2p; and (C) Ni 2p XP spectra of 'CoFeNiO'@HMC.

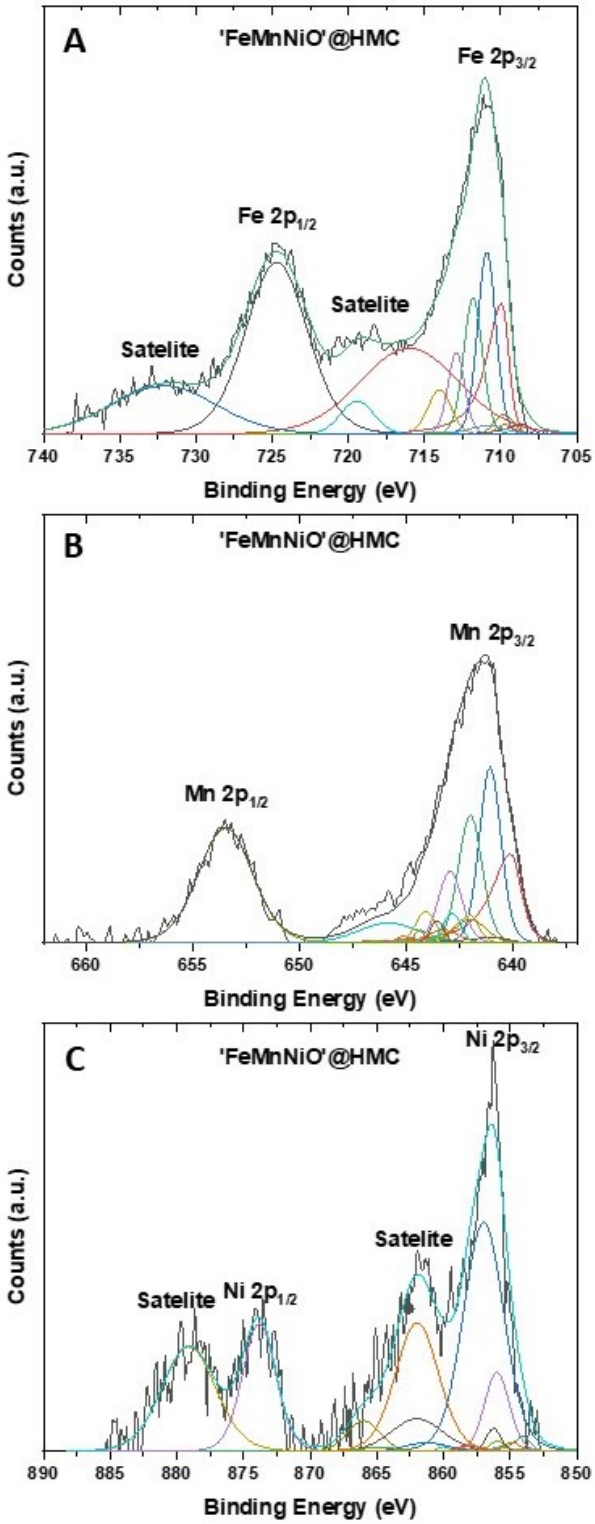

Figure 3-27. Deconvoluted (A) Fe 2p; (B) Mn 2p; and (C) Ni 2p XP spectra of 'FeMnNiO@HMC.

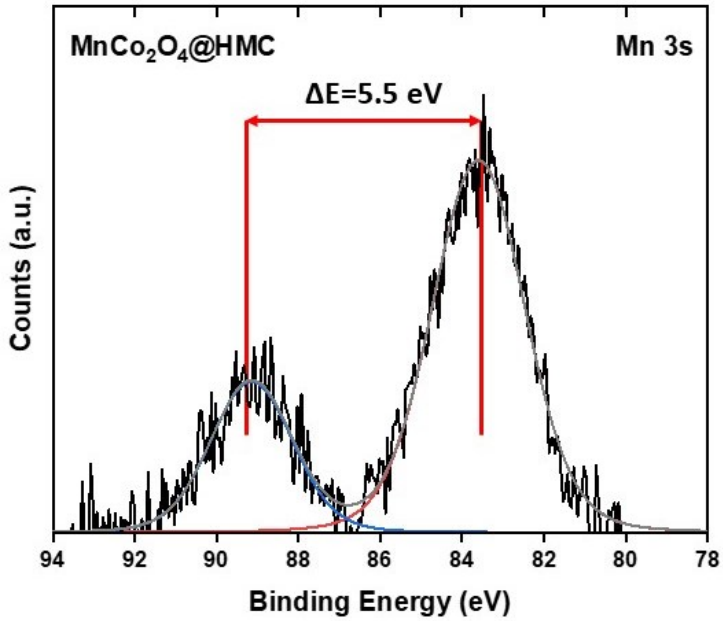

Figure 3-28. Deconvoluted Mn 3s X-ray photoelectron (XP) spectrum of $MnCo_2O_4$@HMC.

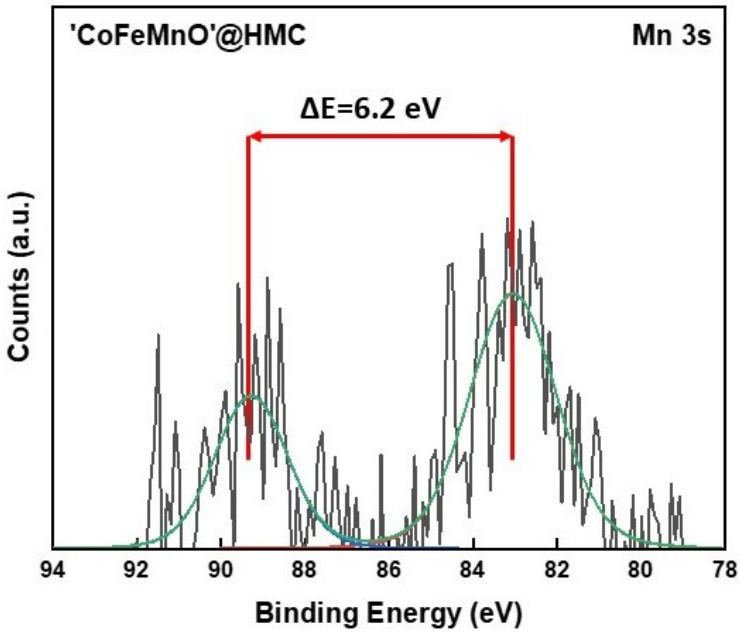

Figure 3-29. Deconvoluted Mn 3s X-ray photoelectron (XP) spectrum of 'CoFeMnO'@HMC.

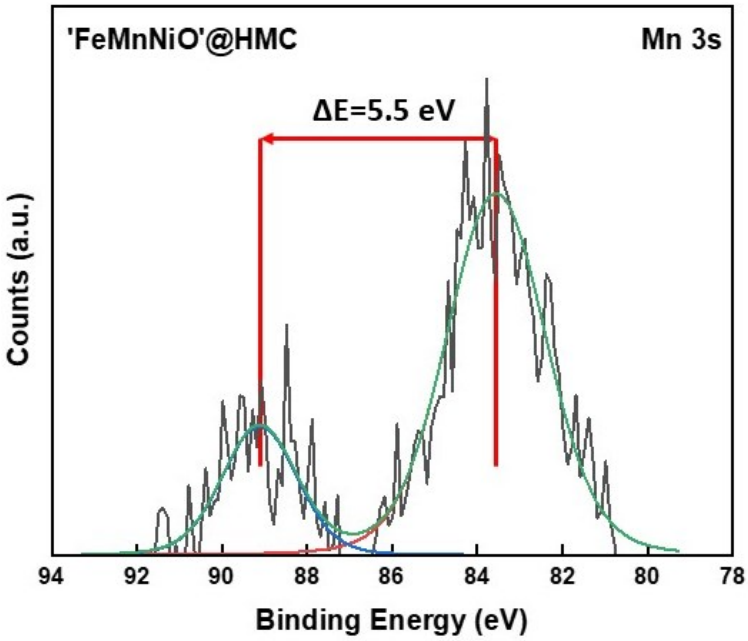

Figure 3-30. Deconvoluted Mn 3s X-ray photoelectron (XP) spectrum of 'FeMnNiO@HMC.

The ORR and OER electrocatalytic activities of as-synthesized metal oxide decorated HMCs were first evaluated using linear sweep voltammetry (LSV; Fig. 3-31 and 3-32) and these metrics were compared to the corresponding performance of pristine HMC as well as a Pt-Ru benchmark. Catalyst loaded GDLs were prepared using a impregnation method and used as working electrodes.[35] Hg/HgO and a Pt wire were used as reference and counter electrodes, respectively. Onset potentials, defined as the potential at which the absolute value of current density surpasses 10 mA cm^{-2}, measured for the present hybrids are summarized in Table 3-3.[36, 37] ORR onset potentials for Co_3O_4@HMC and $MnCo_2O_4$@HMC catalysts were -0.076 V and -0.060 V, respectively (Fig. 3-31A). In both cases, these ORR onset potentials

correspond to a performance improvement over pristine HMC (i.e., -0.156 V) and comparable performance to that of the Pt-Ru benchmark (i.e., -0.077 V). Relative to the standard half-cell potential of ORR (0.303 V vs. Hg/HgO), the overpotentials for Pt-Ru, pristine HMC, Co_3O_4@HMC and $MnCo_2O_4$@HMC are -0.380, -0.459, -0.379, and -0.363 V, respectively. This observation was expected and arises as a result of the incorporation of Co (III) and Mn (III) into the hybrid catalysts - these ions facilitate ORR.[38, 39] The picture for OER activity is very different, only the Co_3O_4@HMC showed improvement over pristine HMC (i.e., 0.635 V vs. 0.667 V; Fig. 3-31B), closing the gap with Pt-Ru. However, the OER activity of $MnCo_2O_4$@HMC worsened compared to that of pristine HMC (i.e., 0.701 V vs. 0.667 V). While the origin of this behavior is being investigated, the lack of Mn (IV) in the hybrid may play a role.[40]

Table 3-3. ORR and OER onset potentials for 'MO'@HMC.

Material	**ORR onset potential vs. Hg/HgO (V)**	**OER onset potential vs. Hg/HgO (V)**
HMC	-0.156	0.667
Co_3O_4@HMC	-0.076	0.635
$MnCo_2O_4$ @HMC	-0.060	0.701
'CoFeMnO'@HMC	-0.100	0.609
'CoFeNiO'@HMC	-0.136	0.587
'FeMnNiO'@HMC	-0.144	0.443
Pt-Ru	-0.077	0.576

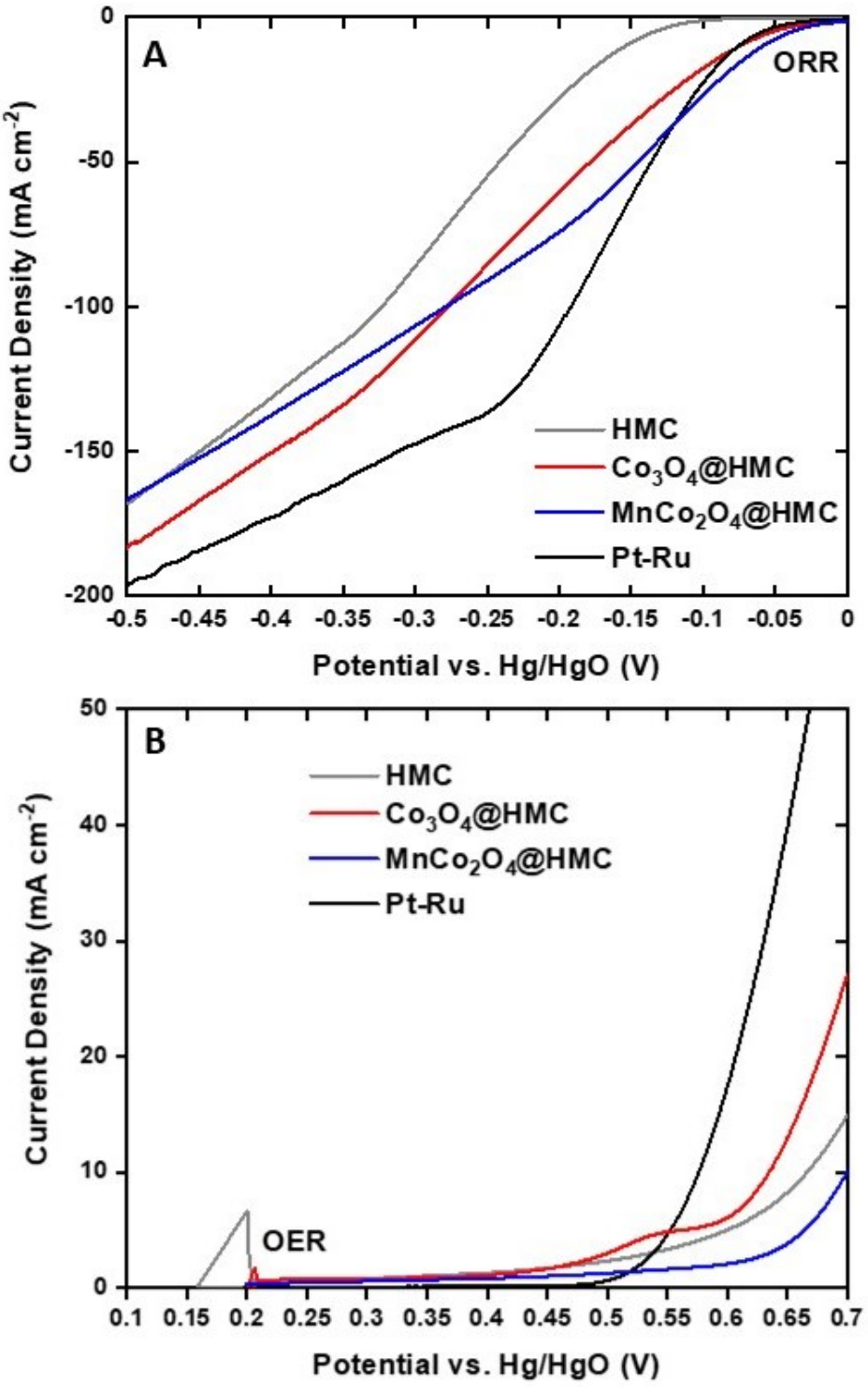

Figure 3-31. Linear sweep voltammograms of (A) Co_3O_4@HMC and $MnCo_2O_4$@HMC in ORR; and (B) Co_3O_4@HMC and $MnCo_2O_4$@HMC in OER.

Turning attention to the HMCs decorated with ternary metal oxide nanoparticles, the ORR onset potentials improved slightly from that of pristine HMCs (-0.156 V) to -0.100, -0.136 and -0.144 V for 'CoFeMnO'@HMC, 'CoFeNiO'@HMC, and 'FeMnNiO'@HMC, respectively (Fig. 3-32A). We also note that the OER onset potentials improved from that of pristine HMC (0.667 V) to 0.609, 0.587, and 0.443 V for 'CoFeMnO'@HMC, 'CoFeNiO'@HMC, and 'FeMnNiO'@HMC, respectively (Fig. 3-32B). Remarkably, the OER activities of 'CoFeNiO'@HMC and 'FeMnNiO'@HMC are comparable to the Pt-Ru benchmark catalyst (i.e., 0.576 V) when considering onset potentials. These enhanced OER activities can be attributed to the presence of Fe (III) and Ni (II) species.[41, 42] It is important to note that a wave arising from Ni oxidation was observed at 0.47-0.49 V for both Ni-containing hybrids. This is not expected to hinder the OER catalytic activity.

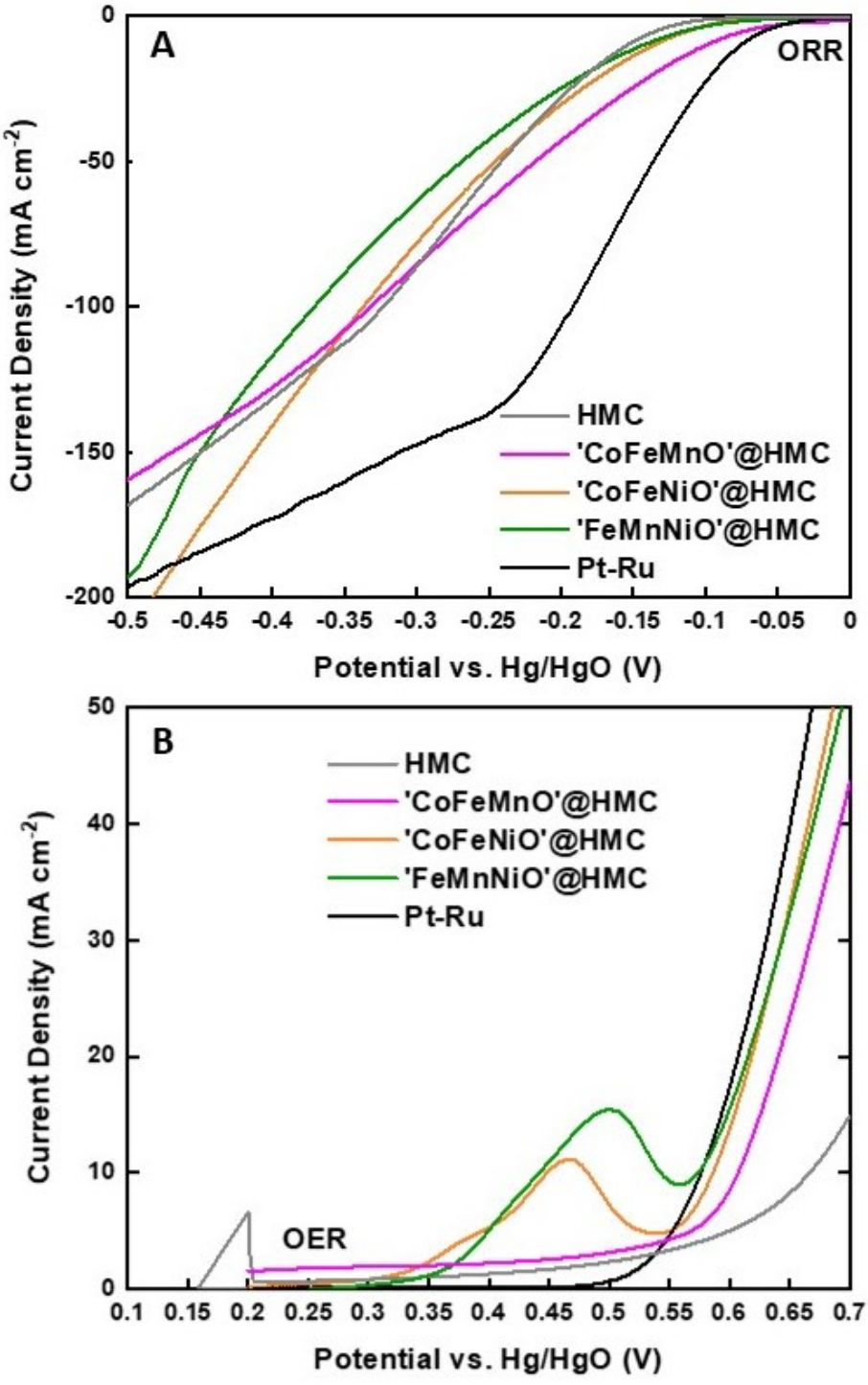

Figure 3-32. Linear sweep voltammograms of (A) 'CoFeMnO'@HMC, 'CoFeNiO'@HMC, and 'FeMnNiO'@HMC in ORR; and (B) 'CoFeMnO'@HMC, 'CoFeNiO'@HMC, and 'FeMnNiO'@HMC in OER.

To probe the origin of the enhanced ORR and OER catalytic activities of the hybrids, deconvoluted high-resolution N 1s XP spectra were obtained and analyzed (Fig. 3-33). The binding energies of the N are summarized in Table 3-4. In the pristine HMC, pyridinic and pyrrolic N were observed at 398.2 and 400.4 eV, respectively. Upon the incorporation of 'MO' nanoparticles, both N peaks shifted toward higher binding energies, indicating the possible synergistic interactions between the N sites on HMC and the 'MO' NPs. Moreover, a new peak corresponding to N^{+}-O^{-} was observed in all hybrids and its binding energy was measured at between 403.0 and 404.0 eV depending upon the metal oxides.[43] These data suggest interactions between the N sites in HMC and the oxygen in the metal oxides. These interactions are speculated to enhance the ORR and OER catalytic activities in the hybrid materials and are the subject of ongoing investigations.

Table 3-4. Binding energies of different types of N in pristine HMC and 'MO'@HMC.

Material	B.E. of pyridinic N (eV)	B.E. of pyrrolic N (eV)	B.E. of N^+-O^- (eV)
Pristine HMC	398.2	400.4	-
Co_3O_4@HMC	398.5	400.8	404.0
$MnCo_2O_4$@HMC	398.6	400.9	403.0
'CoFeMnO'@HMC	398.4	400.8	404.0
'CoFeNiO'@HMC	398.7	400.9	403.0
'CoFeMnO'@HMC	398.4	400.6	403.1

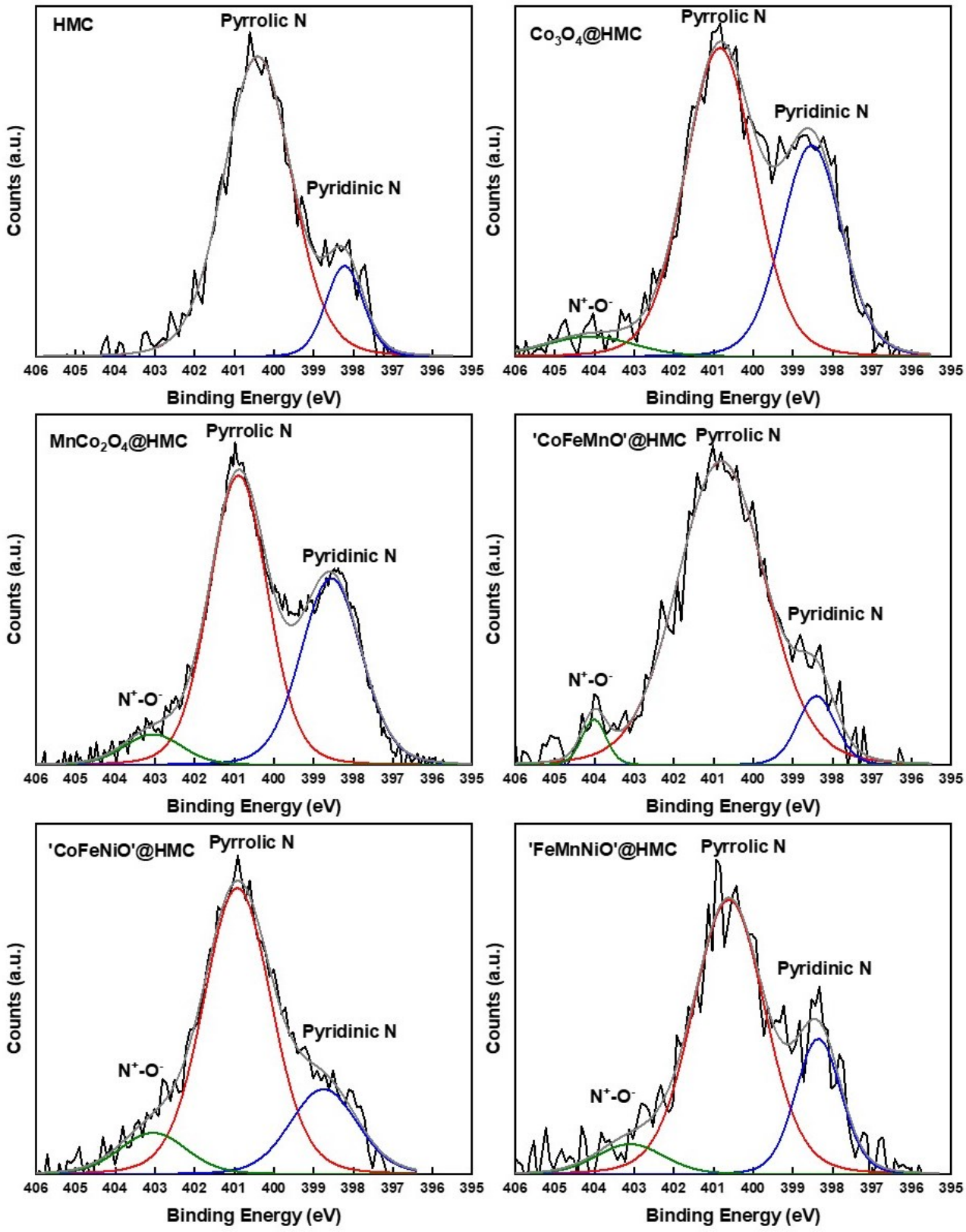

Figure 3-33. Deconvoluted N 1s XP spectra for pristine HMC and the hybrids.

Having evaluated the OER and ORR activity of the 'MO'@HMC, full cell rate testing was performed to evaluate the discharge and charge potentials for each catalyst (Fig. 3-34, 3-35 and Table 3-5). Cells were fabricated using catalyst-loaded GDL and Zn sheet as electrodes, and 6 M KOH and 0.25 M ZnO aqueous solution as electrolyte. All charging/discharge potentials were evaluated at 2, 5, 10, and 20 mA cm^{-2} and each current density was held for 10 min. At 10 mA cm^{-2}, pristine HMC initially exhibited 1.19 V and 2.04 V for discharge and charge potentials, respectively. Upon incorporation of Co_3O_4 and $MnCo_2O_4$, the Co_3O_4@HMC and $MnCo_2O_4$@HMC displayed enhanced discharge potentials of 1.26 and 1.28 V at 10 mA cm^{-2}, respectively. This is consistent with the LSV results. These values are superior to benchmark Pt-Ru (1.25 V) as well as recently reported literature values (Table 3-6). The lower charge potential of 2.01 V at 10 mA cm^{-2} noted for the Co_3O_4@HMC catalyst is consistent with the OER activity noted in the presented LSV data. This is comparable to the benchmark Pt-Ru. The excellent ORR and OER catalytic activity make Co_3O_4@HMC a cost-effective bifunctional alternative to Pt-Ru for Zn-air batteries. All ternary oxide nanoparticle decorated HMCs exhibited enhanced discharge potentials at low current densities (i.e., 2 and 5 mA cm^{-2}) reflecting the enhanced ORR activity seen in LSV analysis. These discharge potentials dropped to below 1.21 V at high current density (10 and 20 mA cm^{-2}) and may result from the degradation of ternary oxide nanoparticles. Charging potentials

for these same devices were determined to be 1.98, 1.96, and 1.97 V for 'CoFeMnO'@HMC, 'CoFeNiO'@HMC, and 'FeMnNiO'@HMC, respectively at 10 mA cm^{-2}. These metrics are lower than the pristine HMCs (2.04 V) and Pt-Ru benchmark (2.01 V) as well as literature values (Table 3-6) and are consistent with enhanced OER activity. This makes them much more affordable and efficient OER catalysts than the precious metal Pt-Ru benchmark.

Table 3-5. Summary of rate testing results.

Materials	Discharge potential @10 mA cm^{-2} (V)	Discharge potential @20 mA cm^{-2} (V)	Charge potential @10 mA cm^{-2} (V)	Charge potential @20 mA cm^{-2} (V)
HMC	1.19	1.15	2.04	2.09
Co_3O_4 @HMC	1.26	1.23	2.01	2.07
$MnCo_2O_4$ @HMC	1.28	1.24	2.03	2.1
'CoFeMnO' @HMC	1.21	1.12	1.98	2.04
'CoFeNiO' @HMC	1.21	1.14	1.96	2.02
'FeMnNiO' @HMC	1.19	1.09	1.97	2.03
Pt-Ru	1.25	1.21	2.01	2.08

Table 3-6. Summary of recently reported transition metal/carbon nanomaterial catalysts.

Catalyst	$E_{discharge}$ (V)	$E_{charging}$ (V)	Cycling Conditions	Cycling Efficiency%	Ref
Co_3O_4@HMC	1.23 @ 20 mA cm^{-2}	2.07 @ 20 mA cm^{-2}	10 mA cm^{-2} for 200 cycles (100 h)	63% initial 56.5% final	This work
$CoFe_2O_4$@CNT	1.1 @ 20 mA cm^{-2}	2.00 @ 5 mA cm^{-2}	5 mA cm^{-2} for 1200 cycles (200 h)	60% initial 50% final	[44]
$Co_{0.5}Fe_{0.5}O_x$/NrGO	-	-	10 mA cm^{-2} for 60 cycles (120 h)	62.6% initial 56.2% final	[45]
Co_3O_4@DMC	1.1 @10 mA cm^{-2}	2.01 @ 10 mA cm^{-2}	10 mA cm^{-2} for 72 cycles (24 h)	54.7% initial 49.3% final	[46]
$(CoFe)_3O_4$ @N-CNT	1.19 @ 20 mA cm^{-2}	1.99 @ 20 mA cm^{-2}	20 mA cm^{-2} for 100 cycles (50 h)	58.7% initial 53.5% final	[47]
$ZnCoO_x$/N-CNT	1.15 @ 20 mA cm^{-2}	2.08 @ 20 mA cm^{-2}	10 mA cm^{-2} for 200 cycles (100 h)	54.6% initial 55.8% final	[21]
$ZnMnO_x$/N-CNT	1.23 @ 20 mA cm^{-2}	2.14 @ 20 mA cm^{-2}	10 mA cm^{-2} for 200 cycles (100 h)	62.6% initial 56.6% final	[21]
Mn_3O_4/N-CNT	1.25 @ 10 mA cm^{-2}	~2.05 @ 10 mA cm^{-2}	10 mA cm^{-2} for 200 cycles (100 h)	63.1% initial 53.6% final	[35]

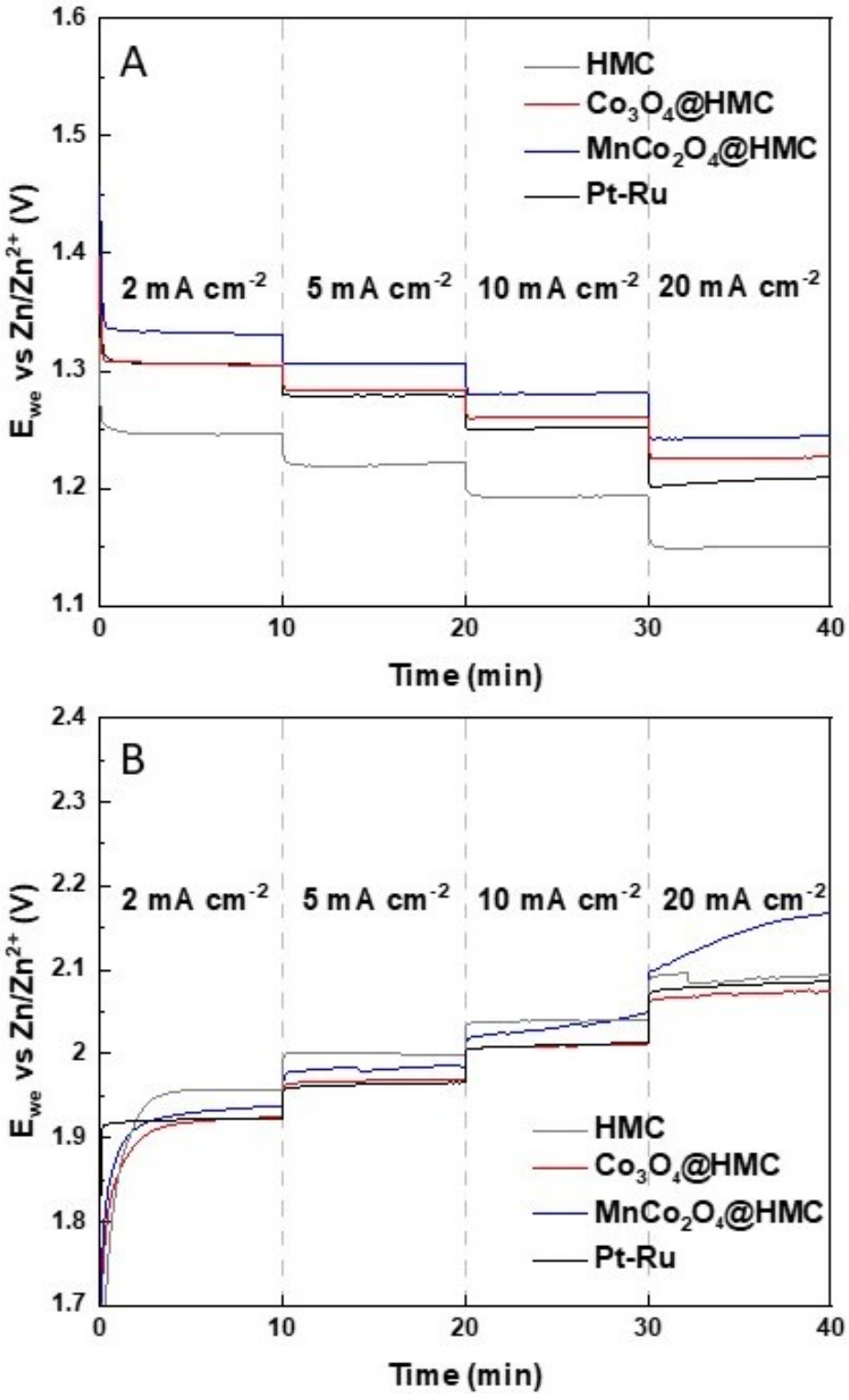

Figure 3-34. Full cell rate testing of (A) Co_3O_4@HMC and $MnCo_2O_4$@HMC discharge; and (B) Co_3O_4@HMC and $MnCo_2O_4$@HMC charge.

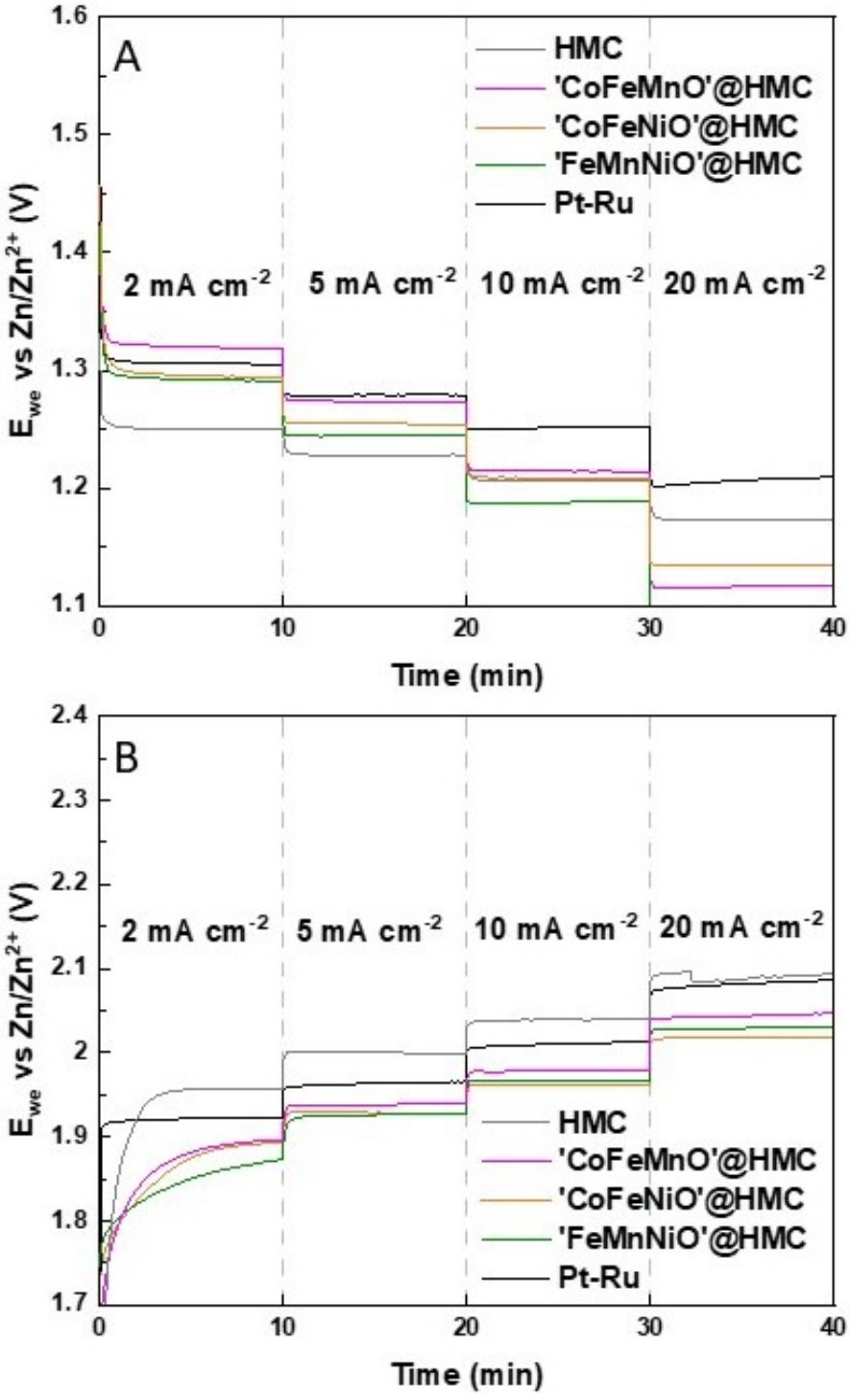

Figure 3-35. Full cell rate testing of (A) 'CoFeMnO'@HMC, 'CoFeNiO'@HMC, and 'FeMnNiO'@HMC discharge; and (B) 'CoFeMnO'@HMC, 'CoFeNiO'@HMC, and 'FeMnNiO'@HMC charge.

Zn-air battery bifunctional cycling test was also performed at 10 mA cm^{-2} to assess the stability of the as-synthesized hybrid catalyst (30 min/cycle). The Pt-Ru benchmark catalyst was also cycled in an identical fashion for comparison. During the first cycle, Pt-Ru displayed 1.23 V discharge potential and 1.99 V charge potential, which corresponds to 61.8 % efficiency (Fig. 3-36A). The cycling was stopped after 50 h, as its discharge potential deteriorated to 1.13 V and charge potential increased to 2.25 V, equivalent to 50.2 % efficiency. Among the hybrids, Co_3O_4@HMC was chosen to be cycled, as it exhibits the highest catalytic activity toward both ORR and OER (i.e., bifunctional activity) in previous LSV and rate testing. The hybrid was cycled bifunctionally for 100 h (equivalent to 200 cycles) at 10 mA cm^{-2}. During the first cycle, the initial discharge and charge potentials were measured at 1.26 and 2.00 V respectively, corresponding to 63.0 % efficiency (Fig. 3-36B). This makes the Co_3O_4@HMC marginally better than Pt-Ru in bifunctional catalytic efficiency. After 200 cycles, it exhibited 1.17 V of discharge potential and 2.07 V of charge potential, equivalent to 56.5 % efficiency. This is higher than the 50.2 % efficiency of the Pt-Ru, indicating the superior stability of Co_3O_4@HMC compared to Pt-Ru. The observed efficiency is comparable to recent literature values (Table 3-6).

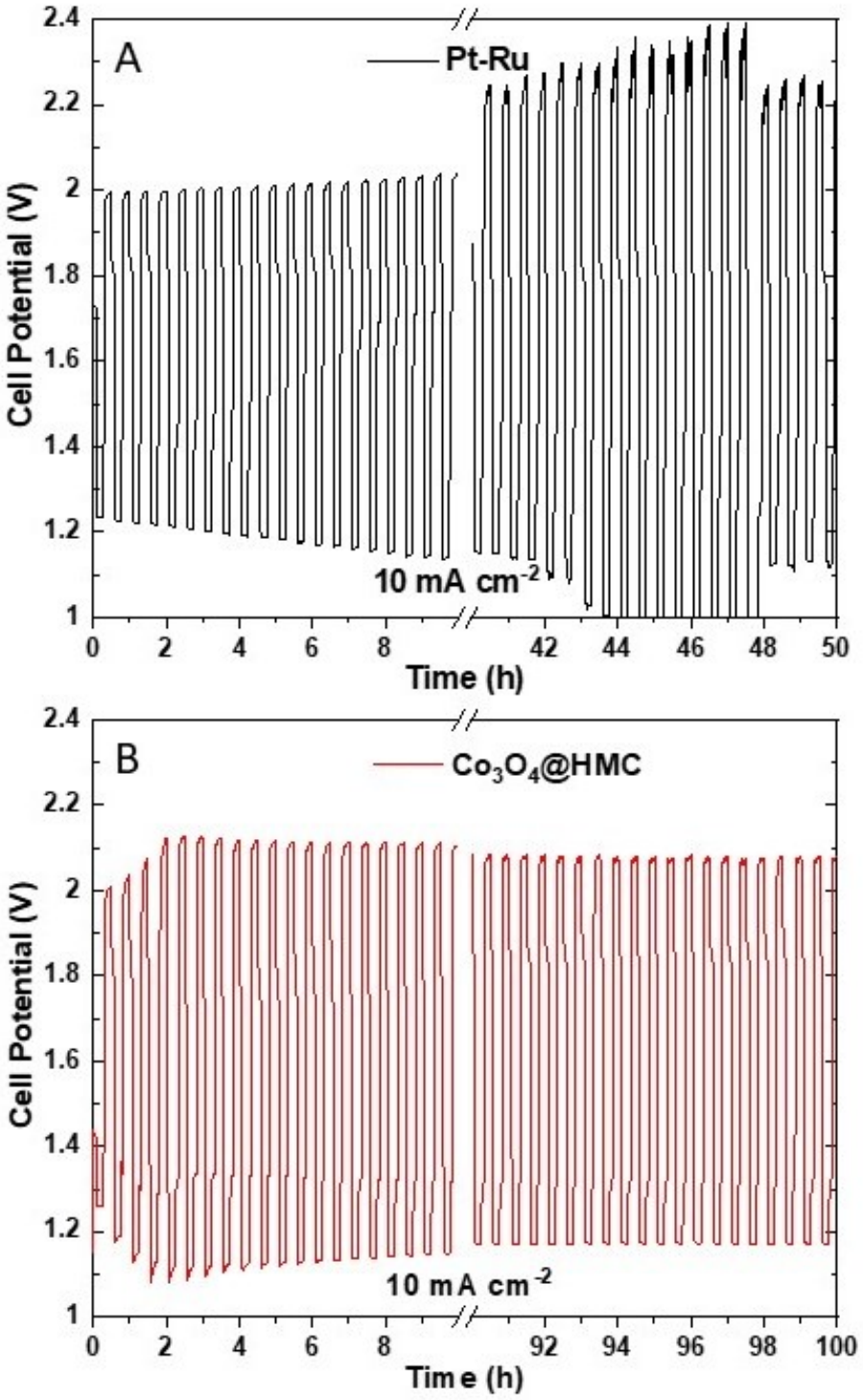

Figure 3-36. Cycling data of (A) Co_3O_4@HMC; and (B) Pt-Ru. Both materials were cycled bifunctionally at 10 mA cm^{-2} for 100 h (30 min/cycle, 200 cycles).

3.4 Conclusions

In the present study, a series of non-precious metal oxide nanoparticles decorated nitrogen-doped hollow mesoporous carbon were synthesized using convenient template driven synthesis followed by hydrothermal nanoparticle deposition. The nature of the nanoparticles was successfully identified via electron microscopy imaging, energy dispersive X-ray spectroscopy, and X-ray photoelectron spectroscopy analysis. Co_3O_4@HMC and $MnCo_2O_4$@HMC exhibited excellent ORR activity, while 'CoFeMnO'@HMC, 'CoFeNiO'@HMC, 'FeMnNiO'@HMC showed superior OER activity to the Pt-Ru benchmark catalyst. Co_3O_4@HMC was cycled for 100 h (equivalent to 200 cycles) at 10 mA cm^{-2} and exhibited higher efficiency before and after cycling than Pt-Ru and as well as displaying promising stability. By combining transition metal oxide nanoparticles and HMC, we have achieved earth abundant, affordable, and efficient ORR and OER catalysts for Zn-air batteries.

3.5 References

(1) Saint Akadiri, S.; Alola, A. A.; Akadiri, A. C.; Alola, U. V. *Energ. Policy* **2019**, *132*, 803-810.
(2) Liu, W. F.; Zhang, X. P.; Feng, S. D. *Renew. Energ.* **2019**, *135*, 635-642.
(3) Babatunde, O. M.; Munda, J. L.; Hamam, Y. *Int. J. Energ. Res.* **2019**, *43* (12), 6078-6107.
(4) Abujarad, S. Y.; Mustafa, M. W.; Jamian, J. J. *Renew. Sust. Energ. Rev.* **2017**, *70*, 215-223.
(5) Li, Y. G.; Lu, J. *ACS Energy Lett.* **2017**, *2* (6), 1370-1377.
(6) Zhang, J.; Zhou, Q. X.; Tang, Y. W.; Zhang, L.; Li, Y. G. *Chem. Sci.* **2019**, *10* (39), 8924-8929.
(7) Shen, X.; Liu, H.; Cheng, X. B.; Yan, C.; Huang, J. Q. *Energy Storage Mater.* **2018**, *12*, 161-175.
(8) Gu, P.; Zheng, M. B.; Zhao, Q. X.; Xiao, X.; Xue, H. G.; Pang, H. *J. Mater. Chem. A* **2017**, *5* (17), 7651-7666.
(9) Nykvist, B.; Nilsson, M. *Nat. Clim. Change.* **2015**, *5* (4), 329-332.
(10) Li, Y. G.; Dai, H. J. *Chem. Soc. Rev.* **2014**, *43* (15), 5257-5275.
(11) Fu, J.; Cano, Z. P.; Park, M. G.; Yu, A. P.; Fowler, M.; Chen, Z. W. *Adv. Mater.* **2017**, *29* (7), 1604685.
(12) Pan, J.; Tian, X. L.; Zaman, S.; Dong, Z. H.; Liu, H. F.; Park, H. S.; Xia, B. Y. *Batteries Supercaps* **2019**, *2* (4), 336-347.
(13) Zhao, Z. Q.; Fan, X. Y.; Ding, J.; Hu, W. B.; Zhong, C.; Lu, J. *ACS Energy Lett.* **2019**, *4* (9), 2259-2270.
(14) Lee, J. S.; Kim, S. T.; Cao, R.; Choi, N. S.; Liu, M.; Lee, K. T.; Cho, J. *Adv. Energy Mater.* **2011**, *1* (1), 34-50.
(15) Cheng, F. Y.; Chen, J. *Chem. Soc. Rev.* **2012**, *41* (6), 2172-2192.
(16) Fu, J.; Liang, R. L.; Liu, G. H.; Yu, A. P.; Bai, Z. Y.; Yang, L.; Chen, Z. W. *Adv. Mater.* **2019**, *31* (31), 1805230.
(17) Wei, L. C.; Ang, E. H.; Yang, Y.; Qin, Y. L.; Zhang, Y. F.; Ye, M. H.; Liu, Q.; Li, C. C. *J. Power Sources* **2020**, *477*.
(18) Wu, C.; Song, L.; Li, L. H.; Xia, W.; Jiang, C.; Gao, B.; Du, Y. Q.; Wang, T.; He, J. P. *Chemelectrochem* **2019**, *6* (15), 4010-4015.
(19) Hadidi, L.; Davari, E.; Iqbal, M.; Purkait, T. K.; Ivey, D. G.; Veinot, J. G. C. *Nanoscale* **2015**, *7* (48), 20547-20556.
(20) Shao, Y.; Xiao, X.; Zhu, Y. P.; Ma, T. Y. *Angew. Chem. Int. Edit.* **2019**, *58* (41), 14599-14604.
(21) Aasen, D. A.; Shen, Y.; Ivey, D. G. *Chemelectrochem* **2020**, *7* (10), 2283-2296.

(22) He, J. Z.; Niu, W. J.; Wang, Y. P.; Sun, Q. Q.; Liu, M. J.; Wang, K. Y.; Liu, W. W.; Liu, M. C.; Yu, F. C.; Chueh, Y. L. *Electrochim. Acta.* **2020**, *362*.
(23) Niu, W. J.; He, J. Z.; Wang, Y. P.; Sun, Q. Q.; Liu, W. W.; Zhang, L. Y.; Liu, M. C.; Liu, M. J.; Chueh, Y. L. *Nanoscale* **2020**, *12* (38), 19644-19654.
(24) Xu, Y. J.; Sumboja, A.; Groves, A.; Ashton, T.; Zong, Y.; Darr, J. A. *RSC Adv.* **2020**, *10* (68), 41871-41882.
(25) Chen, J. Y.; Li, H.; Fan, C.; Meng, Q. W.; Tang, Y. W.; Qiu, X. Y.; Fu, G. T.; Ma, T. Y. *Adv. Mater.* **2020**, *32* (30), 2003134.
(26) Wang, B.; Ye, Y. Z.; Xu, L.; Quan, Y.; Wei, W. X.; Zhu, W. S.; Li, H. M.; Xia, J. X. *Adv. Funct. Mater.* **2020**, *30* (51), 2005834.
(27) He, Y. J.; Aasen, D.; Yu, H. Y.; Labbe, M.; Ivey, D. G.; Veinot, J. G. C. *Nanoscale Adv.* **2020**, *2* (8), 3367-3374.
(28) Zhang, M. D.; Dai, Q. B.; Zheng, H. G.; Chen, M. D.; Dai, L. M. *Adv. Mater.* **2018**, *30* (10), 1705431.
(29) Dasog, M.; Smith, L. F.; Purkait, T. K.; Veinot, J. G. C. *Chem. Commun.* **2013**, *49* (62), 7004-7006.
(30) Liang, Y. Y.; Wang, H. L.; Diao, P.; Chang, W.; Hong, G. S.; Li, Y. G.; Gong, M.; Xie, L. M.; Zhou, J. G.; Wang, J.; Regier, T. Z.; Wei, F.; Dai, H. J. *J. Am. Chem. Soc.* **2012**, *134* (38), 15849-15857.
(31) Marco, J. F.; Gancedo, J. R.; Gracia, M.; Gautier, J. L.; Rios, E.; Berry, F. J. *J. Solid State Chem.* **2000**, *153* (1), 74-81.
(32) Biesinger, M. C.; Payne, B. P.; Grosvenor, A. P.; Lau, L. W. M.; Gerson, A. R.; Smart, R. S. *Appl. Surf. Sci.* **2011**, *257* (7), 2717-2730.
(33) Prabaharan, D. D. M.; Sadaiyandi, K.; Mahendran, M.; Sagadevan, S. *Appl. Phys. A-Mater.* **2017**, *123* (4), 264.
(34) Krishnan, S. G.; Ab Rahim, M. H.; Jose, R. *J. Alloy. Compd.* **2016**, *656*, 707-713.
(35) Aasen, D.; Clark, M.; Ivey, D. G. *Batteries Supercaps* **2019**, *2* (10), 882-893.
(36) He, X. B.; Yin, F. X.; Li, G. R. *Int. J. Hydrogen Energ.* **2015**, *40* (31), 9713-9722.
(37) Clark, M. P.; Muneshwar, T.; Xiong, M.; Cadien, K.; Ivey, D. G. *ACS Appl. Nano Mater.* **2019**, *2* (1), 267-277.
(38) Liu, J.; Bao, H. L.; Zhang, B. S.; Hua, Q. F.; Shang, M. F.; Wang, J. Q.; Jiang, L. H. *ACS Appl. Mater. Inter.* **2019**, *11* (13), 12525-12534.
(39) Tang, Q. W.; Jiang, L. H.; Liu, J.; Wang, S. L.; Sun, G. Q. *ACS Catal.* **2014**, *4* (2), 457-463.
(40) Antoni, H.; Xia, W.; Masa, J.; Schuhmann, W.; Muhler, M. *Phys. Chem. Chem. Phys.* **2017**, *19* (28), 18434-18442.
(41) Godwin, I. J.; Lyons, M. E. G. *Electrochem. Commun.* **2013**, *32*, 39-42.

(42) Gong, L.; Chng, X. Y. E.; Du, Y. H.; Xi, S. B.; Yeo, B. S. *ACS Catal.* **2018**, *8* (2), 807-814.
(43) Zhuang, S. Q.; Lee, E. S.; Lei, L.; Nunna, B. B.; Kuang, L. Y.; Zhang, W. *Int. J. Energ. Res.* **2016**, *40* (15), 2136-2149.
(44) Xu, N. N.; Qiao, J. L.; Nie, Q.; Wang, M.; Xu, H.; Wang, Y. D.; Zhou, X. D. *Catal. Today* **2018**, *318*, 144-149.
(45) Wei, L.; Karahan, H. E.; Zhai, S. L.; Liu, H. W.; Chen, X. C.; Zhou, Z.; Lei, Y. J.; Liu, Z. W.; Chen, Y. *Adv. Mater.* **2017**, *29* (38), 1701410.
(46) An, K. L.; Zheng, Y.; Xu, X. X.; Wang, Y. *J. Solid State Chem.* **2019**, *270*, 539-546.
(47) Aasen, D.; Clark, M. P.; Ivey, D. G. *Batteries Supercaps* **2020**, *3* (2), 174-184.

Chapter 4: CoNi Nanoparticle Decorated ZIF-67 Derived Hollow Carbon Cubes as Efficient and Durable Bifunctional Electrocatalyst for Zn-Air Batteries

4.1 Introduction

Stationary energy storage technology has gained substantial popularity in recent years owing to its potential to support a decarbonized economy powered by supply-safe renewable energy.[1] Batteries are excellent candidates for stationary energy storage, as they are energy efficient, responsive, scalable, and easy to install.[2] Lithium-ion batteries (Li-ion) are one of the most commercially successful battery technologies, especially in their recent applications in portable electronics and electric vehicles (EV).[3, 4] However, Li-ion batteries experience multiple drawbacks for large scale stationary energy storage ranging from cost to environmental impact to device safety. The rising cost of lithium has pushed its price per unit energy to a record high ($250 kW^{-1} h^{-1}) and lithium extraction has detrimental environmental impacts.[5, 6] In addition, Li-ion battery failures have resulted in many fires and explosions that are in part due to their utilization of flammable organic electrolyte.[7, 8]

Rechargeable alkaline zinc-air batteries (Zn-air) have received considerable interest as an attractive candidate for stationary energy storage because of a variety of inherent advantages. Zn-air batteries possess a high specific energy of 1353 Wh kg^{-1} (excluding oxygen) that is significantly higher than status quo Li-ion batteries (350 Wh kg^{-1}).[9-11] Raw materials used in Zn-air batteries (e.g., Zn) are substantially

cheaper than those for Li-ion batteries and Zn-air batteries provide a much lower cost per unit energy of \$100 Wh^{-1} h^{-1} (potentially < \$10 Wh^{-1} h^{-1}).[11-14] Last but not least, alkaline Zn-air batteries utilize aqueous alkaline electrolytes (e.g., KOH), which eliminates the risk of fire and explosion.[15, 16]

Rechargeable alkaline Zn-air batteries rely upon separating the oxidation of metallic Zn into two half reactions (Figure 4-1). When the battery discharges, the Zn electrode reacts with hydroxide (i.e., OH^-) ions supplied by the electrolyte to form zincate anions (i.e., $[Zn(OH)_4]^{2-}$) and electrons. The electrons travel through the external circuit to the air electrode, where atmospheric oxygen (i.e., O_2) is reduced to OH^- replenishing the electrolyte. This process is commonly referred to as the oxygen reduction reaction (ORR). When the battery is recharged, the reverse reactions occur and O_2 is regenerated from OH^-.[17] The reverse reaction is referred to as the oxygen evolution reaction (OER). Both ORR and OER are kinetically sluggish and require electrocatalysts for the battery to function efficiently.[18, 19]

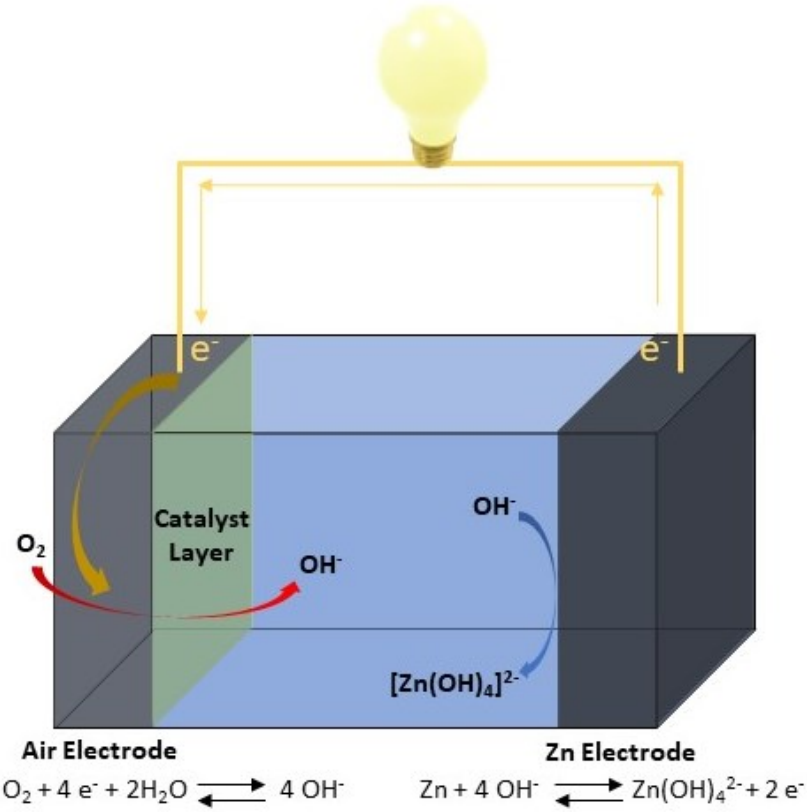

Figure 4-1. A pictorial presentation of an alkaline Zn-air battery during discharge.

Despite the aforementioned advantages of Zn-air batteries, challenges remain if they are to realize their full potential. Without question, the biggest hurdle to widespread commercialization of rechargeable alkaline Zn-air batteries is realizing efficient and affordable bifunctional electrocatalysts that facilitate the ORR and OER reactions. Traditionally, precious metals and their oxides (e.g., platinum (Pt) and ruthenium oxide (RuO_2)) have been used for ORR and OER, respectively. Not only are these catalysts costly and scarce, they are also unifunctional, catalyzing only one of the core reactions efficiently.[20-22] Moreover, precious metal catalysts

suffer from poor durability in part because they form agglomerates and/or detach from carbon supports.[23]

Far reaching investigations targeting the design and development of alternative electrocatalysts for Zn-air batteries have appeared. In particular, heteroatom-doped carbon nanomaterials, such as N-doped graphene nanosheets, carbon aerogels, and hollow mesoporous carbon nanospheres, have been explored extensively as they exhibit impressive bifunctional catalytic activity and durability.[24-27] Transition metal nanoparticles (e.g., Mn_3O_4, Fe_3O_4, and Co_3O_4) supported by carbon nanomaterials have also shown promising Zn-air battery performance.[28-33] Furthermore, metal-organic-frameworks (MOF) and zeolitic imidazolate frameworks (ZIF) have gained popularity as a precursor in the synthesis of highly porous carbon nanoparticles as Zn-air battery catalysts.[34-36]

In this work, we report the preparation and characterization of CoNi nanoparticle decorated hollow carbon cubes (CoNi@HCC) obtained from a ZIF-67 sacrificial template. By taking advantage of the thermal instability of ZIF-67, we successfully combined carbonization, template removal, and metal nanoparticle decoration into a single step to generate hollow graphitic structures while simultaneously introducing metal nanoparticles into the carbon matrices. CoNi@HCC exhibited good ORR and OER performance when benchmarked against costly Pt-Ru (30% Pt and 15% RuO_2 on carbon black). Prototype Zn-air

batteries equipped with CoNi@HCC exhibited a discharge potential of 1.21 V at 20 mA cm^{-2}, marginally higher than Pt-Ru (1.20 V). CoNi@HCC also demonstrated 2.04 V of charging potential at 20 mA cm^{-2}, outperforming Pt-Ru (2.08 V). After 90 h of bifunctional cycling at 10 mA cm^{-2}, CoNi@HCC only experienced a minor drop of 3.4% in battery efficiency (58.7% to 55.3%), displaying good durability. In contrast, the battery efficiency of Pt-Ru plummeted from 56.2% to 41.7% after just 60 h of cycling.

4.2 Experimental Section

4.2.1 Materials and reagents

Dopamine hydrochloride (DA·HCl), anhydrous ethanol (≤0.005% water), 2-methylimidazole, *N*, *N*, *N'*, *N'*-tetramethylethylenediamine (TEMED), dicyandiamide, sucrose, cobalt acetate tetrahydrate ($Co(CH_3COO)_2 \cdot 4H_2O$), cobalt nitrate hexahydrate ($Co(NO_3)_2 \cdot 6H_2O$), and nickel acetate tetrahydrate ($Ni(CH_3COO)_2 \cdot 4H_2O$) were purchased from Sigma-Aldrich. Anhydrous methanol (≥99.8%) and denatured alcohol were obtained from Fisher Scientific. Pt-Ru powder (30% Pt and 15% RuO_2 on carbon black) and Nafion solution (D521, 5% w/w in water and isopropanol) were acquired from Alfa Aesar. PTFE-coated porous carbon paper (SGL 39BB gas diffusion layer; GDL) was obtained from the Fuel Cell Store. All reagents were used as received unless otherwise specified.

4.2.2 ZIF-67 template synthesis

ZIF-67 nanoparticle (NP) templates were synthesized using a modified literature method.[37] In a typical synthesis, 2.0 g (6.8 mmol) of $Co(NO_3)_2 \cdot 6H_2O$ and 4.4 g (54 mmol) of 2-methylimidazole were each dissolved in 100 mL of anhydrous methanol. The two solutions were stirred for 30 min to ensure complete dissolution after which they were combined to form a dark purple mixture that was stirred at 500 rpm for 30 min. The stirring was stopped and the mixture was left undisturbed for 24 h. The ZIF-67 NPs were separated from the mixture via centrifugation at 11,400 rpm for 35 min. The obtained ZIF-67 NPs were re-dispersed in anhydrous methanol via sonication and purified using centrifugation. The purification process was repeated three additional times. After purification, the ZIF-67 NPs were dried in vacuum for 12 h before being transferred to a vial and stored until use.

4.2.3 CoNi-PDA@ZIF and PDA@ZIF synthesis

Polydopamine coated ZIF-67 containing Co and Ni precursors (CoNi-PDA@ZIF) were synthesized using a modified literature method, with ZIF-67 as a template.[38, 39] Briefly, 0.2 g ZIF-67 was dispersed in 100 mL anhydrous methanol. The ZIF-67 dispersion was sonicated for 20 min. In the next step, 1.0 mL of TEMED was added to the reaction mixture. 0.10 g (0.53 mmol) of DA·HCl and a combination of 0.060 g (0.24 mmol) of $Co(CH_3COO)_2 \cdot 4H_2O$ and 0.087 g (0.35 mmol) of

$Ni(CH_3COO)_2 \cdot 4H_2O$ were each dissolved in 5 mL of deionized H_2O. All solutions were combined with the methanol dispersion of ZIF-67 and the mixture was stirred at 500 rpm at room temperature (25 °C) for 24 h. The CoNi-PDA@ZIF was recovered via centrifugation at 11,400 rpm for 35 min before being washed with anhydrous methanol three times. The CoNi-PDA@ZIF was air-dried for 12 h and then transferred and stored in a vial. PDA@ZIF was prepared using the same procedures without the addition of Co and Ni precursors.

4.2.4 HCC and CoNi@HCC synthesis

CoNi nanoparticle decorated hollow carbon cubes (CoNi@HCC) were synthesized using a modified literature method by annealing CoNi-PDA@ZIF at high temperature under Ar.[39] Briefly, 0.500 g of CoNi-PDA@ZIF was mixed with 0.060 g (0.24 mmol) of $Co(CH_3COO)_2 \cdot 4H_2O$, 0.060 g (0.24 mmol) of $Ni(CH_3COO)_2 \cdot 4H_2O$, 1.0 g (12 mmol) of dicyandiamide, and 0.12 g (0.35 mmol) sucrose in an agate mortar. The contents were ground and mixed well, before being transferred to a quartz boat. The boat was then placed in a tube furnace and annealed under flowing Ar. The temperature of the furnace was increased to 400 °C at 1 °C min^{-1} ramp rate and maintained at 400 °C for 2 h. The boat was then heated to 600 °C at 5 °C min^{-1} and kept at that temperature for an additional 2 h. In the last stage, the temperature was further increased to 915 °C at 5 °C min^{-1} and maintained at that temperature for 3 h. Finally, the furnace was cooled to room temperature (25 °C).

Hollow carbon cubes (HCC) were synthesized by annealing PDA@ZIF without the additional ingredients using an identical heating profile.

4.2.5 Materials characterization

Scanning electron microscopy (SEM) was performed on a Zeiss Sigma 300 VP-FESEM equipped with backscattered electron, secondary electron, and in-lens detectors using accelerating voltages between 5 and 20 kV. SEM samples were prepared by placing a drop an ethanol suspension of material of interest onto an aluminum (Al) stub. The coated stub was then air-dried at room temperature (25 °C) for 1 h before characterization. Transmission electron microscopy (TEM) and scanning transmission electron microscopy (STEM) images were obtained using a JEOL JEMARM200CF TEM/STEM (accelerating voltage of 200 kV) equipped with energy dispersive X-ray (EDX) spectrometer. High resolution TEM (HRTEM) images were processed using Gatan Digital Micrograph (Version 3.22.1461.0) and ImageJ (Version 1.53P) software. TEM samples were prepared by drop-coating a diluted ethanol suspension of material of interest onto an ultra-thin (UL) carbon coated Cu grid (Electron Microscopy Sciences). Subsequently, the TEM sample was dried under high vacuum for at least 16 h before characterization.

X-ray photoelectron spectroscopy (XPS) was performed on a Kratos Axis 165 Ultra X-ray spectrometer operating in energy spectrum mode under ultra-high

vacuum. XPS samples were prepared by drop-casting a concentrated ethanol suspension of material of interest onto a 5×5 mm^2 Cu foil. Subsequently, the substrate was dried under vacuum for at least 16 h. A monochromatic Al K source (λ= 8.34 Å) was used with a take-off angle of 90° and a charge neutralizer was utilized when necessary. CasaXPS software (VAMAS) was employed to process XPS data. A Shirley-type function was subtracted to account for the intrinsic loss background. All spectra were calibrated by setting the deconvoluted adventitious C 1s peak to 284.8 eV. Asymmetrical XPS fittings were performed for transition metal XP spectra using literature parameters.[40, 41]

Powder X-ray diffraction (PXRD) was performed by placing a ground and purified sample on a zero-background Si wafer. The measurement took place on a Bruker D8 advance diffractometer equipped with Cu Kα radiation source (λ = 1.5418 Å) and a scan range of 10˚ to 80˚ at a step rate of 0.02˚ s^{-1}.

4.2.6 Electrochemical Testing

Initial evaluation of the catalytic activity of the samples of interest was performed using linear sweep voltammetry (LSV). LSV was performed on a three-electrode cell at a scan rate of 5 mV s^{-1} using a potentiostat (Biologic VSP) and a 1 M KOH aqueous electrolyte. The electrolyte was purged with O_2 for 15 min and continuously bubbled with O_2 at 0.04 L min^{-1} during testing. The working electrode

was prepared as follows. The catalyst of interest (50 mg) was dispersed in 15 mL denatured alcohol (90% ethanol, 5% methanol, and 5% isopropanol) with 1 mL of 5% Nafion solution and sonicated for 2 h to provide an "ink". A pre-cut circular piece of GDL (diameter = 4.5 cm) was submerged in the catalyst ink and sonicated for 20 min. The GDL was then removed from the ink and air-dried at 25 °C for 15 min. Subsequently, 5 mL of the catalyst ink was passed through the GDL via vacuum filtration, producing an impregnated GDL with mass loading of approximately 1 mg cm^{-2} (±10%). 30% Pt and 15% RuO_2 on carbon black (Pt-Ru) was used as a benchmark catalyst for comparison. A Pt-Ru catalyst ink was prepared by dispersing 50 mg of Pt-Ru in deionized water (1 mL), denatured ethanol (2 mL), and 5% Nafion (0.1 mL). The Pt-Ru ink was then spray-coated onto a pre-cut circular GDL (diameter = 4.5 cm). The catalyst-coated GDLs were cut into 1 × 2 cm^2 rectangular pieces and used as the working electrode, ensuring the exposed surface area was 1 cm^2. Hg/HgO (0.098 V vs. SHE) and a platinum wire were used as reference and counter electrodes, respectively. The reported current densities were normalized to the exposed surface area of the working electrode (1 cm^2). All reported potentials were IR compensated (R_u = 2-4 Ω). Experimental errors are not reported due to the variability of the complex device structure.

4.2.7 Zn-air Battery assembly and testing

The catalysts of interest were incorporated into prototype Zn-air batteries and tested. Specifically, galvanostatic rate testing and discharge/charge cycling were performed. In all battery testing, a zinc sheet (8 g) and a catalyst-loaded GDL were used as zinc and air electrodes, respectively. 6 M KOH solution containing 0.25 M ZnO was utilized as the electrolyte. Galvanostatic rate tests were performed using an in-house fabricated vertical cell designed to minimize background signals from bubbles. Discharge/charge cycling was conducted with a horizontal cell to prevent flooding.[42] Additional electrolyte was added to the cell via a pump (0.95 mL h^{-1}) to compensate for electrolyte loss due to cell leakage. All cycling tests were performed by discharging the battery at 10 mA cm^{-2} for 10 min and resting it for 5 min, followed by recharging it at 10 mA cm^{-2} for another 10 min and resting it for 5 min (one cycle). The cycles were repeated for 90 h (180 cycles) or until failure. Experimental errors are not reported due to the variability of the complex device structure.

4.3 Results and Discussion

Figure 4-2 shows representative SEM and TEM images of hollow carbon cubes (HCC) and CoNi decorated HCC (CoNi@HCC). The HCC exhibits a cubic morphology, shown in Figure 4-2A and 4-3. CoO_x nanoparticles (NPs) were observed on the surface of HCC due to the presence of Co in the ZIF-67 template.

The TEM image (Figure 4-2B) is consistent with the HCC being hollow. CoNi@HCC are also hollow, and their surfaces are clearly decorated with polydisperse nanoparticles that appear in the SEM and TEM images (Figures 4-2C, 4-2D, and 4-4). The identities of the particles were investigated using EDX, XPS and PXRD analyses (vide infra). In addition to the HCCs, we also note a variety of hollow carbon nanostructure morphologies, including structures that could be carbon nanotubes (CNTs), based upon their apparent "bamboo structure", dispersed throughout the CoNi@HCC (Figures 4-2D and 4-5, indicated by red arrows).[43] We propose that these structures result from reactions involving sucrose and dicyandiamide that are added prior to the annealing step. A detailed investigation of these structures and their formation is beyond the scope of the present study and is the subject of ongoing investigation.

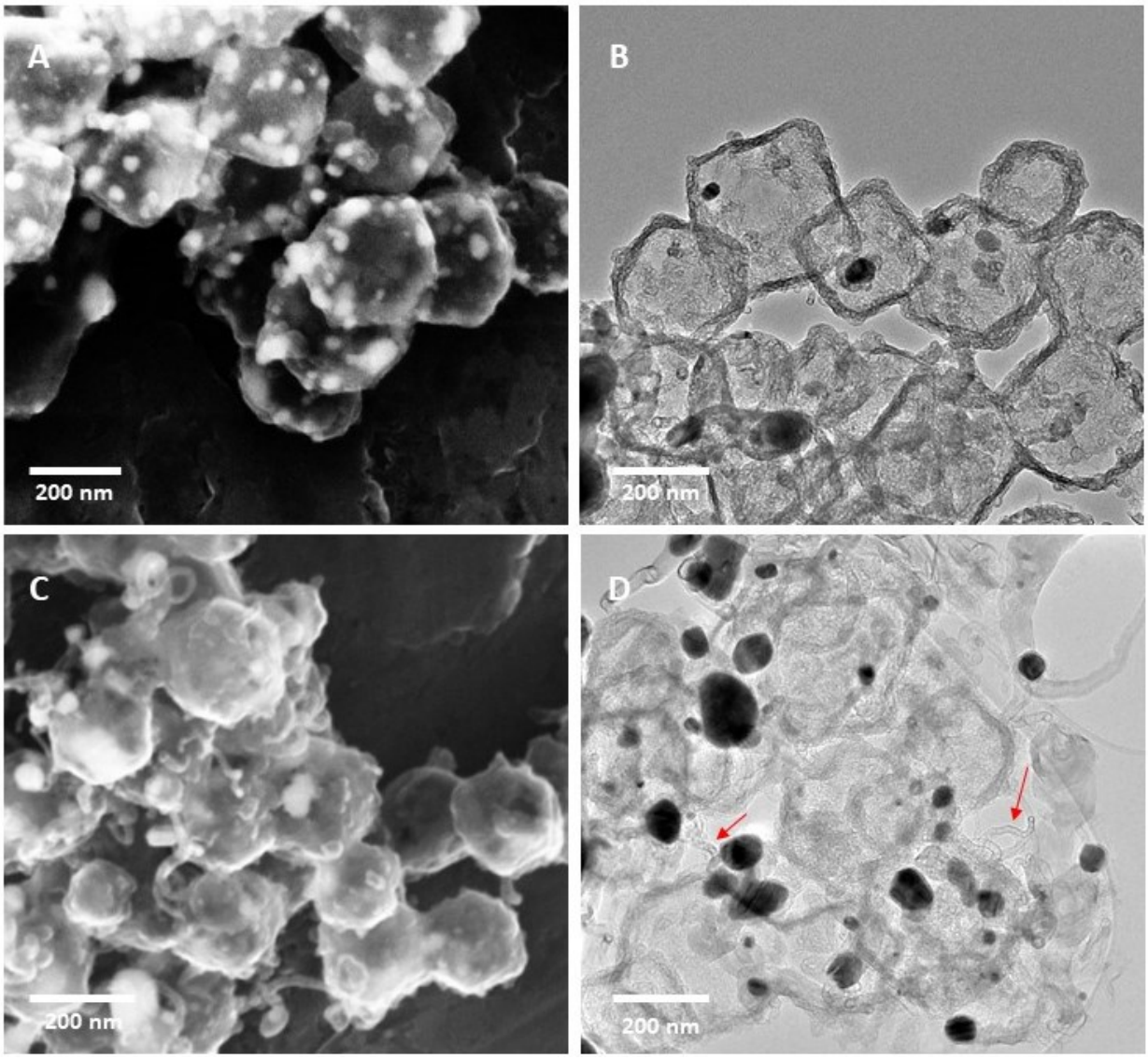

Figure 4-2. (A) Scanning electron microscopy secondary electron (SEM SE) image of HCC; (B) Transmission electron microscopy bright field (TEM BF) image of HCC; (C) SEM SE image of CoNi@HCC; (D) TEM BF image of CoNi@HCC.

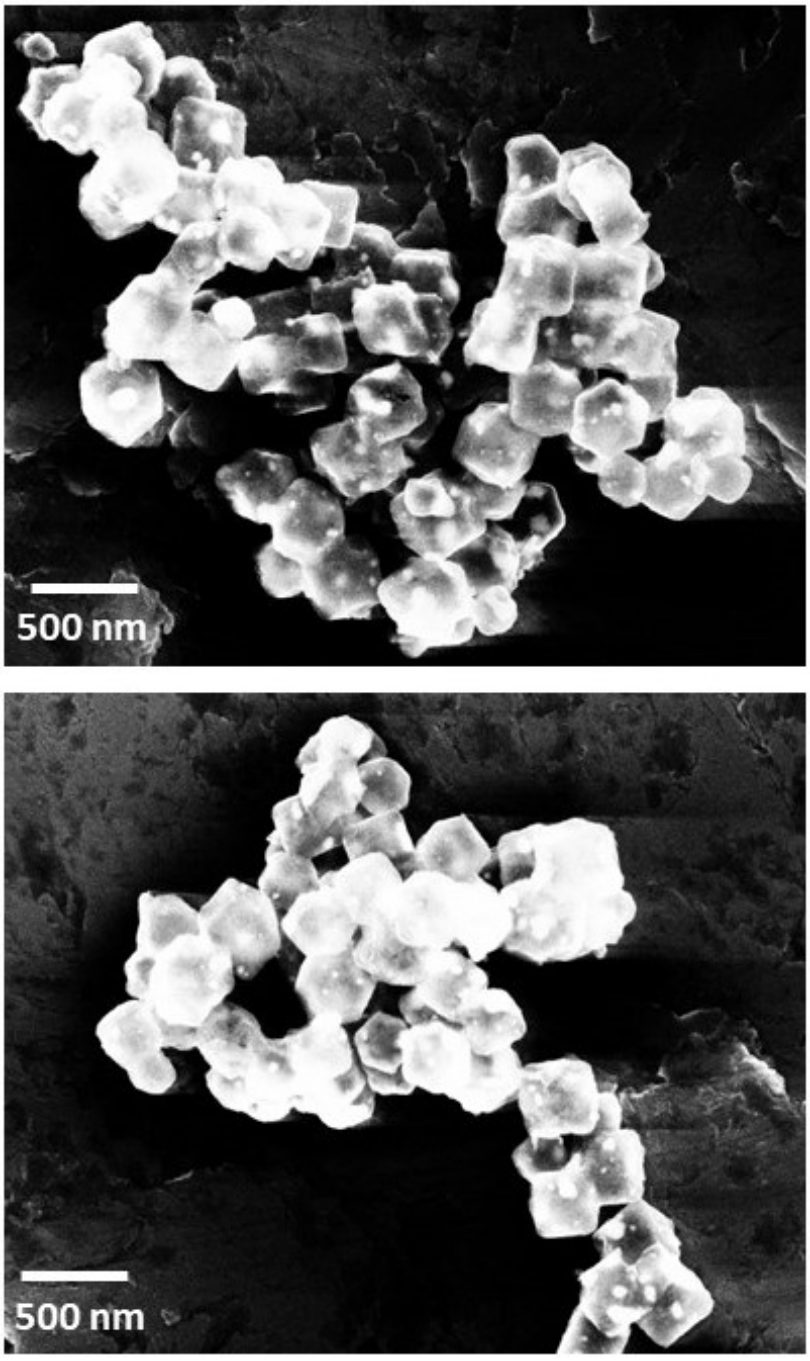

Figure 4-3. SEM SE images of HCC.

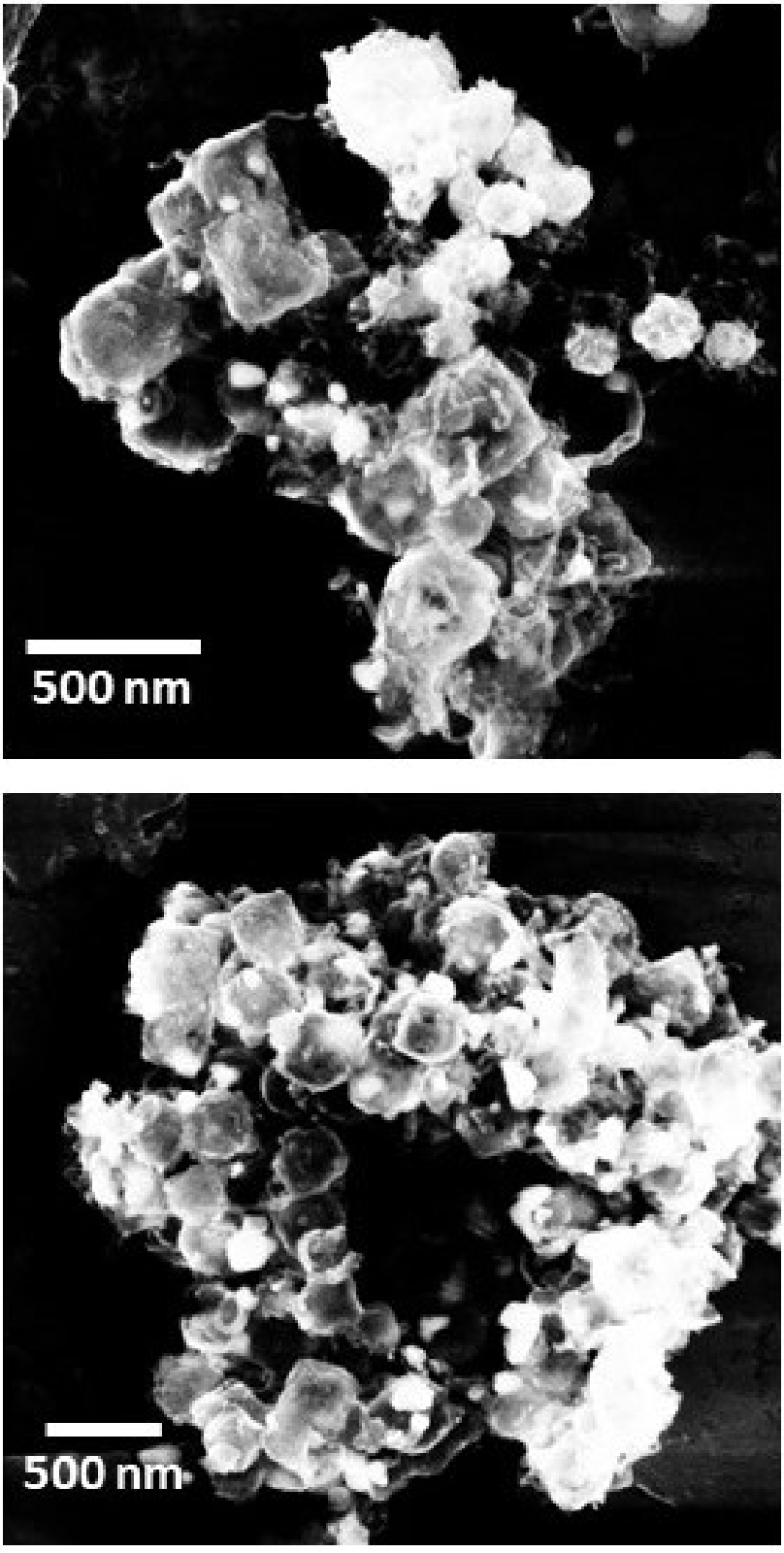

Figure 4-4. SEM SE images of CoNi@HCC.

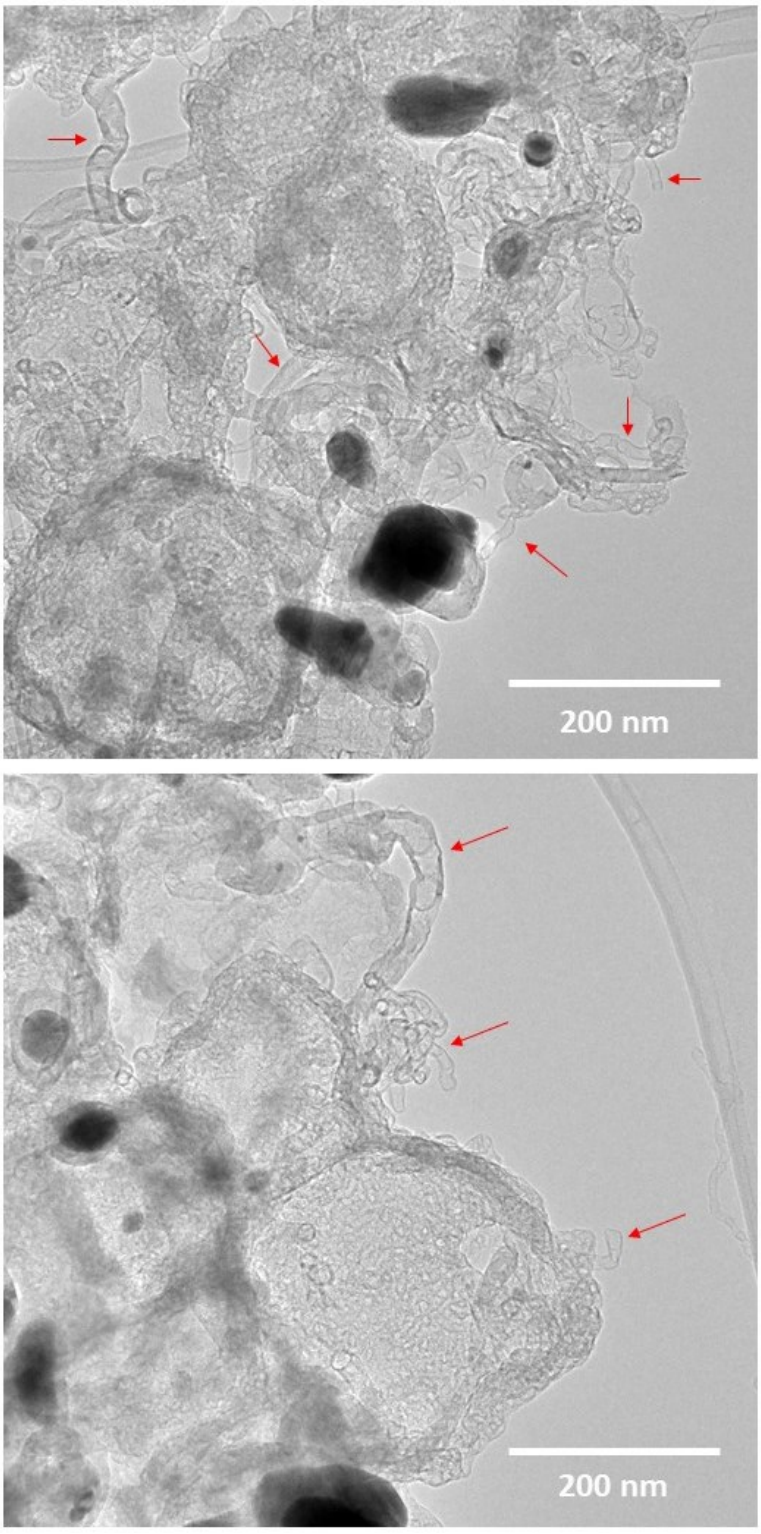

Figure 4-5. TEM BR images of CoNi@HCC. The red arrows indicate carbon nanostructures resembling carbon nanotubes.

EDX mapping of HCC and CoNi@HCC is shown in Figure 4-6 and 4-7. For HCC, the STEM annular dark field (ADF) image is co-localized with the C and N emissions consistent with HCC being uniformly N-doped. It is reasonable that the sources of N are the ZIF-67 and the dopamine coating. Co emission co-localize with bright regions in the STEM ADF image, suggesting that the nanoparticles on the HCC surfaces are Co-based. While the oxygen emissions show limited localization in these regions, oxygen is noted throughout the entire structure. Hence, any conclusion drawn from EDX analysis related to the oxidation of Co must be made with care. For CoNi@HCC, the C and N signals overlap with the general HCC structure and the Co and Ni signals overlap with the bright spots in the STEM ADF images. This combination of observations suggests the formation of CoNi nanoparticles in addition to the already present CoO_x. Furthermore, the newly formed hollow carbon nanostructures also appear to be N-doped according to the EDX mapping, shown in Figure 4-8.

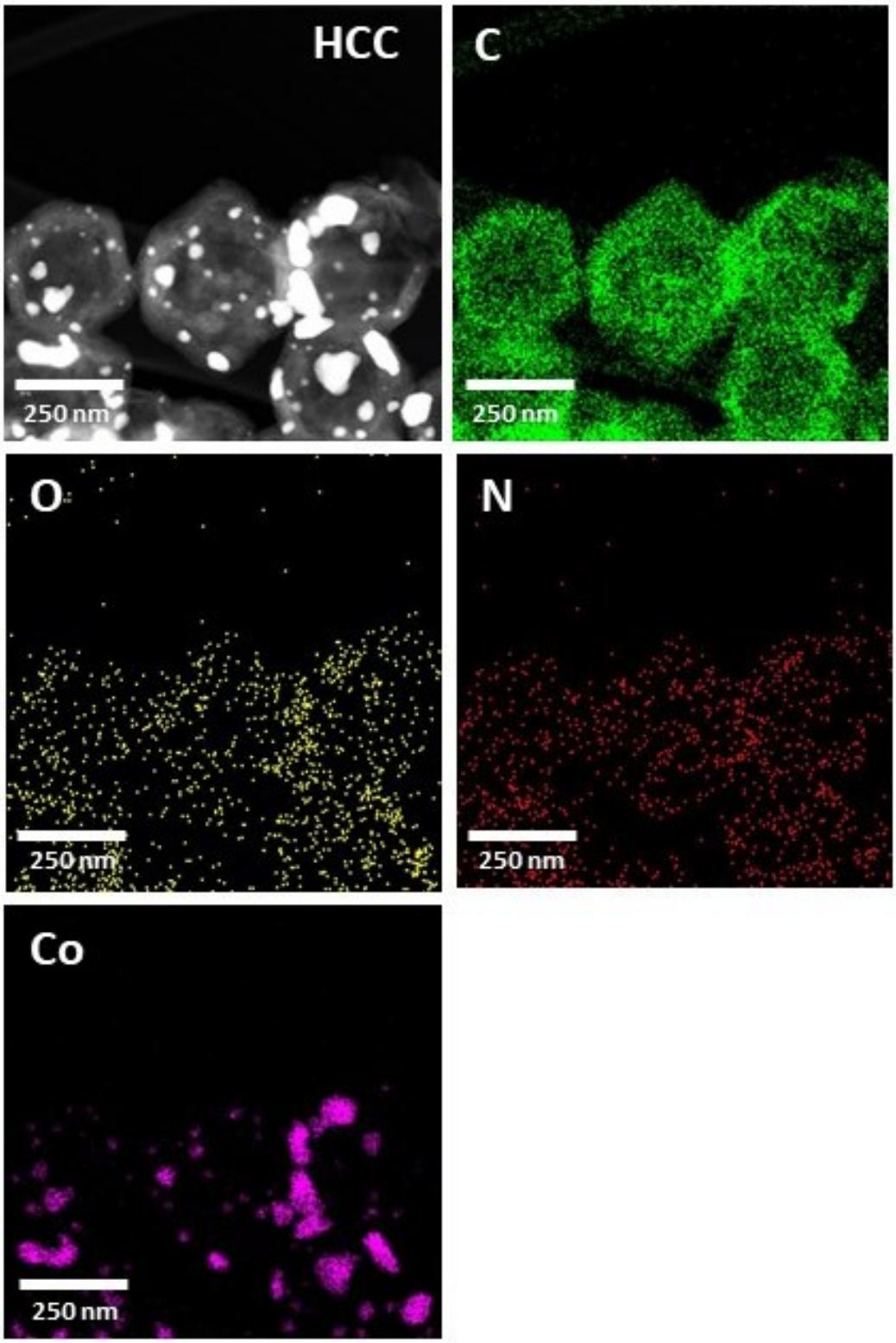

Figure 4-6. STEM annular dark field (ADF) images and EDX mapping of HCC.

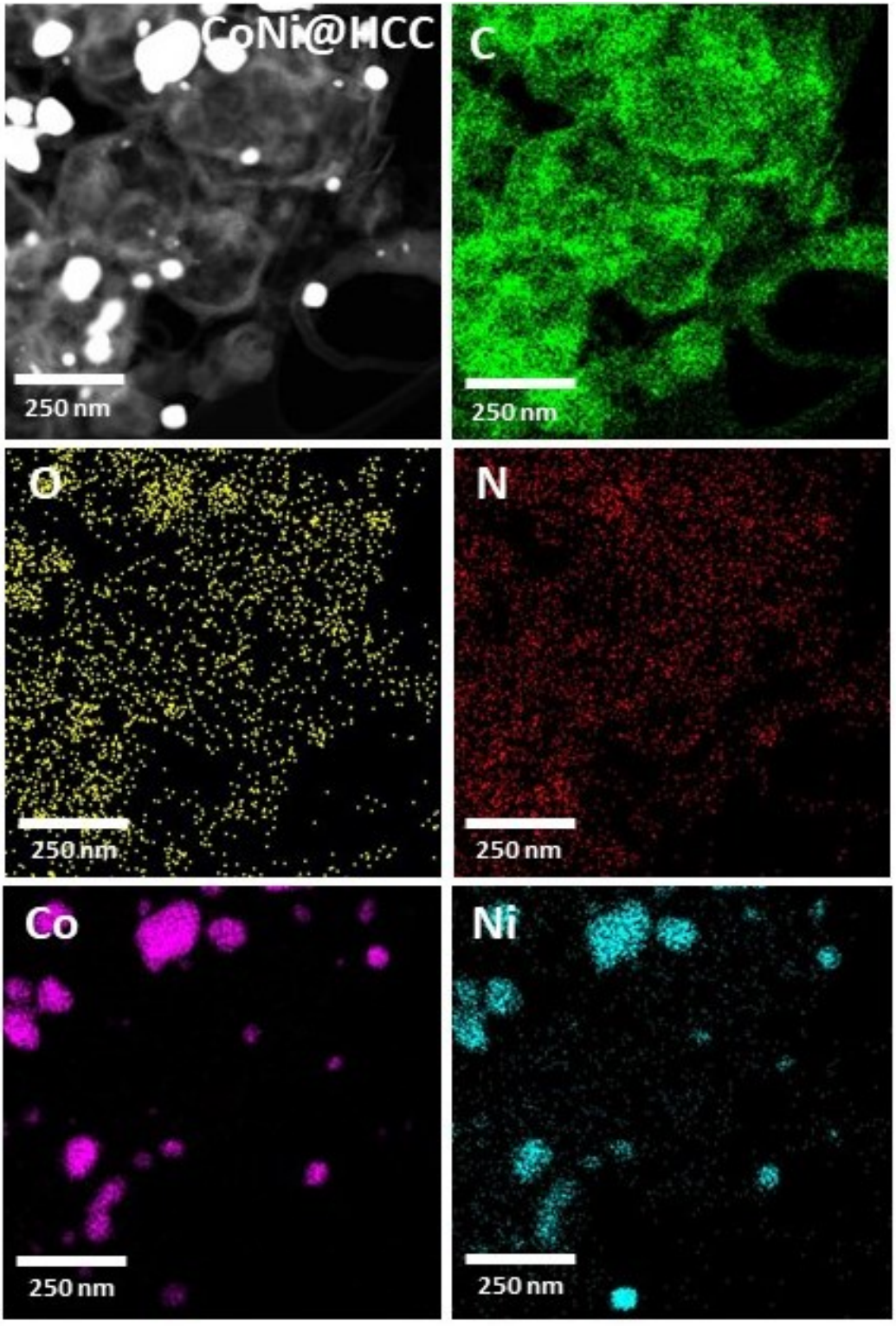

Figure 4-7. STEM annular dark field (ADF) images and EDX mapping of CoNi@HCC.

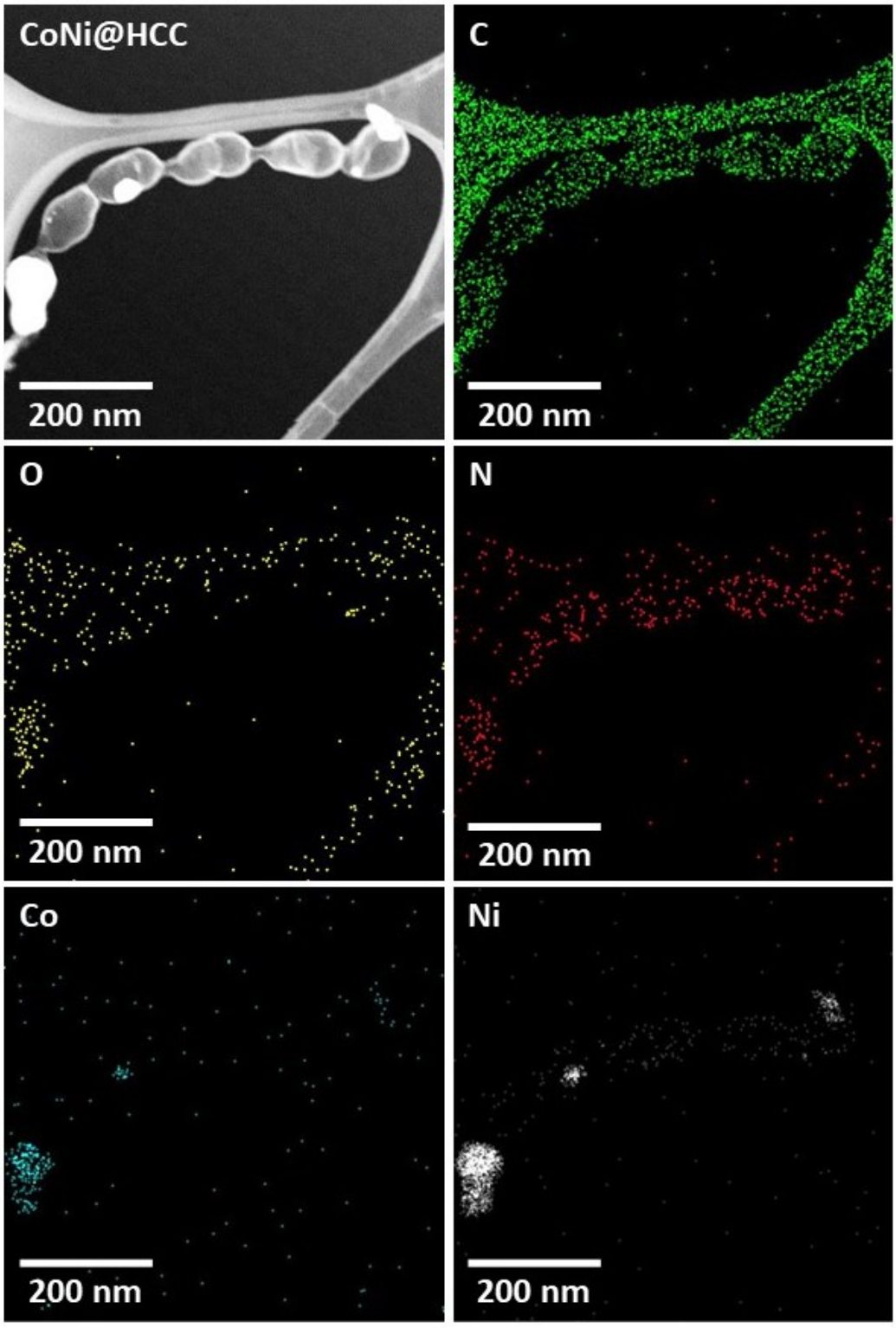

Figure 4-8. STEM annular dark field (ADF) images and EDX mapping of a hollow carbon nanostructure in CoNi@HCC.

PXRD was used to interrogate the identity of the nanoparticles. For HCC, reflections are noted at 2θ equal to 44.3˚, 51.6˚, and 75.9˚, which is consistent with the (111), (200), and (220) planes of metallic cobalt (Figure 4-9).[44] A reflection corresponding to graphite (002) plane is also present indicating the carbon shells possess some graphitic content.[45] Consistent with the PXRD analysis, HRTEM of HCC shows clear indication of 3.8 Å and 2.1 Å lattice fringes that correspond to the (002) planes of graphite and the (111) planes of metallic Co , respectively (Figure 4-10). Turning attention to the PXRD analysis of CoNi@HCC, reflections appear at 2θ of 44.3˚, 51.6˚, and 76.0˚. These peaks are shifted slightly relative to those for HCC and suggest the formation of a CoNi alloy, as shown in the magnified PXRD patterns (Figure 4-11 to 4-13).[39] d-Spacings of 3.8 Å and 2.2 Å are observed in the HRTEM of CoNi@HCC as well, which is consistent with the PXRD pattern (Figure 4-14).

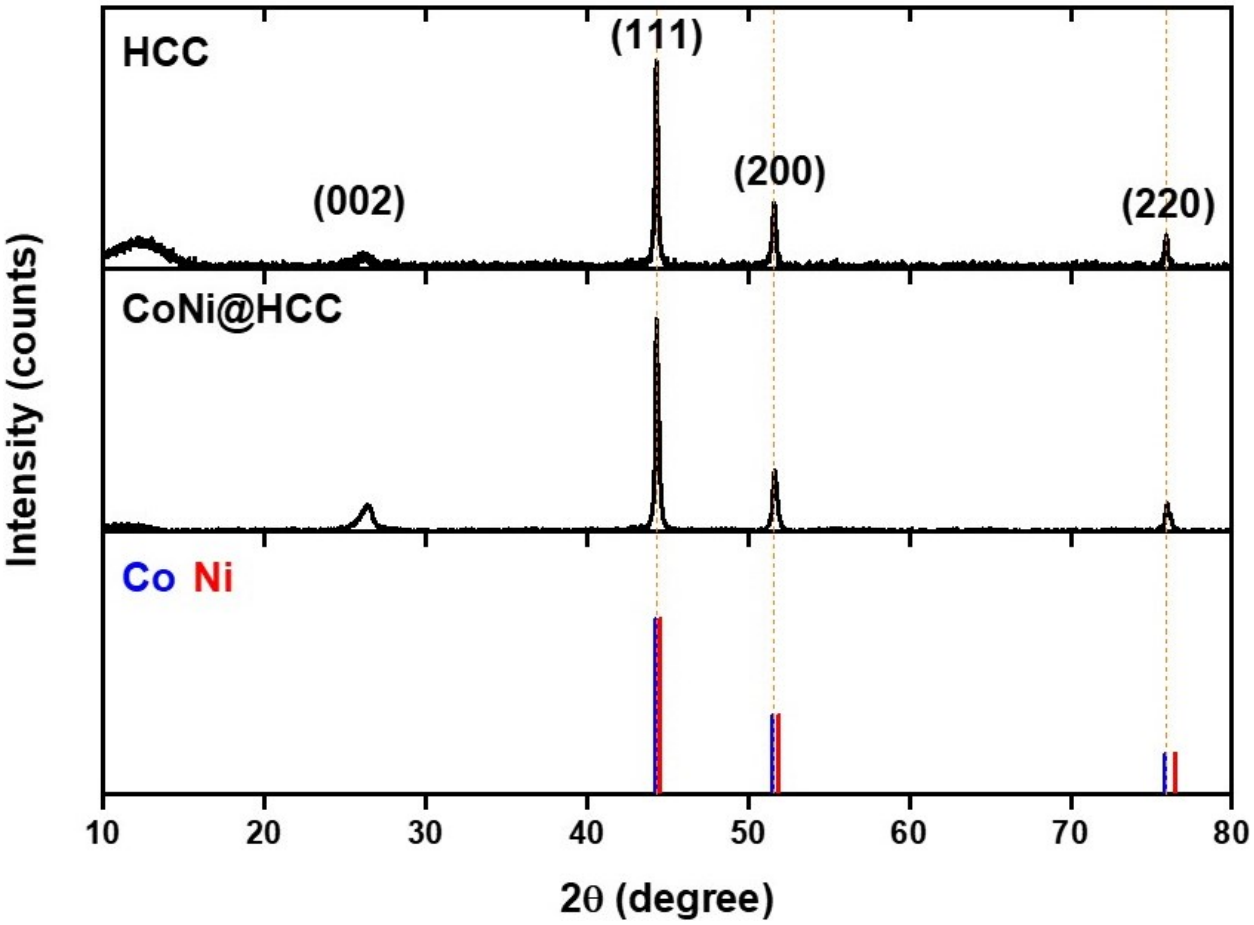

Figure 4-9. PXRD patterns of CoNi@HCC and reference face centered cubic Co (JCPDS no. 15-0806) and Ni (JCPDS no. 04-0850).[44, 46-48]

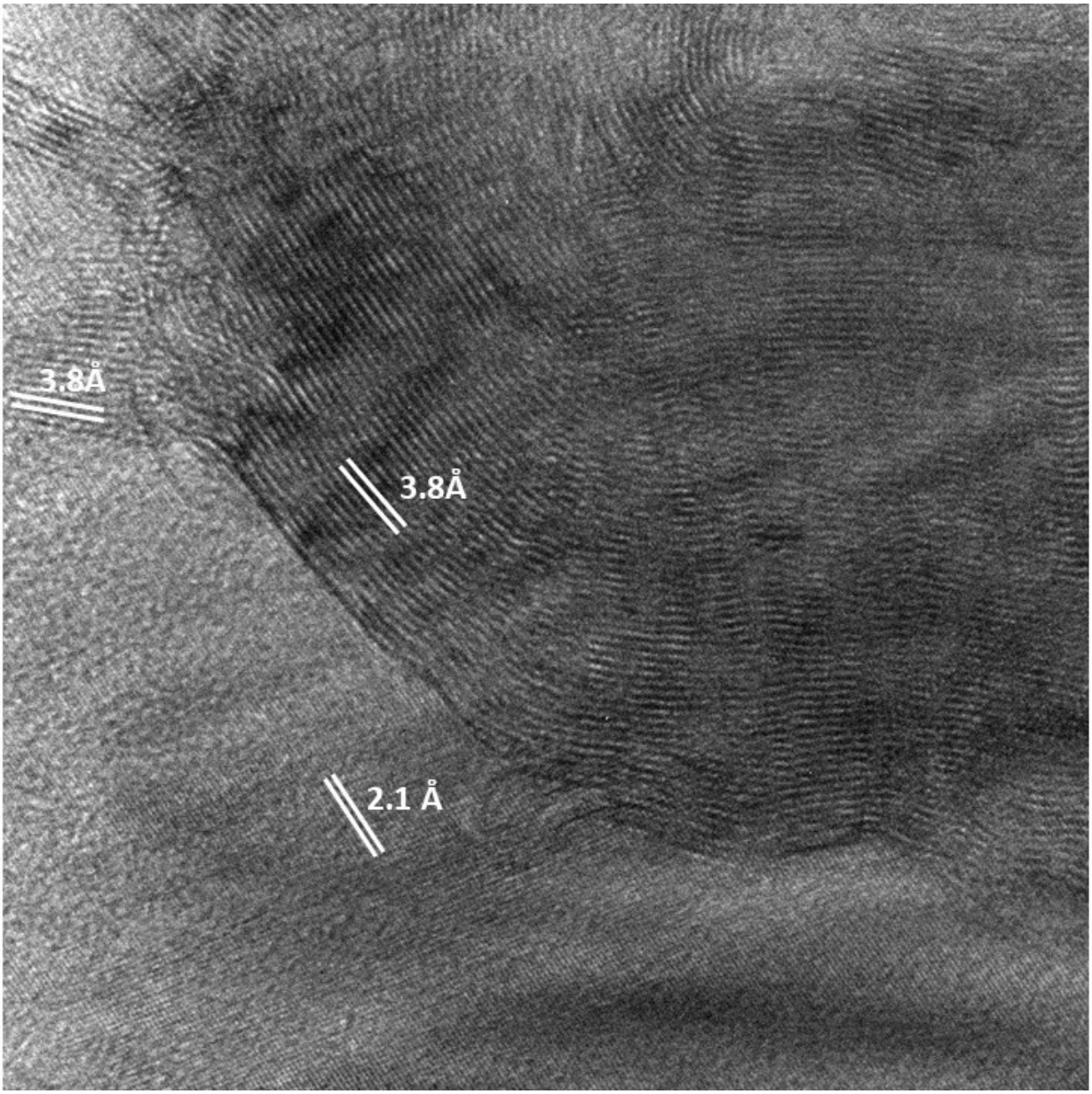

Figure 4-10. HRTEM of HCC showing d-spacings of 3.8 Å and 2.1 Å.

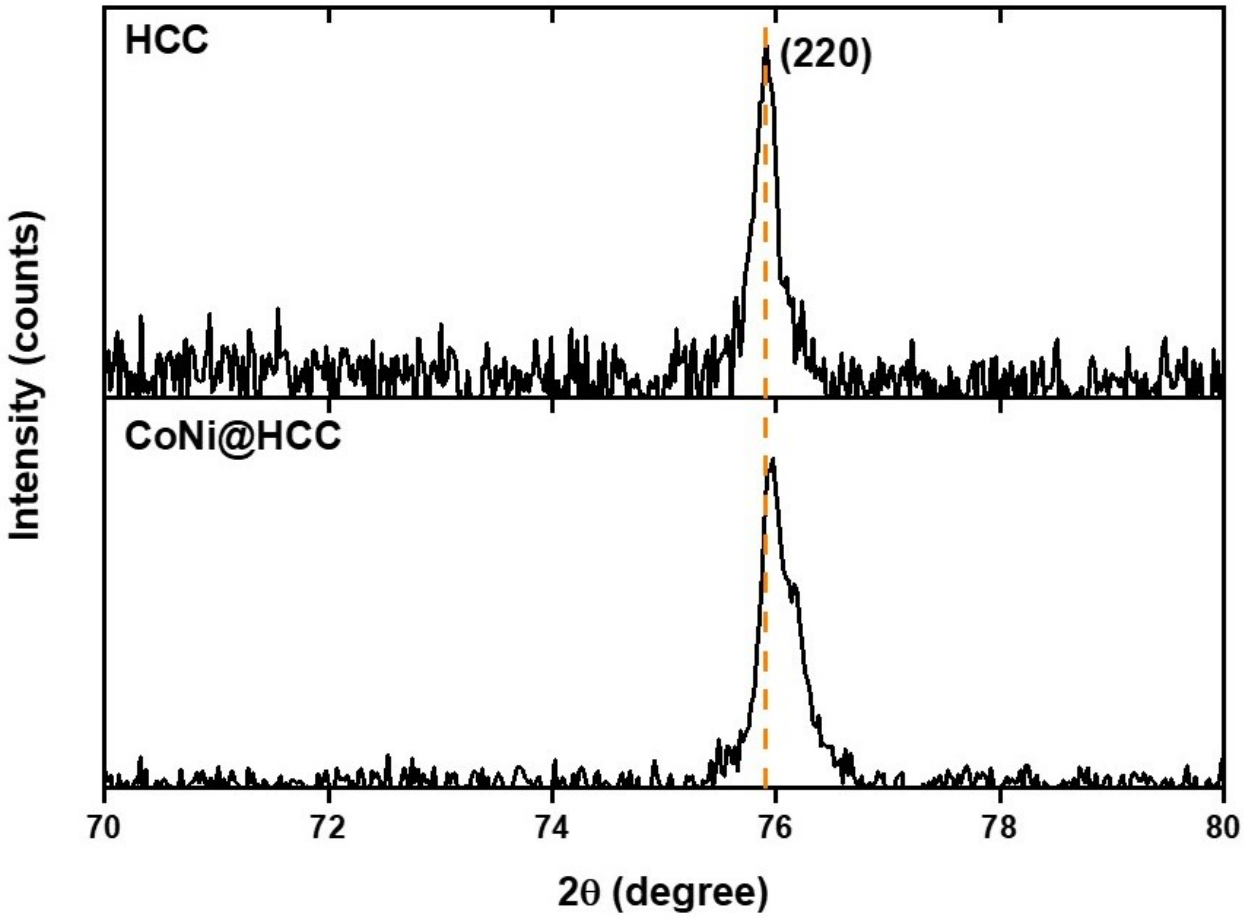

Figure 4-11. Magnified (220) peak from PXRD for HCC and CoNi@HCC.

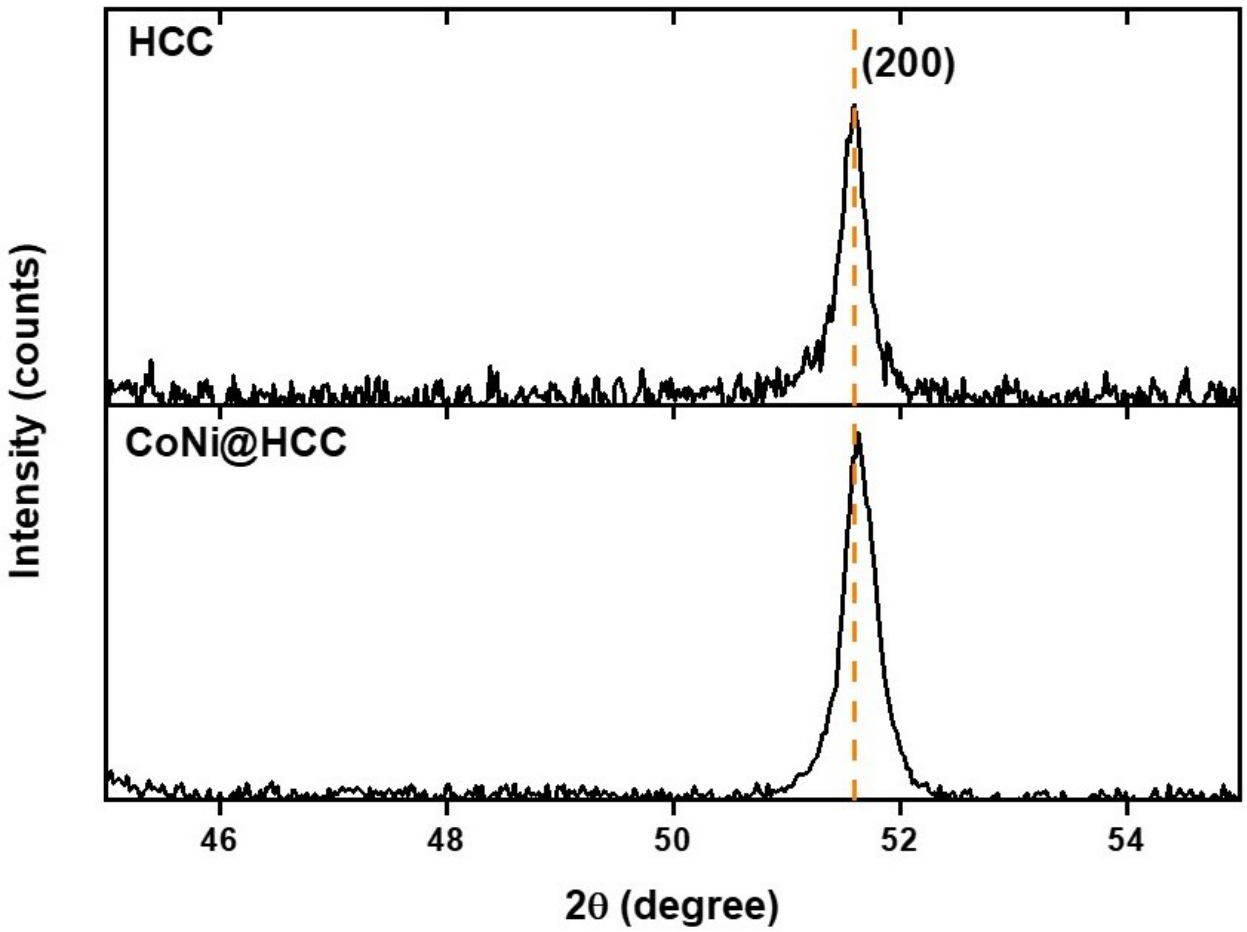

Figure 4-12. Magnified (200) peak from PXRD for HCC and CoNi@HCC.

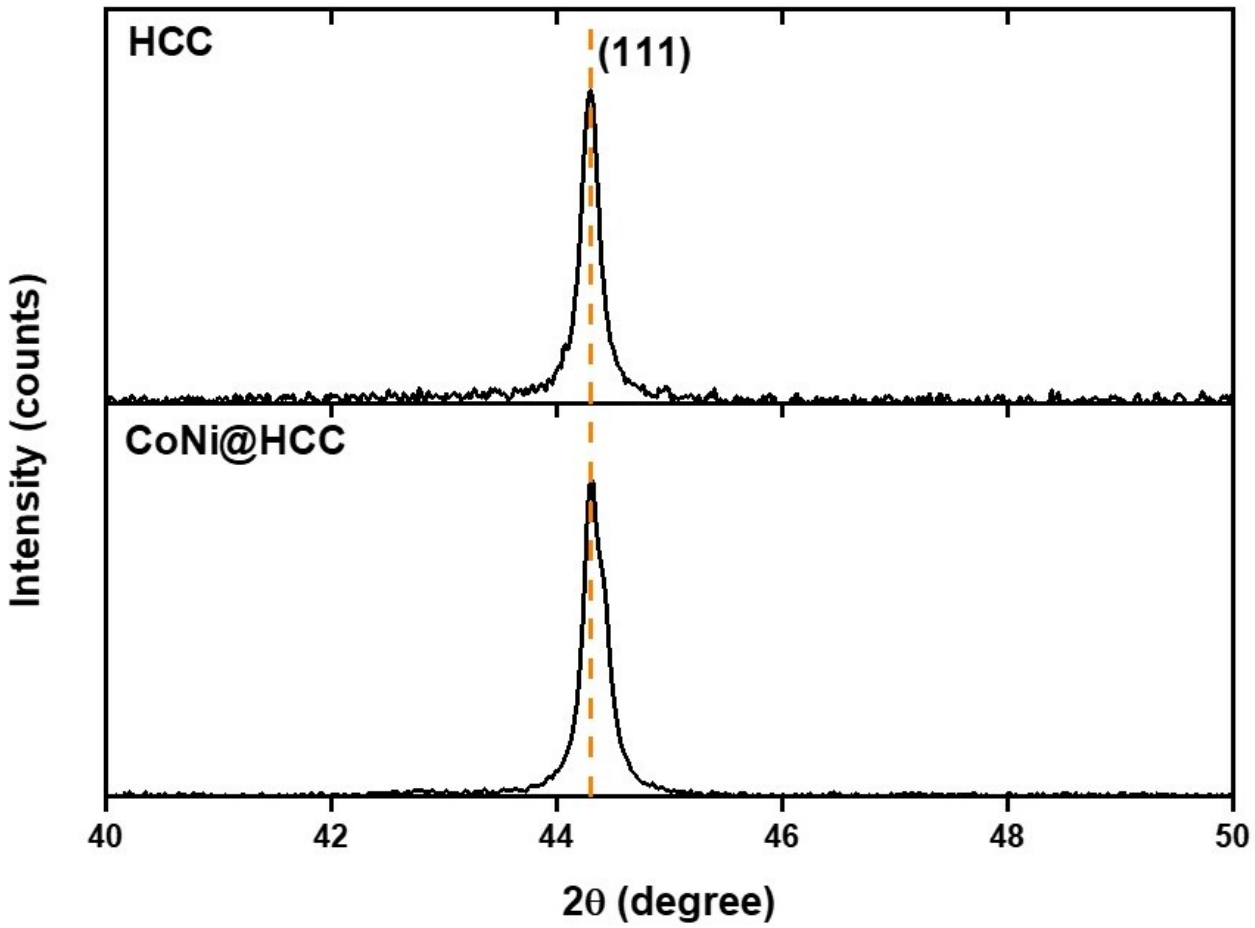

Figure 4-13. Magnified (111) peak from PXRD for HCC and CoNi@HCC.

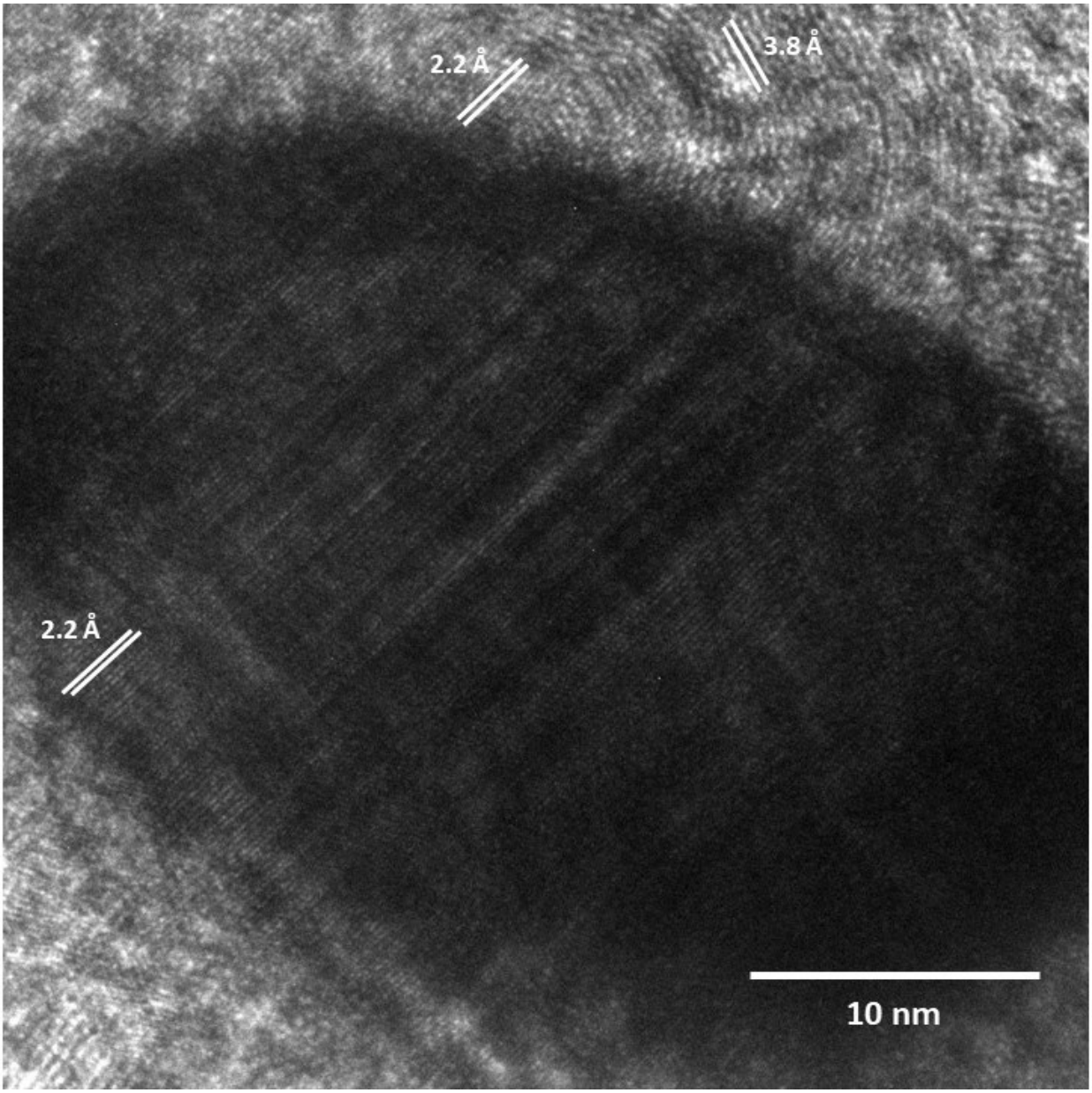

Figure 4-14. HRTEM of CoNi@HCC showing d-spacings of of 3.8 Å AND 2.2 Å.

To gain insight into the composition and speciation (i.e., metal oxidation state) of HCC and CoNi@HCC, XP spectroscopy was employed. The survey XP spectrum of HCC (Figure 4-15) indicates that it is composed of C, O, N, and Co, in agreement with the EDX mapping (Figure 4-6 and 4-7). Deconvolution of the high resolution

N 1s spectrum for HCC indicates the presence of pyrrolic N (400.5 eV) and pyridinic N (399.0 eV) (Figure 4-16). The high resolution Co 2p spectrum was fitted using accepted literature parameters and reveals the emission is dominated by Co (II) (i.e., $2p_{3/2}$ = 781.1 eV) with a comparatively small contribution (i.e., 9.7 at%) from Co (0) (i.e., $2p_{3/2}$ = 778.4 eV).[41] This is consistent with the presence of metallic Co peaks in the PXRD pattern. This suggests a large presence of amorphous CoO. The small Co (0) peak is consistent with the metallic Co peaks in the PXRD pattern.

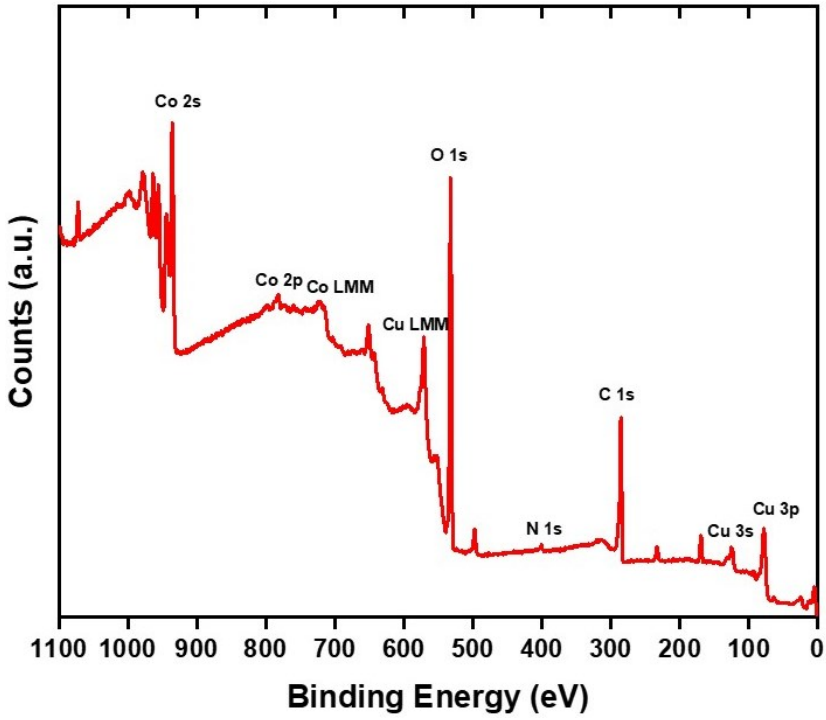

Figure 4-15. Survey XP spectrum of HCC.

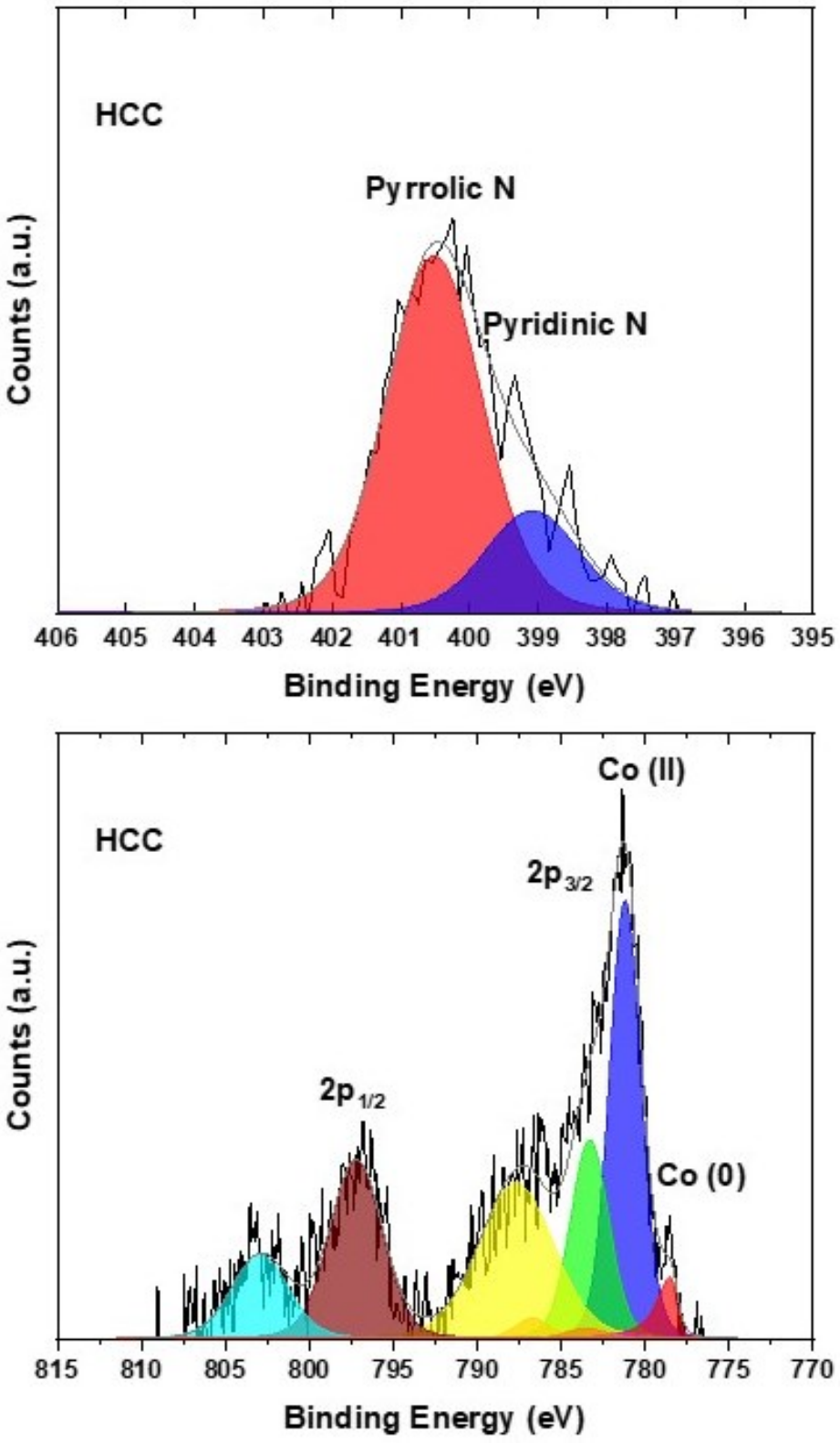

Figure 4-16. Deconvoluted XP spectra of N 1s and Co 2p for HCC.

Turning to the survey spectrum of CoNi@HCC (Figure 4-17), as expected, and consistent with the EDX analysis, we note characteristic emissions from C, O, N, Co, and Ni. The relative amount of C in CoNi@HCC (81.7 at%) is substantially higher than C in HCC (54.65 at%, Table 4-1). This difference is proposed to be the result of the formation of the new hollow nanostructures in CoNi@HCC, which were identified in the TEM imaging (vide supra). The deconvoluted high resolution N 1s spectrum for CoNi@HCC (Figure 4-18) shows pyrrolic N at 400.9 eV and pyridinic N at 399.0 eV. The noted increase in the peak area arising from pyridinic N for CoNi@HCC relative to HCC suggests that the additional hollow carbon nanostructures are N-doped, which is consistent with the EDX mapping. The increase in observed binding energy of pyrrolic N (0.4 eV) can be attributed to its synergistic interaction with oxygen in CoO. The deconvoluted Co 2p spectrum shows $2p_{3/2}$ components arising from Co (II) at 780.7 eV and Co (0) at 778.4 eV (Figure 4-18), while the Ni 2p spectrum shows Ni (0) at 853.7 eV and Ni (II) at 854.8 eV. The marked increase in peak area for Co (0) when compared to equivalent analysis of the HCC, as well as the additional emission arising from Ni (0) combined with the EDX mapping and PXRD patterns, are consistent with the formation of CoNi alloy NPs. The decrease in binding energy of Co (II) $2p_{3/2}$ peak (0.4 eV) may result from the synergistic interactions between the oxygen in CoO NPs and the pyrrolic N, which is consistent with the change in the binding energy of pyrrolic N.

The presence of $^{+}$N-O^{-} at 403.7 eV also support this explanation. Graphitic N was also observed at 402.2 eV, which corresponds to the literature value.[49]

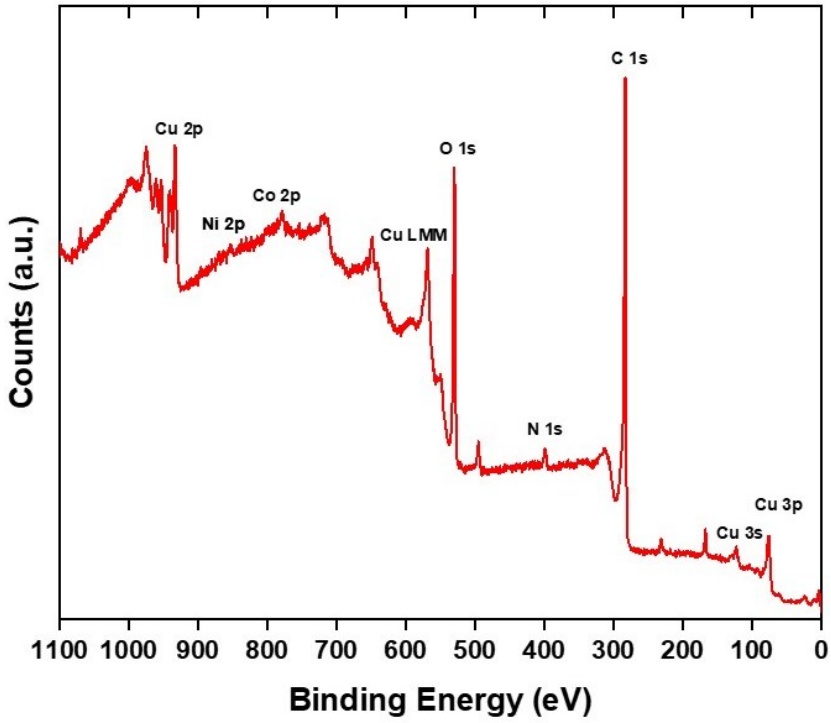

Figure 4-17. Survey XP spectrum of CoNi@HCC.

Table 4-1. Relative atomic percentage from XP survey spectra.

	C	N	O	Co	Ni
HCC	54.65%	1.07%	43.8%	0.48%	N/A
CoNi@HCC	81.70%	1.96%	16.17%	0.14%	0.03%

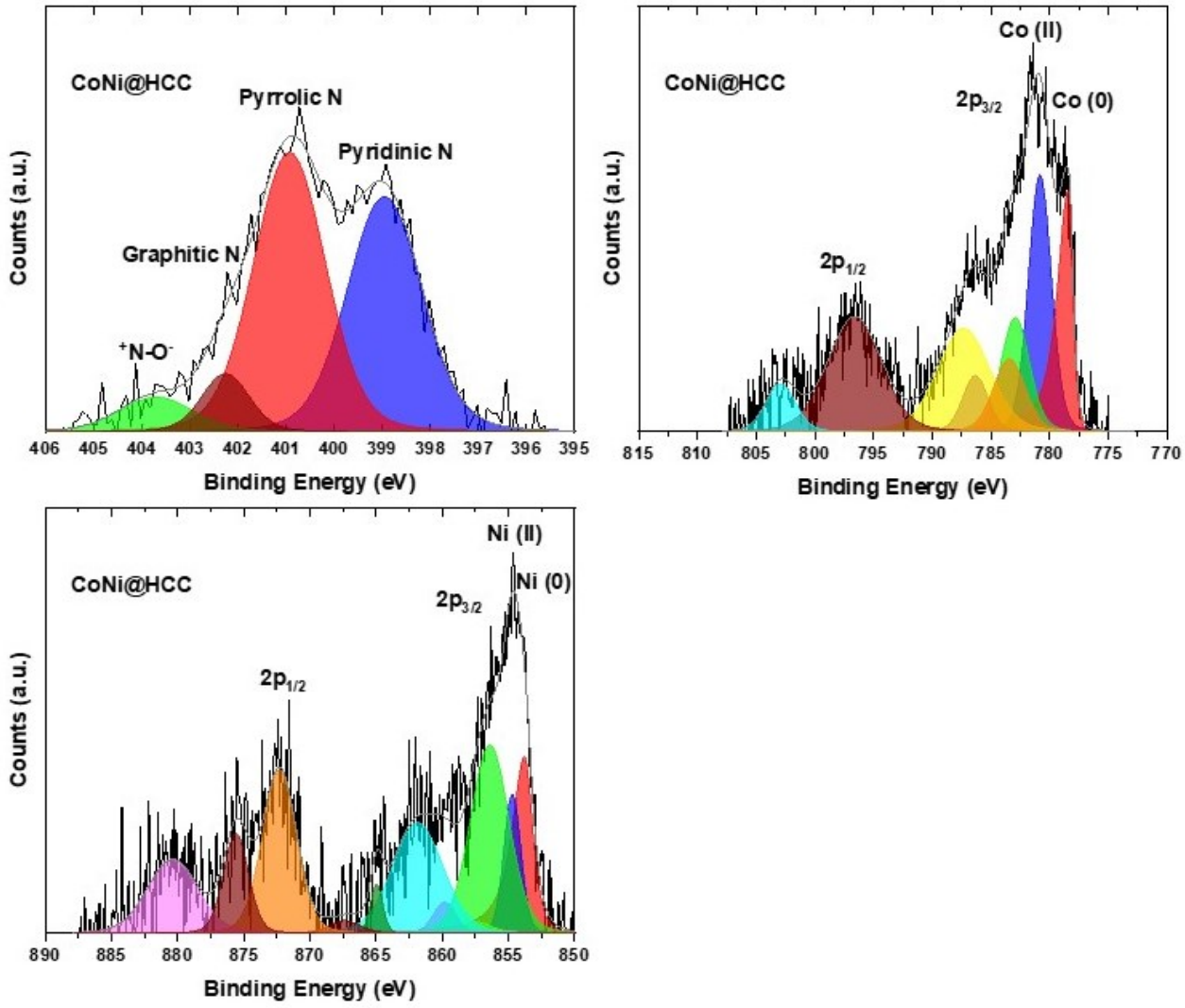

Figure 4-18. Deconvoluted XP spectra of N 1s, Co 2p, and Ni 2p for CoNi@HCC.

Linear sweep voltammetry (LSV) was used to evaluate the catalytic activity for HCC and CoNi@HCC (Figure 4-19) with Pt-Ru as a benchmark catalyst. In this work, onset potential is defined as the potential at which the measured current density reaches 10 mA cm^{-2}. Maximum current density is measured at – 0.5 V and 1 V (vs. Hg/HgO) for ORR and OER, respectively. For ORR, the onset potential and maximum current density of HCC were measured as – 0.165 V vs. Hg/HgO and

192.3 mA cm^{-2}, respectively. After introducing CoNi NPs to form CoNi@HCC, there was an improvement in ORR performance with an onset potential of – 0.116 V vs. Hg/HgO and a maximum current density of 290.8 mA cm^{-2}. Putting this improvement into context, the onset potential of CoNi@HCC is comparable to Pt-Ru (– 0.102 V vs. Hg/HgO) and its maximum current density surpasses that of Pt-Ru (206.5 mA cm^{-2}).

Turning our attention to OER performance, CoNi@HCC showed an onset potential of 0.697 V (vs. Hg/HgO) which is superior to HCC (0.794 V vs. Hg/HgO) and approaches that of Pt-Ru (0.567 V vs. Hg/HgO). The maximum current density for CoNi@HCC was measured at 307.8 mA cm^{-2}, which is higher than the values for both HCC (250.1 mA cm^{-2}) and Pt-Ru (157.3 mA cm^{-2}). These metrics demonstrate the promising bifunctional catalytic activity of CoNi@HCC for ORR and OER. The enhanced catalytic activity can be attributed to the presence and activity of CoNi alloy NPs.[50-52] In addition, pyridinic N has been suggested to facilitate ORR.[53-55] Therefore, the possible contributions of the higher concentration of carbon nanomaterials containing pyridinic N to the CoNi@HCC catalytic activity cannot be discounted. Finally, the synergistic effect between CoO and pyrrolic N as evidenced by XPS may also play a role.[31]

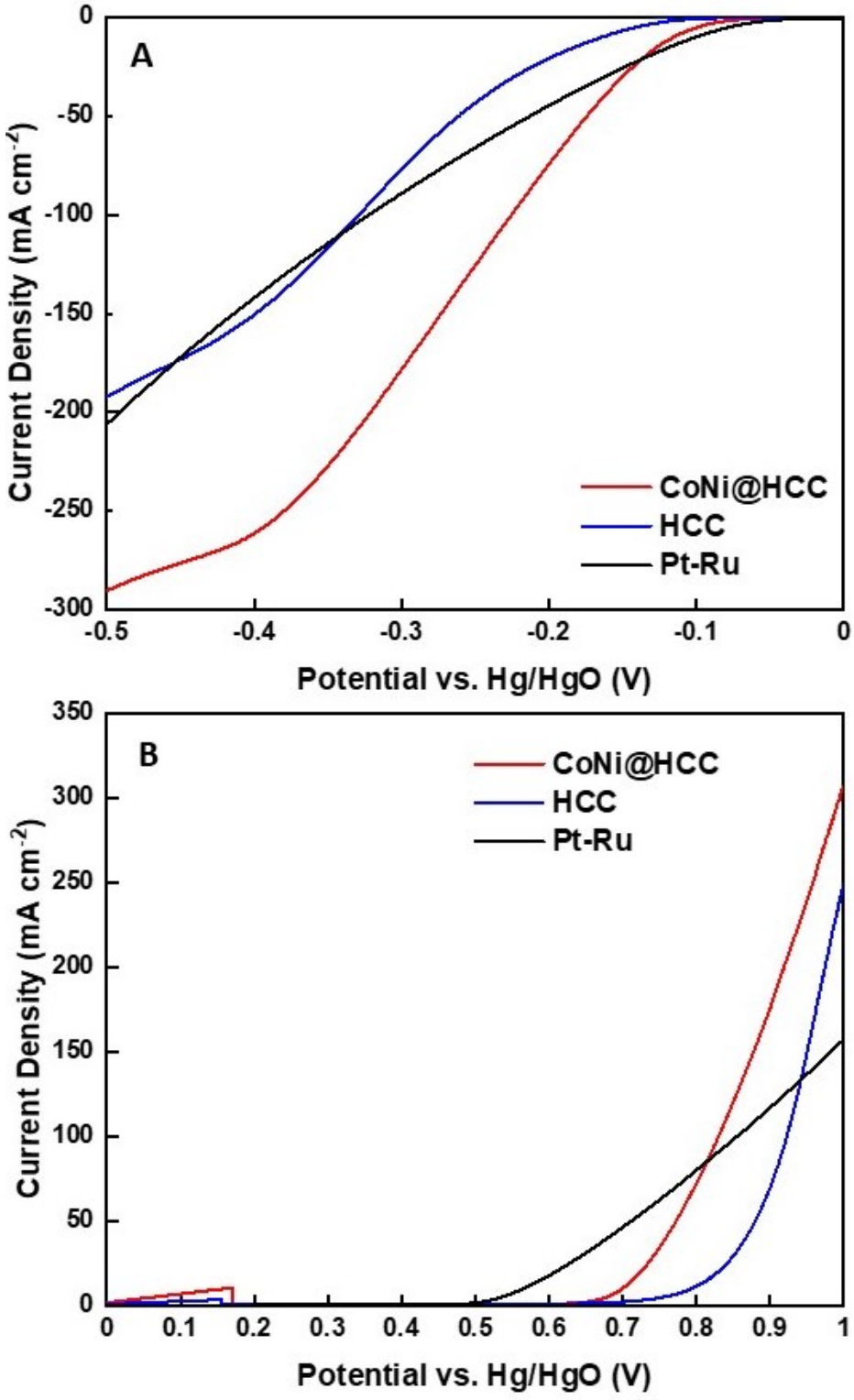

Figure 4-19. LSV plots of CoNi@HCC, HCC, and Pt-Ru in the potential windows of (A) ORR and (B) OER.

To further explore the activity of the HCC and CoNi@HCC catalysts, they were incorporated into prototype Zn-air batteries and galvanostatic rate tests were performed; the data is summarized in Table 4-2. Figure 4-20A clearly shows that batteries incorporating CoNi@HCC exhibit high discharge potentials of 1.25 V and 1.21 V at 10 mA cm^{-2} and 20 mA cm^{-2}, respectively. These values are comparable to Pt-Ru discharge potentials obtained under identical conditions (i.e., 1.25 and 1.20 V at 10 and 20 mA cm^{-2}, respectively). In contrast, batteries with HCC only displayed lower discharge potentials of 1.15 and 1.09 V at the same current densities. CoNi@HCC also demonstrated low charging potentials of 2.00 and 2.04 V at 10 and 20 mA cm^{-2}, respectively. These metrics are lower than what is observed for both HCC and Pt-Ru. The rate tests demonstrate that CoNi@HCC exhibits excellent bifunctional catalytic activity, consistent with the LSV results. The polarization curves and the associated power density curves are shown in Figure 4-20B. The cell discharge potentials for CoNi@HCC are comparable to Pt-Ru for current densities up to ~50 mA cm^{-2} and are significantly higher than Pt-Ru from ~80 to 350 mA cm^{-2}. CoNi@HCC has a peak power density of 159.6 mW cm^{-2} at 257.2 mA cm^{-2}, which is higher than the peak power densities for both HCC (76.2 mW cm^{-2} at 182.6 mA cm^{-2}) and Pt-Ru (120.2 mW cm^{-2} at 211.83 mA cm^{-2}). These observations show that CoNi@HCC has impressive performance in prototype batteries.

Table 4-2. Battery performance for catalysts of interest.

	Discharge potential (V) @ 10 mA cm^{-2}	Discharge potential (V) @ 20 mA cm^{-2}	Charging potential (V) @ 10 mA cm^{-2}	Charging potential (V) @ 20 mA cm^{-2}	Peak Power Density (mW cm^{-2})
HCC	1.15	1.09	2.06	2.11	76.2
CoNi@HCC	1.25	1.21	2.00	2.04	159.6
Pt-Ru	1.25	1.20	2.02	2.08	120.2

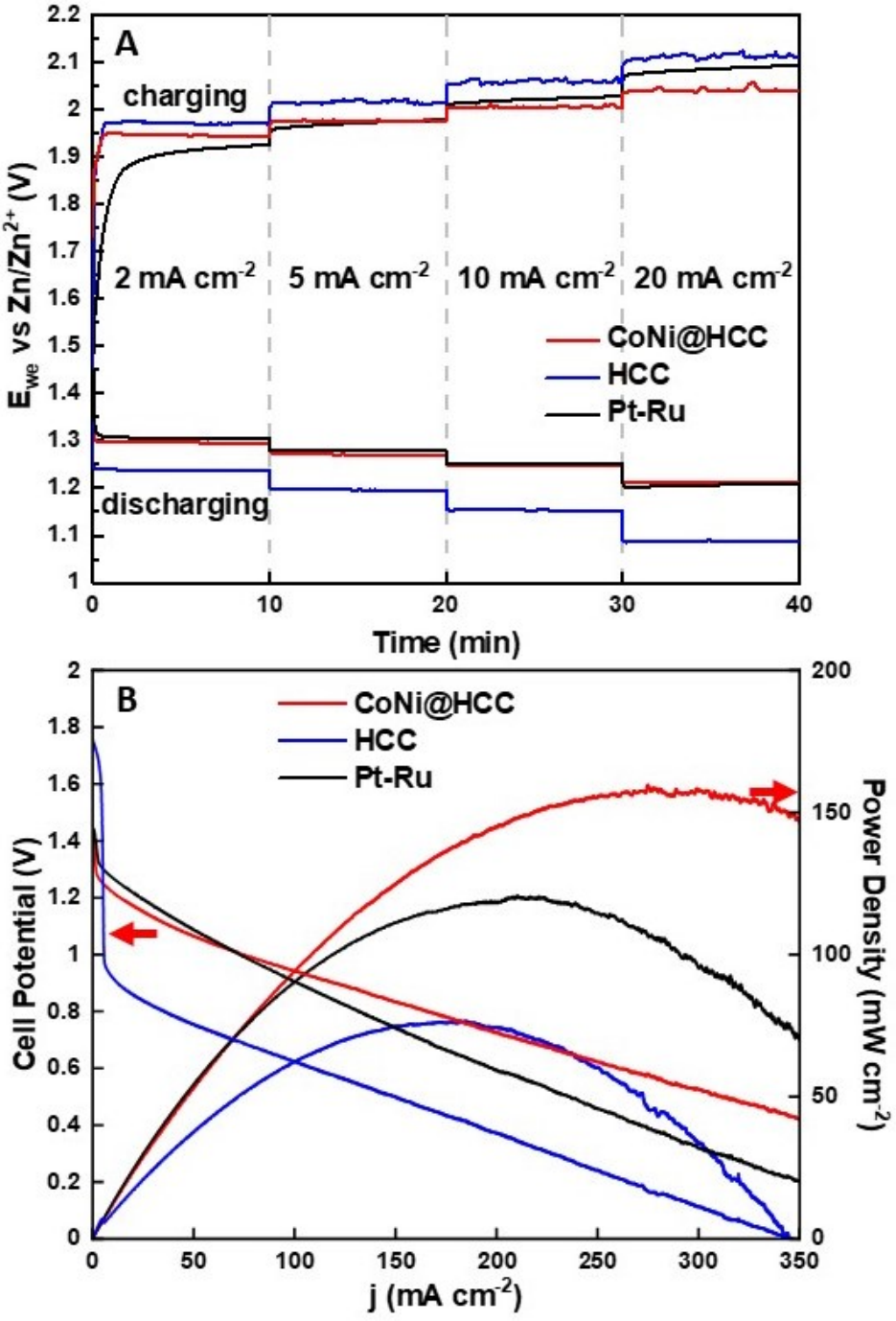

Figure 4-20. (A) Galvanostatic rate tests and (B) polarization and power density curves for CoNi@HCC, HCC, and Pt-Ru.

Discharge/charge cycling was performed to evaluate the durability and long term performance of the catalysts. CoNi@HCC and Pt-Ru were both cycled bifunctionally at 10 mA cm^{-2}. During the first cycle, CoNi@HCC exhibited a discharge potential of 1.22 V and charge potential of 2.08 V, corresponding to a battery efficiency of 58.7%. After 90 h of cycling (180 cycles), the discharge potential decreased to 1.15 V while the charge potential remained unchanged (Figure 4-21A). This corresponds to an efficiency of 55.3%. In other words, CoNi@HCC only experienced a 3.4% drop in efficiency after 90 h of bifunctional cycling, which demonstrates the long term stability of the catalyst. In contrast, Pt-Ru had an initial discharge potential of 1.17 V and a charge potential of 2.08 V during the first cycle, which corresponds to an efficiency of 56.2%. After just 60 h of cycling, the discharge potential plummeted to 1.01 V and the charge potential increased to 2.42 V (Figure 4-21B). This corresponds to a low battery efficiency of 41.7% (14.5% drop), indicating the poor stability of the Pt-Ru catalyst. Note that there is some fluctuation in the charge/discharge potentials during cycling of CoNi@HCC. This is due to O_2 bubbles accumulating on (during OER) and releasing from the air electrode. The performance appears to degrade during bubble formation, because of partial coverage of the air electrode, but is restored when the bubbles are released.

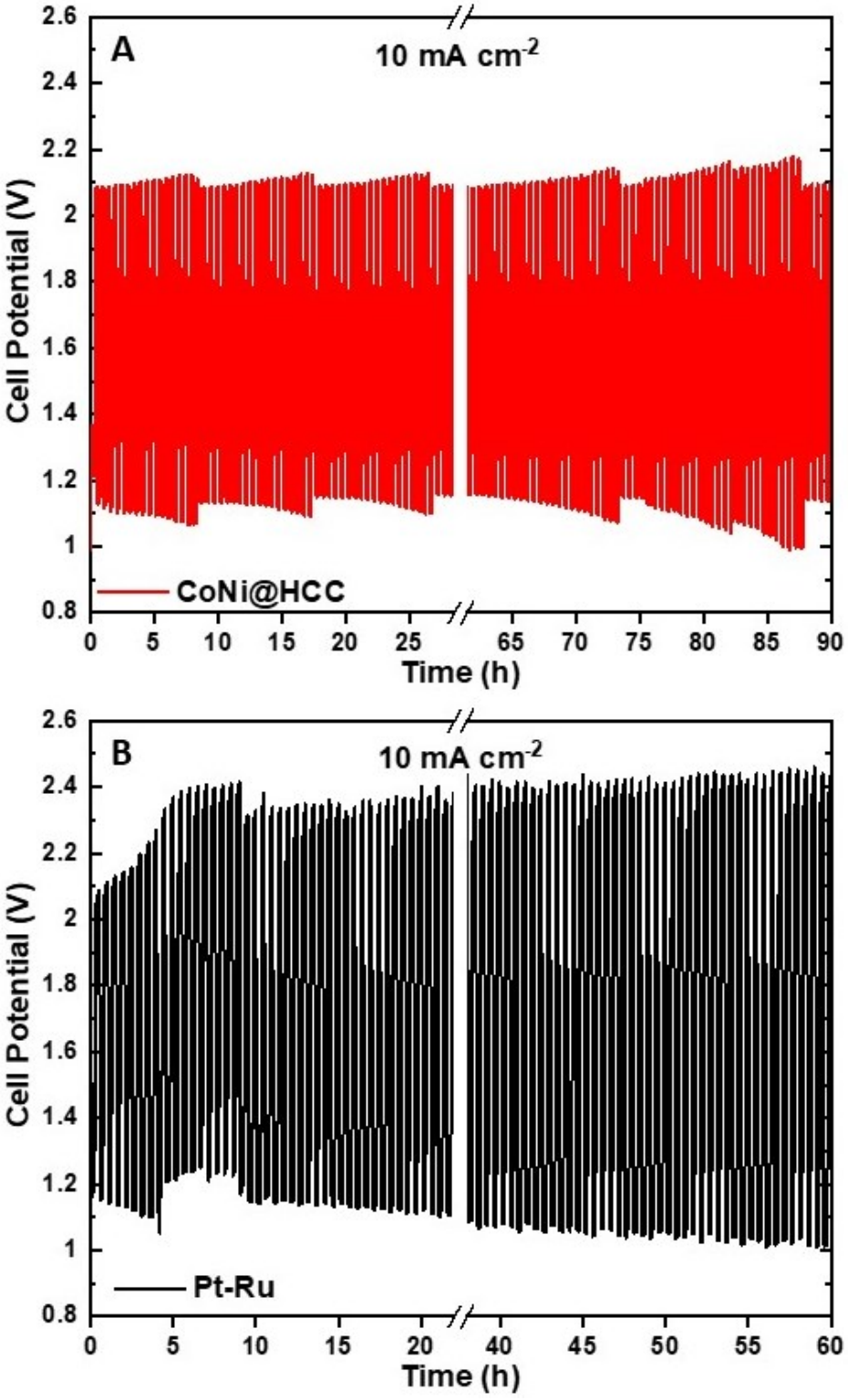

Figure 4-21. Cell potential of prototype Zn-air batteries during bifunctional cycling for batteries with (A) CoNi@HCC catalysts and (B) Pt-Ru catalysts.

4.4 Conclusions

CoNi nanoparticle decorated hollow carbon cubes (CoNi@HCC) were successfully synthesized with ZIF-67 as a sacrificial template, utilizing its thermal instability. CoNi@HCC exhibited excellent bifunctional catalytic activity for both ORR and OER, outperforming 30% Pt and 15% RuO_2 on carbon black. A battery prepared with an air electrode with CoNi@HCC as the electrocatalyst demonstrated a peak power density of 159.6 mW cm^{-2}, which was higher than that for Pt-Ru. During bifunctional cycling, the battery efficiency decreased by a small amount from 58.7% at the first cycle to 55.3% after 90 h (180 cycles), indicating its promising durability.

4.5 References

(1) Figgener, J.; Stenzel, P.; Kairies, K. P.; Linssen, J.; Haberschusz, D.; Wessels, O.; Angenendt, G.; Robinius, M.; Stolten, D.; Sauer, D. U. *J. Energy Storage* **2020**, *29*, 101153.
(2) Faessler, B. *Energies* **2021**, *14* (8), 2335.
(3) Lu, L. G.; Han, X. B.; Li, J. Q.; Hua, J. F.; Ouyang, M. G. *J. Power Sources* **2013**, *226*, 272-288.
(4) Manthiram, A. *ACS Central Sci.* **2017**, *3* (10), 1063-1069.
(5) Wanger, T. C. *Conserv. Lett.* **2011**, *4* (3), 202-206.
(6) Fan, E. S.; Li, L.; Wang, Z. P.; Lin, J.; Huang, Y. X.; Yao, Y.; Chen, R. J.; Wu, F. *Chem. Rev.* **2020**, *120* (14), 7020-7063.
(7) Chen, Y. Q.; Kang, Y. Q.; Zhao, Y.; Wang, L.; Liu, J. L.; Li, Y. X.; Liang, Z.; He, X. M.; Li, X.; Tavajohi, N.; Li, B. H. *J. Energy Chem.* **2021**, *59*, 83-99.
(8) Chen, Z. Y.; Xiong, R.; Lu, J. H.; Li, X. G. *Appl. Energ.* **2018**, *213*, 375-383.
(9) Zheng, H. F.; Han, X.; Guo, W. B.; Lin, L.; Xie, Q. S.; Liu, P. F.; He, W.; Wang, L. S.; Peng, D. L. *Mater. Today Energy* **2020**, *18*, 100518.

(10) Goh, F. W. T.; Liu, Z. L.; Hor, T. S. A.; Zhang, J.; Ge, X. M.; Zong, Y.; Yu, A. S.; Khoo, W. *J. Electrochem. Soc.* **2014**, *161* (14), A2080-A2086.
(11) Zhang, J.; Zhou, Q. X.; Tang, Y. W.; Zhang, L.; Li, Y. G. *Chem. Sci.* **2019**, *10* (39), 8924-8929.
(12) Gu, P.; Zheng, M. B.; Zhao, Q. X.; Xiao, X.; Xue, H. G.; Pang, H. *J. Mater. Chem. A* **2017**, *5* (17), 7651-7666.
(13) Li, Y. G.; Dai, H. J. *Chem. Soc. Rev.* **2014**, *43* (15), 5257-5275.
(14) Fu, J.; Cano, Z. P.; Park, M. G.; Yu, A. P.; Fowler, M.; Chen, Z. W. *Adv. Mater.* **2017**, *29* (7), 1604685.
(15) Mainar, A. R.; Iruin, E.; Colmenares, L. C.; Kvasha, A.; de Meatza, I.; Bengoechea, M.; Leonet, O.; Boyano, I.; Zhang, Z. C.; Blazquez, J. A. *J. Energy Storage* **2018**, *15*, 304-328.
(16) Chen, P.; Zhang, K. Y.; Tang, D. J.; Liu, W. L.; Meng, F. C.; Huang, Q. W.; Liu, J. H. *Front. Chem.* **2020**, *8*, 372.
(17) Lee, J. S.; Kim, S. T.; Cao, R.; Choi, N. S.; Liu, M.; Lee, K. T.; Cho, J. *Adv. Energy Mater.* **2011**, *1* (1), 34-50.
(18) Suen, N. T.; Hung, S. F.; Quan, Q.; Zhang, N.; Xu, Y. J.; Chen, H. M. *Chem. Soc. Rev.* **2017**, *46* (2), 337-365.
(19) Kulkarni, A.; Siahrostami, S.; Patel, A.; Norskov, J. K. *Chem. Rev.* **2018**, *118* (5), 2302-2312.
(20) Favaro, M.; Valero-Vidal, C.; Eichhorn, J.; Toma, F. M.; Ross, P. N.; Yano, J.; Liu, Z.; Crumlin, E. J. *J. Mater. Chem. A* **2017**, *5* (23), 11634-11643.
(21) Tenkortenaar, M. V.; Vente, J. F.; Ijdo, D. J. W.; Muller, S.; Kotz, R. *J. Power Sources* **1995**, *56* (1), 51-60.
(22) Petrykin, V.; Macounova, K.; Shlyakhtin, O. A.; Krtil, P. *Angew. Chem. Int. Edit.* **2010**, *49* (28), 4813-4815.
(23) Labata, M. F.; Li, G. F.; Ocon, J.; Chuang, P. Y. A. *J. Power Sources* **2021**, *487*, 229356.
(24) Liang, H. W.; Wu, Z. Y.; Chen, L. F.; Li, C.; Yu, S. H. *Nano Energy* **2015**, *11*, 366-376.
(25) Zhang, J. T.; Zhao, Z. H.; Xia, Z. H.; Dai, L. M. *Nat. Nanotechnol.* **2015**, *10* (5), 444-452.
(26) Patra, S.; Choudhary, R.; Roy, E.; Madhuri, R.; Sharma, P. K. *Nano Energy* **2016**, *30*, 118-129.
(27) Hadidi, L.; Davari, E.; Iqbal, M.; Purkait, T. K.; Ivey, D. G.; Veinot, J. G. C. *Nanoscale* **2015**, *7* (48), 20547-20556.
(28) Wang, M.; Zhang, C. T.; Meng, T.; Pu, Z. H.; Jin, H. H.; He, D. P.; Zhang, J. N.; Mu, S. C. *J. Power Sources* **2019**, *413*, 367-375.
(29) Wu, F. W.; Feng, B. M.; Li, W.; Liu, H.; Mei, Y. H.; Hu, W. H. *Int. J. Hydrogen Energ.* **2019**, *44* (48), 26387-26395.

(30) Ji, D. X.; Fan, L.; Tao, L.; Sun, Y. J.; Li, M. G.; Yang, G. R.; Tran, T. Q.; Ramakrishna, S.; Guo, S. J. *Angew. Chem. Int. Edit.* **2019**, *58* (39), 13840-13844.
(31) He, Y. J.; Aasen, D.; Yu, H. Y.; Labbe, M.; Ivey, D. G.; Veinot, J. G. C. *Nanoscale Adv.* **2020**, *2* (8), 3367-3374.
(32) Abedi, Z.; Leistenschneider, D.; Chen, W. X.; Ivey, D. G. *Batteries Supercaps* **2022**, *5* (2), e202100339.
(33) McDougall, A.; Abedi, Z.; Ivey, D. G. *J. Appl. Electrochem* **2022**, *52* (3), 437-459.
(34) Muthurasu, A.; Tiwari, A. P.; Chhetri, K.; Dahal, B.; Kim, H. Y. *Nano Energy* **2021**, *88*.
(35) Cheng, W. Z.; Liang, J. L.; Yin, H. B.; Wang, Y. J.; Yan, W. F.; Zhang, J. N. *Rare Metals* **2020**, *39* (7), 815-823.
(36) Li, J. T.; Meng, Z.; Brett, D. J. L.; Shearing, P. R.; Skipper, N. T.; Parkin, I. P.; Gadipelli, S. *ACS Appl. Mater. Inter.* **2020**, *12* (38), 42696-42703.
(37) Lashgari, S. M.; Yari, H.; Mahdavian, M.; Ramezanzadeh, B.; Bahlakeh, G.; Ramezanzadeh, M. *Corros. Sci.* **2021**, *178*, 109099.
(38) Liu, X. H.; Kang, J. J.; Wang, Y. Q.; Li, W.; Guo, H. L.; Xu, L.; Guo, X. H.; Zhou, F.; Jia, X. *Macromol. Rapid Comm.* **2018**, *39* (12), e1800160.
(39) Sheng, K.; Yi, Q. F.; Chen, A. L.; Wang, Y. B.; Yan, Y. H.; Nie, H. D.; Zhou, X. L. *ACS Appl. Mater. Inter.* **2021**, *13* (38), 45394-45405.
(40) Grosvenor, A. P.; Biesinger, M. C.; Smart, R. S.; McIntyre, N. S. *Surf. Sci.* **2006**, *600* (9), 1771-1779.
(41) Biesinger, M. C.; Payne, B. P.; Grosvenor, A. P.; Lau, L. W. M.; Gerson, A. R.; Smart, R. S. C. *Appl. Surf. Sci.* **2011**, *257* (7), 2717-2730.
(42) Xiong, M.; Clark, M. P.; Labbe, M.; Ivey, D. G. *J. Power Sources* **2018**, *393*, 108-118.
(43) Feng, J. M.; Li, Y. L.; Hou, F.; Zhong, X. H. *Mat. Sci. Eng. A-Struct.* **2008**, *473* (1-2), 238-243.
(44) Nam, K. M.; Shim, J. H.; Ki, H.; Choi, S. I.; Lee, G.; Jang, J. K.; Jo, Y.; Jung, M. H.; Song, H.; Park, J. T. *Angew. Chem. Int. Edit.* **2008**, *47* (49), 9504-9508.
(45) Jeong, H. K.; Lee, Y. P.; Lahaye, R. J. W. E.; Park, M. H.; An, K. H.; Kim, I. J.; Yang, C. W.; Park, C. Y.; Ruoff, R. S.; Lee, Y. H. *J. Am. Chem. Soc.* **2008**, *130* (4), 1362-1366.
(46) Jung, H. J.; Choi, M. Y. *J. Phys. Chem. C* **2014**, *118* (26), 14647-14654.
(47) Zhang, D. E.; Ni, X. M.; Zheng, H. G.; Li, Y.; Zhang, X. J.; Yang, Z. P. *Mater. Lett.* **2005**, *59* (16), 2011-2014.
(48) Garcia-Cerda, L. A.; Bernal-Ramos, K. M.; Montemayor, S. M.; Quevedo-Lopez, M. A.; Betancourt-Galindo, R.; Bueno-Baques, D. *J Nanomater* **2011**, *2011*, 162495.

(49) He, Y. J.; Aasen, D.; McDougall, A.; Yu, H. Y.; Labbe, M.; Ni, C. Y.; Milliken, S.; Ivey, D. G.; Veinot, J. G. C. *ChemElectroChem* **2021**, *8* (8), 1455-1463.
(50) Li, C. L.; Wu, M. C.; Liu, R. *Appl. Catal. B-Environ.* **2019**, *244*, 150-158.
(51) Xie, X. Y.; Shang, L.; Shi, R.; Waterhouse, G. I. N.; Zhao, J. Q.; Zhang, T. R. *Nanoscale* **2020**, *12* (24), 13129-13136.
(52) Li, J. M.; Kang, Y. M.; Wei, W. L.; Li, X.; Lei, Z. Q.; Liu, P. *Chem. Eng. J.* **2021**, *407*, 127961.
(53) Rauf, M.; Zhao, Y. D.; Wang, Y. C.; Zheng, Y. P.; Chen, C.; Yang, X. D.; Zhou, Z. Y.; Sun, S. G. *Electrochem. Commun.* **2016**, *73*, 71-74.
(54) Lv, Q.; Si, W. Y.; He, J. J.; Sun, L.; Zhang, C. F.; Wang, N.; Yang, Z.; Li, X. D.; Wang, X.; Deng, W. Q.; Long, Y. Z.; Huang, C. S.; Li, Y. L. *Nat. Commun.* **2018**, *9* (1), 3376.
(55) Ning, X. M.; Li, Y. H.; Ming, J. Y.; Wang, Q.; Wang, H. J.; Cao, Y. H.; Peng, F.; Yang, Y. H.; Yu, H. *Chem. Sci.* **2019**, *10* (6), 1589-1596.

Chapter 5: Conclusions and Future Work

5.1 Conclusions

Zn-air batteries are promising candidates for stationary energy storage owing to its high specific energy, low cost, and safe design.[1] Despite this promise, Zn-air technology is plagued by the sluggish kinetics of the oxygen reduction and evolution reactions (ORR and OER, respectively).[2] Traditional catalysts for these reactions contain precious metals whose scarcity and high cost limit the feasibility of Zn-air batteries.[3] The work presented in Chapters 2, 3 and 4 showcases a series of precious-metal free electrocatalysts for Zn-air batteries. These catalysts were designed and prepared by incorporating transition metal oxide nanoparticles (NPs) into high surface area carbon nanomaterials such as hollow mesoporous carbon nanospheres (HMC) and hollow carbon cubes (HCC).

Chapter 2 presents a hybrid catalyst, Mn_3O_4 nanoparticle decorated HMC (Mn_3O_4@HMC), that was prepared via straightforward sonication. Mn_3O_4 NPs were observed on the interior and exterior surfaces of the HMC using SEM and TEM. EDX and XPS analyses were utilized to identify the NPs as Mn_3O_4. The crystallinity of the hybrid, probed by PXRD, SAED, and HRTEM, is consistent with hausmannite Mn_3O_4 from literature.[4] The catalytic performance of Mn_3O_4@HMC was evaluated via LSV, indicating excellent ORR activity. Prototype Zn-air battery equipped with the hybrid demonstrated higher discharge potential and superior durability to Pt-Ru

(30% Pt and 15% RuO_2 on carbon black). This work was the first time HMC was utilized as a carbon support for transition metal oxide nanoparticles and serves as a proof of concept.

Chapter 3 expands the system in Chapter 2 to a large variety of transition metal oxides. Co_3O_4@HMC, $MnCo_2O_4$@HMC, 'CoFeMnO'@HMC, 'CoFeNiO'@HMC, and 'FeMnNiO'@HMC were synthesized via hydrothermal reactions and characterized thoroughly with SEM, TEM, EDX, XPS, and PXRD. Among the hybrids, Co_3O_4@HMC and $MnCo_2O_4$@HMC exhibited good ORR performance in LSV and galvanostatic rate tests, while the ternary metal oxide nanoparticle decorated HMC all displayed excellent OER activities. Interestingly, Co_3O_4@HMC also demonstrated improved OER performance, suggesting bifunctional catalytic activity. As a result, Co_3O_4@HMC was chosen for battery cycling and exhibited superior durability to Pt-Ru.

Chapter 4 steps away from HMC synthesized via hydrofluoric acid (HF) etching and introduces HCC prepared by thermal annealing. This novel annealing method utilizes the thermal instability of ZIF-67 and combines carbonization, template removal, and metal decoration into one single step, dramatically simplifying the synthesis of hollow carbon materials. The CoNi decorated HCC (CoNi@HCC) exhibited comparable ORR and OER catalytic activity compared to a Pt-Ru benchmark. Most importantly, the hybrid only experienced a small

efficiency loss (3.4%) after 90 h of bifunctional cycling, demonstrating good durability.

5.2 Future Projects

This thesis features a large selection of earth abundant, affordable, and efficient electrocatalysts for Zn-air batteries, as well as a new annealing method that produces hollow carbon nanostructures (Chapter 4). The catalysts are broadly applicable to alternative devices and the annealing method can be further explored. These applications are discussed in the following sections.

5.2.1 Fuel cells

The oxygen reduction reaction (ORR) and the associated challenges are not limited to Zn-air batteries; it is also essential to fuel cell operation.[5] Fuel cells are excellent candidates for portable energy conversion applications including automobiles and aircraft because of their high efficiency and reduced emissions.[6, 7] Similar to Zn-air batteries, fuel cells function by separating the oxidation of fuels (e.g., H_2 and methanol) into half-reactions including ORR.[8] Consequently, fuel cells also face challenges related to the sluggish kinetics of ORR. Chapters 2-4 present a variety of ORR catalysts which are also promising fuel cell catalysts and can be easily incorporated into these devices. Their potential application in fuel cells can be explored.

5.2.2 Water splitting

Just like ORR, oxygen evolution reaction (OER) is also utilized in other applications such as water splitting to generate hydrogen.[9] Hydrogen is a key component in the Haber-Bosch process and is critical to the global economy for fertilizer production.[10] Currently, 96% of global H_2 is produced via hydrocarbon reforming such as petroleum fraction, coal gasification, and steam reforming (natural gas), while only 4% of H_2 is generated via electrolysis.[11] Hydrogen production from hydrocarbon reforming is responsible for 500 Mt CO_2 emission (~1.4% of total CO_2 emission) per year.[12, 13] Water splitting via electrolysis powered by clean energy such as solar, wind, and nuclear produces green hydrogen, which is crucial for the world to reach net-zero carbon emission. As water splitting and Zn-air battery share OER as a half-reaction, catalysts are also required for water splitting to proceed efficiently.[14] The earth-abundant OER electrocatalysts discussed in this thesis can potentially be utilized in water splitting as well.

5.2.3 MOFs as sacrificial template

The annealing method discussed in Chapter 4 serves as a proof of concept for a one-step synthesis that achieves carbonization, hollow structure, and metal introduction. Thermally unstable alternatives in the metal organic framework (MOF) family should be explored as sacrificial templates. Owing to the high tailorability of

MOF composition, hollow carbon nanostructures with various dopants, metal alloy, and metal oxides can be synthesized and may yield interesting catalytic activity.

5.3 References

(1) Sun, W.; Wang, F.; Zhang, B.; Zhang, M. Y.; Kupers, V.; Ji, X.; Theile, C.; Bieker, P.; Xu, K.; Wang, C. S.; Winter, M. *Science* **2021**, *371* (6524), 46-51.
(2) Radenahmad, N.; Khezri, R.; Mohamad, A. A.; Nguyen, M. T.; Yonezawa, T.; Somwangthanaroj, A.; Kheawhom, S. *J. Alloy. Compd.* **2021**, *883*.
(3) Balamurugan, J.; Nguyen, T. T.; Kim, N. H.; Kim, D.; Lee, J. H. *Nano Energy* **2021**, *85*.
(4) Goncalves, P. R.; De Abreu, H. A.; Duarte, H. A. *J. Phys. Chem. C* **2018**, *122* (36), 20841-20849.
(5) Bing, Y. H.; Liu, H. S.; Zhang, L.; Ghosh, D.; Zhang, J. J. *Chem. Soc. Rev.* **2010**, *39* (6), 2184-2202.
(6) Wang, C. Y. *Chem. Rev.* **2004**, *104* (10), 4727-4765.
(7) Sharaf, O. Z.; Orhan, M. F. *Renew. Sust. Energ. Rev.* **2014**, *32*, 810-853.
(8) Mekhilef, S.; Saidur, R.; Safari, A. *Renew. Sust. Energ. Rev.* **2012**, *16* (1), 981-989.
(9) You, B.; Sun, Y. J. *Accounts Chem. Res.* **2018**, *51* (7), 1571-1580.
(10) Vojvodic, A.; Medford, A. J.; Studt, F.; Abild-Pedersen, F.; Khan, T. S.; Bligaard, T.; Norskov, J. K. *Chem. Phys. Lett.* **2014**, *598*, 108-112.
(11) Franchi, G.; Capocelli, M.; De Falco, M.; Piemonte, V.; Barba, D. *Membranes* **2020**, *10* (1), 10.
(12) Liu, Z.; Ciais, P.; Deng, Z.; Lei, R.; Davis, S. J.; Feng, S.; Zheng, B.; Cui, D.; Dou, X.; Zhu, B.; Guo, R.; Ke, P.; Sun, T.; Lu, C.; He, P.; Wang, Y.; Yue, X.; Wang, Y.; Lei, Y.; Zhou, H.; Cai, Z.; Wu, Y.; Guo, R.; Han, T.; Xue, J.; Boucher, O.; Boucher, E.; Chevallier, F.; Tanaka, K.; Wei, Y.; Zhong, H.; Kang, C.; Zhang, N.; Chen, B.; Xi, F.; Liu, M.; Breon, F. M.; Lu, Y.; Zhang, Q.; Guan, D.; Gong, P.; Kammen, D. M.; He, K.; Schellnhuber, H. J. *Nat. Commun.* **2020**, *11* (1), 5172.
(13) Voldsund, M.; Jordal, K.; Anantharaman, R. *Int. J. Hydrogen Energ.* **2016**, *41* (9), 4969-4992.
(14) Yu, F.; Zhou, H. Q.; Huang, Y. F.; Sun, J. Y.; Qin, F.; Bao, J. M.; Goddardiii, W. A.; Chen, S.; Ren, Z. F. *Nat. Commun.* **2018**, *9*, 2551.

Bibliography

Chapter 1

(1) Al-mulali, U.; Sab, C. N. B. C.; Fereidouni, H. G. *Energy* **2012**, *46* (1), 156-167.
(2) Waheed, R.; Chang, D. F.; Sarwar, S.; Chen, W. *J. Clean. Prod.* **2018**, *172*, 4231-4238.
(3) Peters, G. P.; Andrew, R. M.; Canadell, J. G.; Friedlingstein, P.; Jackson, R. B.; Korsbakken, J. I.; Le Quere, C.; Peregon, A. *Nat. Clim. Change.* **2020**, *10* (1), 3-6.
(4) Kweku, D.; Bismark, O.; Maxwell, A.; Desmond, K.; Danso, K.; Oti-Mensah, E.; Quachie, A.; Adormaa, B. *JSRR* **2017**, *17* (6), 1-9.
(5) Gielen, D.; Boshell, F.; Saygin, D.; Bazilian, M. D.; Wagner, N.; Gorini, R. *Energy Strateg. Rev.* **2019**, *24*, 38-50.
(6) Le, T. H.; Chang, Y.; Park, D. *Energ J.* **2020**, *41* (2), 73-92.
(7) Panwar, N. L.; Kaushik, S. C.; Kothari, S. *Renew. Sust. Energ. Rev.* **2011**, *15* (3), 1513-1524.
(8) Sinsel, S. R.; Riemke, R. L.; Hoffmann, V. H. *Renew. Energ.* **2020**, *145*, 2271-2285.
(9) Notton, G.; Nivet, M. L.; Voyant, C.; Paoli, C.; Darras, C.; Motte, F.; Fouilloy, A. *Renew. Sust. Energ. Rev.* **2018**, *87*, 96-105.
(10) Grubler, A.; Wilson, C.; Bento, N.; Boza-Kiss, B.; Krey, V.; McCollum, D. L.; Rao, N. D.; Riahi, K.; Rogelj, J.; De Stercke, S.; Cullen, J.; Frank, S.; Fricko, O.; Guo, F.; Gidden, M.; Havlik, P.; Huppmann, D.; Kiesewetter, G.; Rafaj, P.; Schoepp, W.; Valin, H. *Nat. Energy* **2018**, *3* (6), 515-527.
(11) Zhang, C.; Wei, Y. L.; Cao, P. F.; Lin, M. C. *Renew. Sust. Energ. Rev.* **2018**, *82*, 3091-3106.
(12) Soloveichik, G. L. *Annu. Rev. Chem. Biomol.* **2011**, *2*, 503-527.
(13) Chen, T.; Jin, Y.; Lv, H.; Yang, A.; Liu, M.; Chen, B.; Xie, Y.; Chen, Q. *Trans. Tianjin Univ.* **2020**, *26* (3), 208-217.
(14) Van Noorden, R. *Nature* **2014**, *507* (7490), 26-28.
(15) Zhang, J.; Zhou, Q. X.; Tang, Y. W.; Zhang, L.; Li, Y. G. *Chem. Sci.* **2019**, *10* (39), 8924-8929.
(16) Lee, J. S.; Kim, S. T.; Cao, R.; Choi, N. S.; Liu, M.; Lee, K. T.; Cho, J. *Adv. Energy Mater.* **2011**, *1* (1), 34-50.
(17) Li, Y. G.; Dai, H. J. *Chem. Soc. Rev.* **2014**, *43* (15), 5257-5275.
(18) Fu, J.; Cano, Z. P.; Park, M. G.; Yu, A. P.; Fowler, M.; Chen, Z. W. *Adv. Mater.* **2017**, *29* (7), 1604685.
(19) Wang, K.; Pei, P.; Zuo, Y.; Wei, M.; Wang, H.; Zhang, P.; Chen, Z.; Shang, N. *Iscience* **2022**, *25* (2), 103837.
(20) Zhang, W.; Lai, W. Z.; Cao, R. *Chem. Rev.* **2017**, *117* (4), 3717-3797.

(21) Zalka, D.; Peter, L. *J. Solid State Electr.* **2020**, *24* (11-12), 2595-2602.
(22) Kissinger, P. T. *Curr. Sep.* **2002**, *20* (2), 51-53.
(23) Hoyt, N. C.; Savinell, R. F.; Wainright, J. S. *Chem. Eng. Sci.* **2016**, *144*, 288-297.
(24) Mandin, P.; Derhoumi, Z.; Roustan, H.; Rolf, W. *Electrochim. Acta.* **2014**, *128*, 248-258.
(25) Norskov, J. K.; Rossmeisl, J.; Logadottir, A.; Lindqvist, L.; Kitchin, J. R.; Bligaard, T.; Jonsson, H. *J. Phys. Chem. B* **2004**, *108* (46), 17886-17892.
(26) Zhou, R. F.; Zheng, Y.; Jaroniec, M.; Qiao, S. Z. *ACS Catal.* **2016**, *6* (7), 4720-4728.
(27) Qiu, K. P.; Chai, G. L.; Jiang, C. R.; Ling, M.; Tang, J. W.; Guo, Z. X. *ACS Catal.* **2016**, *6* (6), 3558-3568.
(28) Wiggins-Camacho, J. D.; Stevenson, K. J. *J. Phys. Chem. C* **2011**, *115* (40), 20002-20010.
(29) Peng, L. S.; Shang, L.; Zhang, T. R.; Waterhouse, G. I. N. *Adv. Energy Mater.* **2020**, *10* (48), 2003018.
(30) Stephens, I. E. L.; Bondarenko, A. S.; Gronbjerg, U.; Rossmeisl, J.; Chorkendorff, I. *Energ. Environ. Sci.* **2012**, *5* (5), 6744-6762.
(31) Dau, H.; Limberg, C.; Reier, T.; Risch, M.; Roggan, S.; Strasser, P. *Chemcatchem* **2010**, *2* (7), 724-761.
(32) Suen, N. T.; Hung, S. F.; Quan, Q.; Zhang, N.; Xu, Y. J.; Chen, H. M. *Chem. Soc. Rev.* **2017**, *46* (2), 337-365.
(33) Zhu, X. F.; Hu, C. G.; Amal, R.; Dai, L. M.; Lu, X. Y. *Energ. Environ. Sci.* **2020**, *13* (12), 4536-4563.
(34) Fu, J.; Liang, R. L.; Liu, G. H.; Yu, A. P.; Bai, Z. Y.; Yang, L.; Chen, Z. W. *Adv. Mater.* **2019**, *31* (31), 1805230.
(35) Jung, C. Y.; Kim, T. H.; Kim, W. J.; Yi, S. C. *Energy* **2016**, *102*, 694-704.
(36) Shen, Y. W.; Kordesch, K. *J. Power Sources* **2000**, *87* (1-2), 162-166.
(37) Wang, R. Y.; Kirk, D. W.; Zhang, G. X. *J. Electrochem. Soc.* **2006**, *153* (5), C357-C364.
(38) Lee, T. S. *J. Electrochem. Soc.* **1971**, *118* (8), 1278.
(39) Huang, J. H.; Yang, Z. H.; Wang, R. J.; Zhang, Z.; Feng, Z. B.; Xie, X. E. *J. Mater. Chem. A* **2015**, *3* (14), 7429-7436.
(40) Lee, D. U.; Fu, J.; Park, M. G.; Liu, H.; Kashkooli, A. G.; Chen, Z. W. *Nano Lett.* **2016**, *16* (3), 1794-1802.
(41) Li, H. F.; Xu, C. J.; Han, C. P.; Chen, Y. Y.; Wei, C. G.; Li, B. H.; Kang, F. Y. *J. Electrochem. Soc.* **2015**, *162* (8), A1439-A1444.
(42) Parker, J. F.; Chervin, C. N.; Nelson, E. S.; Rolison, D. R.; Long, J. W. *Energ. Environ. Sci.* **2014**, *7* (3), 1117-1124.

(43) Yi, J.; Liang, P. C.; Liu, X. Y.; Wu, K.; Liu, Y. Y.; Wang, Y. G.; Xia, Y. Y.; Zhang, J. J. *Energ. Environ. Sci.* **2018**, *11* (11), 3075-3095.
(44) Zhao, Z. Q.; Fan, X. Y.; Ding, J.; Hu, W. B.; Zhong, C.; Lu, J. *ACS Energy Lett.* **2019**, *4* (9), 2259-2270.
(45) Pei, P. C.; Wang, K. L.; Ma, Z. *Appl. Energ.* **2014**, *128*, 315-324.
(46) Mainar, A. R.; Iruin, E.; Colmenares, L. C.; Kvasha, A.; de Meatza, I.; Bengoechea, M.; Leonet, O.; Boyano, I.; Zhang, Z. C.; Blazquez, J. A. *J. Energy Storage* **2018**, *15*, 304-328.
(47) Chen, P.; Zhang, K. Y.; Tang, D. J.; Liu, W. L.; Meng, F. C.; Huang, Q. W.; Liu, J. H. *Front. Chem.* **2020**, *8*, 372.
(48) Mainar, A. R.; Leonet, O.; Bengoechea, M.; Boyano, I.; de Meatza, I.; Kvasha, A.; Guerfi, A.; Blazquez, J. A. *Int. J. Energ. Res.* **2016**, *40* (8), 1032-1049.
(49) Sapkota, P.; Kim, H. *J. Ind. Eng. Chem.* **2009**, *15* (4), 445-450.
(50) See, D. M.; White, R. E. *J. Chem. Eng. Data* **1997**, *42* (6), 1266-1268.
(51) Qiao, J. L.; Xu, L.; Ding, L.; Shi, P. H.; Zhang, L.; Baker, R.; Zhang, J. J. *Int. J. Electrochem. Sc.* **2013**, *8* (1), 1189-1208.
(52) Lapicque, F.; Belhadj, M.; Bonnet, C.; Pauchet, J.; Thomas, Y. *J. Power Sources* **2016**, *336*, 40-53.
(53) Lim, C.; Wang, C. Y. *Electrochim. Acta.* **2004**, *49* (24), 4149-4156.
(54) Ralph, T. R.; Hards, G. A.; Keating, J. E.; Campbell, S. A.; Wilkinson, D. P.; Davis, M.; StPierre, J.; Johnson, M. C. *J. Electrochem. Soc.* **1997**, *144* (11), 3845-3857.
(55) Benziger, J.; Nehlsen, J.; Blackwell, D.; Brennan, T.; Itescu, J. *J. Membrane Sci.* **2005**, *261* (1-2), 98-106.
(56) Bhattacharya, P. K. *Directions* **2015**, *15*, 24-33.
(57) Li, H.; Tang, Y. H.; Wang, Z. W.; Shi, Z.; Wu, S. H.; Song, D. T.; Zhang, J. L.; Fatih, K.; Zhang, J. J.; Wang, H. J.; Liu, Z. S.; Abouatallah, R.; Mazza, A. *J. Power Sources* **2008**, *178* (1), 103-117.
(58) Cindrella, L.; Kannan, A. M.; Lin, J. F.; Saminathan, K.; Ho, Y.; Lin, C. W.; Wertz, J. *J. Power Sources* **2009**, *194* (1), 146-160.
(59) Gostick, J. T.; Ioannidis, M. A.; Fowler, M. W.; Pritzker, M. D. *Electrochem. Commun.* **2009**, *11* (3), 576-579.
(60) Omrani, R.; Shabani, B. *Int. J. Hydrogen Energ.* **2017**, *42* (47), 28515-28536.
(61) Schweiss, R.; Steeb, M.; Wilde, P. M. *Fuel Cells* **2010**, *10* (6), 1176-1180.
(62) Chen, J.; Xu, H.; Zhang, H.; Yi, B. *J. Power Sources* **2008**, *182* (2), 531-539.
(63) Fluckiger, R.; Freunberger, S. A.; Kramer, D.; Wokaun, A.; Scherer, G. G.; Buchi, F. N. *Electrochim. Acta.* **2008**, *54* (2), 551-559.
(64) Kang, S.; Yu, J. S.; Kruk, M.; Jaroniec, M. *Chem. Commun.* **2002**, (16), 1670-1671.

(65) Liu, D. L.; Tong, Y. Y.; Yan, X.; Liang, J.; Dou, S. X. *Batteries Supercaps* **2019**, *2* (9), 743-765.
(66) Zhong, Y. J.; Xu, X. M.; Wang, W.; Shao, Z. P. *Batteries Supercaps* **2019**, *2* (4), 272-289.
(67) Perez, G.; Pastor, E.; Zinola, C. F. *Int. J. Hydrogen Energ.* **2009**, *34* (23), 9523-9530.
(68) Favaro, M.; Valero-Vidal, C.; Eichhorn, J.; Toma, F. M.; Ross, P. N.; Yano, J.; Liu, Z.; Crumlin, E. J. *J. Mater. Chem. A* **2017**, *5* (23), 11634-11643.
(69) Tenkortenaar, M. V.; Vente, J. F.; Ijdo, D. J. W.; Muller, S.; Kotz, R. *J. Power Sources* **1995**, *56* (1), 51-60.
(70) Petrykin, V.; Macounova, K.; Shlyakhtin, O. A.; Krtil, P. *Angew. Chem. Int. Edit.* **2010**, *49* (28), 4813-4815.
(71) Labata, M. F.; Li, G. F.; Ocon, J.; Chuang, P. Y. A. *J. Power Sources* **2021**, *487*, 229356.
(72) Roduner, E. *Chem. Soc. Rev.* **2006**, *35* (7), 583-592.
(73) Wang, X. Q.; Li, Z. J.; Qu, Y. T.; Yuan, T. W.; Wang, W. Y.; Wu, Y.; Li, Y. D. *Chem* **2019**, *5* (6), 1486-1511.
(74) Liang, H. W.; Cao, X. A.; Zhou, F.; Cui, C. H.; Zhang, W. J.; Yu, S. H. *Adv. Mater.* **2011**, *23* (12), 1467-1471.
(75) Laha, S.; Lee, Y.; Podjaski, F.; Weber, D.; Duppel, V.; Schoop, L. M.; Pielnhofer, F.; Scheurer, C.; Muller, K.; Starke, U.; Reuter, K.; Lotsch, B. V. *Adv. Energy Mater.* **2019**, *9* (15), 1803795.
(76) Ding, J. B.; Shao, Q.; Feng, Y. G.; Huang, X. Q. *Nano Energy* **2018**, *47*, 1-7.
(77) Hornberger, E.; Mastronardi, V.; Brescia, R.; Pompa, P. P.; Klingenhof, M.; Dionigi, F.; Moglianetti, M.; Strasser, P. *ACS Appl. Energ. Mater.* **2021**, *4* (9), 9542-9552.
(78) Mahata, A.; Rawat, K. S.; Choudhuri, I.; Pathak, B. *J. Mater. Chem. A* **2016**, *4* (33), 12756-12767.
(79) Wang, G. Z.; Chang, J. F.; Koul, S.; Kushima, A.; Yang, Y. *J. Am. Chem. Soc.* **2021**, *143* (30), 11595-11601.
(80) li, Z.; Niu, W. H.; Yang, Z. Z.; Zaman, N.; Samarakoon, W.; Wang, M. Y.; Kara, A.; Lucero, M.; Vyas, M. V.; Chao, H.; Zhou, H.; Sterbinsky, G. E.; Feng, Z. X.; Du, Y. G.; Yang, Y. *Energ. Environ. Sci.* **2020**, *13* (3), 884-895.
(81) Behm, K.; McIntosh, R. D. *Chempluschem* **2020**, *85* (12), 2611-2618.
(82) Hansen, H. A.; Viswanathan, V.; Norskov, J. K. *J. Phys. Chem. C* **2014**, *118* (13), 6706-6718.
(83) Wang, H. Y.; Weng, C. C.; Yuan, Z. Y. *J. Energy Chem.* **2021**, *56*, 470-485.
(84) Davis, D. J.; Lambert, T. N.; Vigil, J. A.; Rodriguez, M. A.; Brumbach, M. T.; Coker, E. N.; Limmer, S. J. *J. Phys. Chem. C* **2014**, *118* (31), 17342-17350.

(85) Zhan, Y.; Xu, C. H.; Lu, M. H.; Liu, Z. L.; Lee, J. Y. *J. Mater. Chem. A* **2014**, *2* (38), 16217-16223.
(86) Wang, Y.; Li, J.; Wei, Z. D. *J. Mater. Chem. A* **2018**, *6* (18), 8194-8209.
(87) Saddeler, S.; Bendt, G.; Salamon, S.; Haase, F. T.; Landers, J.; Timoshenko, J.; Rettenmaier, C.; Jeon, H. S.; Bergmann, A.; Wende, H.; Cuenya, B. R.; Schulz, S. *J. Mater. Chem. A* **2021**, *9* (45), 25381-25390.
(88) Liu, J.; Bao, H. L.; Zhang, B. S.; Hua, Q. F.; Shang, M. F.; Wang, J. Q.; Jiang, L. H. *ACS Appl. Mater. Inter.* **2019**, *11* (13), 12525-12534.
(89) He, X. B.; Yin, F. X.; Li, G. R. *Int. J. Hydrogen Energ.* **2015**, *40* (31), 9713-9722.
(90) Guan, C.; Sumboja, A.; Wu, H. J.; Ren, W. N.; Liu, X. M.; Zhang, H.; Liu, Z. L.; Cheng, C. W.; Pennycook, S. J.; Wang, J. *Adv. Mater.* **2017**, *29* (44).
(91) Li, B.; Ge, X. M.; Goh, F. W. T.; Hor, T. S. A.; Geng, D. S.; Du, G. J.; Liu, Z. L.; Zhang, J.; Liu, X. G.; Zong, Y. *Nanoscale* **2015**, *7* (5), 1830-1838.
(92) Zhao, J.; He, Y.; Chen, Z. L.; Zheng, X. R.; Han, X. P.; Rao, D. W.; Zhong, C.; Hu, W. B.; Deng, Y. D. *ACS Appl. Mater. Inter.* **2019**, *11* (5), 4915-4921.
(93) Lee, D. U.; Choi, J. Y.; Feng, K.; Park, H. W.; Chen, Z. W. *Adv. Energy Mater.* **2014**, *4* (6).
(94) Da, P. F.; Wu, M. Y.; Qiu, K. W.; Yan, D. Y.; Li, Y. J.; Mao, J.; Dong, C. K.; Ling, T.; Qiao, S. Z. *Chem. Eng. Sci.* **2019**, *194*, 127-133.
(95) Xu, L.; Wang, C.; Deng, D. J.; Tian, Y. H.; He, X. Y.; Lu, G. F.; Qian, J. C.; Yuan, S. Q.; Li, H. N. *ACS Sustain. Chem. Eng.* **2020**, *8* (1), 343-350.
(96) He, Y.; Zhang, J. F.; He, G. W.; Han, X. P.; Zheng, X. R.; Zhong, C.; Hu, W. B.; Deng, Y. D. *Nanoscale* **2017**, *9* (25), 8623-8630.
(97) Lee, J. S.; Lee, T.; Song, H. K.; Cho, J.; Kim, B. S. *Energ. Environ. Sci.* **2011**, *4* (10), 4148-4154.
(98) Gorlin, Y.; Lassalle-Kaiser, B.; Benck, J. D.; Gul, S.; Webb, S. M.; Yachandra, V. K.; Yano, J.; Jaramillo, T. F. *J. Am. Chem. Soc.* **2013**, *135* (23), 8525-8534.
(99) Liu, B.; Sun, Y. L.; Liu, L.; Xu, S.; Yan, X. B. *Adv. Funct. Mater.* **2018**, *28* (15).
(100) Tang, Q.; Jiang, L.; Liu, J.; Wang, S.; Sun, G. *ACS Catal.* **2014**, *4* (2), 457-463.
(101) Xue, Q.; Pei, Z. X.; Huang, Y.; Zhu, M. S.; Tang, Z. J.; Li, H. F.; Huang, Y.; Li, N.; Zhang, H. Y.; Zhi, C. Y. *J. Mater. Chem. A* **2017**, *5* (39), 20818-20823.
(102) Clark, M. P.; Xiong, M.; Cadien, K.; Ivey, D. G. *ACS Appl. Energ. Mater.* **2020**, *3* (1), 603-613.
(103) Lee, J. S.; Park, G. S.; Lee, H. I.; Kim, S. T.; Cao, R. G.; Liu, M. L.; Cho, J. *Nano Lett.* **2011**, *11* (12), 5362-5366.

(104) Jia, Q. Y.; Ramaswamy, N.; Tylus, U.; Strickland, K.; Li, J. K.; Serov, A.; Artyushkova, K.; Atanassov, P.; Anibal, J.; Gumeci, C.; Barton, S. C.; Sougrati, M. T.; Jaouen, F.; Halevi, B.; Mukerjee, S. *Nano Energy* **2016**, *29*, 65-82.
(105) Ferrandon, M.; Kropf, A. J.; Myers, D. J.; Artyushkova, K.; Kramm, U.; Bogdanoff, P.; Wu, G.; Johnston, C. M.; Zelenay, P. *J. Phys. Chem. C* **2012**, *116* (30), 16001-16013.
(106) Zhang, Z. P.; Sun, J. T.; Wang, F.; Dai, L. M. *Angew. Chem. Int. Edit.* **2018**, *57* (29), 9038-9043.
(107) Wang, J.; Wu, H. H.; Gao, D. F.; Miao, S.; Wang, G. X.; Bao, X. H. *Nano Energy* **2015**, *13*, 387-396.
(108) Zang, Y. P.; Zhang, H. M.; Zhang, X.; Liu, R. R.; Liu, S. W.; Wang, G. Z.; Zhang, Y. X.; Zhao, H. J. *Nano Res.* **2016**, *9* (7), 2123-2137.
(109) Kuhlenbeck, H.; Shaikhutdinov, S.; Freund, H. J. *Chem. Rev.* **2013**, *113* (6), 3986-4034.
(110) Lu, Q.; Lattanzi, M. W.; Chen, Y. P.; Kou, X. M.; Li, W. F.; Fan, X.; Unruh, K. M.; Chen, J. G. G.; Xiao, J. Q. *Angew. Chem. Int. Edit.* **2011**, *50* (30), 6847-6850.
(111) Liu, H.; Wang, G. X.; Liu, J.; Qiao, S. Z.; Ahn, H. J. *J. Mater. Chem.* **2011**, *21* (9), 3046-3052.
(112) Ma, N.; Jia, Y.; Yang, X. F.; She, X. L.; Zhang, L. Z.; Peng, Z.; Yao, X. D.; Yang, D. J. *J. Mater. Chem. A* **2016**, *4* (17), 6376-6384.
(113) Qian, J. M.; Bai, X. W.; Xi, S. B.; Xiao, W.; Gao, D. Q.; Wang, J. L. *ACS Appl. Mater. Inter.* **2019**, *11* (34), 30865-30871.
(114) Vasilescu, A.; Hayat, A.; Gaspar, S.; Marty, J. L. *Electroanal.* **2018**, *30* (1), 2-19.
(115) Zhu, J.; Holmen, A.; Chen, D. *Chemcatchem* **2013**, *5* (2), 378-401.
(116) Hu, C. G.; Dai, L. M. *Adv. Mater.* **2019**, *31* (7), 1804672.
(117) Das, A.; Pisana, S.; Chakraborty, B.; Piscanec, S.; Saha, S. K.; Waghmare, U. V.; Novoselov, K. S.; Krishnamurthy, H. R.; Geim, A. K.; Ferrari, A. C.; Sood, A. K. *Nat. Nanotechnol.* **2008**, *3* (4), 210-215.
(118) Antolini, E. *Appl. Catal. B-Environ.* **2012**, *123*, 52-68.
(119) Bonaccorso, F.; Sun, Z.; Hasan, T.; Ferrari, A. C. *Nat. Photonics* **2010**, *4* (9), 611-622.
(120) Chung, C.; Kim, Y. K.; Shin, D.; Ryoo, S. R.; Hong, B. H.; Min, D. H. *Accounts Chem. Res.* **2013**, *46* (10), 2211-2224.
(121) Pyatkov, F.; Futterling, V.; Khasminskaya, S.; Flavel, B. S.; Hennrich, F.; Kappes, M. M.; Krupke, R.; Pernice, W. H. P. *Nat. Photonics* **2016**, *10* (6), 420-+.
(122) Flavel, B. S.; Yu, J. X.; Shapter, J. G.; Quinton, J. S. *J. Mater. Chem.* **2007**, *17* (45), 4757-4761.

(123) Steiner, M.; Engel, M.; Lin, Y. M.; Wu, Y. Q.; Jenkins, K.; Farmer, D. B.; Humes, J. J.; Yoder, N. L.; Seo, J. W. T.; Green, A. A.; Hersam, M. C.; Krupke, R.; Avouris, P. *Appl. Phys. Lett.* **2012**, *101* (5).
(124) Varga, A.; Pfohl, M.; Brunelli, N. A.; Schreier, M.; Giapis, K. P.; Haile, S. M. *Phys. Chem. Chem. Phys.* **2013**, *15* (37), 15470-15476.
(125) Landi, B. J.; Ganter, M. J.; Cress, C. D.; DiLeo, R. A.; Raffaelle, R. P. *Energ. Environ. Sci.* **2009**, *2* (6), 638-654.
(126) Tatsuura, S.; Furuki, M.; Sato, Y.; Iwasa, I.; Tian, M. Q.; Mitsu, H. *Adv. Mater.* **2003**, *15* (6), 534-537.
(127) Engel, M.; Moore, K. E.; Alam, A.; Dehm, S.; Krupke, R.; Flavel, B. S. *ACS Nano* **2014**, *8* (9), 9324-9331.
(128) Avouris, P.; Freitag, M.; Perebeinos, V. *Nat. Photonics* **2008**, *2* (6), 341-350.
(129) Jiao, Y.; Zheng, Y.; Jaroniec, M.; Qiao, S. Z. *J. Am. Chem. Soc.* **2014**, *136* (11), 4394-4403.
(130) You, C. H.; Liao, S. J.; Li, H. L.; Hou, S. Y.; Peng, H. L.; Zeng, X. Y.; Liu, F. F.; Zheng, R. P.; Fu, Z. Y.; Li, Y. W. *Carbon* **2014**, *69*, 294-301.
(131) Zhang, J. T.; Qu, L. T.; Shi, G. Q.; Liu, J. Y.; Chen, J. F.; Dai, L. M. *Angew. Chem. Int. Edit.* **2016**, *55* (6), 2230-2234.
(132) Zheng, Y.; Chen, S.; Zhang, K. A. I.; Zhu, J. X.; Xu, J. S.; Zhang, C.; Liu, T. X. *ACS Appl. Mater. Inter.* **2021**, *13* (11), 13328-13337.
(133) Chen, W.; Xu, L.; Tian, Y. H.; Li, H. A.; Wang, K. *Carbon* **2018**, *137*, 458-466.
(134) Liu, X.; Wang, L.; Yu, P.; Tian, C. G.; Sun, F. F.; Ma, J. Y.; Li, W.; Fu, H. G. *Angew. Chem. Int. Edit.* **2018**, *57* (49), 16166-16170.
(135) Lee, D. U.; Park, H. W.; Park, M. G.; Ismayilov, V.; Chen, Z. W. *ACS Appl. Mater. Inter.* **2015**, *7* (1), 902-910.
(136) Zhou, H. C.; Kitagawa, S. *Chem. Soc. Rev.* **2014**, *43* (16), 5415-5418.
(137) Lee, Y. R.; Kim, J.; Ahn, W. S. *Korean J. Chem. Eng.* **2013**, *30* (9), 1667-1680.
(138) Aguado, S.; Canivet, J.; Farrusseng, D. *J. Mater. Chem.* **2011**, *21* (21), 7582-7588.
(139) Chen, X. R.; Tong, R. L.; Shi, Z. Q.; Yang, B.; Liu, H.; Ding, S. P.; Wang, X.; Lei, Q. F.; Wu, J.; Fang, W. J. *ACS Appl. Mater. Inter.* **2018**, *10* (3), 2328-2337.
(140) Ding, M. L.; Flaig, R. W.; Jiang, H. L.; Yaghi, O. M. *Chem. Soc. Rev.* **2019**, *48* (10), 2783-2828.
(141) Ding, M. L.; Cai, X. C.; Jiang, H. L. *Chem. Sci.* **2019**, *10* (44), 10209-10230.
(142) Shen, K.; Chen, X. D.; Chen, J. Y.; Li, Y. W. *ACS Catal.* **2016**, *6* (9), 5887-5903.

(143) Li, Y. W.; Zhang, W. J.; Li, J.; Ma, H. Y.; Du, H. M.; Li, D. C.; Wang, S. N.; Zhao, J. S.; Dou, J. M.; Xu, L. Q. *ACS Appl. Mater. Inter.* **2020**, *12* (40), 44710-44719.
(144) Wu, H. B.; Wang, J.; Yan, J.; Wu, Z. X.; Jin, W. *Nanoscale* **2019**, *11* (42), 20144-20150.
(145) Dogan, A. U.; Dogan, M.; Onal, M.; Sarikaya, Y.; Aburub, A.; Wurster, D. E. *Clay. Clay Miner.* **2006**, *54* (1), 62-66.
(146) Tarleton, E.; Tarleton, E. S.; Elsevier. *Progress in filtration and separation*; Academic Press, 2015.
(147) Elgrishi, N.; Rountree, K. J.; McCarthy, B. D.; Rountree, E. S.; Eisenhart, T. T.; Dempsey, J. L. *J. Chem. Educ.* **2018**, *95* (2), 197-206.
(148) Bard, A. J. *ELECTROCHEMICAL METHODS*; 1980.
(149) Sapkota, P.; Kim, H. *J. Ind. Eng. Chem.* **2010**, *16* (1), 39-44.
(150) Davis, R. E.; Horvath, G. L.; Tobias, C. W. *Electrochim. Acta.* **1967**, *12* (3), 287-297.
(151) Nikolic, J.; Exposito, E.; Iniesta, J.; Gonzalez-Garcia, J.; Montiel, V. *J. Chem. Educ.* **2000**, *77* (9), 1191-1194.
(152) Chen, W. L.; Xiang, Q.; Peng, T.; Song, C. Y.; Shang, W.; Deng, T.; Wu, J. B. *Iscience* **2020**, *23* (10), 101532.
(153) Vayner, E.; Sidik, R. A.; Anderson, A. B.; Popov, B. N. *J. Phys. Chem. C* **2007**, *111* (28), 10508-10513.
(154) Gilliam, R. J.; Graydon, J. W.; Kirk, D. W.; Thorpe, S. J. *Int. J. Hydrogen Energ.* **2007**, *32* (3), 359-364.
(155) Shivkumar, R.; Kalaignan, G. P.; Vasudevan, T. *J. Power Sources* **1995**, *55* (1), 53-62.
(156) Zia, A. I.; Mukhopadhyay, S. C. *Electrochemical Sensing: Carcinogens in Beverages*; Springer International Publishing, 2016.
(157) Bredar, A. R. C.; Chown, A. L.; Burton, A. R.; Farnum, B. H. *ACS Appl. Energ. Mater.* **2020**, *3* (1), 66-98.
(158) Park, S. M.; Yoo, J. S. *Anal. Chem.* **2003**, *75* (21), 455a-461a.

Chapter 2

(1) Chu, S.; Cui, Y.; Liu, N. *Nat. Mater.* **2017**, *16* (1), 16-22.
(2) Roger, I.; Shipman, M. A.; Symes, M. D. *Nat. Rev. Chem.* **2017**, *1* (1), 0003.
(3) Cano, Z. P.; Banham, D.; Ye, S. Y.; Hintennach, A.; Lu, J.; Fowler, M.; Chen, Z. W. *Nat. Energy* **2018**, *3* (4), 279-289.
(4) Sui, S.; Wang, X. Y.; Zhou, X. T.; Su, Y. H.; Riffatc, S.; Liu, C. J. *J. Mater. Chem. A* **2017**, *5* (5), 1808-1825.

(5) Zuo, W. H.; Li, R. Z.; Zhou, C.; Li, Y. Y.; Xia, J. L.; Liu, J. P. *Adv. Sci.* **2017**, *4* (7).
(6) Wang, Y. X.; Liu, B.; Li, Q. Y.; Cartmell, S.; Ferrara, S.; Deng, Z. Q. D.; Xiao, J. *J. Power Sources* **2015**, *286*, 330-345.
(7) Girishkumar, G.; McCloskey, B.; Luntz, A. C.; Swanson, S.; Wilcke, W. *J. Phys. Chem. Lett.* **2010**, *1* (14), 2193-2203.
(8) Liu, X.; Huang, J. Q.; Zhang, Q.; Mai, L. Q. *Adv. Mater.* **2017**, *29* (20), 1601759.
(9) Hwang, J. Y.; Myung, S. T.; Sun, Y. K. *Chem. Soc. Rev.* **2017**, *46* (12), 3529-3614.
(10) Fu, J.; Cano, Z. P.; Park, M. G.; Yu, A. P.; Fowler, M.; Chen, Z. W. *Adv. Mater.* **2017**, *29* (7), 1604685.
(11) Pan, J.; Xu, Y. Y.; Yang, H.; Dong, Z. H.; Liu, H. F.; Xia, B. Y. *Adv. Sci.* **2018**, *5* (4), 1700691
(12) Li, Y. G.; Lu, J. *ACS Energy Lett.* **2017**, *2* (6), 1370-1377.
(13) Zhang, W.; Lai, W. Z.; Cao, R. *Chem. Rev.* **2017**, *117* (4), 3717-3797.
(14) Cheng, F. Y.; Chen, J. *Chem. Soc. Rev.* **2012**, *41* (6), 2172-2192.
(15) Ren, M. Q.; Zhang, J. B.; Tour, J. M. *ACS Appl. Energ. Mater.* **2019**, *2* (2), 1460-1468.
(16) Qu, L. T.; Liu, Y.; Baek, J. B.; Dai, L. M. *ACS Nano* **2010**, *4* (3), 1321-1326.
(17) Wang, H. P.; Keum, J. K.; Hiltner, A.; Baer, E.; Freeman, B.; Rozanski, A.; Galeski, A. *Science* **2009**, *323* (5915), 757-760.
(18) Liu, M. K.; Song, Y. F.; He, S. X.; Tjiu, W. W.; Pan, J. S.; Xia, Y. Y.; Liu, T. X. *ACS Appl. Mater. Inter.* **2014**, *6* (6), 4214-4222.
(19) Koza, J. A.; He, Z.; Miller, A. S.; Switzer, J. A. *Chem. Mater.* **2012**, *24* (18), 3567-3573.
(20) Cheng, F. Y.; Su, Y.; Liang, J.; Tao, Z. L.; Chen, J. *Chem. Mater.* **2010**, *22* (3), 898-905.
(21) Li, L. Q.; Yang, J.; Yang, H. B.; Zhang, L. P.; Shao, J. J.; Huang, W.; Liu, B.; Dong, X. C. *ACS Appl. Energ. Mater.* **2018**, *1* (3), 963-969.
(22) Hadidi, L.; Davari, E.; Iqbal, M.; Purkait, T. K.; Ivey, D. G.; Veinot, J. G. C. *Nanoscale* **2015**, *7* (48), 20547-20556.
(23) Dasog, M.; Smith, L. F.; Purkait, T. K.; Veinot, J. G. C. *Chem. Commun.* **2013**, *49* (62), 7004-7006.
(24) Shirley, D. A. *Phys. Rev. B* **1972**, *5* (12), 4709-4714.
(25) Xiong, M.; Clark, M. P.; Labbe, M.; Ivey, D. G. *J. Power Sources* **2018**, *393*, 108-118.
(26) Wu, T. H.; Hesp, D.; Dhanak, V.; Collins, C.; Braga, F.; Hardwick, L. J.; Hu, C. C. *J. Mater. Chem. A* **2015**, *3* (24), 12786-12795.
(27) Lee, J. W.; Hall, A. S.; Kim, J. D.; Mallouk, T. E. *Chem. Mater.* **2012**, *24* (6), 1158-1164.

(28) Chigane, M.; Ishikawa, M.; Izaki, M. *J. Electrochem. Soc.* **2001**, *148* (7), D96-D101.
(29) Gorlin, Y.; Jaramillo, T. F. *J. Am. Chem. Soc.* **2010**, *132* (39), 13612-13614.
(30) Yu, X.; Fan, H. L.; Liu, Y.; Shi, Z. J.; Jin, Z. X. *Langmuir* **2014**, *30* (19), 5497-5505.
(31) Dubal, D. P.; Dhawale, D. S.; Salunkhe, R. R.; Pawar, S. M.; Lokhande, C. D. *Appl. Surf. Sci.* **2010**, *256* (14), 4411-4416.
(32) Xing, W.; Yin, G.; Zhang, J.; Elsevier. *Rotating electrode methods and oxygen reduction electrocatalysts*; Elsevier, 2014.
(33) Paulus, U. A.; Schmidt, T. J.; Gasteiger, H. A.; Behm, R. J. *J. Electroanal. Chem.* **2001**, *495* (2), 134-145.
(34) Zhang, J. T.; Zhao, Z. H.; Xia, Z. H.; Dai, L. M. *Nat. Nanotechnol.* **2015**, *10* (5), 444-452.
(35) Wu, Z. S.; Yang, S. B.; Sun, Y.; Parvez, K.; Feng, X. L.; Mullen, K. *J. Am. Chem. Soc.* **2012**, *134* (22), 9082-9085.
(36) Chen, L.; Sun, L. J.; Luan, F.; Liang, Y.; Li, Y.; Liu, X. X. *J. Power Sources* **2010**, *195* (11), 3742-3747.
(37) Vijayakumar, S.; Ponnalagi, A. K.; Nagamuthu, S.; Muralidharan, G. *Electrochim. Acta.* **2013**, *106*, 500-505.
(38) Laurent, S.; Forge, D.; Port, M.; Roch, A.; Robic, C.; Elst, L. V.; Muller, R. N. *Chem. Rev.* **2008**, *108* (6), 2064-2110.
(39) Aasen, D.; Clark, M.; Ivey, D. G. *Batteries Supercaps* **2019**, *2* (10), 882-893.
(40) Huang, Z. X.; Qin, X. P.; Gu, X. F.; Li, G. Z.; Mu, Y. C.; Wang, N. G.; Ithisuphalap, K.; Wang, H. X.; Guo, Z. P.; Shi, Z. C.; Wu, G.; Shao, M. H. *ACS Appl. Mater. Inter.* **2018**, *10* (28), 23900-23909.
(41) Fu, J.; Hassan, F. M.; Li, J. D.; Lee, D. U.; Ghannoum, A. R.; Lui, G.; Hoque, M. A.; Chen, Z. W. *Adv. Mater.* **2016**, *28* (30), 6421-6428.
(42) Wei, L.; Karahan, H. E.; Zhai, S. L.; Liu, H. W.; Chen, X. C.; Zhou, Z.; Lei, Y. J.; Liu, Z. W.; Chen, Y. *Adv. Mater.* **2017**, *29* (38), 1701410.
(43) Li, F. Y.; Li, H.; Liu, X. X.; Wang, L. B.; Lu, Y.; Hu, X. L. *Chem-Eur. J.* **2019**, *25* (2), 635-641.
(44) Ge, X. M.; Liu, Y. Y.; Goh, F. W. T.; Hor, T. S. A.; Zong, Y.; Xiao, P.; Zhang, Z.; Lim, S. H.; Li, B.; Wang, X.; Liu, Z. L. *ACS Appl. Mater. Inter.* **2014**, *6* (15), 12684-12691.
(45) Sumboja, A.; Ge, X. M.; Goh, F. W. T.; Li, B.; Geng, D. S.; Hor, T. S. A.; Zong, Y.; Liu, Z. L. *Chempluschem* **2015**, *80* (8), 1341-1346.
(46) Meng, F. L.; Zhong, H. X.; Bao, D.; Yan, J. M.; Zhang, X. B. *J. Am. Chem. Soc.* **2016**, *138* (32), 10226-10231.
(47) Zhang, W.; Li, D. H.; Zhang, L. Z.; She, X. L.; Yang, D. J. *J. Energy Chem.* **2019**, *39*, 39-53.

Chapter 3

(1) Saint Akadiri, S.; Alola, A. A.; Akadiri, A. C.; Alola, U. V. *Energ. Policy* **2019**, *132*, 803-810.
(2) Liu, W. F.; Zhang, X. P.; Feng, S. D. *Renew. Energ.* **2019**, *135*, 635-642.
(3) Babatunde, O. M.; Munda, J. L.; Hamam, Y. *Int. J. Energ. Res.* **2019**, *43* (12), 6078-6107.
(4) Abujarad, S. Y.; Mustafa, M. W.; Jamian, J. J. *Renew. Sust. Energ. Rev.* **2017**, *70*, 215-223.
(5) Li, Y. G.; Lu, J. *ACS Energy Lett.* **2017**, *2* (6), 1370-1377.
(6) Zhang, J.; Zhou, Q. X.; Tang, Y. W.; Zhang, L.; Li, Y. G. *Chem. Sci.* **2019**, *10* (39), 8924-8929.
(7) Shen, X.; Liu, H.; Cheng, X. B.; Yan, C.; Huang, J. Q. *Energy Storage Mater.* **2018**, *12*, 161-175.
(8) Gu, P.; Zheng, M. B.; Zhao, Q. X.; Xiao, X.; Xue, H. G.; Pang, H. *J. Mater. Chem. A* **2017**, *5* (17), 7651-7666.
(9) Nykvist, B.; Nilsson, M. *Nat. Clim. Change.* **2015**, *5* (4), 329-332.
(10) Li, Y. G.; Dai, H. J. *Chem. Soc. Rev.* **2014**, *43* (15), 5257-5275.
(11) Fu, J.; Cano, Z. P.; Park, M. G.; Yu, A. P.; Fowler, M.; Chen, Z. W. *Adv. Mater.* **2017**, *29* (7), 1604685.
(12) Pan, J.; Tian, X. L.; Zaman, S.; Dong, Z. H.; Liu, H. F.; Park, H. S.; Xia, B. Y. *Batteries Supercaps* **2019**, *2* (4), 336-347.
(13) Zhao, Z. Q.; Fan, X. Y.; Ding, J.; Hu, W. B.; Zhong, C.; Lu, J. *ACS Energy Lett.* **2019**, *4* (9), 2259-2270.
(14) Lee, J. S.; Kim, S. T.; Cao, R.; Choi, N. S.; Liu, M.; Lee, K. T.; Cho, J. *Adv. Energy Mater.* **2011**, *1* (1), 34-50.
(15) Cheng, F. Y.; Chen, J. *Chem. Soc. Rev.* **2012**, *41* (6), 2172-2192.
(16) Fu, J.; Liang, R. L.; Liu, G. H.; Yu, A. P.; Bai, Z. Y.; Yang, L.; Chen, Z. W. *Adv. Mater.* **2019**, *31* (31), 1805230.
(17) Wei, L. C.; Ang, E. H.; Yang, Y.; Qin, Y. L.; Zhang, Y. F.; Ye, M. H.; Liu, Q.; Li, C. C. *J. Power Sources* **2020**, *477*.
(18) Wu, C.; Song, L.; Li, L. H.; Xia, W.; Jiang, C.; Gao, B.; Du, Y. Q.; Wang, T.; He, J. P. *Chemelectrochem* **2019**, *6* (15), 4010-4015.
(19) Hadidi, L.; Davari, E.; Iqbal, M.; Purkait, T. K.; Ivey, D. G.; Veinot, J. G. C. *Nanoscale* **2015**, *7* (48), 20547-20556.
(20) Shao, Y.; Xiao, X.; Zhu, Y. P.; Ma, T. Y. *Angew. Chem. Int. Edit.* **2019**, *58* (41), 14599-14604.
(21) Aasen, D. A.; Shen, Y.; Ivey, D. G. *Chemelectrochem* **2020**, *7* (10), 2283-2296.
(22) He, J. Z.; Niu, W. J.; Wang, Y. P.; Sun, Q. Q.; Liu, M. J.; Wang, K. Y.; Liu, W. W.; Liu, M. C.; Yu, F. C.; Chueh, Y. L. *Electrochim. Acta.* **2020**, *362*.

(23) Niu, W. J.; He, J. Z.; Wang, Y. P.; Sun, Q. Q.; Liu, W. W.; Zhang, L. Y.; Liu, M. C.; Liu, M. J.; Chueh, Y. L. *Nanoscale* **2020**, *12* (38), 19644-19654.
(24) Xu, Y. J.; Sumboja, A.; Groves, A.; Ashton, T.; Zong, Y.; Darr, J. A. *RSC Adv.* **2020**, *10* (68), 41871-41882.
(25) Chen, J. Y.; Li, H.; Fan, C.; Meng, Q. W.; Tang, Y. W.; Qiu, X. Y.; Fu, G. T.; Ma, T. Y. *Adv. Mater.* **2020**, *32* (30), 2003134.
(26) Wang, B.; Ye, Y. Z.; Xu, L.; Quan, Y.; Wei, W. X.; Zhu, W. S.; Li, H. M.; Xia, J. X. *Adv. Funct. Mater.* **2020**, *30* (51), 2005834.
(27) He, Y. J.; Aasen, D.; Yu, H. Y.; Labbe, M.; Ivey, D. G.; Veinot, J. G. C. *Nanoscale Adv.* **2020**, *2* (8), 3367-3374.
(28) Zhang, M. D.; Dai, Q. B.; Zheng, H. G.; Chen, M. D.; Dai, L. M. *Adv. Mater.* **2018**, *30* (10), 1705431.
(29) Dasog, M.; Smith, L. F.; Purkait, T. K.; Veinot, J. G. C. *Chem. Commun.* **2013**, *49* (62), 7004-7006.
(30) Liang, Y. Y.; Wang, H. L.; Diao, P.; Chang, W.; Hong, G. S.; Li, Y. G.; Gong, M.; Xie, L. M.; Zhou, J. G.; Wang, J.; Regier, T. Z.; Wei, F.; Dai, H. J. *J. Am. Chem. Soc.* **2012**, *134* (38), 15849-15857.
(31) Marco, J. F.; Gancedo, J. R.; Gracia, M.; Gautier, J. L.; Rios, E.; Berry, F. J. *J. Solid State Chem.* **2000**, *153* (1), 74-81.
(32) Biesinger, M. C.; Payne, B. P.; Grosvenor, A. P.; Lau, L. W. M.; Gerson, A. R.; Smart, R. S. *Appl. Surf. Sci.* **2011**, *257* (7), 2717-2730.
(33) Prabaharan, D. D. M.; Sadaiyandi, K.; Mahendran, M.; Sagadevan, S. *Appl. Phys. A-Mater.* **2017**, *123* (4), 264.
(34) Krishnan, S. G.; Ab Rahim, M. H.; Jose, R. *J. Alloy. Compd.* **2016**, *656*, 707-713.
(35) Aasen, D.; Clark, M.; Ivey, D. G. *Batteries Supercaps* **2019**, *2* (10), 882-893.
(36) He, X. B.; Yin, F. X.; Li, G. R. *Int. J. Hydrogen Energ.* **2015**, *40* (31), 9713-9722.
(37) Clark, M. P.; Muneshwar, T.; Xiong, M.; Cadien, K.; Ivey, D. G. *ACS Appl. Nano Mater.* **2019**, *2* (1), 267-277.
(38) Liu, J.; Bao, H. L.; Zhang, B. S.; Hua, Q. F.; Shang, M. F.; Wang, J. Q.; Jiang, L. H. *ACS Appl. Mater. Inter.* **2019**, *11* (13), 12525-12534.
(39) Tang, Q. W.; Jiang, L. H.; Liu, J.; Wang, S. L.; Sun, G. Q. *ACS Catal.* **2014**, *4* (2), 457-463.
(40) Antoni, H.; Xia, W.; Masa, J.; Schuhmann, W.; Muhler, M. *Phys. Chem. Chem. Phys.* **2017**, *19* (28), 18434-18442.
(41) Godwin, I. J.; Lyons, M. E. G. *Electrochem. Commun.* **2013**, *32*, 39-42.
(42) Gong, L.; Chng, X. Y. E.; Du, Y. H.; Xi, S. B.; Yeo, B. S. *ACS Catal.* **2018**, *8* (2), 807-814.

(43) Zhuang, S. Q.; Lee, E. S.; Lei, L.; Nunna, B. B.; Kuang, L. Y.; Zhang, W. *Int. J. Energ. Res.* **2016**, *40* (15), 2136-2149.
(44) Xu, N. N.; Qiao, J. L.; Nie, Q.; Wang, M.; Xu, H.; Wang, Y. D.; Zhou, X. D. *Catal. Today* **2018**, *318*, 144-149.
(45) Wei, L.; Karahan, H. E.; Zhai, S. L.; Liu, H. W.; Chen, X. C.; Zhou, Z.; Lei, Y. J.; Liu, Z. W.; Chen, Y. *Adv. Mater.* **2017**, *29* (38), 1701410.
(46) An, K. L.; Zheng, Y.; Xu, X. X.; Wang, Y. *J. Solid State Chem.* **2019**, *270*, 539-546.
(47) Aasen, D.; Clark, M. P.; Ivey, D. G. *Batteries Supercaps* **2020**, *3* (2), 174-184.

Chapter 4

(1) Figgener, J.; Stenzel, P.; Kairies, K. P.; Linssen, J.; Haberschusz, D.; Wessels, O.; Angenendt, G.; Robinius, M.; Stolten, D.; Sauer, D. U. *J. Energy Storage* **2020**, *29*, 101153.
(2) Faessler, B. *Energies* **2021**, *14* (8), 2335.
(3) Lu, L. G.; Han, X. B.; Li, J. Q.; Hua, J. F.; Ouyang, M. G. *J. Power Sources* **2013**, *226*, 272-288.
(4) Manthiram, A. *ACS Central Sci.* **2017**, *3* (10), 1063-1069.
(5) Wanger, T. C. *Conserv. Lett.* **2011**, *4* (3), 202-206.
(6) Fan, E. S.; Li, L.; Wang, Z. P.; Lin, J.; Huang, Y. X.; Yao, Y.; Chen, R. J.; Wu, F. *Chem. Rev.* **2020**, *120* (14), 7020-7063.
(7) Chen, Y. Q.; Kang, Y. Q.; Zhao, Y.; Wang, L.; Liu, J. L.; Li, Y. X.; Liang, Z.; He, X. M.; Li, X.; Tavajohi, N.; Li, B. H. *J. Energy Chem.* **2021**, *59*, 83-99.
(8) Chen, Z. Y.; Xiong, R.; Lu, J. H.; Li, X. G. *Appl. Energ.* **2018**, *213*, 375-383.
(9) Zheng, H. F.; Han, X.; Guo, W. B.; Lin, L.; Xie, Q. S.; Liu, P. F.; He, W.; Wang, L. S.; Peng, D. L. *Mater. Today Energy* **2020**, *18*, 100518.
(10) Goh, F. W. T.; Liu, Z. L.; Hor, T. S. A.; Zhang, J.; Ge, X. M.; Zong, Y.; Yu, A. S.; Khoo, W. *J. Electrochem. Soc.* **2014**, *161* (14), A2080-A2086.
(11) Zhang, J.; Zhou, Q. X.; Tang, Y. W.; Zhang, L.; Li, Y. G. *Chem. Sci.* **2019**, *10* (39), 8924-8929.
(12) Gu, P.; Zheng, M. B.; Zhao, Q. X.; Xiao, X.; Xue, H. G.; Pang, H. *J. Mater. Chem. A* **2017**, *5* (17), 7651-7666.
(13) Li, Y. G.; Dai, H. J. *Chem. Soc. Rev.* **2014**, *43* (15), 5257-5275.
(14) Fu, J.; Cano, Z. P.; Park, M. G.; Yu, A. P.; Fowler, M.; Chen, Z. W. *Adv. Mater.* **2017**, *29* (7), 1604685.
(15) Mainar, A. R.; Iruin, E.; Colmenares, L. C.; Kvasha, A.; de Meatza, I.; Bengoechea, M.; Leonet, O.; Boyano, I.; Zhang, Z. C.; Blazquez, J. A. *J. Energy Storage* **2018**, *15*, 304-328.

(16) Chen, P.; Zhang, K. Y.; Tang, D. J.; Liu, W. L.; Meng, F. C.; Huang, Q. W.; Liu, J. H. *Front. Chem.* **2020**, *8*, 372.
(17) Lee, J. S.; Kim, S. T.; Cao, R.; Choi, N. S.; Liu, M.; Lee, K. T.; Cho, J. *Adv. Energy Mater.* **2011**, *1* (1), 34-50.
(18) Suen, N. T.; Hung, S. F.; Quan, Q.; Zhang, N.; Xu, Y. J.; Chen, H. M. *Chem. Soc. Rev.* **2017**, *46* (2), 337-365.
(19) Kulkarni, A.; Siahrostami, S.; Patel, A.; Norskov, J. K. *Chem. Rev.* **2018**, *118* (5), 2302-2312.
(20) Favaro, M.; Valero-Vidal, C.; Eichhorn, J.; Toma, F. M.; Ross, P. N.; Yano, J.; Liu, Z.; Crumlin, E. J. *J. Mater. Chem. A* **2017**, *5* (23), 11634-11643.
(21) Tenkortenaar, M. V.; Vente, J. F.; Ijdo, D. J. W.; Muller, S.; Kotz, R. *J. Power Sources* **1995**, *56* (1), 51-60.
(22) Petrykin, V.; Macounova, K.; Shlyakhtin, O. A.; Krtil, P. *Angew. Chem. Int. Edit.* **2010**, *49* (28), 4813-4815.
(23) Labata, M. F.; Li, G. F.; Ocon, J.; Chuang, P. Y. A. *J. Power Sources* **2021**, *487*, 229356.
(24) Liang, H. W.; Wu, Z. Y.; Chen, L. F.; Li, C.; Yu, S. H. *Nano Energy* **2015**, *11*, 366-376.
(25) Zhang, J. T.; Zhao, Z. H.; Xia, Z. H.; Dai, L. M. *Nat. Nanotechnol.* **2015**, *10* (5), 444-452.
(26) Patra, S.; Choudhary, R.; Roy, E.; Madhuri, R.; Sharma, P. K. *Nano Energy* **2016**, *30*, 118-129.
(27) Hadidi, L.; Davari, E.; Iqbal, M.; Purkait, T. K.; Ivey, D. G.; Veinot, J. G. C. *Nanoscale* **2015**, *7* (48), 20547-20556.
(28) Wang, M.; Zhang, C. T.; Meng, T.; Pu, Z. H.; Jin, H. H.; He, D. P.; Zhang, J. N.; Mu, S. C. *J. Power Sources* **2019**, *413*, 367-375.
(29) Wu, F. W.; Feng, B. M.; Li, W.; Liu, H.; Mei, Y. H.; Hu, W. H. *Int. J. Hydrogen Energ.* **2019**, *44* (48), 26387-26395.
(30) Ji, D. X.; Fan, L.; Tao, L.; Sun, Y. J.; Li, M. G.; Yang, G. R.; Tran, T. Q.; Ramakrishna, S.; Guo, S. J. *Angew. Chem. Int. Edit.* **2019**, *58* (39), 13840-13844.
(31) He, Y. J.; Aasen, D.; Yu, H. Y.; Labbe, M.; Ivey, D. G.; Veinot, J. G. C. *Nanoscale Adv.* **2020**, *2* (8), 3367-3374.
(32) Abedi, Z.; Leistenschneider, D.; Chen, W. X.; Ivey, D. G. *Batteries Supercaps* **2022**, *5* (2), e202100339.
(33) McDougall, A.; Abedi, Z.; Ivey, D. G. *J. Appl. Electrochem* **2022**, *52* (3), 437-459.
(34) Muthurasu, A.; Tiwari, A. P.; Chhetri, K.; Dahal, B.; Kim, H. Y. *Nano Energy* **2021**, *88*.
(35) Cheng, W. Z.; Liang, J. L.; Yin, H. B.; Wang, Y. J.; Yan, W. F.; Zhang, J. N. *Rare Metals* **2020**, *39* (7), 815-823.

(36) Li, J. T.; Meng, Z.; Brett, D. J. L.; Shearing, P. R.; Skipper, N. T.; Parkin, I. P.; Gadipelli, S. *ACS Appl. Mater. Inter.* **2020**, *12* (38), 42696-42703.
(37) Lashgari, S. M.; Yari, H.; Mahdavian, M.; Ramezanzadeh, B.; Bahlakeh, G.; Ramezanzadeh, M. *Corros. Sci.* **2021**, *178*, 109099.
(38) Liu, X. H.; Kang, J. J.; Wang, Y. Q.; Li, W.; Guo, H. L.; Xu, L.; Guo, X. H.; Zhou, F.; Jia, X. *Macromol. Rapid Comm.* **2018**, *39* (12), e1800160.
(39) Sheng, K.; Yi, Q. F.; Chen, A. L.; Wang, Y. B.; Yan, Y. H.; Nie, H. D.; Zhou, X. L. *ACS Appl. Mater. Inter.* **2021**, *13* (38), 45394-45405.
(40) Grosvenor, A. P.; Biesinger, M. C.; Smart, R. S.; McIntyre, N. S. *Surf. Sci.* **2006**, *600* (9), 1771-1779.
(41) Biesinger, M. C.; Payne, B. P.; Grosvenor, A. P.; Lau, L. W. M.; Gerson, A. R.; Smart, R. S. C. *Appl. Surf. Sci.* **2011**, *257* (7), 2717-2730.
(42) Xiong, M.; Clark, M. P.; Labbe, M.; Ivey, D. G. *J. Power Sources* **2018**, *393*, 108-118.
(43) Feng, J. M.; Li, Y. L.; Hou, F.; Zhong, X. H. *Mat. Sci. Eng. A-Struct.* **2008**, *473* (1-2), 238-243.
(44) Nam, K. M.; Shim, J. H.; Ki, H.; Choi, S. I.; Lee, G.; Jang, J. K.; Jo, Y.; Jung, M. H.; Song, H.; Park, J. T. *Angew. Chem. Int. Edit.* **2008**, *47* (49), 9504-9508.
(45) Jeong, H. K.; Lee, Y. P.; Lahaye, R. J. W. E.; Park, M. H.; An, K. H.; Kim, I. J.; Yang, C. W.; Park, C. Y.; Ruoff, R. S.; Lee, Y. H. *J. Am. Chem. Soc.* **2008**, *130* (4), 1362-1366.
(46) Jung, H. J.; Choi, M. Y. *J. Phys. Chem. C* **2014**, *118* (26), 14647-14654.
(47) Zhang, D. E.; Ni, X. M.; Zheng, H. G.; Li, Y.; Zhang, X. J.; Yang, Z. P. *Mater. Lett.* **2005**, *59* (16), 2011-2014.
(48) Garcia-Cerda, L. A.; Bernal-Ramos, K. M.; Montemayor, S. M.; Quevedo-Lopez, M. A.; Betancourt-Galindo, R.; Bueno-Baques, D. *J Nanomater* **2011**, *2011*, 162495.
(49) He, Y. J.; Aasen, D.; McDougall, A.; Yu, H. Y.; Labbe, M.; Ni, C. Y.; Milliken, S.; Ivey, D. G.; Veinot, J. G. C. *ChemElectroChem* **2021**, *8* (8), 1455-1463.
(50) Li, C. L.; Wu, M. C.; Liu, R. *Appl. Catal. B-Environ.* **2019**, *244*, 150-158.
(51) Xie, X. Y.; Shang, L.; Shi, R.; Waterhouse, G. I. N.; Zhao, J. Q.; Zhang, T. R. *Nanoscale* **2020**, *12* (24), 13129-13136.
(52) Li, J. M.; Kang, Y. M.; Wei, W. L.; Li, X.; Lei, Z. Q.; Liu, P. *Chem. Eng. J.* **2021**, *407*, 127961.
(53) Rauf, M.; Zhao, Y. D.; Wang, Y. C.; Zheng, Y. P.; Chen, C.; Yang, X. D.; Zhou, Z. Y.; Sun, S. G. *Electrochem. Commun.* **2016**, *73*, 71-74.
(54) Lv, Q.; Si, W. Y.; He, J. J.; Sun, L.; Zhang, C. F.; Wang, N.; Yang, Z.; Li, X. D.; Wang, X.; Deng, W. Q.; Long, Y. Z.; Huang, C. S.; Li, Y. L. *Nat. Commun.* **2018**, *9* (1), 3376.

(55) Ning, X. M.; Li, Y. H.; Ming, J. Y.; Wang, Q.; Wang, H. J.; Cao, Y. H.; Peng, F.; Yang, Y. H.; Yu, H. *Chem. Sci.* **2019**, *10* (6), 1589-1596.

Chapter 5

(1) Sun, W.; Wang, F.; Zhang, B.; Zhang, M. Y.; Kupers, V.; Ji, X.; Theile, C.; Bieker, P.; Xu, K.; Wang, C. S.; Winter, M. *Science* **2021**, *371* (6524), 46-51.
(2) Radenahmad, N.; Khezri, R.; Mohamad, A. A.; Nguyen, M. T.; Yonezawa, T.; Somwangthanaroj, A.; Kheawhom, S. *J. Alloy. Compd.* **2021**, *883*.
(3) Balamurugan, J.; Nguyen, T. T.; Kim, N. H.; Kim, D.; Lee, J. H. *Nano Energy* **2021**, *85*.
(4) Goncalves, P. R.; De Abreu, H. A.; Duarte, H. A. *J. Phys. Chem. C* **2018**, *122* (36), 20841-20849.
(5) Bing, Y. H.; Liu, H. S.; Zhang, L.; Ghosh, D.; Zhang, J. J. *Chem. Soc. Rev.* **2010**, *39* (6), 2184-2202.
(6) Wang, C. Y. *Chem. Rev.* **2004**, *104* (10), 4727-4765.
(7) Sharaf, O. Z.; Orhan, M. F. *Renew. Sust. Energ. Rev.* **2014**, *32*, 810-853.
(8) Mekhilef, S.; Saidur, R.; Safari, A. *Renew. Sust. Energ. Rev.* **2012**, *16* (1), 981-989.
(9) You, B.; Sun, Y. J. *Accounts Chem. Res.* **2018**, *51* (7), 1571-1580.
(10) Vojvodic, A.; Medford, A. J.; Studt, F.; Abild-Pedersen, F.; Khan, T. S.; Bligaard, T.; Norskov, J. K. *Chem. Phys. Lett.* **2014**, *598*, 108-112.
(11) Franchi, G.; Capocelli, M.; De Falco, M.; Piemonte, V.; Barba, D. *Membranes* **2020**, *10* (1), 10.
(12) Liu, Z.; Ciais, P.; Deng, Z.; Lei, R.; Davis, S. J.; Feng, S.; Zheng, B.; Cui, D.; Dou, X.; Zhu, B.; Guo, R.; Ke, P.; Sun, T.; Lu, C.; He, P.; Wang, Y.; Yue, X.; Wang, Y.; Lei, Y.; Zhou, H.; Cai, Z.; Wu, Y.; Guo, R.; Han, T.; Xue, J.; Boucher, O.; Boucher, E.; Chevallier, F.; Tanaka, K.; Wei, Y.; Zhong, H.; Kang, C.; Zhang, N.; Chen, B.; Xi, F.; Liu, M.; Breon, F. M.; Lu, Y.; Zhang, Q.; Guan, D.; Gong, P.; Kammen, D. M.; He, K.; Schellnhuber, H. J. *Nat. Commun.* **2020**, *11* (1), 5172.
(13) Voldsund, M.; Jordal, K.; Anantharaman, R. *Int. J. Hydrogen Energ.* **2016**, *41* (9), 4969-4992.
(14) Yu, F.; Zhou, H. Q.; Huang, Y. F.; Sun, J. Y.; Qin, F.; Bao, J. M.; Goddardiii, W. A.; Chen, S.; Ren, Z. F. *Nat. Commun.* **2018**, *9*, 2551.